VOLUME 11, ISSUE 1, JUNE 2026

JESA

JOURNAL OF ENGINEERING AND SCIENTIFIC ADVANCES



Dhaka University of Engineering & Technology, Gazipur

Journal of Engineering and Scientific Advances Committee

Chief Patron

Prof. Dr. Engr. Mohammad Iqbal
Vice-Chancellor

Patron

Prof. Dr. Engr. Ruma
Pro-Vice-Chancellor

Editor-in-Chief

Prof. Dr. Md. Anwarul Abedin
Department of Electrical and Electronic Engineering

Associate Editor-in-Chief

Prof. Dr. Md. Rezaul Karim
Department of Civil Engineering

Prof. Dr. Mohammad Abu Taher
Department of Mathematics

Prof. Dr. Fazlul Hasan Siddiqui
Department of Computer Science and Engineering

Prof. Dr. Nayeem Md. Lutful Huq
Department of Mechanical Engineering

Editors

Prof. Dr. Mohammad Washim Dewan
Department of Mechanical Engineering

Prof. Dr. Shahjalal Khandaker
Department of Textile Engineering

Prof. Dr. Bayezid Ismail Choudhury
Department of Architecture

Prof. Dr. Md. Abdur Rahman Forhad
Department of Humanities and Social Sciences

Prof. Dr. Md. Mahmudur Rahman
Department of Electrical and Electronic Engineering

Prof. Dr. Md. Monowar Hossain
Department of Civil Engineering

Prof. Dr. Amran Hossain
Department of Computer Science and Engineering

Prof. Dr. Farah Deeba
Department of Physics

Dr. Md. Shahabuddin
Assoc. Prof., Department of Chemistry

Dr. Mohammad Rashidul Hassan
Asst. Prof., Department of Industrial and Production Engineering

Cover Design

Mr. Aqib Mohammad Nibir
Lecturer, Dept. of Architecture

Table of Contents

Sl. No.		Page
01.	Development Deficit and Fertility Persistence in Bangladesh: Revisiting Malthusian Explanations *Maruf Ahmmed, Anwar Hossain Choudhury and Rubel*	1
02.	Performance Analysis of an Electric Motorcycle with IoT Based Monitoring *Md. Anwarul Abedin, Md. Monerul Islam and Anik Kumar Chowdhury*	15
03.	Data Driven Evaluation of Smart Grid Adaptation in Dhaka Electric Supply Company Limited: Challenges and Opportunities *Md Mijanur Rahman, Md Saiful Islam Saif, Md Abdus Salim*	23
04.	Valorization of *Moringa Oleifera* Pod Residues into Functional Lignocellulosic Fiber: A Chemical and Mechanical Performance Study *Md. Ahasan Habib, Habiba Akter, Md. Golam Mortuza Limon, Jannatul Nasrin, Ranajit Kumar Nag, Shomit Roy Prangon, S.M. Osman Ali, Md. Al-Amin, and Mehedi Hasan*	33
05.	Finite Element Analysis of Aluminum-Vanadium Alloyed Titanium Billets Forged under Warm Forming Conditions Using DEFORM-3D *Rotan Kumar Saha, Golap Hossain and Rajib Talukder*	45
06.	Impact of Magnetic Nanoparticle-based Priming on Potato Seed Germination in Bangladesh *Jakia Mustary Lina, Shubro Biswas and Md. Mahmudur Rahman*	55
07.	Development of Rapid Feedback and Optimized Detection Algorithms to Enhance the Spatiotemporal Resolution of the ABEL Trap *Nahid Hasan, Rahul Islam, Md Asif Bin Sayed, Swopan Chandra Barman, Sanjid-E-Elahi and Md. Mahmudur Rahman*	63
08.	Evaluating the Feasibility of a Trumpet Interchange at Shibbari Intersection under Current and Future Traffic Growth: A Microsimulation Approach *Md. Jamil Mahmud Abdullah, Mahiman Zinnurain, Mohammad Kabir Hossain, Noman Hasan Fahim, Md. Zakir Husen and Jahid Hasan*	73
09.	Damage Assessment and Residual Capacity of Fire-Exposed RC Columns: A Multi-Parameter 3D FEA Study *Md. Sadman Sakib Khan, Md. Ashikuzzaman, Syed Samsudduha Bijoy, Md. Shariar Hossain, Mahiman Zinnurain and Shameem Ahmed*	85
10.	GIS-Based Spatial Analysis and Identification of Road Traffic Accident Hotspots: A Case Study of the Dhaka-Mymensingh Highway (N3), Gazipur, Bangladesh *Md Ibrahim Khalil, Pias Pal, Shariful Islam, Mahiman Zinnurain, Mohammad Kabir Hossain and Hriday Chandra Bhoumik*	93
11.	Assessment of Land Use and Land Cover (LULC) Changes along the MRT-6 Corridor in Dhaka Using Multi-Temporal Satellite Data *Pias Pal, Md. Ibrahim Khalil, Swe Kya Waiy Marma, Mahiman Zinnurain, M. Afzal Hossain and Md. Sabbir Hosen*	101
12.	Multi-Objective Optimization of Window-to-Wall Ratio for Thermal and Visual Comfort: The Impact of Vertical Spatial Positioning in Hot-Humid Climates *Maria Jebin, Shunila Binte Ahsan and Md. Galib Nur Anan*	109

Development Deficit and Fertility Persistence in Bangladesh: Revisiting Malthusian Explanations

Maruf Ahmmed*, Anwar Hossain Choudhury and Rubel

Department of Sociology, University of Chittagong, Bangladesh

ABSTRACT

This paper critically examines the dominant Malthusian perspective in the context of Bangladesh, which attributes population growth as the root of the nation's poverty and underdevelopment. Conversely, this study seeks to explore how the diverse socio-economic underdevelopment dynamics across Bangladesh serve as the crucial factors shaping the country's fertility and demographic landscape. By employing a quantitative analysis, assisted by secondary socioeconomic and demographic data from 1991 to 2024, this study redefines conventional views on population-development nexus. The findings of this study convincingly demonstrate that the deep-rooted underdevelopment standpoint in Bangladesh, marked by sluggish industrialization, enduring poverty, and institutional weakness, shapes traditional societal meanings and perceptions, that define gender roles and expectations, which subsequently influence people's fertility behavior. These forces, in turn, worsen imbalanced population momentum and intensify the nation's demographic stress. The standing of this research emerges from exploring the credible association between development insufficiency and population upsurge, prioritizing for a development-first approach to achieve demographic stability in countries like Bangladesh. Furthermore, the study advocates for strong socioeconomic enrichment and emphasizes the transformative impact of these actions to ensure population stabilization. All of which may lead to a prosperous future and inspire hope through stable population dynamics in Bangladesh and beyond.

Keywords: Bangladesh, Fertility Behavior, Demographic Challenges, Structural Underdevelopment, Gender Role.

1. INTRODUCTION

Since the dawn of humanity, the human species has grown from a hypothetical origin of two individuals about a hundred thousand years ago to about 8.2 billion people today [1], [2]. Projections suggest this number will continue to climb over the next 50 or 60 years, reaching a peak of around 10.3 billion people in the world by the mid 2080s [2]. Almost all this population growth is concentrated in the least developed countries (LDCs)[1],where the population is growing at 2.4% annually, more than twice as fast as that of the developed world, is experiencing a decline of 0.2% per year [3]. LDCs have the lowest socio-economic development, with their combined gross domestic product (GDP) accounting for just 1.4 per cent of global GDP in 2022. Despite the economic growth of LDCs remaining slow, their populations are expanding rapidly, expected to increase from 1.2 billion in 2023 to nearly 1.9 billion by 2050[4]**.** Three LDCs are among the 15 most populous countries in the world, including Bangladesh (173 million), followed by Ethiopia (127 million) and the Democratic Republic of the Congo (102 million). By 2050, Bangladesh will be the 8th most populous nation in the world, accounting for a 2.4% share of the world population [5]. These figures have fueled considerable scholarly debate over the past decades about the insight into such demographic trends. Prevailing research knowledge, rooted in classical Malthusian interpretations and later echoed by numerous scholars and development planners, often positions fertility rates and uneven population growth as constraints on development and causes of poverty, underdevelopment, and resource depletion [6-10]. This viewpoint has profoundly influenced decades of policies, especially in least developed countries including Bangladesh, resulting in the adoption of highly restrictive measure to control population growth, often sacrificing the reproductive rights of their citizens [11], [12]. Moreover, contemporary scholarly knowledge also reliably underscores demographic factors or population-

1 More-developed, less-developed, and least-developed regions follow the UN classification (https://www.un.org/ohrlls/content/least-developed-countries)

*Corresponding author's email: marufahmmed@cu.ac.bd

first narratives as dominant in determining socio-economic well-being and shaping economic advancement in different regions of the world [13], [14].

Recent studies on Bangladesh show that, despite low gross domestic product, pervasive poverty, and the persistent income inequality, Bangladesh has achieved substantial fertility decline [15]. Some attribute this to women's empowerment and widespread education [16]. However, this remarkable achievement is offset by the alongside country's ongoing demographic burden, including unwanted fertility and socioeconomic disparities, often described as the "Bangladesh Paradox" [15]. Recognizing all these inconsistencies highlights the need for more comprehensive research to obtain fundamental insights into the factors that conclusively shape demographic patterns in LDC countries such as Bangladesh.

Relying on these deterministic interpretations consistently fails to identify the deeper structural roots of demographic trends, particularly where various socio-economic development constraints play a significant role in determining the demographic outcomes in Bangladesh. However, to the author's best knowledge, there remains limited empirical research to identify the association between these underdevelopment factors and the demographic realities in Bangladesh. Given this complexity, further study is essential to examine the association between the country's diverse socioeconomic underdevelopment context with fertility trends and demographic outcomes. Based on all these considerations, this research aims to address this gap by focusing on the following research question:

How might Bangladesh's deeply entrenched socioeconomic underdevelopment burden contribute to and possibly be associated with people's fertility behavior and existing demographic challenges in Bangladesh, rather than serving as a cause of this burden?

To address this inquiry, the objective of the study is to explore this viewpoint within the context of historical and structural underdevelopment and to provide a broad understanding of the association between numerous socio-economic underdevelopment factors and population outcomes in Bangladesh. By highlighting this, the study contributes to resolving the population–development debate in Bangladesh by emphasizing a development first approach to achieve population equilibrium. This provides new insight into the intersection of structural underdevelopment, fertility behavior and demographic outcomes, which argues that only comprehensive structural improvements can enable the country to unlock its untapped demographic potential.

This paper proceeds as follows: Section 2 comprises an extensive literature review for this research. Section 3 builds the conceptual framework, and Section 4 highlights the methodology of the study. Section 5 presents the historical origin of development constraints in Bangladesh, Section 6 presents result and discussion, limitations and future research prospect of the study, and Section 7 concludes the paper with policy recommendations.

2. RETHINKING THE POPULATION DEVELOPMENT DISCOURSE IN BANGLADESH

The interaction between development and population growth remains an issue of considerable dispute within the development paradigm. At its core, the prominent perspectives termed as the "Alarmist" or "Pessimistic" view, ingrained in Malthusian and Neo-Malthusian scholarly writings, argues that unchecked population growth will outstrip the means of subsistence, exhaust human well-being, create enduring poverty, and diminish happiness [6-8]. The US National Academy of Sciences report [17], Brown [9] further influenced popular perceptions, arguing demographic challenges as a major obstacle to sustainable development, and recommended to limit population growth. These dominant insights tend to oversimplify or overlook the multifaceted socioeconomic realities of a country's demographic outcome [12], [18], 19].

Despite its policy influence, the Malthusian paradigm has increasingly been challenged by scholars such as Marx. Thompson, Kuznets, Simon. They argue that distributive justice of wealth and power, modernized arrangement, industrialization and reshaping economic roles and social institutions are perquisite for balanced population trends-particularly fertility decline [20], [21-23]**.** Yet, these analyses often assume linear modernization pathways that may not reflect the experiences in least-developed economies like Bangladesh.

The contemporary empirical literature relevant to population and development further contribute to this enduring debate. Bayant [24] reframes socioeconomic theory, explaining that fertility behavior in poor and less developed countries determined by incentives to have fewer children rather than driven by development indicators. While Tang and Tey [25] focused on the Malaysian context and demonstrated that the fertility

rate is cointegrated with its structural determinants, such as, female employment, female education, and quality of health care and per capita income. Drawing on econometric evidence, Zakaria et al [26] and Sethi et al [27] disclose the effect of financial sector development on fertility in selected South Asian countries over a specific time. Similarly, research by Lerch [28] has highlighted the fertility differentiation between rural and urban areas in developing countries while Yeung & Abalos [29] investigate the comparative trends of fertility behaviors across Asia, stressing the influence of the interplay of structural, cultural, and policy factors. Moreover, while different literature on Bangladesh demographic perspectives have underlined influence of various socio-cultural and economic factors on fertility outcomes, [30], [31], [32], their studies remain insufficient to establish a definitive association between underdevelopment factors and population burden in Bangladesh. While these studies provide valuable insights, their scope remains confined to analyzing only the interaction between demographic changes and either specific financial or social indicators or broad regional aggregates. Furthermore, several of these studies largely focused on other national contexts, provided little in-depth country specific analysis, particularly for Bangladesh, and often stressed on population growth as the principal cause of underdevelopment. Drawing on these consensuses, the present study emphasizes the Bangladesh context and introduces an alternative analytical perspective through prioritizing macro-structural and micro-social perspective to uncovers how enduring key socio-economic underdevelopment factors continue to shape demographic behavior over time.

3. CONCEPTUAL FRAMEWORK

This study draws on dependency, structuralist [33], [34], and sociological perspectives [35] to explore the deeper systematic underdevelopment in Bangladesh that arises from both internal and external structural constraints which influence population dynamics. Adding these multidimensional frameworks is crucial for understanding how colonial legacies continue to siphon resources from the country, produce a dependent economic structure [33], intertwine with various domestic development constraints [34].All of these create a fragile industrial base, which hindering sustained socio-economic growth for a peripheral nation like Bangladesh. This macro-level analysis is further supplemented by micro-level scrutiny of Blummer's symbolic interactionism [35], which validated the idea is that individual and community actions are guided by the meanings they create in daily social interactions and thus humans' interactions act as active agents in constructing social reality. This insight conjectures that, individual and community conduct associated with family size, gender roles, and reproductive decisions are thereby profoundly influenced by the socially constructed interpretation of meaning. We utilize Baran's [33] view to clarify the structural origin of underdevelopment in Bangladesh through surplus extraction and external dependencies. While Myrdal's [34] conceptualized underdevelopment through his cumulative causation model which shows how weakly articulated modes of production, diminished productivity, poor living standards, fragile institutions, inadequate policy and low literacy level interact to perpetuate cycle of poverty and inequality shaping long trajectories of underdevelopment over time [34]. These internal socio-economic fragilities further construct the collective social perception [35] about family size, and gender norms and roles.

Building on these perspectives, in this study, socio-economic underdevelopment aspects of Bangladesh can be conceptualized as a web of structural, institutional and social constraints arising from historical inability to channel economic surplus toward productive sectors, which impedes the transition from an agrarian peasant economy to a more industrialized one. This stagnation results in increased unemployment, poverty and low income, while it also restricts investment in education, health, and the social security system. These fundamental structural constraints impede the rise of progressive norms, values, and culture within both families and the communities. Such socially embedded customary perception undermines collective well-being and shape socio-cultural perception expressed through large family norms, son preference, early marriage, and persistence of patriarchal values. Altogether, these socio-economic realities halts modernization efforts, dimming the prospect of a more enlightened worldview—a conversion from traditional ways of thinking and behaving [36]. In the end, these restrict women's empowerment, equality and autonomy in fertility choice which set the stage for an imbalanced population dimension in Bangladesh.

When these transformative social and economic elements are effectively aligned, they create such a reasonable social environment that reduces poverty, raises living standards, and fosters more equitable social and economic conditions for all. These progressions contribute to demographic equalization across the country [12], [18]. The study therefore generates hypotheses that deep-

rooted socio-economic development constraints such as weak industrialization, poverty, low education and health attainment, fragile social security system determine that socially embedded gender perspectives have a positive association with the country's demographic challenges.

This contrast disrupts the simplistic Malthusian view, by highlighting the fundamental structural development deficit that caused to demographic challenges (fig. 1) and inviting us to rethink the argument that population pressure in Bangladesh is an indication of its historically entrenched socio-economic underdevelopment perspectives.

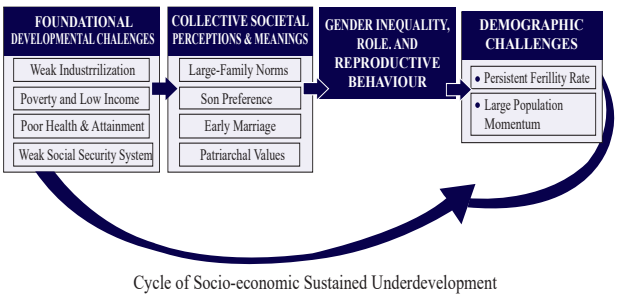


Fig. 1: Conceptual framework

This framework illustrates how, foundational development constraints, shape collective societal perceptions and meanings, which generate gender inequality, determine gender roles, and shape reproductive behavior. These dynamics sustain demographic challenges, ultimately again perpetuating the same cycle of socio-economic constraint and reinforcing underdevelopment.

4. MATERIAL AND METHODS

4.1. Sources of Information

This study employs a quantitative analysis to examine association between socioeconomic underdevelopment indicators and fertility outcomes that intensify demographic challenges in Bangladesh. The data set for each variable is used in this study obtained from rich array of national and international recognized sources including regular social and economic survey of Bangladesh Bureau of Statistics, relevant UN and World Bank estimates [15]. Moreover, additional references, such as books, journals, research reports, and working papers, were also reviewed and analyzed, precisely focusing on literature relevant to Bangladesh. Integration of data from multiple sources minimizes bias and links demographic behavior with socio-economic and institutional patterns, reinforcing the methodological rationale and assessing consistency between observed outcomes and theoretical expectations through pattern matching.

4.2: Data Overview and Analysis

This study utilizes data spanning from 1991 to 2024. The year 1991 was chosen as the starting point because Bangladesh initiated accelerated reforms under the structural development adjustment program during this decade, which substantially influenced the country's demographic dynamics. The data period ended in 2024 since the availability of complete datasets for all variables considered in this study. However, only health expenditure analysis uses data from the year 2000 onwards due to data unavailability and to maintain consistency across sources. In the conceptual framework (Fig. 1), demographic challenges were represented by the persistence fertility rate and large population momentum. However, for the statistical analysis, only fertility rate was considered as dependent variable, since population growth is viewed as the direct outcome of fertility behavior. Moreover, this study considered socioeconomic determinants, including core developmental challenges and gender roles as independent variables, since these factors outline a person's reproductive behavior and contribute to demographic stress in Bangladesh. However, within the analytical framework alongside socioeconomic determints, gender role was considered the key variable for measurement, recognizing the view that, it is shaped not only by the collective societal meanings and norms but also closely tied to women's agency in reproductive behavior. By capturing this, the study quantified how structural barriers and socio-cultural expectations relate to demographic outcomes in Bangladesh.

Table I: summarize and describe representation all the variables analyze in this study.

Variable Description	Proxied By
Fertility rate	Total births per woman,
Industrialization	Industry value added (% of GDP)
Poverty rate	Poverty headcount ratio (% of population)
Income per capita	GNI per capita, PPP (current US$)
Education Attainment	Literacy rate, adult total (% of people ages 15 and above)
Health Attainment	Health expenditure (% of GDP).
Gender Roles	Female labour force participation (% of total labor force).

Note: All data are sourced from World Development Indicators (World Bank), ILO, UNFPA, WHO, BBS

In this study, gender role is proxied by female labour force participation, as it unveils the depth of structural constraints and socio-cultural attitudes that impact female economic empowerment. This demonstrates the behavioral

dimension of gender inequity which links social meanings to women's fertility behavior and demographic outcomes.

Characteristics of all the study variables were summarized using descriptive statistics, which helps us to understand the further analysis. The descriptive statistics of this study examine the direction and strength of possible association between socio-economic underdevelopment factors and fertility trends shaping demographic stress. Pairwise correlation analysis was used to find the direction and strength of relationships among the study variables. Furthermore, to find the individual effect of explanatory variables on Total Fertility rate (TFR), univariate regression analysis was done. Subsequently, a multiple regression model including all predictors was fitted. To detect the problem of multicollinearity, the variance inflation factor (VIF) was calculated. Usually, VIFs are greater than 10 for many independent variables, indicating severe multicollinearity. When multicollinearity exists, regression results are unreliable, and as a result, misleading inferences are drawn. To overcome the disturbance of multicollinearity, Principal Component Analysis (PCA) is a reliable tool, thus ensuring stable and accurate assessments [37], [38]. That's why by using Principal Component Analysis, a socio-economic development index is created by combining six socio-economic independent variables, i.e., industry, poverty, GNI per capita, literacy rate, health expenditure and female labor force. The first principal component, which explained most of the total variance, was used as the index for subsequent regression analyses. Finally, the constructed socio-development index was used in a regression model to estimate its effect on TFR. So, the final model is

$$TFR_i=\beta_o+\beta_1 Socio-development\ index+\epsilon_i$$

Where, ϵ_i is the error term.

The overall analysis offering a possible pathway that may link underdevelopment aspects and fertility as well as population outcomes in Bangladesh.

5. EXAMINING BANGLADESH: HISTORICAL ROOTS, DEVELOPMENT CONSTRAINTS AND ONGOING DEMOGRAPHIC CHALLENGES

Addressing the relationship between underdevelopment and demographic challenges requires a sound understanding of the country's historical root of unprivileged situation. The demographic experiment in Bangladesh has intense structural roots that can be traced back to a long-standing pattern of underdevelopment shaped by 215 years of colonial and post-colonial rule and exploitation, which continues to shape its contemporary development and population paradigms [18]. After the Battle of Plassey (1757), the victory of British power facilitated primitive capital accumulation through the colonial 'structured plunder' where surplus was siphoned out of the Bengali region [39]. William Digby's (1901) evidenced this extraction and stated that, in just 58 years, from Plassey (1757) to Waterloo (1815), approximately five billion pounds worth of capital was transferred from India to the English Bank (as cited in [19]), the bulk of this capital unquestionably came from the British-occupied richest structure of the data and detect potential inconsistencies in province, Bengal. The intensive extraction of economic surplus stalled capital formation and consequently industrial self-reliance, thereby creating a dependent economic structure that contributed to enduring economic fragility in colonial Bengal [18], [19], [39].

In 1947, the two-nation theory resulted in the creation of India and Pakistan. Following partition, Pakistan's state power was used to extract surplus from East Pakistan's (now Bangladesh) agrarian economy while systematically underinvesting in its infrastructure and social welfare.

Following independence in 1971, the newly implemented economic policies of the young nation were further weakened by the powerful interests of the political elite and the state's inability to invest in establishing articulation between agriculture and industry, as well as education and health, thereby weakening the building of human capital [18].

These factors added a layer of complexity to the country's development, reinforced external dependencies, and stalled the rise of self-sustaining industrialization, resulting in a mismatch between development strategies and demographic policies that Bangladesh would face for decades to come.

The result is evident: despite a substantial decline in the fertility rate in Bangladesh from 6.1 children per woman in the 1980s to 2.2 in 2024 [3], Bangladesh is still experiencing a relentless demographic burden. This ongoing challenge steam from economic and institutional fragile conditions, that remains insufficient to the ensure the social progress necessary to absorb demographic burden. Kuznets [21] demonstrated that population trends, particularly fertility decline—follow patterns of industrialization, urbanization, and income growth, reshaping both economic roles and social institutions. The origin of this structural root of underdevelopment provides an important insight for understanding fertility

pattern and its association with underdevelopment factors in Bangladesh. To examine these relations empirically, the following graph and statistical analysis are shown in the results and discussion section which are consistence with analytical expectations.

6. EMPIRICAL RESULT AND DISCUSSION

This section presents empirical results and analyzes how different contemporary socio-economic underdevelopment forces impede the achievement of demographic equilibrium in Bangladesh.

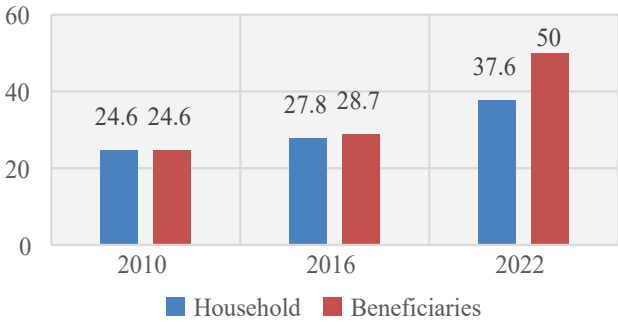
6.1 Foundational Developmental Challenges and Demographic Pattern

Colonial and post-colonial Bengal plundering and post-independence government inability to establish the wave of industrialization in the nation increase dependence on agriculture that failed to increase employment and per capita income. Additionally, persistence of informal labor market and limited technological innovation and diversification, have also resulted in restricted job opportunities. So high levels of Poverty and youth underemployment are inevitable, which can lead to economic instability.

In Bangladesh's workforce is mostly engaged in agriculture, (44.70%), compared to just 17.4% in the industrial sector [40]. Between 2016 and 2022, most are jobs are created in the agriculture sector, where a large number are low-paying and informal positions. During the same period, employment in urban areas grew by only 0.7 million [41]. Limited industrialization, subsequent unemployment and poverty have also led to the hampers access to essential services such as healthcare, education and social security system in which also population pressures manifest. In Bangladesh, only 59% of the population has access to basic sanitation services [42]. Additionally, the literacy rate stands at only 74%, with significant disparities in urban and rural areas [43]. Weak industrialization and limited opportunity for access to education, health care and the social security system confine economic opportunities. Which alternatively boosts the quality of life, increases the cost of raising children and lessens their economic value. This also increases awareness of family planning reducing demographic stress.

Fragile social security system is also another key indicator fueling demographic challenges in Bangladesh. Social security programmes stand as evidence-based intervention to reduce vulnerability and economic insecurity by providing financial aid and essential services to those most in need. The Government of Bangladesh (GOB) introduced the National Social Security Strategy (NSSS) in 2015 to strengthen and consolidate its existing social security programmes [44].

Fig. 2: Percentages of household and beneficiaries enrolled in social security programme from 2010-2022.



Source-HIES 2022, Cabinet Division, 2023

However, due to limited financial space, weak administrative capacity, and flaws in beneficiary selection mechanisms, restrict the truly inclusive social protection system for all deserving people (Fig. 2) [45]. As a result, increases the economic reliance on children, especially son for old age financial security, contributes to higher birth rates. Only the provision of alternative forms of insurance may reduce the perceive economic value of children, subsequently decrease the people's need for more children [46].

Figures, (3-7), provide the graphical presentation between fertility and its association with development factors in Bangladesh. It is evident from these graphs that

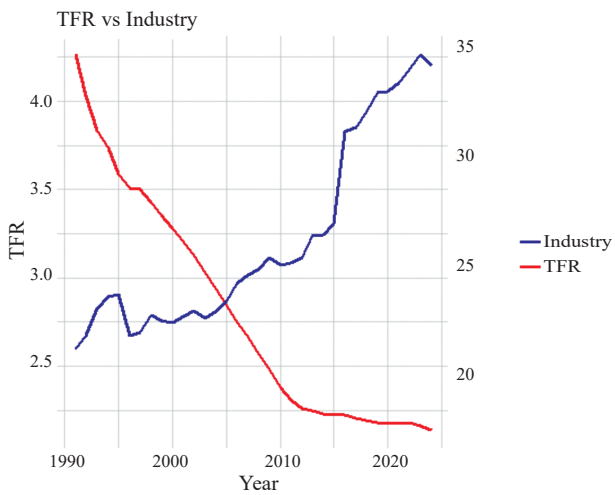


Fig. 3: Fertility and Industrialization

fertility is negatively associated with all variables except, poverty, which has affirmative involvement with fertility. These graphical records again support our hypothesis that demographic outcomes are the consequences of development deficit—not act as its cause.

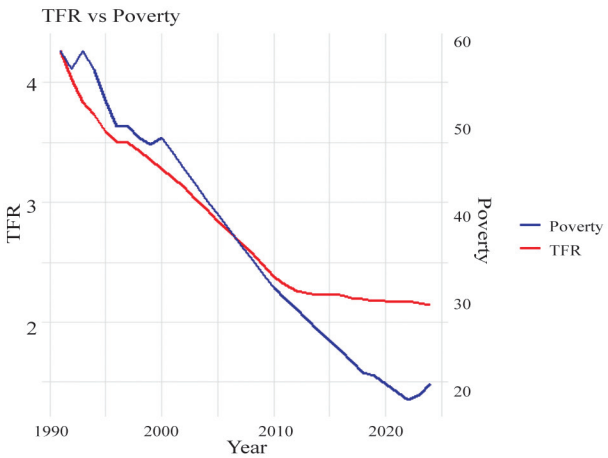


Fig. 4: Fertility and Poverty

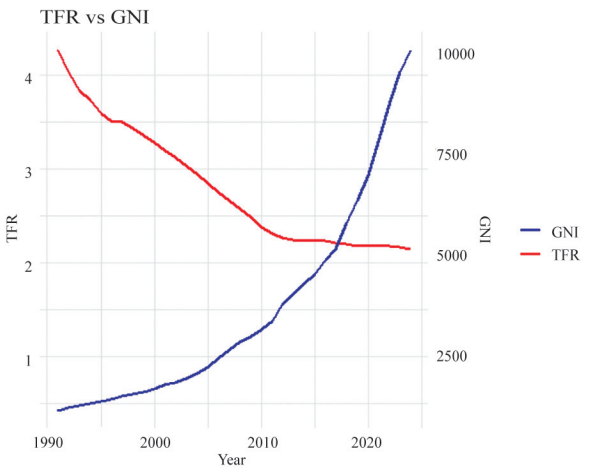


Fig. 5: Fertility and Income (GNI per capita)

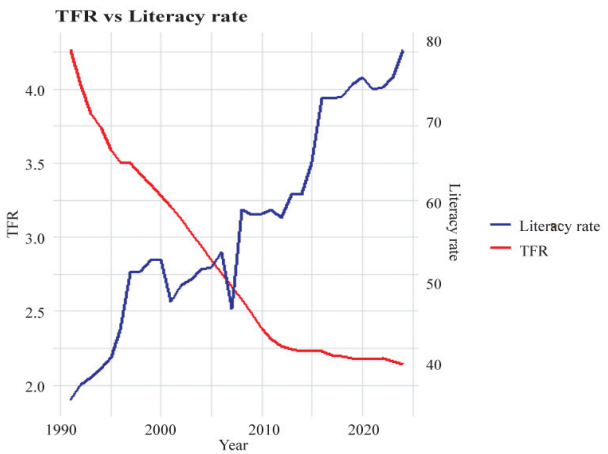


Fig. 6: Fertility and Educational (literacy) Attainment

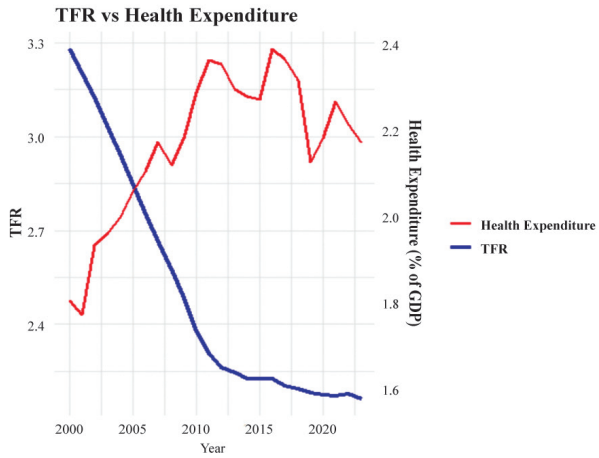


Fig. 7: Fertility and Health Attainment (expenditure)

6.2 Traditional Norms, Gender Roles, and Demographic Outcomes

Gender inequality, traditional norms remain a critical factor in shaping Bangladesh's population dynamics. "Fertility—the number of children a woman has-is not just a barometer for predicting population growth or decline. It can also be a measure of the quality of women's lives, whether they have no children, a few, or many". [47], p-43). In many LDCs like Bangladesh, the last (but not least) cause of high birth rates is the systematic exclusion of women from the development process. Moreover, patriarchal social norms, economic and social subordination of women, absence of a social security system, and inability to participate in the skilled labor force combine to force many women into having more children than they want. For example, in Bangladesh, child marriage by age 18 is about 51% and decision-making on reproductive health and reproductive rights by women is only 64% [48]. As argued by Kathleen Newland [49] in her extensive study of women, within the socio-cultural system, women's positive images are allied to their reproductive role, which seen as the only way for women to attain a sense of purpose and accomplishment. For instance, Children are often seen here as the main sources of a woman's pride, self-respect, and economic security. In the absence of inclusive social security system and faced with the very real possibility of widowhood, divorce, or abandonment, many women need children, especially sons, both for old-age support and to protect their rights to land and other property[12]. A team of demographers studied a village in Bangladesh and concluded: "The risk and insecurity that patriarchy imposes on women represent a powerful systemic incentive for high fertility.

Table II: Correlation Matrix

	Fertility	Poverty	Industry	GNI per Capita	Literacy rate	Health expenditure	Female Labor force
Fertility	1						
Poverty	0.975*	1					
Industrialization	-0.776*	-0.878*	1				
Income per Capita	-0.775*	-0.875*	0.962*	1			
Education Attainment	-0.899*	-0.951*	0.911*	0.900*	1		
Health expenditure	-0.892*	-0.788*	0.527*	0.481*	0.594*	1	
Gender Role	-0.924*	-0.975*	0.924*	0.923*	0.949*	0.673*	1

* Indicates that the correlation coefficient is significant at 5 % level of significance

The best risk insurance for women ...is to produce sons, as many and as soon as possible." ([50], p.432).

Female literacy and employment are also associated with high birth rates and infant mortality. Although female literacy rates have been rising here, they still fall considerably short those of men. Household income and Expenditure Survey [43], shows that, males have a higher literacy rate (75.8%) than females (72.3%) in Bangladesh. Beyond literacy, women's employment in the skilled labor force is also linked to fertility decline (fig. 8), not only because of competition with motherhood, but because the availability of such jobs serves as an incentive to families to educate girls [12], [51]

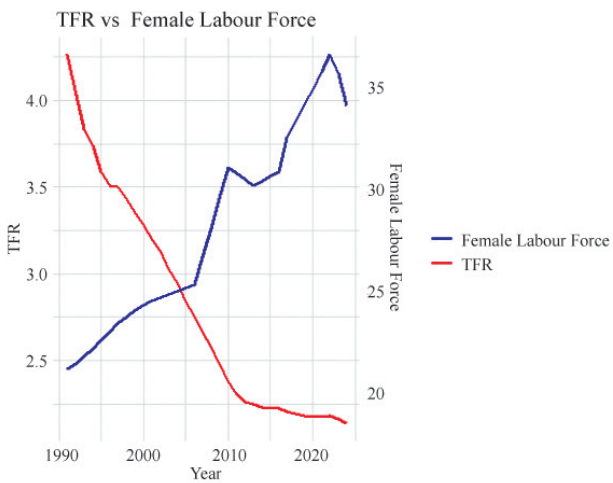


Fig. 8: Fertility and Gender Roles

The Bangladesh Labour Force Survey [40] estimates that 71.71 million people were participated in the labour force. However, momentous gender disparities are observed here: the male labour force accounted for 67%, while the female represented for only 33% [40].

An educated woman is usually less closely confined, physically and psychologically, and has a broader worldview. So, discrimination and socioeconomic barriers, traditional norms and cultural aspect often prevent women and adolescents from making autonomous decisions about their reproductive health [2]. Consequently, such conditions tend to prevent or postpone the reduction of fertility in populations that are growing rapidly, in countries like Bangladesh. In a traditional agricultural society like Bangladesh, high fertility rates persist, largely because social standing is determined mainly by family membership; children contribute a lot but do not cost much, religious and cultural support for having more children, which consequently exacerbates demographic stress. According to G. Carlson, "Birth control behavior is contagious, and the fertility behavior of a population is not the simple aggregate of isolated individual decisions, but the end product of complex social interactions." (as cited [52] p.374).

The statistical analysis of this study again supports our hypothesis pathway and conceptual expectations about the outcomes of the control variables. Table-II provides correlation matrix between the variables. All variables have statistically significant negative correlation with fertility except poverty, which is significantly positively correlated with fertility. These results corroborate theoretical and analytical justification

Table III displays the univariate regression analysis, which revealed that all the explanatory variables are statistically significantly associated with the total fertility rate at 5% level of significance.

Table III: Results of Univariate Regression Analysis

Independent Variable	Co-efficients	Standard Error	p-value
Poverty	0.048	0.002	0.00
Industrialization	-0.114	0.016	0.00
Income per capita	-0.000192	0.000028	0.00
Education attainment	-0.047	0.004	0.00
Health expenditure	-1.957	0.212	0.00
Female Labor force	-0.123	0.009	0.00

Here, poverty showed a strong positive association with TFR, whereas all other variables exhibited significant negative associations with TFR. Higher poverty levels are associated with higher fertility rates. Specifically, a 1 unit increase in poverty is associated with an increase of 0.048 children per woman. In contrast, Industrialization is negatively associated with TFR, indicating that a 1 unit increase in industrialization results in a 0.114 decrease in children per woman. Similarly, income (GNI) per capita is associated negatively with TFR, with a 1 unit increase corresponding to a decrease of 0.000192 children per woman. Education (Literacy) shows the same pattern, where an increase in literacy (1 unit) is associated with a decrease of 0.047 children per woman. Furthermore, A strong negative association is found between health expenditure and TFR, indicating that a one unit increase in health expenditure corresponds to a decrease of 1.957 children per woman.

Gender role as proxied by female labor force participation also shows an adverse relationship, indicating that a 1-unit increase in female labor force participation is associated with a decrease of 0.123 children per woman. However, socio-economic variables are generally connected; therefore, this relationship may be affected by multicollinearity. A multivariate analysis is subsequently done to assess this.

Table IV presents the results of the multivariate analysis, indicating that only a subset of the variables is statistically significant after controlling for other factors. Moreover, VIF is greater than 10 for all the variables except health expenditure, which indicates that the data is suffering from severe multicollinearity. These high VIF values suggest that the regression coefficient may be unstable and difficult to interpret due to strong correlations among the explanatory variables. So, to solve this problem, a socio-economic development index is computed from those explanatory variables by using Principal Component Analysis (PCA).

Table IV: Results of Multivariate Regression Analysis

Independent Variable	Co-efficients	Standard Error	p-value	VIF
Poverty	0.0502	0.00523	0.000	56.31
Industrialization	0.0306	0.00913	0.004	33.90
Income per capita	0.000029	0.00001	0.063	26.43
Education attainment	0.0008	0.00291	0.775	19.49
Health expenditure	-0.1764	0.12055	0.162	9.64
Female Labor force	-0.0127	0.00806	0.133	23.83

The results of PCA are shown in Table V, which revealed that the first principal component explained 86.31% of total variance and is interpreted as a socio-economic development index.

Table V: Results of Principal Component Analysis

Component	Eigen value	Variance Explained (%)	Cumulative (%)
Component-1	5.178	86.31	86.31
Component-2	0.654	10.91	97.22
Component-3	0.095	1.59	98.81
Component-4	0.043	0.69	99.49
Component-5	0.017	0.28	99.77
Component-6	0.014	0.23	100

The PCA-based regression results presented in Table-VI indicate that the socio-economic development index (β=−0.153, p=0.014) is strongly and significantly negatively associated with TFR. Specifically, one unit increase in the socio-development index is associated with a decrease of 0.153 children per woman, which is consistent with the methodological rigor, where this study becomes operationalized and allow us to identify the underlying configurations, that contest the conventional Malthusian diagnosis regarding the population-development paradigm.

Table VI: Results of Regression Analysis After PCA

Independent Variable	Co-efficients	Standard Error	p-value
Constant	2.503	0.030	0.000
Socio economic development index	-0.153	0.014	0.000

Across all the dimensions, evidence the Bangladesh's population pressures closely associate with its historical and structural underdevelopment root. As such, population stabilization requires deep institutional reform, industrial diversification, and inclusive human development.

The developmental and demographic landscape of Bangladesh also resonates with the experiences of key Southeast, East Asian and Western nations perspectives. During the nineteen-century massive industrial boom in Western world, fueled an enormous shift from agriculture to industry as a chief source of employment, income, thereby renovating livelihoods and social prosperity

[20], [53]. To sustain and further elevate this prosperity along with maintaining standards of livelihood, European societies also began to favor small family norms, leading to a decline in population growth in the early twentieth century [18].

The experience of key Southeast and East Asian nations such as Japan, South Korea, Taiwan, Singapore, Thailand and Indonesia standout as notable case. Back in 1960s these countries were poor, largely agrarian, traditional. However, within 1960 to 1990, these nations underwent remarkable socioeconomic enrichment through the adoption of comprehensive trade and industrialization process, greater access to education, health care, and social support system, as well as improvements in women's status, including increased occupation opportunities outer the home [54]. This structural transformation can absorb the growing youth population and raise income per capita while also bringing meaning shift in behavioral changes. Furthermore, narrowing the gap between male and female education has made it rational for parents to invest in daughters, so long as the parents can recoup their investment before a daughter marries and leaves home [55]. This has raised the average age at marriage and age at first birth, leading to women's complete fertility decline and rate of population growth has slowed throughout the region. The area that the Bangladesh state covers today, during the Mughal period, its population was much less than one million [18]. Today, it has increased seventeen times to more than approximately 170 million, the country has one of the highest population densities in the world with approximately 1,300 people per square kilometer [56]. Frank W. Notestein contended that the decline in fertility is closely associated with changes in ways of living and thinking, which are, in turn, products of industrialization (as cited in [19]). Together, these findings link dependency, structuralist and sociological perspectives [33], [34], [35], where country's failed industrialization and modernization effort, reproducing dependency, cycle of poverty and subsequent underdevelopment, shape the societal norms, values and institution and gender role, contributing to demographic stress. These overall outcomes reflect a development failure that perpetuates demographic challenges in Bangladesh.

6.3. Limitations and Future Research Prospects

Reliance on secondary correlation data and the absence of field-level interviews are the main constraints of this study. The objective of the study is to examine the possible association between underdevelopment indicators and demographic challenges, rather than to investigate dynamic time-series relationships or to provide forecasting. Principal Component Analysis (PCA) was employed to reduce dimensionality and address multicollinearity among socio-economic indicators. Therefore, our analysis focused on the potential structural relationships among the variables rather than on time-series modeling. Future research focusing on dynamic relationships should use appropriate time-series method. Additionally, longitudinal or experimental research is essential to establish causality between underdevelopment and demographic outcome as suggested for future work. Despite these limitations, this study, analyzes data with a theoretically grounded interpretation to ensure the credibility of its findings.

7. CONCLUSION AND POLICY RECOMMENDATIONS

This study contests the long-held Malthusian prognosis that population growth will slow and ultimately stabilize, not because of "natural" forces of famine and pandemic, but rather because of improvements in living standards and other socio-economic changes that alter the need for many children [12].

This paper contributes to resolving debates by reframing population pressures as products of institutional and structural stagnation, rather than autonomous drivers of poverty and underdevelopment in Bangladesh. The approach of the study is significant due to its potential value for diverse Global South contexts, such as Sub-Saharan Africa or Latin America, which are experiencing the same kinds of demographic challenges and facing similar underdevelopment experiences. In brief, this study proof that societal transformation from a traditional to a modernized way of living where fertility restriction is always prevalent, which supports the conceptual model of a development-first approach to population stabilization. From both a practical and ethical standpoint, the most sustainable population policy approach is to prioritize human substantive freedom across multiple dimensions.

As Teitelbaum [57] concludes, "Take care of the population, and population growth will come down"

This study carries few policy recommendations, including first, promote decentralized industrial development to absorb the growing working-age population including women aiming to reduce poverty and gender inequality to ensure equal opportunity for

women in formal sector employment. Second: expansion of inclusive secondary and higher education policy to enhance enrollment ratio, especially female enrollment to ensure women agency on reproductive behavior. Third: reforming traditional norms, values, gender roles as well as strengthen policies to provide access to all desired people to social security systems and pension system so that households' incentives to produce more children may decrease. Fourth: Policy formulation and interventions such as family planning service, reproductive education, maternal health care service are essential and prioritize the improving the quality of life which is necessary for low fertility. The government of Bangladesh had stepped up its population stabilization efforts considerably in collaboration with various non-government organizations and development initiatives. Among these initiatives mostly include promoting women's education, restricting early marriage, ensuring women's participation in economic activity where export-oriented apparel industry standing out as prime example. These changes reflect the women's autonomy and improve the lives of women which has alter the country's fertility situation positively—and not for the better, simply due to government resources hardly focusing on controlling the "quantity of births" rather than improving the "quality of people's lives" [12]. The positive association between development and fertility reduction is thus often summarized by the universally used phrase

"Development is the best contraceptive." [57].

By showcasing Bangladesh as a successful example, the population consensus must offer a fresh perspective on development, which lies not in focusing on policy priorities but in comprehensive economic well-being, social justice that is conducive to the fulfillment of basic human desires and holds the key to a more equitable and demographically stable conditions for Bangladesh.

Conflicts of Interest: The authors declare no conflict of interest.

ACKNOWLEDGEMENT

The authors gratefully acknowledge the Research and Publication Cell of the University of Chittagong for funding this study. Sincere gratitude is also extended to Assistant Professor Mr. Sukanta Chakraborty and the anonymous reviewers for their intellectual contributions and assessments.

REFERENCES

[1] A. J. Coale, "The Demographic Transition.," *The Pakistan Development Review, Vol. 23, No. 4, 531–52*, vol. 23, no. 4, pp. 531–552, 1984, Accessed: Apr. 10, 2026. [Online]. Available: https://www.jstor.org/stable/4125933

[2] United Nations, *World Population Prospects 2024: Summary of Results*. United Nations, New York., 2024. [Online]. Available: UNDESA/POP/2024/TR/NO. 9.

[3] PRB, "World Population Data Sheet," Washington DC.USA., 2024.

[4] UN Population Division, *Population Prospects of Countries in Special Situations*. 2024. doi: 10.18356/9789213587942.

[5] United Nations, "The world at six billion.," *United Nations Publication*, Oct. 1999.

[6] T. R. Malthus, *An Essay on the Principle of Population*, vol. 1. Readex Microprint, 1798.

[7] P. Ehrlich, *The Population Bomb*. Ballantine Books, New York., 1968. doi: 10.12987/9780300188479-007.

[8] G. Hardin, "The Tragedy of the Commons Garrett Hardin," *Science (1979).*, vol. 162, no. 3859, 1968.

[9] L. R. Brown, "In the Human Interest. A Strategy to Stabilize World Population," *Q. Rev. Biol.*, vol. 50, no. 4, 1975, doi: 10.1086/408930.

[10] *World Development Report*. Oxford University Press, New York, 1984.

[11] A. Mason, (Ed.). *Population Change and Economic Development in East Asia: Challenges met, opportunities seized*. Stanford University Press., 2002. doi: 10.1515/9780804779999.

[12] B. Hartmann, *Reproductive Rights and Wrongs: The Global Politics of Population Control*. 2016.

[13] D. E. Bloom, D. Canning, and P. N. Malaney, "Population Dynamics and Economic Growth in Asia," 2000. [Online]. Available: https://about.jstor.org/terms

[14] D. E. Bloom and J. E. Finlay, "Demographic change and economic growth in Asia," *Asian Economic Policy Review*, vol. 4, no. 1, pp. 45–64, 2009, doi: 10.1111/j.1748-3131.2009.01106.x.

[15] A. M. R. Chowdhury, A. Bhuiya, M. E. Chowdhury, S. Rasheed, Z. Hussain, and L. C. Chen, "The Bangladesh paradox: Exceptional health achievement despite economic poverty," 2013, *Elsevier B.V.* doi: 10.1016/S0140-6736(13)62148-0.

[16] J. K. Bora, N. Saikia, E. B. Kebede, and W. Lutz, "Revisiting the causes of fertility decline in Bangladesh: the relative importance of female education and family planning programs," *Asian Population. Studies.*, vol. 19, no. 1, pp. 81–104, 2023, doi: 10.1080/17441730.2022.2028253.

[17] United States National Academy of Sciences., *Rapid population growth: Consequences and policy Implications*, vol. 2. Baltimore: Johns Hopkins University Press, 1971.

[18] Anupam Sen, *Bangladesh: Rashtra O samaj (Bangladesh: The State and Society-A socio Economic Study),* , 4th ed. Dhaka: Abosar, 2018.

[19] A. Sen, *The state, industrialization and class formations in India: A Neo-Marxist Perspective on Colonialism, Underdevelopment and Development*. 2009. doi: 10.4324/9781315229881.

[20] Warren. S. Thompson, "Population," *American Journal of Sociology, 34, pp. 959-975.*, 1929.

[21] S. Kuznets, "Population Trends and Modern Economic Growth (Notes Toward an Historical Perspective)," 1973, [Online]. Available: https://www.econstor.eu/bitstream/10419/160120/1/cdp191.pdf

[22] J. L. Simon, *The Ultimate Resource*. Princeton University Press Princeton., 1981.

[23] K. Bruce. Newbold, *Population Geography*. Rowman & Littlefield Publishers, New York, 2010.

[24] J. Bryant, "Theories of Fertility Decline and the Evidence from Development Indicators," 2007.

[25] C. F. Tang and N. P. Tey, "Low fertility in Malaysia: Can it be explained?" *J. Population. Research.*, vol. 34, no. 2, 2017, doi: 10.1007/s12546-017-9187-2.

[26] M. Zakaria, B. A. Fida, S. Y. Janjua, and S. J. H. Shahzad, "Fertility and Financial Development in South Asia," *Soc. Indic. Res.*, vol. 133, no. 2, pp. 645–668, Sep. 2017, doi: 10.1007/s11205-016-1382-6.

[27] N. Sethi, N. R. Jena, and N. Loganathan, "Does financial development influence fertility rate in South Asian economies? An empirical insight," *Business Strategy and Development*, vol. 4, no. 2, pp. 94–108, Jun. 2021, doi: 10.1002/bsd2.131.

[28] M. Lerch, "Fertility Decline in Urban and Rural Areas of Developing Countries," *Popul. Dev. Rev.*, vol. 45, no. 2, pp. 301–320, Jun. 2019, doi: 10.1111/padr.12220.

[29] W. J. Jean Yeung and J. B. Abalos, "Social determinants of low fertility in Asia: a comparative review of trends in East, Southeast and South Asia," 2025. doi: 10.1016/j.lanwpc.2025.101724.

[30] S. Islam and H. K.- Journal, "Influences of selected socio-economic and demographic variables on fertility in Bangladesh," *Asia. Pac. Population. J.*, no. 10(2), pp. 51–63, 1995, [Online]. Available: https://www.un-ilibrary.org/content/journals/15644278/10/2/7

[31] S. Abedin, "Identification of fertility enhancing and inhibiting factors: A study on married adolescents in Bangladesh," *Asian Soc. Sci.*, vol. 7, no. 5, 2011, doi: 10.5539/ass.v7n5p191.

[32] M. N. M. Chowdhury and Md. M. Hossain, "Population Growth and Economic Development in Bangladesh: Revisited Malthus," *American Economic & Social Review*, vol. 5, no. 2, 2019, doi: 10.46281/aesr.v5i2.326.

[33] Paul A. Baran., "The Political Economy of Growth.," *American Political Science Review*, vol. 52, no. 1, 1957, doi: 10.1017/s0003055400232267.

[34] G. Myrdal, *Asian Drama. An Inquiry Into the Poverty of Nations.* . Pantheon, 1968.

[35] H. Blumer, *Symbolic interactionism: Perspective and method.* . Englewood Cliffs, NJ: Prentice-Hall., 1969.

[36] J. R. Weeks, *Population An Introduction to Concepts and Issues*, 12th ed. CENGAGE, USA, 2016.

[37] R. X. Liu, J. Kuang, Q. Gong, and X. L. Hou, "Principal component regression analysis with SPSS," *Computer. Methods Programs Biomed.*, vol. 71, no. 2, 2003, doi: 10.1016/S0169-2607(02)00058-5.

[38] C. Davino, R. Romano, and D. Vistocco, "Handling multicollinearity in quantile regression through the use of principal component regression," *Metron*, vol. 80, no. 2, 2022, doi: 10.1007/s40300-022-00230-3.

[39] H. Chowdhury, "Revisiting Globalisation," *India Quarterly: A Journal of International Affairs*, vol. 67, no. 3, pp. 245–262, Sep. 2011, doi: 10.1177/097492841106700304.

[40] Bangladesh Bureau of Statistics (BBS), "Bangladesh Labor Force Survey ," Dhaka, 2024.

[41] World Bank., "Bangladesh development update: Special focus: creating job for better future," Dhaka, 2024. [Online]. Available: www.worldbank.org/bd

[42] World Health Organization 2024: "The Global Health Observatory," 2024.

[43] Bangladesh Bureau of Statistics (BBS), "Household Income and Expenditure Survey," Dhaka, 2022.

[44] Cabinet Division., "Bangladesh Social Protection System Assessment Based on the Core Diagnostic Instrument (CODI) Cabinet Division Government of the People's Republic of Bangladesh," Dhaka, 2023.

[45] M. A Razzaque *et al.*, "Dynamics of Targeting Errors in Bangladesh's Social Protection Programmes," Apr. 2025.

[46] M. Cain, "Fertility as an adjustment to risk," in *Gender and the life course,* A. S.Rossi, Ed., London: Routledge, 2018, pp. 145–159. doi: 10.4324/9781351329040-10.

[47] R. Kollodge, Ed., *State of World Population 2011 : people and possibilities in a world of 7 billion*. United Nations Publication Fund, 2011.

[48] R. Kollodge, Ed., *State of World Population 2025: The Real Fertility Crisis-The Pursuit of Reproductive Agency in a Changing World*. UNFPA, 2025.

[49] E. H. and K. Newland, "The Sisterhood of Man.," *Population. Dev. Rev.*, vol. 5, no. 3, 1979, doi: 10.2307/1972092.

[50] M. Cain, S. R. Khanam, and S. Nahar, "Class, patriarchy, and women's work in Bangladesh.," *Population. Dev. Rev.*, vol. 5, no. 3, 1979, doi: 10.2307/1972079.

[51] W. Bank., "World Development Indicators," *World Bank Group.*, 2024.

[52] D. Kirk, "Demographic Transition Theory," *Population. Studies. (NY).*, vol. 50, no. 50(3), 361–87., pp. 361–387, 1996, [Online]. Available: https://about.jstor.org/terms

[53] J. C. Caldwell and B. K. Caldwell, "The Causes of Asian Fertility Decline," *Asian Population. Studies.*, vol. 1, no. 1, pp. 31–46, Mar. 2005, doi: 10.1080/17441730500125714.

[54] World Bank, *The East Asian miracle: Economic growth and public policy*. Oxford University Press, 1993.

[55] S. Greenhalgh, "Sexual stratification: the other side of 'growth with equity' in East Asia.," *Population. Division. Rev.*, vol. 11, no. 2, 1985, doi: 10.2307/1973489.

[56] Bangladesh Bureau of Statistics, "Population and Housing Census 2022," Bangladesh Bureau of Statistics.

[57] M. S. Teitelbaum, "Relevance of Demographic Transition Theory for Developing Countries," *New Series (Vol. 188, Number 4187).*, vol. 188, no. 4187, pp. 420–425, 1975.

Performance Analysis of an Electric Motorcycle with IoT Based Monitoring

Md. Anwarul Abedin[1*], Md. Monerul Islam[2] and Anik Kumar Chowdhury[3]

[1]Department of Electrical and Electronic Engineering, Dhaka University of Engineering & Technology, Gazipur, Bangladesh
[2]Operations and Maintenance, Kishorganj Polli Bidyut Samity, Kishorganj, Bangladesh
[3]IC Physical Design, Ulkasemi Private limited, Dhaka, Bangladesh

ABSTRACT

The rapid shift toward electric vehicles (EVs) is reshaping the global transportation landscape, driven by the need for sustainable and energy-efficient alternatives to internal combustion engine (ICE) vehicles. Among various EV categories, electric motorcycles (E-bike) have emerged as a practical solution for urban mobility due to their compact size, low emissions and reduced operational costs. However, challenges such as performance reliability, battery efficiency, and system integration must be addressed to support their widespread adoption. This study presents the design and implementation of an Internet of Things (IoT)-based monitoring system for real-time performance evaluation of an E-bike. The system integrates multiple sensors to monitor key parameters, including battery voltage, current, temperature, wheel RPM, bike speed, and AC power consumption during charging. Real-time data is displayed on an onboard LCD and uploaded to the ThinkSpeak IoT platform for remote monitoring and future analysis. During charging, the battery voltage increased steadily with the AC charging current drawn by the battery is around 1.5 A. The charging power averaged around 218 W, demonstrating that the bike can be conveniently charged using a standard household power socket. From the data and the graph, it may be predicted that to charge the battery fully it will take around 8 to 10 hours. In discharging tests, motor current showed a linear correlation with speed, and power consumption increased accordingly, peaking at higher speeds. The battery range was estimated at 60 – 65 km per full charge. Battery and component temperatures rose gradually and linearly during operation, with no abrupt spikes, suggesting effective thermal management. The results confirm that IoT integration enhances the reliability, safety, and user awareness of E-bike performance. The developed system provides a valuable framework for future smart mobility solutions and lays the groundwork for more advanced electric vehicle management systems aimed at improving efficiency and user experience.

Keywords: Electric Motorcycle (E-bike), Internet of Things (IoT), Real-Time Monitoring and Battery Performance

1. INTRODUCTION

Electric motorcycles are two-wheeled vehicles powered by electric motors and rechargeable batteries, representing a shift away from internal combustion engines (ICE) traditionally used in motorcycles. With advancements in battery technology, motor efficiency, and charging infrastructure, electric motorcycles have gained significant traction in recent years, offering a cleaner, quieter, and more energy-efficient alternative to gasoline-powered bikes [1]. Unlike conventional motorcycles, electric motorcycles deliver instant torque, providing superior acceleration and a smoother ride. They are nearly maintenance-free due to fewer moving parts, lack of oil changes, and absence of complex exhaust systems. Modern electric motorcycles also incorporate advanced technologies such as regenerative braking, smart connectivity, and customizable ride modes, enhancing the rider's experience [2].

Electric motorcycles play a crucial role in addressing some of the most pressing challenges associated with transportation today, including air pollution, greenhouse gas emissions, and noise pollution [3]. Their importance can be summarized in several key points:

Reduction of Greenhouse Gas Emissions

Transportation accounts for a significant share of global carbon dioxide (CO_2) emissions, with motorcycles contributing to this problem. Electric motorcycles produce zero tailpipe emissions, significantly reducing their carbon footprint compared to gasoline-powered vehicles.

*Corresponding author's email: abedin@duet.ac.bd

When powered by renewable energy sources, their environmental impact is further minimized, supporting global efforts to combat climate change.

Improved Urban Air Quality

In densely populated urban areas, vehicle emissions are a major contributor to air pollution, leading to respiratory and cardiovascular diseases. Electric motorcycles eliminate exhaust emissions, making them an ideal solution for reducing air pollution and improving public health, especially in cities.

Energy Efficiency

Electric motors are inherently more efficient than internal combustion engines. While ICE motorcycles convert only about 20 – 30% of the energy from fuel into motion, electric motorcycles can achieve efficiencies of 85 – 90%. This high efficiency means more energy is used for actual movement, reducing overall energy consumption.

Noise Pollution Reduction

Electric motorcycles operate much more quietly than their gas-powered counterparts, which can significantly reduce noise pollution in urban environments. This is especially important in residential and high-traffic areas, where excessive noise negatively impacts quality of life.

Support for Renewable Energy Integration

Electric motorcycles can be charged using electricity generated from renewable energy sources such as solar, wind, and hydroelectric power. This promotes the integration of clean energy into the transportation sector and reduces reliance on fossil fuels.

Economic and Social Benefits

- **Lower Operating Costs:** Electric motorcycles have lower operating costs due to reduced fuel expenses and maintenance requirements, making them an attractive option for cost-conscious consumers.
- **Energy Security:** By reducing dependence on imported fossil fuels, widespread adoption of electric motorcycles contributes to energy security at a national level.
- **Job Creation:** The electric vehicle industry, including manufacturing, battery development, and charging infrastructure, is a growing sector that creates new opportunities for employment and economic growth.

Addressing Global Sustainability Goals

Electric motorcycles align with global initiatives like the Paris Agreement, which aims to limit global warming, and the United Nations Sustainable Development Goals (SDGs), particularly Goal 11 (Sustainable Cities and Communities) and Goal 13 (Climate Action).

The demand for electric motorbikes is increasing in Bangladesh for being an eco-friendly, cost-effective mode of transport and government policy and support [4]. In 2020, the Bangladesh Road Transport Authority issued a policy for registering electric vehicles. The use of electric motorbikes has increased since then, with the biggest spike seen in 2022 [5]. The adoption of electric two-wheelers has ramped up as they are more environmentally friendly and cost-effective than those powered by fossil fuel. Besides, advancements in the required components, such as quickly rechargeable batteries and lightweight motors, are also driving demand.

One such contribution to this sustainable transportation movement is the electric bike named "Bondhu" developed by Akij Motors. As a locally manufactured electric bike, Bondhu aims to provide an eco-friendly and cost-effective alternative to traditional fuel-based motorcycles. While the adoption of electric bikes is increasing, the ability to continuously monitor and analyze the performance of these vehicles in real-time remains limited. This gap opens up an opportunity for research and development in intelligent monitoring systems that can ensure better efficiency, reliability, and user experience.

Since the industry is rapidly growing, there is a need of performance testing of these vehicles. On the other hand, if during testing and running, the required values like current, voltage, speed is logged and monitored, it will be a good opportunity for the researcher and motorcycle owner to observe and analyze his vehicle. Design of electric motorcycle has been done in [6]. In their paper, the authors have tested the electric motorcycle and given some test data but these are not monitored online. Intelligent monitoring of motorcycle was implemented in [7] where IoT based safety monitoring like speed monitoring and whether the driver has worn the helmet or not has been monitored. The authors of [8] proposed a preliminary road test procedure used to measure and collect the performance characteristics data of electric motorcycles. They have not used any IoT devices to monitor and record the test data.

This research project focuses on the Internet of Things (IoT)-based performance analysis and controller

evaluation of the Bondhu electric bike. The core objective of this work is to implement a smart system that collects, analyzes, and transmits real-time data related to the bike's electrical and mechanical parameters. To achieve this, various sensors have been integrated into the bike's system. DC current and voltage sensors are used to monitor the battery's behavior during charging and discharging cycles. These readings are crucial for understanding the efficiency of energy storage and usage. To evaluate the power input to the charger, AC current and voltage sensors are used to monitor the alternating current drawn from the grid. This helps assess the power consumption during charging and overall energy conversion efficiency. A temperature sensor is installed to measure the temperature of the battery. Since battery temperature significantly affects the performance and lifespan of electric vehicles, this data ensures safe and optimal operation. An infrared (IR) based speed sensor is also implemented to measure the rotational speed (RPM) of the wheels. This data is then used to calculate the real-time speed of the bike, which is vital for analyzing ride dynamics and energy usage during motion. All the collected data is displayed on an LCD screen mounted on the bike for local monitoring. In addition, the data is uploaded to the ThinkSpeak IoT platform, allowing remote access to the bike's condition from anywhere via the internet. This feature enables users or researchers to monitor battery health, charging status, temperature, and speed in real-time, providing valuable insights into the overall performance of the bike.

The primary aim of this research is to create a low-cost, real-time monitoring and data analysis system for electric bikes. This system not only provides a deeper understanding of the performance and control behavior of the Bondhu electric bike but also sets a foundation for future development of intelligent electric vehicles in Bangladesh. With further advancements, such systems can be expanded to include predictive maintenance, performance optimization, and integration with smart transportation infrastructure.

The aims of this project are:

- To design and implement a real-time performance monitoring system for an electric bike.
- To analyze different data of battery, motor and controller to check the performance of these devices.
- To use IoT devices for remote monitoring of different parameters of the battery, motor and controller using mobile phone or PC.

2. IMPLEMENTATION OF THE PROJECT

The implementation of this project involved the integration of multiple hardware components and sensors with a microcontroller-based system to monitor the performance of the Bondhu electric bike. DC current and voltage sensors were used to track the battery's charging and discharging status, while AC sensors monitored the power input during the charging process. A temperature sensor was installed to observe the thermal condition of the battery, and an IR-based speed sensor was used to measure the wheel's RPM and calculate the bike's speed. All collected data was displayed on an LCD screen for local monitoring and simultaneously uploaded to the ThinkSpeak IoT platform for remote access and analysis. This implementation enabled a comprehensive and real-time evaluation of the electric bike's performance and controller behavior.

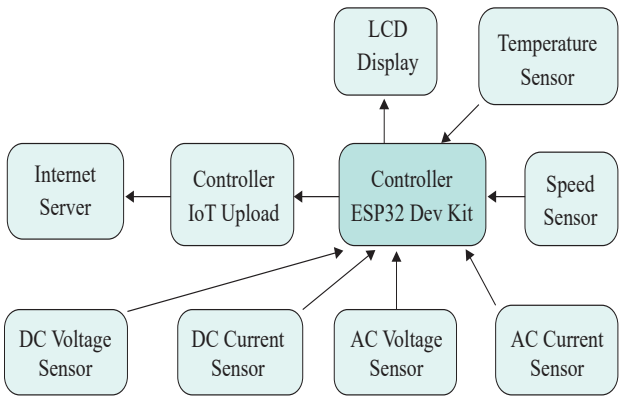


Fig. 1: Block diagram of the system

This block diagram in Fig. 1 illustrates a system centered around an ESP32 Dev Kit, acting as a controller to monitor various electrical and electric bike parameters. It interfaces with DC and AC voltage and current sensors, a temperature sensor, and a speed sensor to gather data. This information is then displayed on an LCD and uploaded to an internet server via a controller for IoT upload, suggesting a remote monitoring or control application.

In order to implement the project, several components have been used (given in Table I)

Table I: Component list of the project

SI. No.	Component's Name	Required Quantity
1.	ESP32 Dev Kit	2 Nos.
2.	AC Current Sensor (ZMC103C)	1 No.
3.	AC Voltage Sensor (ZMPT101B)	1 No.
4.	DC Current Sensor (ACS712-30A)	1 No.

SI. No.	Component's Name	Required Quantity
5.	DC Voltage Sensor Module	1 No.
6.	Temperature Sensor (DS18B20)	1 No.
7.	IR Sensor	1 No.
8.	Buck Converter	1 No.
9.	Mobile Phone	1 Unit
10.	Akij Bondhu Electric Bike	1 Unit
11.	Multimeter	1 Unit
12.	LCD Display with I2C Module	1 No.

The system collects real-time data on battery status, charger input, battery temperature, and bike speed. This data is displayed on the LCD and simultaneously uploaded to ThinkSpeak for remote performance monitoring. The diagram provides a clear view of the signal flow and system functionality, ensuring easy implementation and troubleshooting. Figure 2(a) and (b) show the implemented circuit with the sensors. The implemented circuit is mounted on the rare side of the bike in a box.



(a)



(b)

Fig. 2: Assembled circuit with sensors in the electric bike

2.1 Working Principle

The IoT-based electric bike performance monitoring system is designed to continuously collect and analyze key parameters related to the bike's battery and overall ride performance. The system utilizes two ESP32 Dev Kits for optimized functionality. One ESP32 is dedicated for sensor data collection and processing, while the second ESP32 handles Wi-Fi-based IoT communication, uploading the data to ThingSpeak server for remote monitoring.

The system integrates several sensors to monitor different parameters of the bike's performance. The DC voltage and current sensors are connected to the series connected five 12V batteries on the bike, allowing real-time tracking of battery health. Battery voltage and current flow are continuously monitored to assess the charging and discharging processes. To monitor the energy input, AC voltage and current sensors are installed on the charger input. The AC voltage typically ranges from 220V to 250V, ensuring the proper charging voltage is being supplied to the bike. These sensors provide real-time feedback on how much power is being drawn from the grid during the charging process. A DS18B20 temperature sensor is placed near the battery to measure its temperature. This is crucial for maintaining optimal operating conditions and preventing overheating, which could cause battery damage or reduced lifespan. The temperature data allows the system to detect abnormal conditions that could affect the bike's overall performance and safety. An IR-based speed sensor is used to measure the wheel's RPM, which is then converted into speed in kilometers per hour. This sensor provides real-time feedback on the bike's speed, offering valuable data for both the rider and for performance analysis.

The main ESP32 unit collects all the sensor data, processes it, and sends it to the second ESP32, which is solely responsible for uploading this information to ThingSpeak. Once uploaded, the data can be accessed remotely on ThingSpeak, where it is visualized in real-time. The monitored parameters include battery voltage (for each of the five batteries), battery current, AC voltage (220-250V), AC current, temperature, speed (in km/h), and battery status in percentage. The system's ability to display battery status in percentage is especially useful for keeping track of the bike's charge level and ensuring the rider is aware of remaining battery life. This setup enables users to monitor the performance of their electric bike in real-time, providing insights into battery health, charging efficiency, ride speed, and temperature, while also enabling proactive maintenance through remote monitoring.

2.2 Calibrations

Calibration in this system involves adjusting the sensors to ensure accurate data readings. Each sensor, such as the voltage, current, and temperature sensors, is calibrated to standard values using known reference measurements. This ensures that the data collected from the bike, such as battery voltage, current, and temperature, are accurate and reliable. Regular calibration helps maintain the system's precision and ensures that performance monitoring remains correct over time. To calculate the percentage error, we have used the formula:

$$\%Error = \left(\frac{Sensor\ Value - Acual\ Value}{Actual\ Value} \right) \times 100\%$$

The maximum errors for DC voltage, AC voltage, DC current, AC current, temperature, and speed were found to be 0.87%, 0.91%, 2.00%, 2.38%, 1.85%, and 7.00%, respectively.

3. RESULTS AND DISCUSSION

A 20×4-character LCD display has been used here with I2C interface to display the different measured parameters of the e-bike. At the same time IoT technology has been used to upload the data to the ThingSpeak server. This allows for real-time storage and visualization of the electric bike's performance data, including parameters such as battery voltage, current, speed, temperature, and battery storage status.

To present the results, we have divided the analysis into two main parts: charging conditions and discharging conditions. Under charging conditions, we present the trends such as AC charging current, power consumption of the battery, battery voltage and % of battery storage. In the discharging condition, we analyzed the trends like battery supplied current and power consumption of the motor for different speed, % of battery storage with distance, battery voltage related to % of battery storage, temperature variation with distance etc. These trends provide valuable insights into the electric bike's performance under both charging and discharging scenarios. Fig. 3(a) shows the data on mobile phone when the AC voltage was applied for charging battery. On the other hand, Fig. 3(b) shows the different parameters of the e-bike when the bike is running on the road.

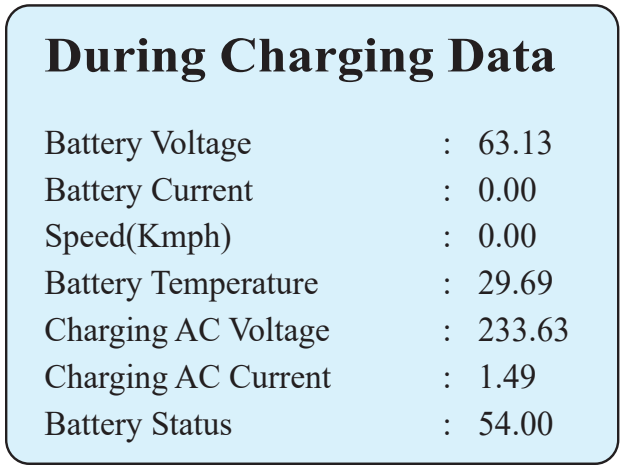


Fig. 3: Data showing in the phone while (a) charging and (b) running condition

3.1 Different Parameters of the Electric Bike During Charging

This section discusses and demonstrates the behavior of the electric bike under charging conditions. It shows how various parameters, such as AC charging current, power consumption of the battery, battery voltage and % of battery storage over time providing insight into the performance of the bike during the charging process.

The AC charging current drawn by the battery during charging is shown in Fig. 4. The graph shows that the AC current drawn by the battery is around 1.5 A. At that time the battery voltage gradually increases from 56 V to 64 volts and the maximum value is controlled by the charge controller. The average power required for charging is around 218 W which indicates that the e-bike can be charged with a simple household power socket.

The graph in Fig. 5, illustrates the charging behavior of an electric bike battery over a period of 120 minutes. It shows a steady increase in battery charge percentage, starting from 40% and rising to 60%. From the data and the graph, it may be predicted that to charge the battery fully it will take around 8 to 10 hours. This gradual rise indicates a consistent charging process, likely under a constant voltage or current mode.

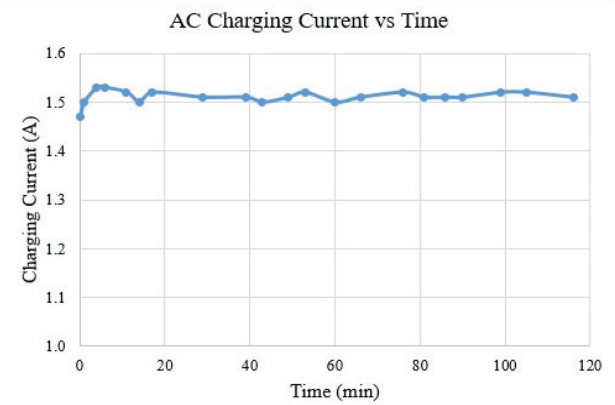


Fig. 4: AC current drawn by the battery vs time during charging

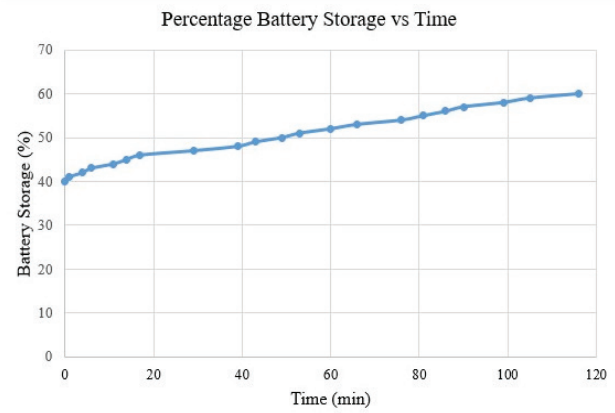


Fig. 5: Percentage of battery storage vs time

3.2 Different Parameters During Discharging/ Running Condition

The relationship between the battery supplied current i.e. current drawn by the motor and the speed of the electric bike is shown in Fig. 6. The data shows a linear increase in motor current as the bike's speed increases, indicating a proportional relationship between speed and current demand. As the bike accelerates, the motor requires more current to maintain higher speeds, resulting in a steadily rising curve. At that time the power demand by the motor varies from 70 to 419 W.

The trend of battery percentage decreasing over distance travelled during the operation of the electric bike is shown in Fig. 7. As the bike runs, it consumes electrical energy to power the motor and other electronic systems, leading to a gradual decline in battery charge. This reduction of battery percentage also reduces the battery terminal voltage and it varies from 60.5 to 58.2 V. It is clear from the graph that after running around 12 km the battery % decreases around 8% so we can predict that for a fully charged bike around 60 to 65 km can be run before it needs charging. We have also observed the temperature rise of the battery and the surroundings at that time which was from 31.10 to 31.75 °C as shown in Fig. 8.

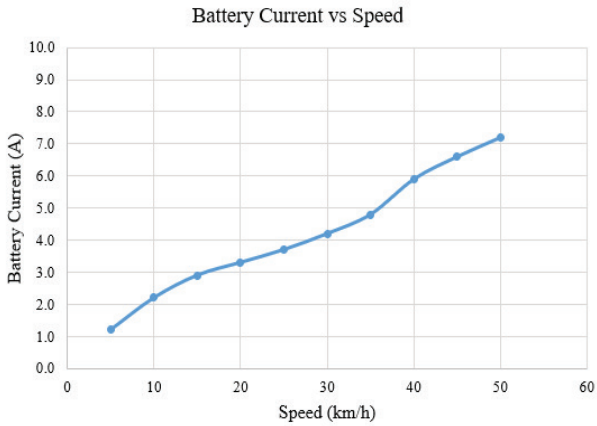


Fig. 6: Battery current vs speed

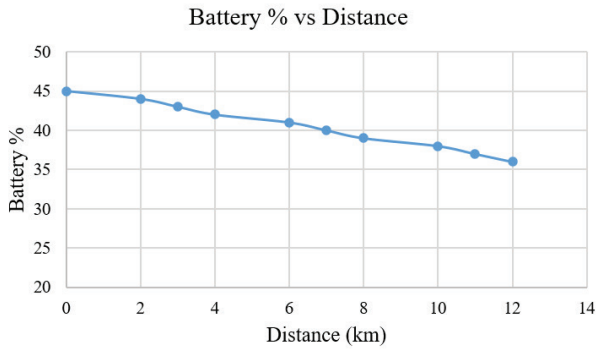


Fig. 7: Battery % vs distance

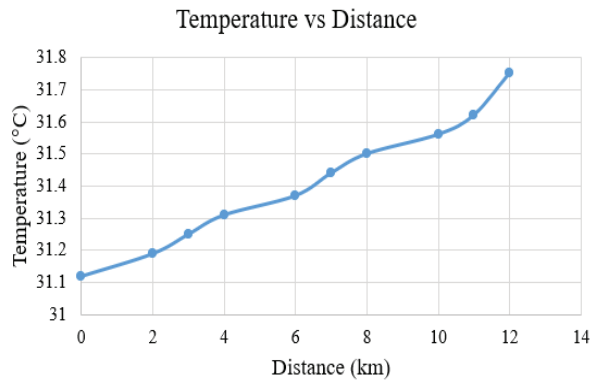


Fig. 8: Battery temperature rise trend

4. CONCLUSION

The global transportation sector is undergoing a significant transformation with the rapid adoption of EVs as a sustainable alternative to fossil fuel-based vehicles. Among EVs, electric motorcycles (e-motorcycles) have gained considerable attention due to their compact size, energy efficiency, and lower operational costs compared to cars. However, the widespread adoption of e-motorcycles faces challenges related to performance, reliability, and battery lifespan**.** Unlike conventional motorcycles, which rely on well-understood internal combustion engines, e-motorcycles depend on the seamless integration of three critical components like electric motor, battery pack and motor controller. A minor inefficiency in any of these components can lead to reduced range, overheating, or even catastrophic failure, highlighting the need for rigorous performance testing and real-time monitoring**.**

In the present work, through the integration of various sensors, the system was able to continuously monitor critical parameters such as battery voltage, battery current, battery temperature, wheel RPM, bike speed, and AC power consumption during charging. By utilizing DC and AC voltage and current sensors, the charging and discharging behaviors of the bike's battery were effectively analyzed. An IR-based speed sensor accurately measured the wheel's RPM, enabling reliable calculation of the bike's speed. The system's continuous tracking of battery temperature ensured operational safety by identifying any unusual heating patterns. The real-time data was displayed on an onboard LCD screen, providing immediate feedback to the user, and was simultaneously uploaded to the ThinkSpeak IoT platform for remote monitoring and future analysis. This dual approach of local and cloud-based data presentation enhanced the accessibility and usefulness of the monitoring system.

The analysis of the electric bike's performance under both charging and discharging conditions provides valuable insights into its operational efficiency, energy consumption, and battery behavior. During charging, the battery voltage increased steadily with the AC charging current drawn by the battery is around 1.5 A. The charging power averaged around 218 W, demonstrating that the bike can be conveniently charged using a standard household power socket. The battery charge percentage showed a steady increase in battery charge percentage, starting from 40 % and rising to 60 %. From the data and the graph, it may be predicted that to charge the battery fully it will take around 8 to 10 hours. Under discharging (running) conditions, the motor current exhibited a linear relationship with speed, reflecting higher current demand as the bike accelerated. Power consumption also increased with speed, peaking at higher velocities due to greater energy requirements. The battery percentage decreased non-linearly with distance, with an estimated range of 60 – 65 km on a full charge. Temperature monitoring revealed a gradual and linear rise in battery and component temperatures during operation, suggesting effective thermal management without abrupt spikes.

Overall, the project demonstrated the effectiveness of combining IoT technology with electric vehicle systems for smart monitoring. The data collected and analyzed through this project will not only support further improvement of the "Bondhu" electric bike but will also contribute to future developments in smart electric mobility solutions. This work lays the foundation for more advanced and intelligent electric vehicle management systems aimed at enhancing safety, efficiency, and user experience.

ACKNOWLEDGEMENT

I would like to thank all the committee members of "CASR, DUET" for selecting this research to support. Special thanks go to Head, Department of Electrical and Electronic Engineering and Director, Research and Extension for their continuous support during the research. This work was supported by "University Teachers' Research Fund" of Dhaka University of Engineering & Technology, Gazipur.

REFERENCES

[1] R. Zahedi, A. A. Pourezzat, and M. Jafari, "Hybrid Energy Storage System for Electric Motorcycles: Technical and Economic Analysis," Case studies in thermal engineering, Vol. 60, pp. 104613–104613, Aug. 2024.

[2] P. Suwignjo, M. N. Yuniarto, Y. U. Nugraha, A. F. Desanti, I. Sidharta, S. E. Wiratno, and T. Yuwono, "Benefits of Electric Motorcycle in Improving Personal Sustainable Economy: A View from Indonesia Online Ride-Hailing Rider," International Journal of Technology, Vol. 14, No. 1, p. 38, Jan. 2023.

[3] T. Eccarius and C.-C. Lu, "Powered two-wheelers for sustainable mobility: A review of consumer adoption of electric motorcycles," Transportation

Research Part D: Transport and Environment, Vol. 63, pp. 66–86, 2018.

[4] S. Nurunnahar, M. S. Islam and M. Rahman, "Electric vehicles in Bangladesh: Impact on the environment, mobility and the economy of an impending ban," Public Health Challenges, Vol. 1, Issue 4, Dec 2022.

[5] Demand for electric bikes gaining momentum, Energy and Power, 2nd August 2023.

[6] S. S. Thakur, E. A. Roy, S. K. Dhakad and E. A. Jain, "Design of Electric Motorcycle," IEEE International Students' Conference on Electrical, Electronics and Computer Science (SCEECS), 2020.

[7] S. S. Tashfia, R. Islam, S. I. Sultan, M. W. Rahman, M. A. Habib and L. Y. Pinky, "Intelligent Motorcycle Monitoring Scheme using IoT with Expert System in Bangladesh," International Conference on Computer and Information Technology (ICCIT), 2020.

[8] D. T. Le, T. D. Dang and K. H. Ngo, "Preliminary Study on Road Test for Performance Evaluation of Electric Motorcycles in Vietnam," Easy Chair Preprint, October 8, 2022.

Data Driven Evaluation of Smart Grid Adaptation in Dhaka Electric Supply Company Limited: Challenges and Opportunities

Md Mijanur Rahman[1*], Md Saiful Islam Saif[1], Md Abdus Salim[2]

[1]Department of Electrical and Electronic Engineering, Dhaka University of Engineering and Technology, Gazipur, Bangladesh
[2]GIS Cell, Dhaka Electric Supply Company (DESCO) Limited, Bangladesh

ABSTRACT

This paper presents a data-driven evaluation of smart grid adaptation in the distribution network of Dhaka Electric Supply Company Limited (DESCO) using actual feeder-level operational data. The study analyzes feeder load characteristics, consumer distribution, reliability performance, and GIS-supported network information to assess smart grid readiness across selected urban distribution feeders in Dhaka. Key performance indicators, including load factor, connected feeder load, and demand patterns, are evaluated to identify operational challenges such as load imbalance and uneven asset utilization. The results reveal significant temporal and spatial variations in electricity demand among the selected feeders, reflecting differences in consumer concentration and network utilization. Based on these findings, a data-driven smart grid adaptation framework is proposed that links the identified operational challenges with appropriate technologies, including advanced metering infrastructure, distribution automation, outage management systems, and demand response. The proposed framework provides a practical and scalable roadmap for improving the operational efficiency, reliability, and resilience of urban distribution networks. The findings offer valuable insights for the phased implementation of smart grid technologies in Bangladesh and other developing countries.

Keywords: Smart Grid, DESCO, Distribution System, GIS, Load Analysis

1. INTRODUCTION

Demand of electricity is increasing speedily over the world due to rapid industrial expansion, rising appliance ownership (AC, electric cookers, washing machines) and urbanization. Peak demand of residential consumers has also been growing sharply. In Bangladesh, the distribution companies are facing persistent challenges, including poor system visibility, high technical and non-technical losses and poor load management. As a major utility serving the northern region of Dhaka, Dhaka Electric Supply Company (DESCO) Limited plays a critical role in ensuring reliable electricity supply in one of the most densely populated cities in the world.

The basic requirements of smart grid are to create a digitalized, robust and sustainable power network by means of developing two-way communication using real-time data. Fundamental necessities include advanced metering infrastructure (AMI), secure communication network, computerized controls for self-healing, integration of renewable sources and robust cybersecurity [1]. Higher level of monitoring and coordination can be achieved by means of modern technologies which allows us to incorporate the renewable sources with fully monitoring, flexible operation of DGs and lower operational cost.

Currently, Bangladesh power system facing some major problem in implementing smart grid such as poor planning of distribution network, overloading of system components, lack of reactive power support and regulating service, power theft, low metering and monitoring efficiency and lack of sufficient funds [2]. Some fundamental developments including implementing smart meter and employing bidirectional communication system has been recommended for sustainable implementation of smart grid in Bangladesh [3].

A techno-economic assessment has been proposed using Tongi 33/11 kV substation under DESCO for system loss reduction using the Electrical Transient Analyzer Program (ETAP) and system losses reduction is claimed through simulation by 5.86% [4]. However, actual DESCO operational data (total load, feeder measurements, GIS) has not been considered to perform a comprehensive load characterization and drive smart grid deployment priorities. GIS-driven site suitability design framework

*Corresponding author's email: mijan.duet@duet.ac.bd

for small scale microgrid is proposed along with AI based short term load forecasting without incorporating direct metering data [5]. Recently, smart grid technologies have been extensively investigated considering smart meter analytics, advanced communication structure and IoT for improving operational efficiency and distribution system monitoring [6-7]. However, most existing studies emphasize specific applications such as load forecasting, topology identification, state estimation, or network reconfiguration rather than providing a comprehensive assessment of smart grid readiness using operational feeder-level data [8], [9].

Furthermore, although GIS has been widely adopted for network visualization and asset management, relatively few studies integrate GIS with actual feeder operational data to evaluate smart grid adaptation from a utility perspective [10]. Consequently, a significant research gap remains in developing data-driven frameworks that combine feeder-level operational data with GIS-based information for practical smart grid readiness assessment. This study addresses this gap by utilizing real feeder data from DESCO to evaluate smart grid adaptation within an integrated, utility-oriented analytical framework.

2. SMART GRID IMPLEMENTATION

To increase the distribution system performance, smart grid technologies have been studied extensively. To implement the smart grid irrespective of area, facilities have to be ensured in major three categories such as power utilities, consumers and government and regulators. The power utility authority facilities include (i) increased system reliability and efficiency, (ii) reduced the technical and nontechnical losses of the distribution system, (iii) rapid restoration of the system, (iv) increased grid visibility, (v) renewable integration and (vi) peak load management [11]. The consumer facilities include (i) Smart power outage management, (ii) supply stable system voltage and frequency, (iii) load shifting facility during peak hour and (iv) user friendly and transparent tariff [12]. Studies have recommended the following key requirements that should be implemented for smart grid from the conventional one and all the points are figured in Fig. 2 for better understanding.

a) Implementation of the advanced metering Infrastructure
b) Distribution Automation
c) Integration of renewable energy
d) Implementation of two-way communication system
e) Integrating energy storage solutions
f) Demand side management or Demand response
g) Supervisory control and data acquisition

Studies have revealed that smart grid employment can considerably decrease the losses, enhance reliability, and improve voltage profile.

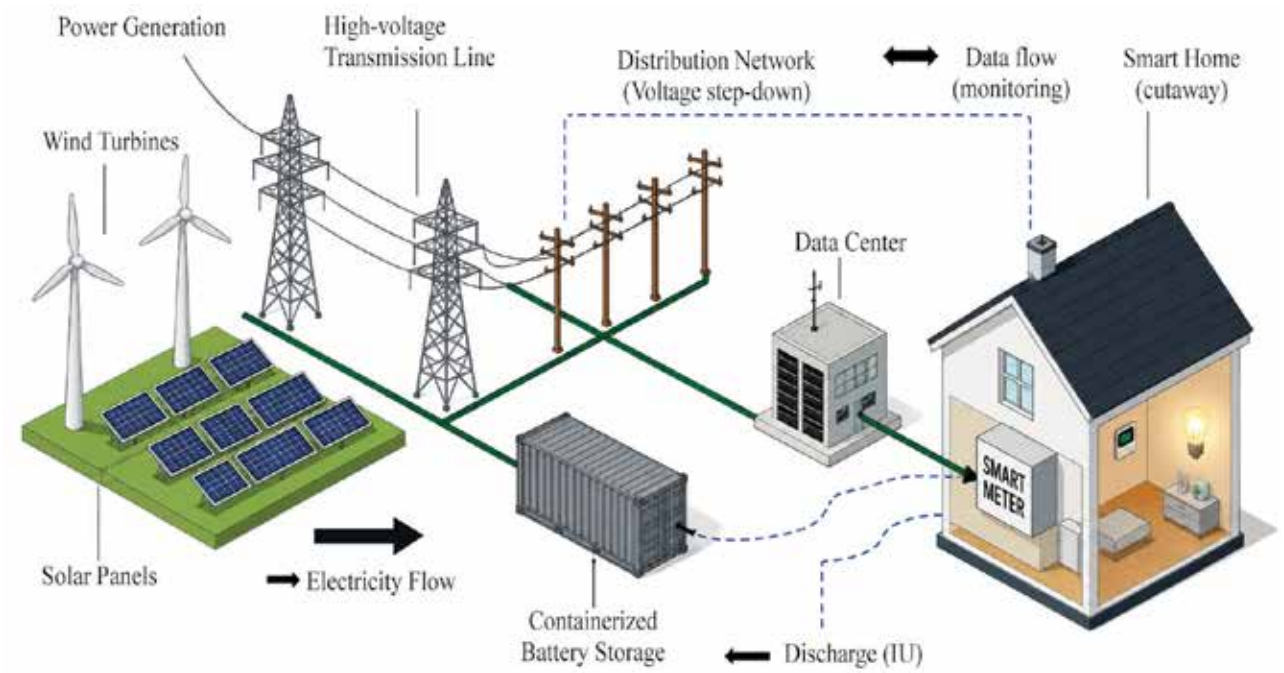


Fig. 1: General framework for implementation of smart grid echnology replacing a traditional grid system

3. SMART GRID IN DEVELOPING COUNTRIES

Several developing countries like India, China and Brazil are making their grid smarter [13-15]. Hence, many pilot projects have been taken in hand and started implementation them gradually. Journey of smart grid in India has been started in around 2010 to 2013 by modernizing the aging infrastructure, taking steps for reducing system losses and integrating renewable sources. Strategic indicators comprise of planning about transition by "India smart grid task force" (ISGTF) in 2010, fixing target to transform the power sector into a secure, adaptive, and sustainable network by "smart grid vision and roadmap for India" in 2013, forming the national smart grid mission (NSGF) in 2015 for implementing the smart grid and it started its operation in January, 2016. India start replacing the conventional meter into smart meter along with the improving tariff system and reducing theft in 2016 under the smart meter national program. To implement SACDA and advanced communication technologies, several pilot projects have been commenced under the smart city initiatives [16].

China starts the research about smart grid in 1990s with research into digital power system and established their first digital substation in 2006. In 2009, the state grid corporation of China formally offered the strong smart grid converting the conventional power grid technologies along with ultra-high voltage transmission. China has invested $285 billion from 2011 to 2020 for smart grid project for developing large scale ultra-high voltage (1000 kV AC and 800kV DC) system development to integrate urban renewable energy sources. Finally, in intelligent improvement and upgradation phase from 2021 to 2025, China focused on automating distribution networks, developing intelligent micro grids, improving operational efficiency and reliability and incorporating gigantic renewable capacity to make the grid cleaner and more proficient [17].

The implementation of smart grid in developing countries faces significant unique challenges including:

a) Primarily high capital costs,
b) Inadequate existing infrastructure,
c) Limited technical expertise,

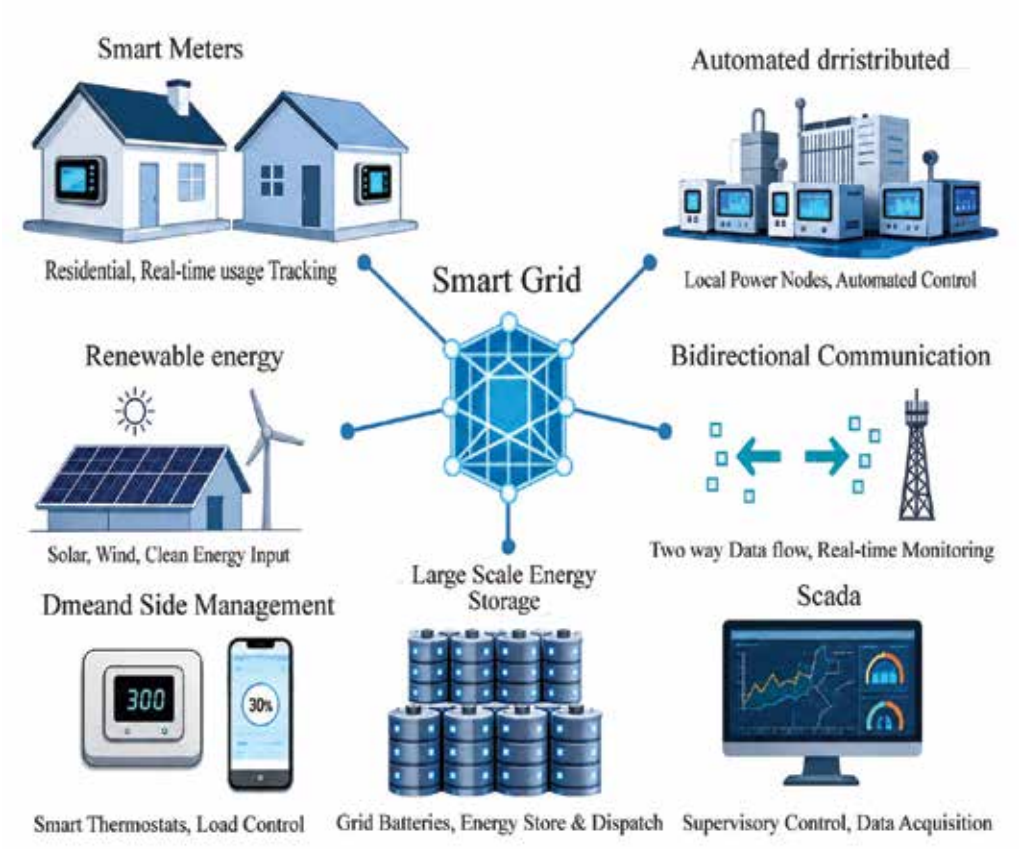


Fig. 2: Primal adaptation features for sustainable implementation of smart grid in Bangladesh

d) Cybersecurity risk
e) Regulatory and policy barriers,
f) Integrating intermittent energy and
g) socio-economic hurdles.

In spite of these challenges, a number of studies highlighted the potential benefits of smart grid adaption, especially in municipal areas with high load density.

4. METHODOLOGY

The methodology for the research on data-driven evaluation of smart grid adaptation in the distribution network of DESCO focusing on feeder-level load behavior, system inefficiency, and network topology is given in Fig. 3.

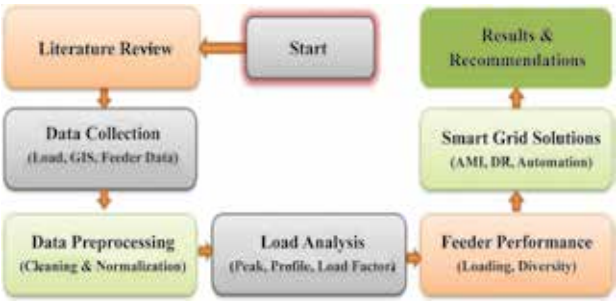


Fig. 3: Research Design

Data Description and Study Area

The study was conducted within the service area of Dhaka Electric Supply Company Limited (DESCO), which supplies electricity to the northern part of Dhaka City and adjoining areas of the Gazipur district. The analysis focuses on the Uttara Sector 13 distribution feeder, selected as a representative case study for evaluating smart grid adaptation at the feeder level.

The analysis is based on actual operational data collected from DESCO over the period of February, 26 to March, 26. The dataset comprises hourly feeder load demand, distribution transformer ratings, substation specifications, feeder capacities, consumer information, and GIS-based distribution network topology. In addition, selected system-level operational data, including national load demand profiles, were obtained from the National Load Dispatch Centre (NLDC) to provide a broader context for assessing smart grid implementation challenges and opportunities.

Prior to analysis, the collected data were preprocessed to ensure consistency and reliability. This process included verification of data completeness, removal of duplicate records, correction of inconsistencies, and integration of operational feeder data with the corresponding GIS network layers. The processed dataset was subsequently used for feeder-level performance evaluation, spatial network analysis, and the assessment of smart grid readiness within the DESCO distribution network.

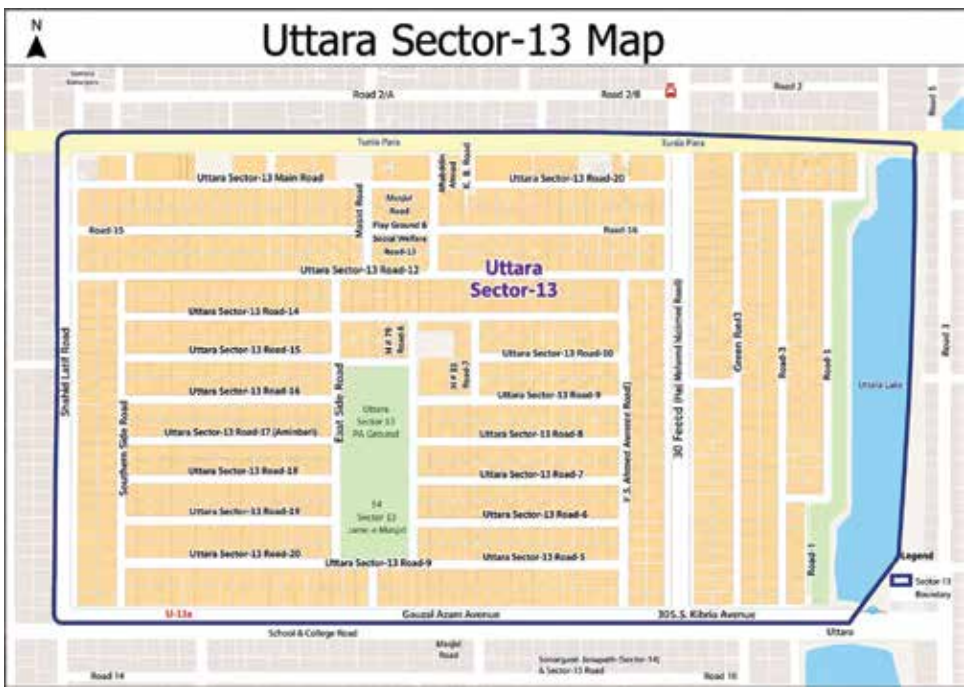


Fig. 4: GIS map of selected study area (Uttara Sector 13)

The Uttara sector 13 is characterized by a mix of residential, commercial, and industrial loads, serving total 8090 consumers. The power distributed network is divided into some feeders to act as primary link that transmit electrical power from a main substation to consumers or through distribution transformer. In the study conducted area six feeders such as Gareeb-E-Newaj, Gausal Azam, Uttara West, GA North, Sector-13, Shah Makdhum are considered. Both single phase and three phase consumers are distributed in each feeder to properly transmitting and distributing the electrical power. Number of consumers along with their load in different feeder is presented in Table 1 for better understanding.

In power system distribution network, there are different types of consumers and the sensitivity of supply to the corresponding consumer may different with respective to time. Such as electrical supply should be continuing without any interruption in medical centers but disturbance is acceptable in any time in residential building. So, number of different types of building should be considered for implementing the smart grid in any distribution network. Gausal Azam feeder was included in Table 1 to present the overall feeder inventory within the DESCO service area however, it was not selected for the detailed feeder-level analysis because other data are not found from authority.

Table 1: Number of consumers with their load in different feeders

Feeder Name	No. of Consumer	Total Load (KW)	Feeder Load Capacity (KW)
GA North	2202	10221	10410
Gareeb-E-Newaj	1993	12580	13233
Gausal Azam	1422	13214	19182
Sector-13	1773	11189	11113
Shah Makdhum	33	290	310
Uttara West	667	3951	4213
Total	8090	51446	58461

5. RESULTS AND DISCUSSION

This section illustrates the results of data driven analysis conducted on the distribution network of DESCO. Load data and GIS based network information is used to determine the load behavior, technical losses and feeder performance. To detect the operational inadequacies and their insinuations for smart grid adaptation in DESCO, load factor, power losses and feeder loading are studied as the fundamental factors.

Load Profile Analysis

The load characteristics of the feeder Gareeb E Newaj is investigated using 24-hour interval real data to assess system efficiency and utilization performance in Fig. 5. The observed load curve illustrates the significant deviation of demand between peak and off-peak demand levels. Peak load consumed during the evening hours at 18.00, while minimum demand is found during early morning hours. During the evening period, the maximum (peak) load is consumed as 205 kW, while the minimum (off peak) demand is recorded as 60 kW during early morning hours. The 3364.8 kW of total energy consumption is calculated over the study period causing in an average load of about 140.19 kW.

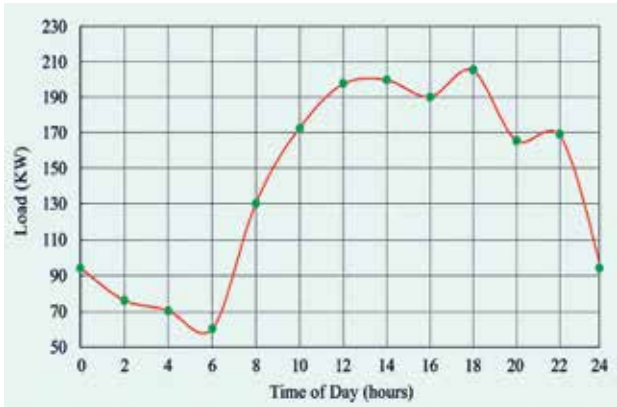


Fig. 5: Daily load curve of Gareeb E Newaj Feeder

Based on the above values, the load factor of the feeder is calculated as 0.684 which indicated the comparatively competent utilization of the feeder capacity. However, a considerable difference between peak and off-peak load recommends the existence of demand variability, which may lead to reduce system efficiency during low load periods and increase the technical losses.

From the smart grid viewpoint, this deviation highlighted the potential reimbursements of employing demand side management (DSM) schemes, such as peak shaving and load shifting. These approaches can lead to flatten the load curve to reduce the stress on distribution network and improving the load factor. Besides, the high peak consumption comparative to the average demand suggests that network components need to be sized to accommodate short duration peaks that may not be

economically appropriate. Hence, the outcomes reveal that while the feeder demonstrates a reasonable high load factor, there leftover opportunity for optimization through involvements of smart grid, mainly in improving load uniformity and decreasing peak demand.

Feeder Performance Analysis

The performance of the designated distribution five feeders is assessed based on key operational signs including peak load, average load, load factor and load changeability. These studies offer insight into feeder utilization, efficiency and appropriateness for smart grid adaptation.

Fig. 6 illustrates the variation in peak and off-peak load demand among the selected feeders. Gareeb E Newaj feeder exhibits the highest peak load of 205 kW, followed by GA North (98.5 kW), Sector 13 (93 kW), Shah Makdhum (52 kW), and Uttara West (46.5 kW). The peak load of Gareeb E Newaj is approximately 2.1 times higher than that of GA North and 4.4 times greater than that of Uttara West, indicating a substantial disparity in feeder loading characteristics.

The minimum off-peak load of 12 kW is recorded for the Shah Makdhum feeder, reflecting the highest variation between peak and off-peak demand among the selected feeders. To quantitatively evaluate feeder utilization, the load factor was calculated as the ratio of average load to peak load for each feeder. The feeder-wise load factor analysis is presented in Table 2.

Table 2: Feeder Performance Based on Load Factor

Feeder	Peak Load (kW)	Average load (kW)	Load Factor (%)
Sector 13	93	72.7	78.2
Gareeb E Newaj	205	140.2	68.4
Shah Makdhum	52	32.4	62.3
GA North	98.5	72.5	73.6
Uttara West	46.5	38.5	82.8

Lower load factors of feeder Shah Makdhum (62.3%) and Gareeb E Newaj (68.4%) indicates the higher load fluctuation, which may lead to increased I^2R losses owing to poor voltage profile stability and peak loading conditions. On the contrary, a relatively balanced load profile is observed in feeder Uttara West (82.8%), which provides the benefits of improved overall efficiency and reduced operational stress.

The results emphasize the significance of feeder level performance valuation in present distribution systems. In the perspective of Bangladesh's urban networks like DESCO, such data driven investigation helps to switch towards smart grid implementation, facilitating enhanced reliability, optimized asset utilization and reduced system losses.

6. SMART GRID ADAPTATION FRAMEWORK

The transition from conventional distribution networks to smart grid systems is indispensable for enhancing

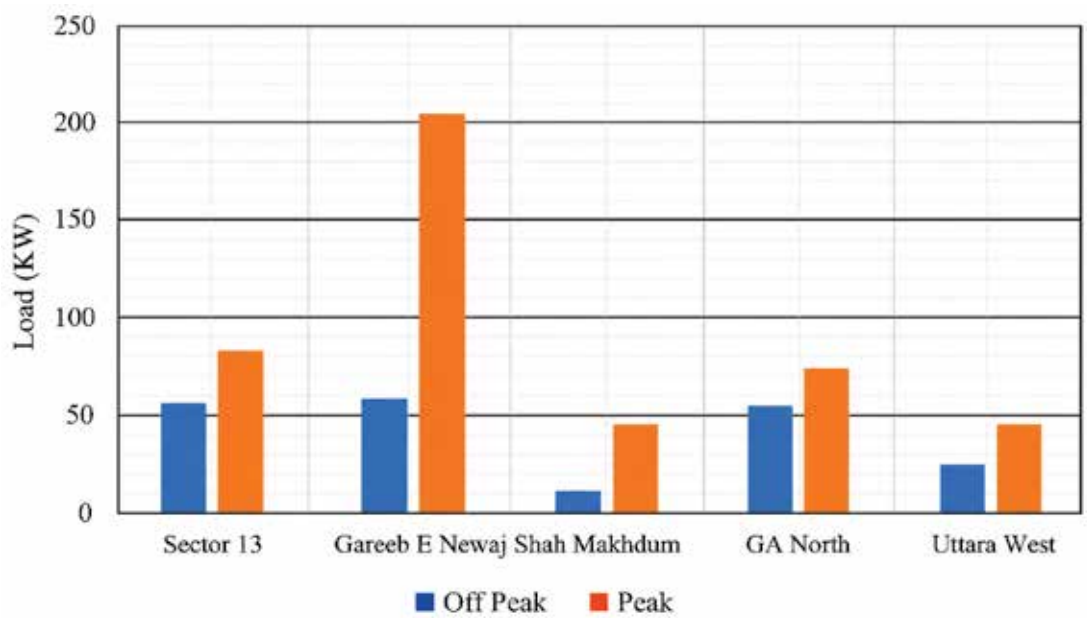


Fig. 6: Peak and off-peak demand of different feeders of study area

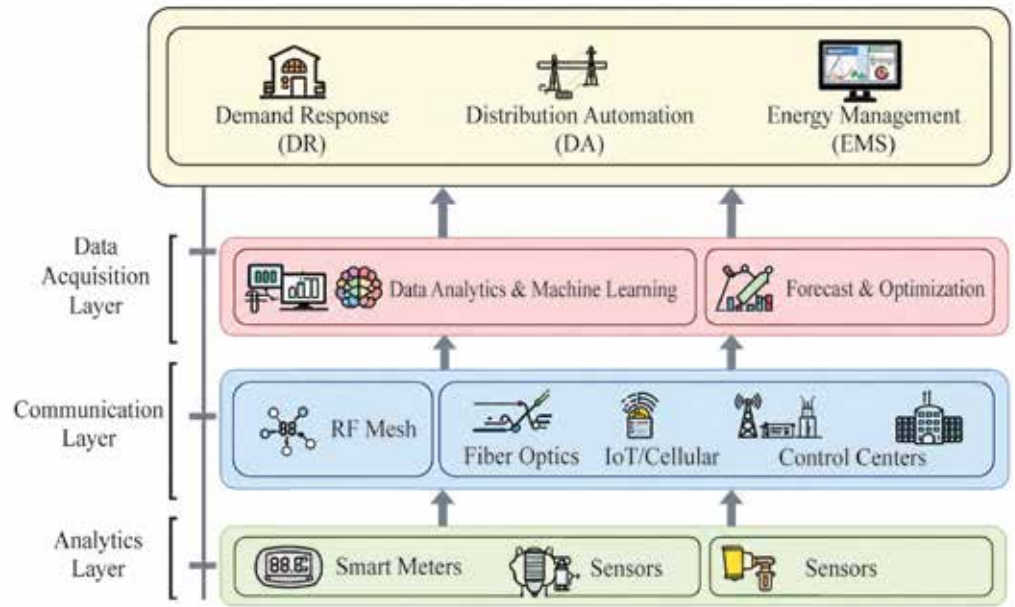


Fig. 7: Smart grid adaptation framework for DESCO

reliability, efficiency, and sustainability in urban distribution system such as those functioned by DESCO. A structured smart grid adaptation framework is offered based on the feeder performance assessment to address system losses, load variability, and peak demand in Fig. 7.

Key Functional Components

The following smart grid components are necessary according to investigated feeder characteristics:

a) Advanced Metering Infrastructure (AMI): Supports DSM and allows monitoring of real time consumption

b) Distribution Automation (DA): Enables automatic fault detection, isolation and supply restoration with improved system reliability.

c) Demand Response (DR): It can shift or reduce load during peak hours and very important for feeders like Gareeb E Newaj, where peak demand is high.

d) Distributed Energy Resources (DER): Integration of battery storage and rooftop solar PV can decrease peak load and improve system flexibility.

e) Energy Management System (EMS): Central Platform for monitoring, controlling and optimization of distribution operations.

Feeder Particular Adaptation Scheme

This framework highlights targeted interventions according to observed feeder performance:

a) **Gareeb E Newaj:** Needs demand response and peak shaving owing to moderate load factor and high peal demand.

b) **Shah Makdhum:** Emphasize on improving utilization efficiency and load flattening.

c) **Sector 13 and GA North:** Due to balanced load profile, these feeders are suitable for the integration of advanced monitoring systems and phased automation.

d) **Uttara West:** Designated as ideal feeder for the pilot smart grid implementation because of its high utilization efficiency and stable demand.

Implementation Challenges

In spite of having numerous advantages of smart grid adaptation, a number of challenges must be addressed:

a) Still need motivation on centralized generation for meeting demand growth.

b) High initial investment cost

c) Limited smart communication infrastructures

d) Grid and distribution code and standards for smart grid not yet implemented

e) Data management and cybersecurity unease

f) Governing and strategy constrictions in Bangladesh

g) Lack of automatic voltage and frequency mechanism

h) Sluggish development of renewable energy

i) Poor affordability of consumer to smart utilizations

7. LIMITATIONS AND FUTURE WORK

We acknowledge that the proposed framework was evaluated using operational data from selected feeders within the DESCO distribution network, which may limit its generalizability to other utilities with different network configurations and operating conditions. In addition, the current study primarily focuses on smart grid readiness assessment and does not incorporate real-time operational data, advanced optimization techniques, or economic feasibility analysis. The integration of real-time IoT, machine learning-based predictive analytics, and digital twin technologies can be included for further studies related to reediness of smart grid.

8. CONCLUSION

Bangladesh needs to go ahead with assaulting planning and implementation for aligning with the sustainable development goals (SDG) to move from the conventional grid system towards smart grid. An inclusive data driven assessment of smart grid adaptation in the distribution network of DESCO is presented in this paper using feeder real load data and GIS based network information. This assessment highlights the spatial heterogeneity of the network, where heavily populated city areas experience higher operational stress and demand concentration. The outcomes underscore the limitations of traditional grid operational in handling dynamic city load growth and reinforce the essential for smart monitoring and control technique. In the perspective, a viable pathway is offered by the smart grid for improving system performance. The implementation of advanced metering infrastructure, feeder automation, and demand side management can considerably improve operational visibility, load management, reduced peak load stress, and overall network efficiency.

REFERENCES

[1] G. Sharma, “A survey on secure communication technologies for smart grid cyber-physical systems,” e-Prime: Advances in Electrical Engineering, Electronics and Energy, vol. 10, Art. no. 100831, 2024.

[2] T. Ali, M. A. Ahmed, Z. B. Shams, S. M. Ferdous, and M. A. Hoque, “An overview of smart grid technology in Bangladesh: Development and opportunities,” in Proc. 2011 Int. Conf. Utility Exhibition on Power and Energy Systems (ICUE), pp. 1–5, 2011.

[3] B. Khan, S. Hussain, H. Ullah, C. Lai, A. A. Mohamed, and U. Eicker, “Low-voltage distribution grids optimization with increasing distributed energy generation: A review,” Energy Reports, vol. 15, Art. no. 108913, 2026.

[4] F. Alam, A. Rahaman, S. Mia, A. C. Dey, and T. H. Chowdhury, “Optimizing distribution losses through ETAP,” International Transactions on Electrical Engineering and Computer Science, vol. 4, no. 3, pp. 168–174, 2025.

[5] J. S. R. Quinlob, J. J. A. Abayan, and R. P. Tarife, “An integrated design framework for barangay microgrid planning using AI load forecasting, MILP economic dispatch, and GIS-based site suitability,” in Proc. IEEE 17th Int. Conf. Humanoid, Nanotechnology, Information Technology, Communication and Control, Environment, and Management (HNICEM), pp. 1–6, 2025.

[6] C. L. Athanasiadis, T. A. Papadopoulos, G. C. Kryonidis, and D. I. Doukas, “A review of distribution network applications based on smart meter data analytics,” Renewable and Sustainable Energy Reviews, vol. 191, Art. no. 114151, 2024.

[7] Z. Chen, A. M. Amani, X. Yu, and M. Jalili, “Control and optimisation of power grids using smart meter data: A review,” Sensors, vol. 23, no. 4, Art. no. 2118, 2023.

[8] D. Deka, V. Kekatos, and G. Cavraro, “Learning distribution grid topologies: A tutorial,” IEEE Transactions on Smart Grid, vol. 14, no. 5, pp. 4101–4120, 2023.

[9] A. A. El-Fergany, “Reviews, challenges, and insights on computational methods for network reconfigurations in smart electricity distribution networks,” Archives of Computational Methods in Engineering, vol. 31, pp. 1233–1253, 2024.

[10] Y. Gao, B. Kang, H. Xiao, Z. Wang, G. Ding, Z. Xu, C. Liu, D. Wang, and Y. Li, “A model for identifying the feeder-transformer relationship in distribution grids using a data-driven machine-learning algorithm,” *Frontiers in Energy Research*, vol. 11, Art. no. 1225407, 2023.

[11] S. R. Akhter, & M. M. Biswas, “Roadmap of smart grid for Bangladesh based on functions and technological challenges.” Electric Power Components and Systems, 44(8), 864-872, 2016.

[12] M. J. Rahaman, "Smart grid technology prospect of implementation in Bangladesh." J. Electr. Power Syst. Eng, 8, 2021.

[13] A. T. Belge, S. Gupta, S. Alegavi, V. Singh, & K. Shukla, "Advancements, challenges, and future prospects of smart grid technology in India." Frontiers in artificial intelligence, 7, 1475604, 2024.

[14] N. S. Boateng, M. C. Liscio, P. Sospiro, & G. Talluri, "Economic cost–benefit analysis on smart grid implementation in China." Sustainability, 17(7), 2946, 2025.

[15] G. G. Dranka, & P. Ferreira, "Towards a smart grid power system in Brazil: Challenges and opportunities." Energy, Policy, 136, 111033, 2020.

[16] R. J. Bhanushankar & D. D. Vyas, "Smart Grid Working Opportunities and Challenges in India–A Review." In 2024 Parul International Conference on Engineering and Technology (PICET) (pp. 1-5). IEEE, 2024.

[17] X. Xie, Y. Liu, X. Wang, & Y. Han, "On Constructing New-Type Power Systems in China." CSEE Journal of Power and Energy Systems, 11(6), 2710-2728, 2025.

Valorization of *Moringa Oleifera* Pod Residues into Functional Lignocellulosic Fiber: A Chemical and Mechanical Performance Study

Md. Ahasan Habib[1*], Habiba Akter[1,2], Md. Golam Mortuza Limon[1,3], Jannatul Nasrin[2], Ranajit Kumar Nag[2], Shomit Roy Prangon[2], S.M. Osman Ali[2], Md. Al-Amin[2], and Mehedi Hasan[2]

[1]Department of Textile Engineering, Dhaka University of Engineering & Technology, Gazipur, Bangladesh
[2]Department of Textile Engineering, BGMEA University of Fashion & Technology (BUFT), Bangladesh.
[3]Department of Textile Engineering, Northern University Bangladesh

ABSTRACT

This study explores the potential of *Moringa oleifera* pod fiber as a sustainable alternative to conventional fibers for reinforcement in various polymer matrix composites. The fibers were extracted and alkali treated to evaluate their suitability for textile and bio-based composite applications. The surface morphology, crystallinity, physical, mechanical, and thermal properties of the fibers were characterized. The fibers exhibited a favorable chemical composition, comprising 54.02% cellulose, 16.57% hemicellulose, and 17.81% lignin. The crystalline index (CI) was determined as 43.75%. The average diameter of the fibers tuft was 116.92 ± 2.65 µm, and the fiber density was 1.25 g/cm³. Additionally, the fibers dissolved in 70% sulfuric acid. Moreover, the fiber exhibited a maximum peak force of 2.02 N at an extension of approximately 15%. Furthermore, thermogravimetric analysis (TGA) indicated that the fiber was thermally stable up to about 250°C. A significant mass loss of 92.91% was observed between 85.1°C and 697.2°C, leaving a char residue of 7.09%. The findings suggest that *Moringa oleifera* pod fiber is a promising reinforcement material, comparable to other established natural fibers, for sustainable applications such as bio-composites, fiber blends, paper products, and eco-friendly packaging.

Keywords: Extraction, *Moringa Oleifera,* Lignocellulosic fiber, Chemical treatment

1. INTRODUCTION

The growing global demand has intensified research into natural fibers, particularly those derived from lignocellulosic biomass, as sustainable and environmentally friendly alternatives to traditional synthetic materials [1]. Natural plant fibers such as flax, jute, coir, banana, palm, and hemp have gained a considerable attention due to their abundance, environmental sustainability, biodegradability, renewability, low density, and cost-effectiveness, in contrast to synthetic fibers such as polyester, glass, carbon, and aramid, which are generally non-biodegradable and relatively expensive [2]. Consequently, numerous studies have focused on the extraction and characterization of lignocellulosic fibers from various plant sources, including bark, twigs, leaves, stems, and fruit bunches, to evaluate their potential applications in the textile, automotive, biomedical, and construction sectors [3].

Over the past decade, *Moringa oleifera* (MO) has attracted considerable research interest due to its medicinal, agricultural, environmental, and industrial potential [4]. It is commonly known as the "horseradish tree" or "drumstick tree" which is widely cultivated and rapidly growing. It is native to Pakistan, India, Bangladesh and Afghanistan as its remarkable drought tolerance enables growth in arid regions and nutrient-deficient soils [5]. The Moringa plant is also referred to as the "Miracle tree" due to its rich medicinal properties and nutritional benefits [6]. Furthermore, Moringa plays a significant role in addressing global challenges related to health, and environmental sustainability through its applications in food and animal feed production, water purification, and various industrial sectors [7]. In addition, different parts of MO, including the leaves, seeds, bark, roots, sap, pods, and flowers, are rich in essential vitamins, minerals, and antioxidants, making them a valuable source of nutrition, particularly in regions affected by food insecurity [8]. The leaves of MO (MOL) are a nutrient dense plant material with considerable health promoting potential. Owing to their rich bioactive composition, MOL exhibits strong antibacterial and antioxidant activities and is

*Corresponding author's email: habib32@duet.ac.bd

widely utilized in functional foods and nutraceutical formulations. [9]. Several research utilizing MOL like natural feed supplement in poultry diets [10], medicinal uses [11] etc. Again, Moringa seeds are a rich source of nutrients, similar to other parts of the plant. They are especially thought to be a good source of protein and high -quality oil. The cosmetics industry extensively utilizes MO seed oil, which is also used for biodiesel production and as an edible cooking oil [12]. Traditionally, MO seed powder has been used as a natural coagulant for pollutant flocculation and drinking water purification [13].

Moreover, *Moringa oleifera* pods (MOP) are round or triangular in shape, and the seeds are enclosed in a covering that may be readily removed. The outer hard and rough pericarp of the fruit is typically discarded as waste after seed extraction. This material is rich in fiber and is often treated as agricultural waste by commercial industries once its economic value has been utilized [14]. The mature MOP used for oil extraction produce a large amount of fibrous residue that is unsuitable for human consumption [14]. Discarding this waste not only increases environmental burdens but also represents a loss of potentially valuable lignocellulosic material. Therefore, MOP fiber can be valorized by repurposing it as a sustainable reinforcing material or raw fiber. Converting this inedible agricultural waste into useful resources supports both waste valorization and circular economy principles. The fibrous fraction can be investigated for use in bio-composites, eco-friendly textiles, paper goods, or biodegradable materials rather than being thrown away [15]. Biopolymer composites reinforced with MO fibers and a PLA matrix have been developed for potential applications in the automotive, aerospace, and packaging industries [16]. In addition, fly ash-modified MO fiber-reinforced epoxy composites have been fabricated and evaluated for sustainable engineering applications [17]. These applications are expected to support sustainable industrial development and improve overall resource efficiency. The global market for Moringa-based products reached USD 7.1 billion in 2021 and is expected to expand at a compound annual growth rate (CAGR) of 8.9 % between 2023 and 2032 [18]. If this underutilized biomass is turned into useful products by developing MOP fiber, it could create significant economic opportunities worldwide. Several studies have investigated different parts of the Moringa tree for various applications; however, the characterization of its fibers after chemical treatment remains limited in the literature. In order to determine the untapped potential of *Moringa oleifera* pod fiber as a novel lignocellulosic material for reinforcing composite materials and other cutting-edge sustainable applications, this study specifically aims to characterize the morphological, chemical, mechanical, and thermal properties of the fiber.

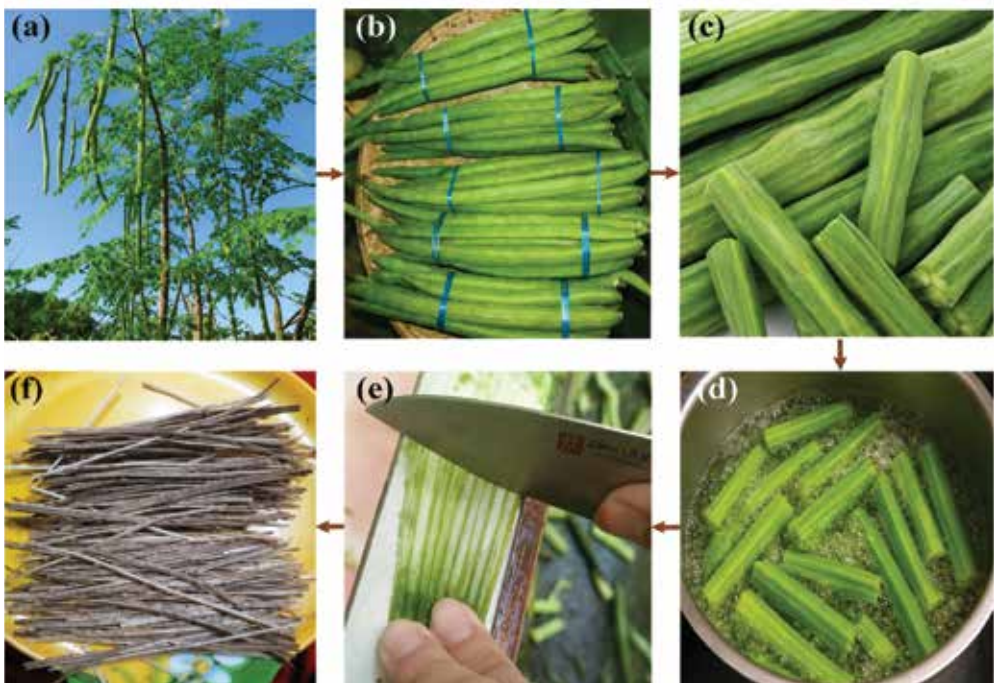


Fig. 1: Schematic representation of the MOP fiber extraction process: (a) *Moringa oleifera* tree; (b) collection of mature pods; (c) chopping of pods; (d) boiling of pods; (e) removal of non-fibrous material; and (f) extracted MOP fiber

2. EXPERIMENTAL

2.1 Materials

Mature Moringa pods were collected from a local market in Trisal Upazila, Mymensingh, Bangladesh. To chemically modify the fibers, sodium hydroxide (NaOH), hydrogen peroxide (H_2O_2), wetting agent, and sodium metasilicate (Na_2SiO_3) were purchased from the local market.

2.2 Fiber Extraction and Chemical Treatment

The collected mature Moringa pods were cut into sections approximately 10 cm in length. To make fiber separation easier, the samples were boiled in water roughly at 90°C for 60 min. Following boiling, the samples were allowed to cool for 2 h at room temperature. All the processes are shown in Fig. 1. After the softened plant material was manually removed, the remaining fibers were compressed to eliminate non-fibrous residue.

The fibers were subsequently cleaned and sun-dried until they reached a consistent moisture content. Chemical treatment of the extracted fibers (60 g) involved a 90 min immersion in a solution of NaOH (4.0%), H_2O_2-35% (4.0%), Na_2SiO_3 (1 g/L), and a wetting agent (1 g/L) at 90°C with 1:20 (M:L). The process concluded with a distilled water wash and fan assisted air drying to prepare the samples for further analysis. The chemical treatment of MOP fiber is shown in Fig. 2.

2.3 Morphological Analysis

The surface morphology of the extracted fibers was analyzed using a scanning electron microscope (SEM). Fiber samples measuring approximately 10 mm were randomly selected for examination. The fibers were mounted on aluminum stubs using double-sided carbon adhesive tape, and sputter-coated with a thin layer of gold to enhance electrical conductivity. The fiber morphology, surface characteristics, and fibrillar structure were examined using SEM at different magnifications. Fiber diameter was measured using ImageJ 1.80 software.

2.4 Fourier Transform Infrared Spectroscopy (FTIR)

An FT/IR-4700 type FTIR spectrometer with an ATR PRO ONE attachment was used to examine the chemical constituents of the MOP fibers. To remove residual moisture, approximately 5 g of fibers were chopped, washed, and oven-dried at 60 °C for 4 h. The dried fibers were then placed directly on the ATR crystal for analysis. FTIR spectra were recorded in the range of 4000–500 cm^{-1}, and the characteristic peaks corresponding to functional groups of cellulose, hemicellulose, lignin, and pectin were identified. Every spectrum was captured at transmittance (% T) in relation to wavenumber (cm^{-1}).

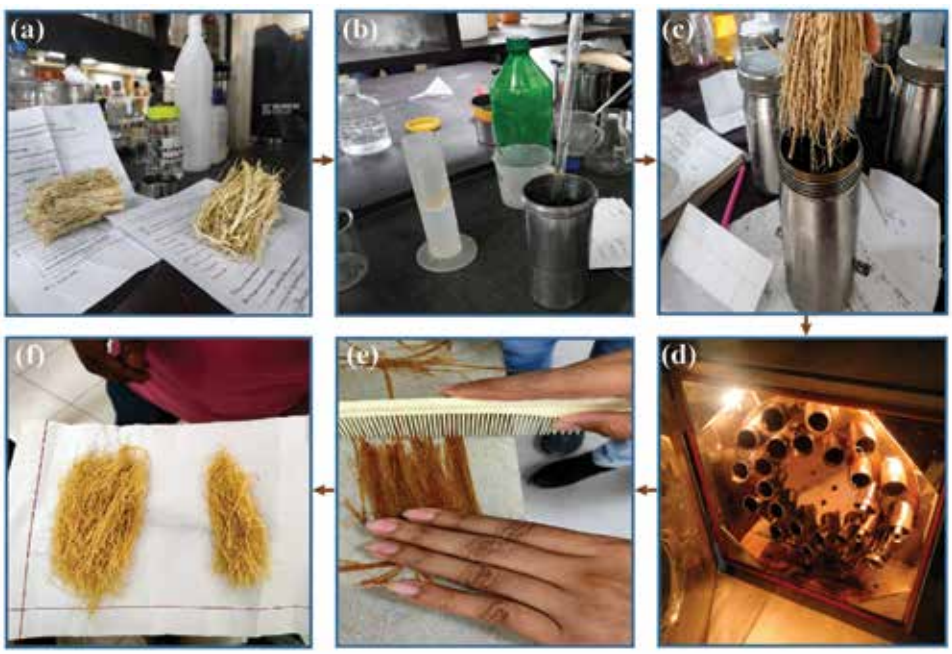


Fig. 2: Sequential steps involved in the chemical treatment of MOP fibers: (a) extracted fibers; (b) preparation of chemical solution; (c) fibers immersion; (d) chemical treatment; (e) combing of the fibers; and (f) treated MOP fiber

2.5 X-ray Diffraction (XRD)

The crystalline structure of the MOP fibers was analyzed using a PANalytical X'Pert PRO X-ray diffractometer equipped with Cu-Kα radiation (λ = 1.5406 Å). Approximately 4 g of fibers were ground into a fine powder, oven-dried at 110°C for 15 min, and the resulting dried sample (3.2 g) was stored in a sealed container prior to analysis to prevent moisture absorption. XRD patterns were recorded in the 2θ range of 10°– 60° with an operating voltage of 40 kV, current of 30 mA, a step size of 0.02°, and a scanning speed of 2°/min. The crystallinity index (CI) of the fibers was calculated using the Eqn. (1):

$$\text{CI}\ (\%) = \frac{I_{002} - I_{am}}{I_{002}} \times 100 \quad (1)$$

Where, I_{002} is the maximum intensity of the (002) lattice reflection at around 2θ = 22° and I_{am} is the intensity of the amorphous background at around 2θ = 18°.

2.6 Chemical Composition and Solubility Analysis

The TAPPI T429 cm-23 and T249 cm-85, T 236 cm-85 procedures were used to determine the percentages of cellulose, hemicellulose, and lignin. Additionally, determining the solubility of MOP fiber and to investigate the chemical resistance, sulfuric acid solutions of varying concentrations (50%, 60%, and 70%) are used.

2.7 Moisture Content and Moisture Regain Analysis

The oven drying method (ASTM D 2495–07 (2019)) was used to determine the weight of dried samples. The moisture content and moisture regain were evaluated as described in Eqn. (2) and (3).

$$\text{Moisture Content}\ \% = \frac{M_1 - M_2}{M_1} \times 100 \quad (2)$$

$$\text{Moisture Regain}\ \% = \frac{M_1 - M_2}{M_2} \times 100 \quad (3)$$

Where, M_1 is the weight of fiber samples at 25 °C and M_2 is the weight of the dried samples at 105°C for 4 h.

2.8 Fiber Density

The fiber density was measured using a gas pycnometer according to Eqn. (4). A precision balance was used to calculate the mass, and a pycnometer (Ultrapyc 5000, Anton Paar) was used to measure the volume.

$$\rho = \frac{m}{v} \times 100 \quad (4)$$

Here, ρ represents the fiber density, m is the mass of the fiber bundle (g), and V is its volume (cm^3).

2.9 Mechanical Properties Analysis

A universal testing machine (UTM) equipped with a 10 N load cell was used to evaluate the tensile properties of the extracted MOP fibers in accordance with ASTM D3822-14. Prior to testing, approximately 5 g of fibers were conditioned for 24 h at 25 ± 2°C and 65 ± 2% relative humidity. To ensure proper alignment and prevent slippage during testing, individual fibers were mounted on paper frames. The UTM was operated with a gauge length of 20 mm and a crosshead speed of 10 mm/min.

2.10 Thermogravimetric Analysis (TGA)

A thermogravimetric analyzer (TGA) was used to evaluate the thermal stability of MOP fibers under a nitrogen atmosphere to prevent oxidation. The fiber samples were cut into small pieces, thoroughly washed, and oven-dried at 60°C prior to analysis to eliminate residual moisture. For examination, around 5 g of the dried fibers were put in a platinum sample pan. The TGA test was carried out with a steady nitrogen flow of 50 mL/min from ambient temperature to 600°C at a heating rate of 10 °C/min. To ascertain the thermal stability, stages of disintegration, residual char content of the fibers, and the weight loss profile were monitored during the heating process.

3. RESULTS AND DISCUSSION

3.1 Morphological Analysis

Morphology and microstructural analyses of MOP fibers were studied using SEM analysis at 2000×, 5000×, and 10,000× magnifications which are shown in Fig. 3. Fig. 3(a) exhibits the lash fiber bundles compacted by several elementary fibers and exhibits relatively good structural continuity and few void contents. Fig. 3(b) demonstrates the longitudinal grooves and surface irregularities. The morphology of the intact bundles shows that the extraction process kept the integrity size of the fibers, which is an advantage for load bearing and reinforcement [19]. In Fig. 3(c), more distinct boundaries of individual fibrils are detectable along with surface irregularity and partial separation lines. These characteristics indicate the residual existence of non-cellulosic materials, such as lignin and hemicellulose that are typically present in untreated natural fibers. These whisker surface properties affect the fiber matrix interaction and are enhanced by chemical pretreatment.

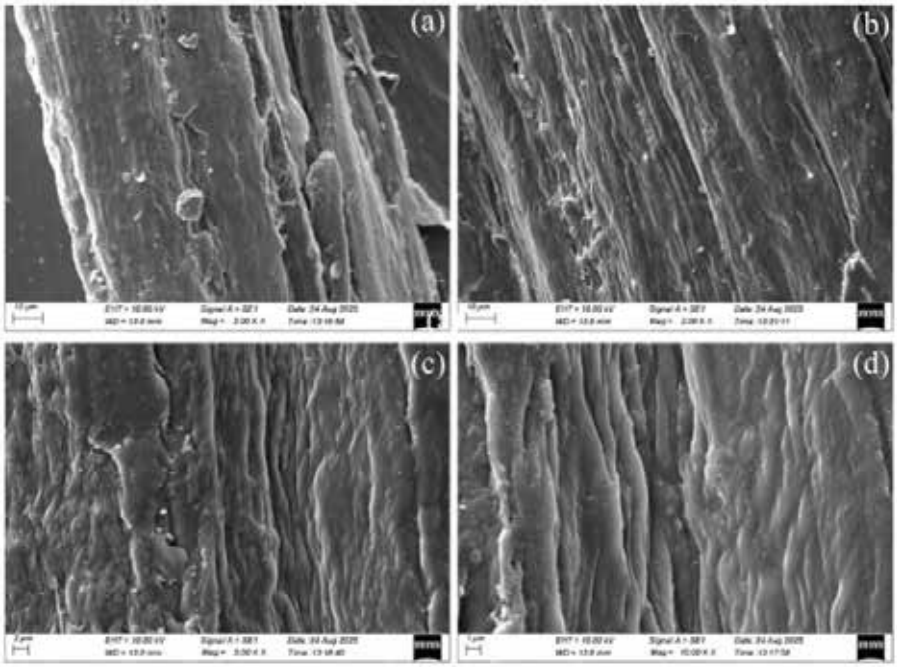


Fig. 3: SEM micrographs of chemically treated MOP fiber: (a) fiber bundle structure and surface irregularities; (b) longitudinal grooves and uneven surface texture, and (c) fibrillar structure, and (d) well-defined microfibrils

The fibers are shown in Fig. 3(d) densely packed and well-orientated cellulose microfibrils that are parallel to the fiber. This alignment of surfaces microfibrillar is responsible for the increase in tension and stiffness [20]. Moreover, the micro scale rough surface texture was good for mechanical interlocking in composites. Additionally, the average fiber diameter for tuft fiber was 116.92 ± 2.65 µm, as determined using ImageJ software.

3.2 Structural Analysis

FTIR spectroscopy was done to determine the functional groups of MOP fiber and to confirm its lignocellulosic nature, represented in Fig. 4. The wide band at around 3476 cm^{-1} in the FTIR spectrum is attributed to O–H stretching vibration of cellulose and hemicellulose implies hydrophilic nature of fiber [21]. This hydroxylated structure is responsible for both moisture absorption and chemical reactivity.

Furthermore peaks at around 1500-1600 cm^{-1} were assigned to aromatic C=C stretching vibrations of lignin present in fiber [22]. The presence of hydroxyl (–OH), carbonyl (C=O), and lignin-associated aromatic groups suggests that MOP fiber possesses chemical characteristics favorable for various value-added applications. The FTIR spectrum also reveals characteristic band in (1200-900 cm^{-1}) due to C–O–C and C–O stretching of cellulose [23]. The results are in good agreement with the reported spectrum of other natural fibers i.e. jute, banana and sisal and shows that MOP fiber is made of cellulose, hemicelluloses and lignin [24]. These functional groups can promote compatibility and interfacial bonding in bio-composite systems, while the lignocellulosic composition makes the fiber potentially suitable for fiber blends, and biodegradable packaging materials [25, 26].

3.3 Chemical Composition Analysis

The chemical compositions of MOP fiber show that it consists of 54.02% cellulose, 16.57% hemicelluloses and 17.81% lignin [27]. Contents of cellulose higher than 50% are desirable for mechanical reinforcement, pulp and composites applications. This value is close to that of the banana fiber and slightly lower than that of jute, thus suggesting good prospect as a strength in stiffness, shown in Table I. The intermediary content of hemicellulose gives enough flexibility and extensibility while it raises moisture sensitivity owing to its hydrophilicity. The higher hygroscopicity of hemicellulose-rich fibers may potentially compromise the dimensional stability in a humid atmosphere. Its higher lignin content than jute or flax contributes to its stiffness, microbial resistance, and thermal stability, but may make it less soft and white in textile grade applications [28]. The near neutral chemical composition indicates that MOP fiber would be most suitable for semi-structural

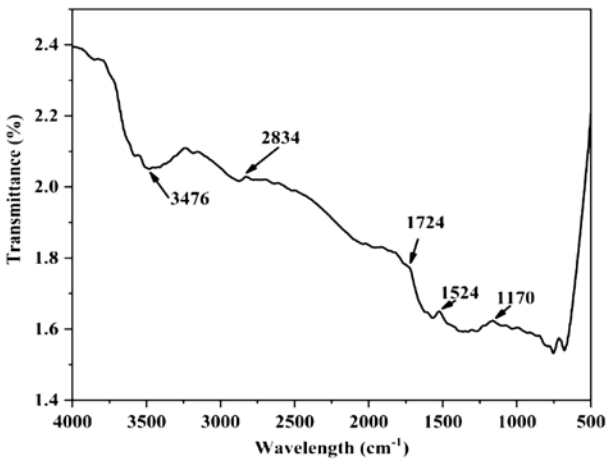


Fig. 4: FTIR spectrum of MOP fiber.

application such as composites, rope, matting paper and packaging. If the chemical treatments applied to decrease lignin and hemicellulose content to the fiber, it could be tailored for higher value textile use as well as biopolymer applications.

3.4 Solubility in Sulfuric Acid

The dissolution study was conducted using sulfuric acid (H_2SO_4), as concentrated sulfuric acid is capable of disrupting the intermolecular and intramolecular hydrogen-bonding network of cellulose, resulting in the dissolution of cellulosic fibers [34]. Accordingly, the dissolving behavior of MOP fiber was studied using concentrated H_2SO_4 solutions of 50%, 60%, and 70% to understand its chemical resistance under strong acidic conditions. The fibers were immersed in the solutions and agitated at room temperature (25 °C). At 50% H_2SO_4, the fibers swelled and softened after 1 h but did not dissolve. A similar trend was observed at 60%, where the fibers showed swelling and some structural damage, yet remained undissolved. However, at 70% H_2SO_4, the fibers rapidly swelled and completely dissolved within 30–60 min, forming a viscous solution. MOP fibers dissolves in 98% sulfuric acid as retting was done by water [35]. This behavior suggests that MOP fiber has comparatively higher acid resistance than typical cellulosic fibers, which usually dissolve at lower acid concentrations [36]. The resistance up to 70% acid can be explained by its stable lignocellulosic structure, where higher cellulose crystallinity, the lignin barrier effect, and intermolecular crosslinking work together to limit acid penetration and slow down degradation [37]. As a result, this fiber shows good potential for applications that require durability and chemical resistance, such as textile processing and composite reinforcement.

3.5 XRD Analysis

The crystalline structure of the MOP fiber was studied using X-ray diffraction (XRD) which is demonstrated in Fig. 5. The diffraction pattern exhibited a main peak at $2\theta \approx 23.04°$, which is attributed to the (002) plane of cellulose I, indicating a crystal structure of cellulose [38]. Additional peaks are located at $2\theta \approx 15.45°$ and $2\theta \approx 17.3°$, due to amorphous phase related to hemicellulose and lignin remaining in the sample [38]. The crystalline index (CI) of MOP fiber was evaluated as 43.75%. The presence of crystalline and amorphous phases proves that the fiber is a semi-crystalline material which is comparable to other natural fibers, including jute, hemp, and sisal [39, 40]. The semi-crystalline nature of MOP fiber provides a good balance of strength and flexibility, which enhances its potential for use in composites, packaging, and other sustainable reinforcement applications.

3.6 Density and Moisture Properties Analysis

The density of MOP fiber is measured to be as 1.25 g/cm^3. The comparison of density of different fibers are shown in Table II. The measured moisture content (9.19%) and moisture regain (10.12%) are also moderate in the matter of the water absorbency of MOP fiber when compared with common textile fibers like cotton and silk shown in

Table I: Chemical composition of different fibers

Fiber name	Cellulose %	Hemicellulose %	Lignin %	References
MOP	54	16.5	17.8	This study
Jute	51 – 73	12.0 – 21.0	5.0 – 16.0	[29]
Flax	60 – 81	14.0 – 21.0	2.0 – 3.0	[30]
Coir	32–44	0.15–0.2	40.0–45.0	[31]
Banana	55	20.3	25.3	[32]
Cotton	82 – 92	2.0 – 6.4	0.0– 1.7	[33]

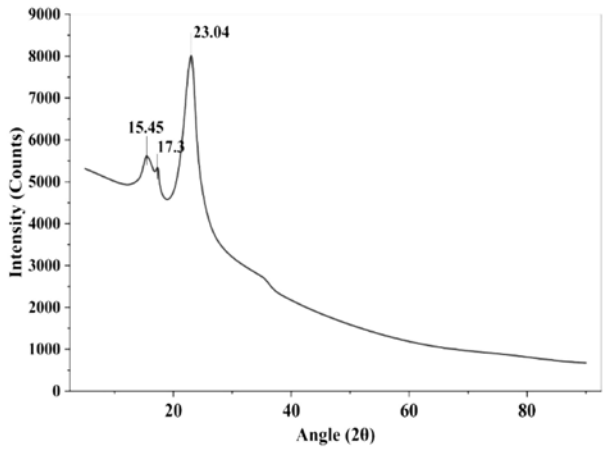


Fig. 5: XRD pattern of MOP fiber.

Table II [41]. It would be better as blended fiber however, while moisture sensitivity may limit operation in a high humidity environment, the use of surface treatment such as silane modification can greatly enhance its performance for composite and packaging applications.

3.7 Mechanical Properties Analysis

Fig. 6 illustrates the tensile behavior of MOP fibers, revealing variations in mechanical performance among the tested samples. Sample 1 reached a maximum force of 1.47 N at an extension of approximately 5%, indicating relatively brittle behavior with limited elongation before failure. In contrast, Sample 2 exhibited a higher maximum force of 2.02 N at an extension of about 15%, suggesting greater ductility and flexibility. These differences in mechanical performance may be attributed to variations in fiber maturity, microfibril orientation, or the efficiency of the extraction process [42]. The strength combined with the flexibility in tensile results indicates that, depending upon processing conditions, MOP fiber is customizable to various applications. This behavior is beneficial for blended fibers and composites where both structural strength and impact absorption are necessary.

3.8 Thermogravimetric Analysis

The thermal stability and degradation behavior of MOP fibers were analyzed using thermogravimetric analysis (TGA) under a nitrogen atmosphere, which is demonstrated in Fig. 7. Typical three stages of decomposition are found on TGA curves typical of lignocellulosic fibers. Weight loss of 5–10% below 150°C is due to evaporation of absorbed moisture and volatile material [43, 44]. The main degradation of which occurs in the range 200°C-400°C is mainly concerned with the thermal decomposition of

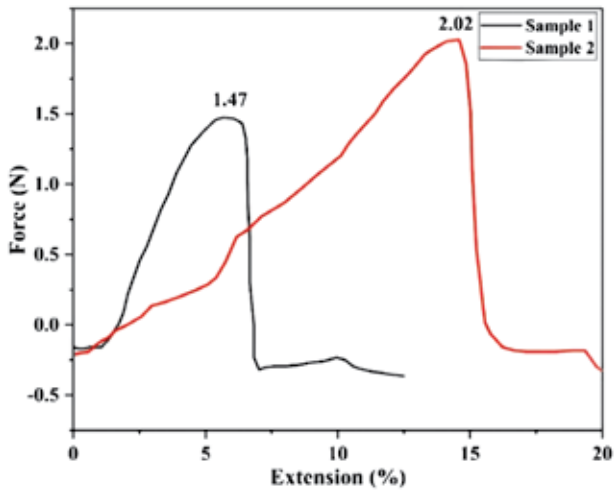


Fig. 6: Force–elongation behavior of MOP fiber

hemicellulose and cellulose [54]. Hemicellulose degrades at lower temperature because of its amorphous structure, while cellulose decomposes at higher temperature as it is crystalline in nature [55]. This first phase is the one that shows the largest mass-loss (those of greater lignin content) [56, 57]. Beyond 400°C, slow decomposition of lignin and formation of char occurs. The fiber is thermally stable at about 250 °C, suggesting potential compatibility with typical thermoset and thermoplastic polymers used in composites processing [57, 58].

Table II: Comparison of different fiber properties

Fiber	Density (g/ cm³)	Moisture Regain (%)	Peak Force (N)	Extension (%)	Thermal Stability (°C)	Char Residue (%)	References
MOP	1.25	10.12	2.02	15.00	250.0	7.09	This work
Banana	1.35	9.00-11.00	4.00–6.00	10.87	200.0	6.00	[45, 46]
Cotton	1.52-1.56	7.00-8.50	0.20–0.50	3.00-12.00	220.0	18.80	[26, 47]
Jute	1.30-1.50	12.00-23.00	3.50–5.50	1.10-3.30	205.0	21.00	[26, 48]
Flax	1.54	12.00	6.00–12.00	1.20-12.00	220.0	22.50	[26, 49]
Coconut	1.15-1.20	13.00-14.00	1.50-3.00	14.00	228.6	15.90-29.50	[50-53]

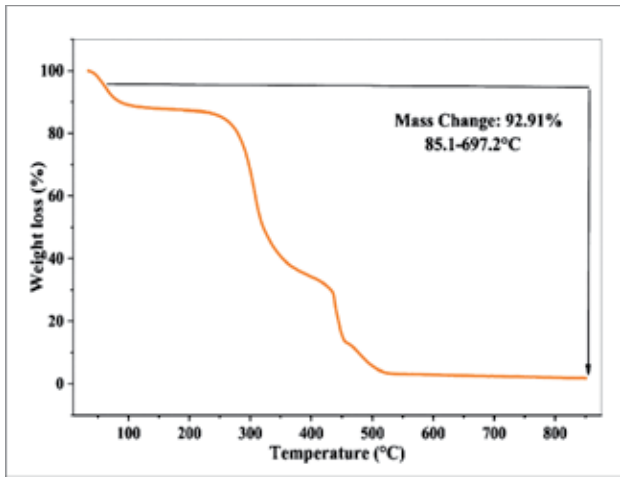


Fig. 7: TGA curve of MOP fiber.

The significant mass loss of 92.91% from 85.1°C to about 697.2°C and its char residue 7.09% suggests that MOP fiber is biodegradable with potential applications as reinforcement in sustainable polymer composites and biodegradable packaging systems.

4. CONCLUSION

The potential of *Moringa oleifera* pod fiber as a sustainable lignocellulosic material is systematically investigated in this study. The extraction, alkali treatment, and subsequent physical, mechanical, and chemical characterization of MOP fiber revealed a chemical composition of 54.02 % cellulose, 16.57 % hemicellulose, and 17.81 % lignin. The crystalline index (CI) of moringa fiber was evaluated as 43.75 %. Its semi-crystalline structure, flexibility, and micro fibril alignment contribute to good tensile strength, thermal stability, and biodegradability. Alkali-induced modifications reduced the inherent stiffness of the extracted fibers, resulting in a more flexible structure. This increase in flexibility transformed the previously un-spinnable material into a viable candidate for yarn production in fiber blends. Compared to established fibers such as jute, banana, and hemp, *Moringa oleifera* pod fiber shows competitive properties, particularly in durability and reinforcement potential. Although its higher lignin content requires chemical or enzymatic pretreatments to improve softness and whiteness, the fiber still offers excellent prospects for eco-friendly composites, packaging, and low-load construction materials. Moreover, advanced studies on fiber modification, large-scale production, composite fabrication, and life cycle assessment are required to establish moringa fiber as a viable alternative in the textile and allied industries.

REFERENCES

[1] Y. G. Thyavihalli Girijappa, S. Mavinkere Rangappa, J. Parameswaranpillai, and S. Siengchin, "Natural fibers as sustainable and renewable resource for development of eco-friendly composites: a comprehensive review," *Frontiers in materials,* vol. 6, p. 481024, 2019.

[2] A. Arevalo-Gallegos, Z. Ahmad, M. Asgher, R. Parra-Saldivar, and H. M. Iqbal, "Lignocellulose: a sustainable material to produce value-added products with a zero waste approach—a review," *International journal of biological and macromolecules,* vol. 99, pp. 308-318, 2017.

[3] T. Eleutério, M. J. Trota, M. G. Meirelles, and H. C. Vasconcelos, "A review of natural fibers: classification, composition, extraction, treatments, and applications," *Fibers,* vol. 13, no. 9, p. 119, 2025.

[4] C. Trigo, M. L. Castello, M. D. Ortola, F. J. Garcia-Mares, and M. Desamparados Soriano, "Moringa oleifera: An unknown crop in developed countries with great potential for industry and adapted to climate change," *Foods,* vol. 10, no. 1, p. 31, 2020.

[5] H. Mahaveerchand and A. A. Abdul Salam, "Environmental, industrial, and health benefits of Moringa oleifera," *Phytochemistry Reviews,* vol. 23, no. 5, pp. 1497-1556, 2024.

[6] S. V. Patil, B. V. Mohite, K. R. Marathe, N. S. Salunkhe, V. Marathe, and V. S. Patil, "Moringa tree, gift of nature: a review on nutritional and industrial potential," *Current Pharmacology Reports,* vol. 8, no. 4, pp. 262-280, 2022.

[7] H. El Bilali *et al.*, "Research on moringa (Moringa oleifera Lam.) in Africa," *Plants,* vol. 13, no. 12, p. 1613, 2024.

[8] E. Seifu and A. Angassa, "Food and nonfood applications of the African moringa plant (Moringa stenopetala)," in *Processing, Nutrition and Value Addition Principles of Neglected and Underutilized African Foods*: Elsevier, 2026, pp. 209-226.

[9] S. J. Stohs and M. J. Hartman, "Review of the safety and efficacy of Moringa oleifera," *Phytotherapy Research,* vol. 29, no. 6, pp. 796-804, 2015.

[10] S. Mahfuz and X. S. Piao, "Application of Moringa (Moringa oleifera) as natural feed supplement in poultry diets," *Animals,* vol. 9, no. 7, p. 431, 2019.

[11] L. Gopalakrishnan, K. Doriya, and D. S. Kumar, "Moringa oleifera: A review on nutritive importance and its medicinal application," *Food science and human wellness,* vol. 5, no. 2, pp. 49-56, 2016.

[12] M. Shahbaz *et al.*, "Antioxidant, anticancer, and anti-inflammatory potential of Moringa seed and Moringa seed oil: A comprehensive approach," *Food Science and Nutrition,* vol. 12, no. 9, pp. 6157-6173, 2024.

[13] S. Polepalli and C. P. Rao, "Drum stick seed powder as smart material for water purification: role of Moringa oleifera coagulant protein-coated copper phosphate nanoflowers for the removal of heavy toxic metal ions and oxidative degradation of dyes from water," *ACS Sustainable Chemistry and Engineering,* vol. 6, no. 11, pp. 15634-15643, 2018.

[14] L. A. de Moraes Pinto, F. de Oliveira Tavares, R. Bergamasco, M. F. Vieira, and A. M. S. Vieira, "Biosorption of Manganese Using Moringa oleifera Seed Pods: A Sustainable Approach to Water Treatment," *Separations,* vol. 12, no. 9, p. 246, 2025.

[15] M. Ashok Kumar, G. Ramachandra Reddy, H. Raghavendra Rao, K. Hemachandra Reddy, and B. Nanjunda Reddy, "Assessment of glass/drumstick fruit fiber (Moringa oleifera) reinforced epoxy hybrid composites," *International Journal of Polymeric Materials,* vol. 61, no. 10, pp. 759-767, 2012.

[16] B. Kadarkarai *et al.*, "Evaluation of varying properties of Moringa oleifera fiber/polylactic acid biopolymer composites," *Polymer Bulletin,* vol. 83, no. 8, p. 409, 2026.

[17] N. P. Mungle *et al.*, "Development and characterization of fly ash-modified Moringa oleifera fiber epoxy composites for sustainable engineering applications," *Interactions,* vol. 247, no. 1, p. 123, 2026.

[18] S. Sahu, S. Patel, D. Khokhar, T. Sahu, and H. Kumar, "Infrared Drying Kinetics and Mathematical Modeling of Moringa oleifera Leaves," *Heat Transfer,* vol. 55, no. 2, pp. 1294-1307, 2026.

[19] I. O. Oladele, G. S. Ogunwande, A. S. Taiwo, and S. S. Lephuthing, "Development and characterization of moringa oleifera fruit waste pod derived particulate cellulosic reinforced epoxy bio-composites for structural applications," *Heliyon,* vol. 8, no. 6, 2022.

[20] M. de Moraes Valentim and J. F. de Souza Gonçalves, "Characterization of Polymeric Composite Reinforced with Moringa oleifera Pod Fibers," *Semina: Ciências Exatas e Tecnológicas,* vol. 45, pp. e51464-e51464, 2024.

[21] E. Jayamani, T. G. Loong, and M. K. B. Bakri, "Comparative study of Fourier transform infrared spectroscopy (FTIR) analysis of natural fibres treated with chemical, physical and biological methods," *Polymer Bulletin,* vol. 77, no. 4, pp. 1605-1629, 2020.

[22] Y. S. Kurniawan, "A comparative study on phytochemical screening and antioxidant activity of aqueous extract from various parts of Moringa oleifera," *Indonesian Journal of Natural Pigments,* vol. 3, no. 2, pp. 43-47, 2021.

[23] S. Y. Oh *et al.*, "Crystalline structure analysis of cellulose treated with sodium hydroxide and carbon dioxide by means of X-ray diffraction and FTIR spectroscopy," *Carbohydrate research,* vol. 340, no. 15, pp. 2376-2391, 2005.

[24] M. Rosa *et al.*, "Cellulose nanowhiskers from coconut husk fibers: Effect of preparation conditions on their thermal and morphological behavior," *Carbohydrate polymers,* vol. 81, no. 1, pp. 83-92, 2010.

[25] O. Faruk, A. K. Bledzki, H.-P. Fink, and M. Sain, "Biocomposites reinforced with natural fibers: 2000–2010," *Progress in polymer science,* vol. 37, no. 11, pp. 1552-1596, 2012.

[26] K. L. Pickering, M. A. Efendy, and T. M. Le, "A review of recent developments in natural fibre composites and their mechanical performance," *Composites Part A: Applied Science and Manufacturing,* vol. 83, pp. 98-112, 2016.

[27] A. Sharma, G. Dhiman, P. S. Lal, R. D. Godiyal, and B. P. Thapliyal, "Characterisation of Moringa oleifera (drumstick) wood for pulp and paper making," *Cellul Chem Technol,* vol. 55, no. 3-4, pp. 255-262, 2021.

[28] M. Bonyani, I. C. Marincic, and S. Krishnan, "Advancing Sustainable Materials Engineering with Natural-Fiber Biocomposites," *Journal of Composites Science,* 2026.

[29] A. Samir, F. H. Ashour, A. A. Hakim, and M. Bassyouni, "Recent advances in biodegradable polymers for sustainable applications," *Npj Materials Degradation,* vol. 6, no. 1, p. 68, 2022.

[30] L. T. Vo and P. Navard, "Treatments of plant biomass for cementitious building materials–A review," *Construction and Building Materials,* vol. 121, pp. 161-176, 2016.

[31] J. Binoj, R. E. Raj, V. Sreenivasan, and G. R. Thusnavis, "Morphological, physical, mechanical, chemical and thermal characterization of sustainable Indian Areca fruit husk fibers (Areca Catechu L.) as potential alternate for hazardous synthetic fibers," *Journal of Bionic Engineering,* vol. 13, no. 1, pp. 156-165, 2016.

[32] T. Sango *et al.*, "Step–wise multi–scale deconstruction of banana pseudo–stem (Musa acuminata) biomass and morpho–mechanical characterization of extracted long fibres for sustainable applications," *Industrial Crops and Products,* vol. 122, pp. 657-668, 2018.

[33] P. Paulraj, K. Balakrishnan, R. Rajendran, and B. Alagappan, "Investigation on recent research of mechanical properties of natural fiber reinforced polymer (NFRP) materials," *Mater Plast,* vol. 58, no. 2, pp. 100-118, 2021.

[34] C. Wu, J. Li, Y. q. Zhang, X. Li, S. y. Wang, and D. q. Li, "Cellulose dissolution, modification, and the derived hydrogel: a review," *ChemSusChem,* vol. 16, no. 21, p. e202300518, 2023.

[35] M. D. Arumuga, "A Study on Fibre Extracted from Drumstick by Water Retting Method," *A-COMPILATION,* p. 52.

[36] A. H. Mohammed, "Studying the Improvement of the Solubility of Cellulosic Fibers," *Journal of Engineering,* vol. 22, no. 7, pp. 21-37, 2016.

[37] H. Du *et al.*, "Lignocellulosic Films: Preparation, Properties, and Applications," *Chemical Reviews,* vol. 125, no. 24, pp. 11666-11814, 2025.

[38] M.-C. Stanciu, F. Tanasă, and C.-A. Teacă, "Crystallinity changes in modified cellulose substrates evidenced by spectral and X-ray diffraction data," *Polysaccharides,* vol. 6, no. 2, p. 30, 2025.

[39] H. Hajiha, M. Sain, and L. H. Mei, "Modification and characterization of hemp and sisal fibers," *Journal of Natural Fibers,* vol. 11, no. 2, pp. 144-168, 2014.

[40] M. Z. Ul Haq *et al.*, "Mechanical and Durability Performance of Sisal, Jute, and Hemp Fiber-Reinforced Concrete: Effects of Chemical Treatment and Fiber Geometry," *Journal of Natural Fibers,* vol. 22, no. 1, p. 2583855, 2025.

[41] J. Wang, B. Zhong, and W. Chen, "Research on the comprehensive properties of cotton/silk fiber grinding knitted fabrics," *Fibers Polymers,* vol. 26, no. 7, pp. 3203-3215, 2025.

[42] V. Sadrmanesh and Y. Chen, "Bast fibres: structure, processing, properties, and applications," *International Materials Reviews,* vol. 64, no. 7, pp. 381-406, 2019.

[43] M. Jerman and R. Černý, "Effect of moisture content on heat and moisture transport and storage properties of thermal insulation materials," *Energy Buildings,* vol. 53, pp. 39-46, 2012.

[44] M. R. Bhuiyan, H. Akter, S. Islam, M. A. Darda, and M. A. Bari, "Jute-reinforced hybrid biocomposite incorporated with low thermal conductive silica aerogel for improved resistance to conductive and radiative heat," *Industrial Crops and Products,* vol. 222, p. 119773, 2024.

[45] M. M. Rashid, N. Abir, S. Islam, M. A. Reza, R. K. Nag, and M. I. Iqbal, "Extraction and characterization of a noble cellulose-rich cotton-like convoluted, lightweight and soft fiber from the floral part of the banana plant pseudo stem," *Cellulose,* vol. 32, no. 5, pp. 3027-3042, 2025.

[46] R. Bhatnagar, G. Gupta, and S. Yadav, "A review on composition and properties of banana fibers," *Cellulose,* vol. 60, p. 65, 2015.

[47] G. Dorez, L. Ferry, R. Sonnier, A. Taguet, and J.-M. Lopez-Cuesta, "Effect of cellulose, hemicellulose and lignin contents on pyrolysis and combustion of natural fibers," *Journal of Analytical and Applied Pyrolysis,* vol. 107, pp. 323-331, 2014.

[48] J. Shebaz Ahmed, K. Satyasree, R. Rohith Kumar, O. Meenakshisundaram, and S. Shanmugavel, "A comprehensive review on recent developments of natural fiber composites synthesis, processing, properties, and characterization," *Engineering Research Express,* vol. 5, no. 3, p. 032001, 2023.

[49] A. Célino, S. Fréour, F. Jacquemin, and P. Casari, "The hygroscopic behavior of plant fibers: a review," *Frontiers in chemistry,* vol. 1, p. 43, 2014.

[50] M. Siti Alwani, H. Abdul Khalil, O. Sulaiman, M. N. Islam, and R. Dungani, "An Approach to

Using Agricultural Waste Fibres in Biocomposites Application: Thermogravimetric Analysis and Activation Energy Study," *BioResources,* vol. 9, no. 1, 2014.

[51] Y. Kaushik, N. Sooriyaperakasam, U. Rathee, and N. Naik, "A mini review of natural cellulosic fibers: Extraction, treatment and characterization methods," *Comput. Mech. Manag,* vol. 2, pp. 32-47, 2023.

[52] A. Komuraiah, N. S. Kumar, and B. D. Prasad, "Chemical composition of natural fibers and its influence on their mechanical properties," *Mechanics of composite materials,* vol. 50, no. 3, pp. 359-376, 2014.

[53] S. S. Munawar, K. Umemura, and S. Kawai, "Characterization of the morphological, physical, and mechanical properties of seven nonwood plant fiber bundles," *Journal of Wood Science,* vol. 53, no. 2, pp. 108-113, 2007.

[54] W.-H. Chen, C.-W. Wang, H. C. Ong, P. L. Show, and T.-H. Hsieh, "Torrefaction, pyrolysis and two-stage thermodegradation of hemicellulose, cellulose and lignin," *Fuel,* vol. 258, p. 116168, 2019.

[55] M. A. Habib, M. A. Shahid, A. H. Bhuiyan, and H. Akter, "Development of jute-polyethylene nonwoven fabric for sustainable packaging application," *Materials Research Innovations,* vol. 29, no. 2, pp. 85-92, 2025.

[56] T. Sun *et al.*, "Pyrolysis gas proportions analysis of hardwood corresponding to hemicellulose, cellulose and lignin based on the TG-FTIR analysis," *International Journal of Biological Macromolecules,* p. 150964, 2026.

[57] M. R. Bhuiyan *et al.*, "Flame resistance and heat barrier performance of sustainable plain-woven jute composite panels for thermal insulation in buildings," *Applied Energy,* vol. 345, p. 121317, 2023.

[58] Y. Gao, X.-H. Wang, H.-P. Yang, and H.-P. Chen, "Characterization of products from hydrothermal treatments of cellulose," *Energy,* vol. 42, no. 1, pp. 457-465, 2012.

Finite Element Analysis of Aluminum-Vanadium Alloyed Titanium Billets Forged under Warm Forming Conditions Using DEFORM-3D

Rotan Kumar Saha*, Golap Hossain and Rajib Talukder

Department of Industrial and Production Engineering, Dhaka University of Engineering and Technology, Gazipur, Bangladesh

ABSTRACT

Titanium alloys, particularly Ti-6Al-6V-2Sn and Ti-6Al-2Sn-4Zr-2Mo, are extensively used in aerospace, automotive and biomedical applications because of their high specific strength, corrosion resistance and thermal stability. This study presents a comparative finite element analysis of the warm-forming behavior of these alloys using DEFORM-3D V6.1. Three-dimensional simulations of open-die forging were performed at billet temperatures of 200, 400, and 600 °C under press loads of 700, 1000 and 2500 tons. The thermo-mechanical responses were evaluated through damage, effective stress, effective strain, total displacement, ultimate temperature, material velocity and Z-load. The results show that Ti-6Al-6V-2Sn exhibited superior forgeability, achieving the lowest damage (0.106), minimum effective stress (331 MPa) and minimum Z-load (141 tons), indicating stable deformation and reduced forming resistance. In contrast, Ti-6Al-2Sn-4Zr-2Mo demonstrated higher flow strength, with minimum damage (0.295), effective strain (2.23 mm/mm) and effective stress (736 MPa) at 600 °C under a 1000-ton load, while requiring substantially higher forming loads because of its enhanced structural strength. Increasing billet temperature significantly reduced forming stress and Z-load for both alloys, confirming the beneficial effect of thermal softening during warm forging. The comparative process-property relationships established in this study provide practical guidelines for selecting suitable warm-forming conditions and demonstrate the capability of finite element simulation as a reliable tool for optimizing titanium alloy forging processes for advanced engineering applications.

Keywords: Finite Element Analysis, Deform-3D, Titanium alloy, Warm Forming, Optimization

1. INTRODUCTION

Titanium alloys have become critical engineering materials in industries such as aerospace, automotive, biomedical, marine, nuclear and chemical processing owing to their exceptional mechanical properties, corrosion resistance and biocompatibility, which enable the development of lightweight, high-strength components capable of withstanding extreme service conditions [1,2]. Among them, Ti-6Al-6V-2Sn and Ti-6Al-2Sn-4Zr-2Mo alloys stand out because of their unique combination of strength, toughness, ductility and thermal stability, which makes them suitable for a wide range of high-performance applications where reliability and precision are paramount [3]. The manufacturing of titanium alloys, however, remains challenging due to their high strength at elevated temperatures and limited room-temperature formability, which necessitates the use of advanced forming techniques to improve manufacturability while retaining their desirable mechanical characteristics [4]. Warm forming, conducted above room temperature but below the recrystallization range, has emerged as an effective alternative to conventional cold and hot forming because it reduces forming loads, improves ductility and enhances dimensional accuracy while limiting excessive grain growth. These advantages are particularly beneficial for aluminum-vanadium alloyed titanium alloys, where refined α–β microstructures contribute to improved fatigue resistance and mechanical performance [5]. By lowering material flow stress, warm forming enhances malleability without compromising structural integrity, enabling the production of high-quality titanium components with superior surface finish. However, optimization of forming temperature, strain rate and die geometry for such alloys remains insufficiently explored for industrial-scale applications [6]. To address these complexities, researchers have turned to computational modeling and advanced simulation tools. Finite Element Analysis (FEA) has revolutionized the design and optimization of metal forming processes by providing detailed insights into material deformation behavior, thermal effects and stress distribution during forming operations [7]. Among various FEA-based platforms, Deform-3D is widely

*Corresponding author's email: rotansaha@duet.ac.bd

recognized for its ability to simulate complex metal forming processes, including forging, extrusion and rolling, with high predictive accuracy [8].

Deform-3D enables engineers to experiment with different process parameters in a virtual environment, thereby reducing dependence on costly trial-and-error experimentation, minimizing production waste and facilitating data-driven process optimization. For titanium alloys, such simulations are particularly valuable as they allow for the prediction of material flow, temperature gradients and residual stresses, which are critical for achieving high-quality components [9]. Rajesh et al. demonstrated the utility of Deform-3D by modeling the open-die forging of Ti-6Al-4V billets in the temperature range of 500–1000°C, observing that effective strain decreased from 6.84 mm/mm at 500°C to 3.39 mm/mm at 1000°C, while the maximum effective stress was recorded at 715 MPa at 500°C [5]. Similarly, Rajesh et al. also used computational modeling to optimize precision forging operations for steel alloys such as 42CrMo4 and 16CrMo4 [10], while Graf et al. investigated the dynamic interaction between oxidation, microstructural evolution and alloying in steels during elevated-temperature forming, highlighting the significance of understanding thermo-mechanical interactions [11]. Lee et al. proposed an innovative warm-forging method for aluminum alloys to improve automotive component manufacturing by reducing weight and increasing precision [12], whereas Tomcjak et al. optimized rotational compression parameters to achieve superior dimensional control during forging [13]. For titanium alloys, Wang et al. found that the strength of solution-treated Ti-6Al-6V-2Sn decreased with increasing aging temperature, further emphasizing the need for precise control of thermal and mechanical variables during forming [14]. These studies collectively demonstrate the power of FEA and simulation tools like Deform-3D in process optimization; however, they also highlight a significant gap in the application of such methods specifically to the warm forming of titanium alloys containing aluminum and vanadium.

The existing literature, while rich in studies on hot forging, cold forming and general titanium processing, lacks a comprehensive exploration of the warm-forming regime, where the synergistic benefits of reduced forming forces, enhanced ductility and minimized grain coarsening can be fully realized. Furthermore, limited attention has been paid to integrating simulation results with experimental validation, an essential step for translating computational insights into industrially viable manufacturing strategies [15]. This gap is particularly critical given the growing demand for titanium components in aerospace and medical applications, where even minor deviations in dimensional accuracy, residual stress, or microstructural uniformity can compromise component performance. Additionally, while research has investigated the behavior of other materials such as stainless steels (AISI 304, AISI 316), tool steels (AISI H21) and various aluminum alloys under different forming and heat-treatment conditions, studies that systematically examine how temperature, strain rate, and forming velocity interact during the warm forming of titanium billets alloyed with aluminum and vanadium are limited [16]. Furthermore, the lack of research on residual stress control, surface quality improvement and defect minimization within this specific context represents a critical barrier to industrial adoption. These shortcomings underscore the need for a targeted study that leverages the capabilities of FEA and Deform-3D to not only simulate but also optimize warm-forming operations for Ti-Al-V billets, thereby bridging the gap between computational modeling and practical manufacturing.

The present study addresses an important research gap by providing a comprehensive comparative finite element analysis of the warm-forming behavior of two aerospace-grade titanium alloys, Ti-6Al-6V-2Sn and Ti-6Al-2Sn-4Zr-2Mo, using DEFORM-3D. Unlike previous studies that primarily focused on a single alloy or limited processing conditions, this work systematically evaluates the combined effects of forming temperature and press load on damage, effective strain, effective stress, displacement, velocity, ultimate temperature and Z-load. The comparative assessment establishes the process-property relationships governing alloy forgeability and identifies the most favorable processing conditions for each alloy, offering practical guidelines for improving warm-forging efficiency, reducing forming loads, and enhancing component quality in advanced engineering applications.

2. MATERIALS AND EXPERIMENTAL METHODOLOGY

2.1 Materials Description

In this study, two advanced titanium alloys Ti-6Al-6V-2Sn and Ti-6Al-2Sn-4Zr-2Mo were selected for finite element analysis of the warm forming process using Deform-3D. A billet of dimensions 60 mm × 60 mm × 120 mm with a 15 mm corner radius was modeled using SolidWorks and imported into Deform-3D. The primary material of focus, Ti-6Al-6V-2Sn, an aluminum–

vanadium alloyed titanium grade was chosen due to its exceptional mechanical properties, thermal stability and corrosion resistance under elevated temperature and high-stress conditions [17].

Table I: Elemental Composition Table for Ti-6Al-6V-2Sn and Ti-6Al-2Sn-4Zr-2Mo Alloys.

Titanium alloy		
Elemental Composition (Wt. %)	Ti-6Al-6V-2Sn	Ti-6Al-2Sn-4Zr-2Mo
Titanium (Wt. %)	88.5 - 90.5	89.5 - 91.5
Aluminum (Wt. %)	5.5 - 6.5	5.5 - 6.5
Tin (Wt. %)	1.5 - 2.5	1.5 - 2.5
Vanadium (Wt. %)	5.5 - 6.5	-
Zirconium (Wt. %)	-	3.5 - 4.5
Molybdenum (Wt. %)	-	1.5 - 2.5

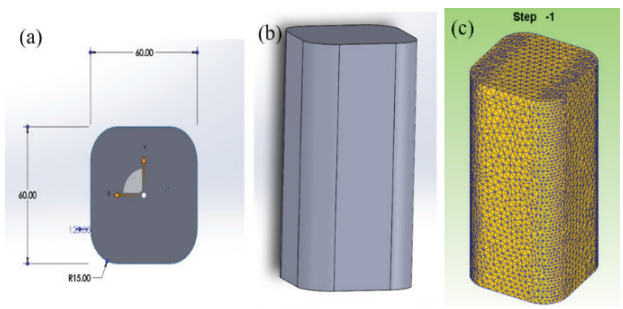


Fig. 1: (a) Dimensions of the billet material, (b) 3D model of the billet designed using SolidWorks, and (c) meshed geometry of the billet after the initial pre-processing step.

These attributes make it particularly well-suited for warm forming applications where dimensional stability, formability and high-temperature strength are critical. The alloy's microstructure, comprising a balanced mixture of α and β phases, provides enhanced toughness, creep resistance and fatigue life, all of which are essential for components subjected to cyclic mechanical and thermal loading. Additionally, the formation of a stable oxide layer at high temperatures offers significant protection against oxidation, further improving its durability in aggressive environments. Table I summarizes the elemental composition of the titanium alloys Ti-6Al-6V-2Sn and Ti-6Al-2Sn-4Zr-2Mo. Fig. 1 illustrates the key stages of model preparation, including (a) the dimensions of the billet material, (b) the 3D model developed using SolidWorks and (c) the meshed geometry generated after the initial preprocessing step. For comparative analysis, Ti-6Al-2Sn-4Zr-2Mo was also considered, as it exhibits excellent performance in extreme aerospace and power generation environments, particularly due to its elevated temperature capability (up to 1000°C), enhanced fracture toughness and superior creep strength. The inclusion of zirconium and molybdenum further improves its resistance to dynamic loading and corrosive media. Both materials offer compelling advantages for high-performance engineering applications. Their selection in this simulation study enables a comprehensive evaluation of material behavior under warm forming conditions, providing critical insights into deformation characteristics, process optimization and final component quality.

2.2 Methodology

Finite element simulations of the warm-forming process were performed using DEFORM-3D V6.1 to investigate the open-die forging behavior of Ti-6Al-6V-2Sn and Ti-6Al-2Sn-4Zr-2Mo titanium alloys. The material behavior was described using the temperature- and strain-rate-dependent constitutive material model available in the DEFORM material database, where flow stress is expressed as a function of plastic strain, strain rate and temperature. The thermo-physical and mechanical properties were adopted from the validated DEFORM database and corresponding published literature for both alloys. A three-dimensional billet model was developed in SolidWorks and imported into DEFORM-3D for analysis under forming temperatures of 200, 400 and 600 °C. The simulations were conducted at an ambient temperature of 30 °C with a convection coefficient of 0.02 N/s/mm/°C. A refined finite-element mesh consisting of 9,184 nodes and 41,459 tetrahedral elements was employed to ensure numerical stability and prediction accuracy.

The open-die forging model consisted of two rigid dies (100 mm × 100 mm × 40 mm) with a corner radius of 15 mm. The upper die was constrained to move along the Z-axis, while the lower die remained fixed, reproducing the kinematic conditions of an industrial mechanical press. The simulation parameters and boundary conditions listed in Table II were consistently applied to all cases, while Fig. 2 presents the complete DEFORM-3D warm-forging simulation workflow. Simulations were performed under press loads of 700, 1000, and 2500 tons at billet temperatures of 200, 400 and 600 °C. The thermo-mechanical behavior of the titanium billets was modeled using the temperature- and strain-rate-dependent constitutive material model available in the DEFORM-3D material database, where flow stress is expressed as a function of plastic strain, strain rate, and temperature.

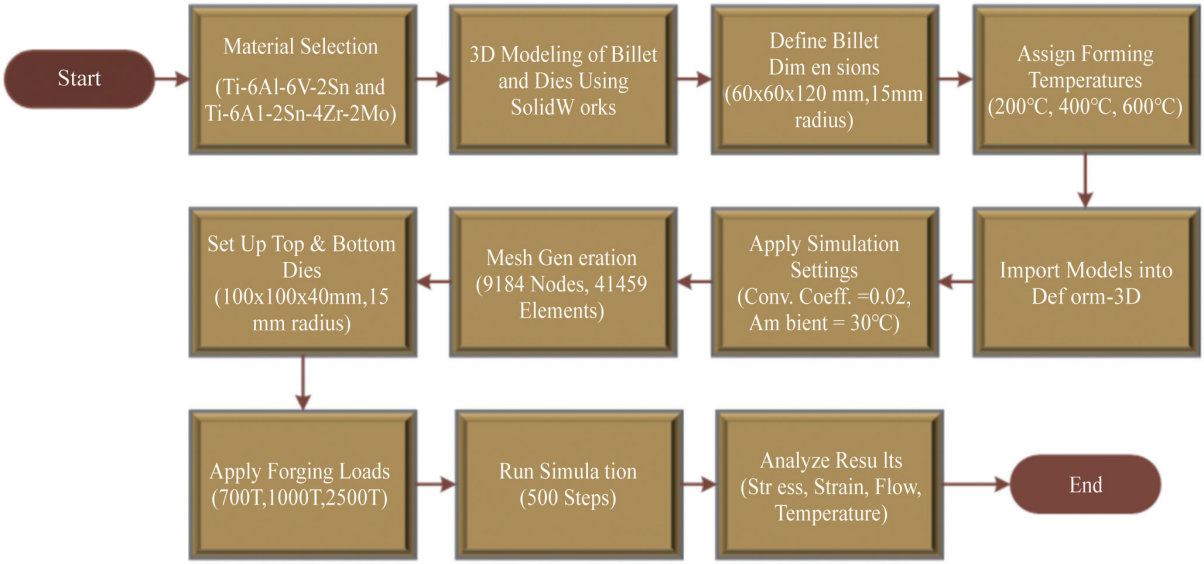


Fig. 2: Workflow of the Finite Element Simulation Process for Warm Forging of Titanium Alloys Using Deform-3D.

The governing finite element formulation employed a Lagrangian incremental approach to solve the coupled thermo-mechanical deformation problem. An ambient temperature of 30 °C and a convection coefficient of 0.02 N/s/mm/°C were applied as thermal boundary conditions. A limited mesh sensitivity analysis confirmed that further mesh refinement produced negligible changes in effective stress and forming load, ensuring satisfactory numerical accuracy. Each simulation was executed for 500 incremental steps, during which damage, effective stress, effective strain, displacement, temperature, velocity, and Z-load were continuously monitored. The numerical predictions were further verified through comparison with published warm-forging studies on titanium alloys, demonstrating good agreement with established thermo-mechanical deformation trends.

Table II: Simulation control parameters used for warm forging analysis in Deform-3D

Simulation Control	Value
Friction coefficient	0.25
Coefficient of convection	0.02 (N/sec/mm/°C)
Heat transfer coefficient	5
Total primary die travel	50 (mm)
Number of steps	500
Step increment	2

3. RESULTS AND DISCUSSION

This study employed Deform-3D V6.1 to conduct a detailed finite-element investigation of the warm-forming behavior of aerospace-grade titanium alloys Ti-6Al-6V-2Sn and Ti-6Al-2Sn-4Zr-2Mo under varying thermo-mechanical conditions. The analysis focused on evaluating the influence of forging force and billet pre-heating temperature on damage evolution, material flow, stress distribution and forming load. Simulations were performed at three press loads (700, 1000, and 2500 tons) and three billet temperatures (200, 400, and 600 °C), summarized in Tables III and IV. For each alloy and process condition, key responses including damage, total displacement, effective strain, effective stress, ultimate temperature, material velocity and Z-load were monitored over 500 simulation steps, enabling a comprehensive comparison of the deformation behavior and forgeability of both titanium alloys. The first stage of the study evaluated billet deformation under a 700-ton press at forming temperatures of 200, 400 and 600 °C. Ti-6Al-6V-2Sn exhibited excellent deformation stability, with damage increasing only slightly from 0.106 to 0.116 as temperature increased, while effective strain remained within 1.36-1.49 mm/mm and displacement stayed nearly constant at 50.6–50.7 mm. A pronounced thermal softening effect was observed, as effective stress decreased from 568 MPa at 200 °C to 347 MPa at 600 °C, accompanied by a reduction in Z-load from 290 to 144 tons. In contrast, Ti-6Al-2Sn-4Zr-2Mo demonstrated substantially higher thermo-mechanical responses, with damage values between 0.298 and 0.351, effective strain

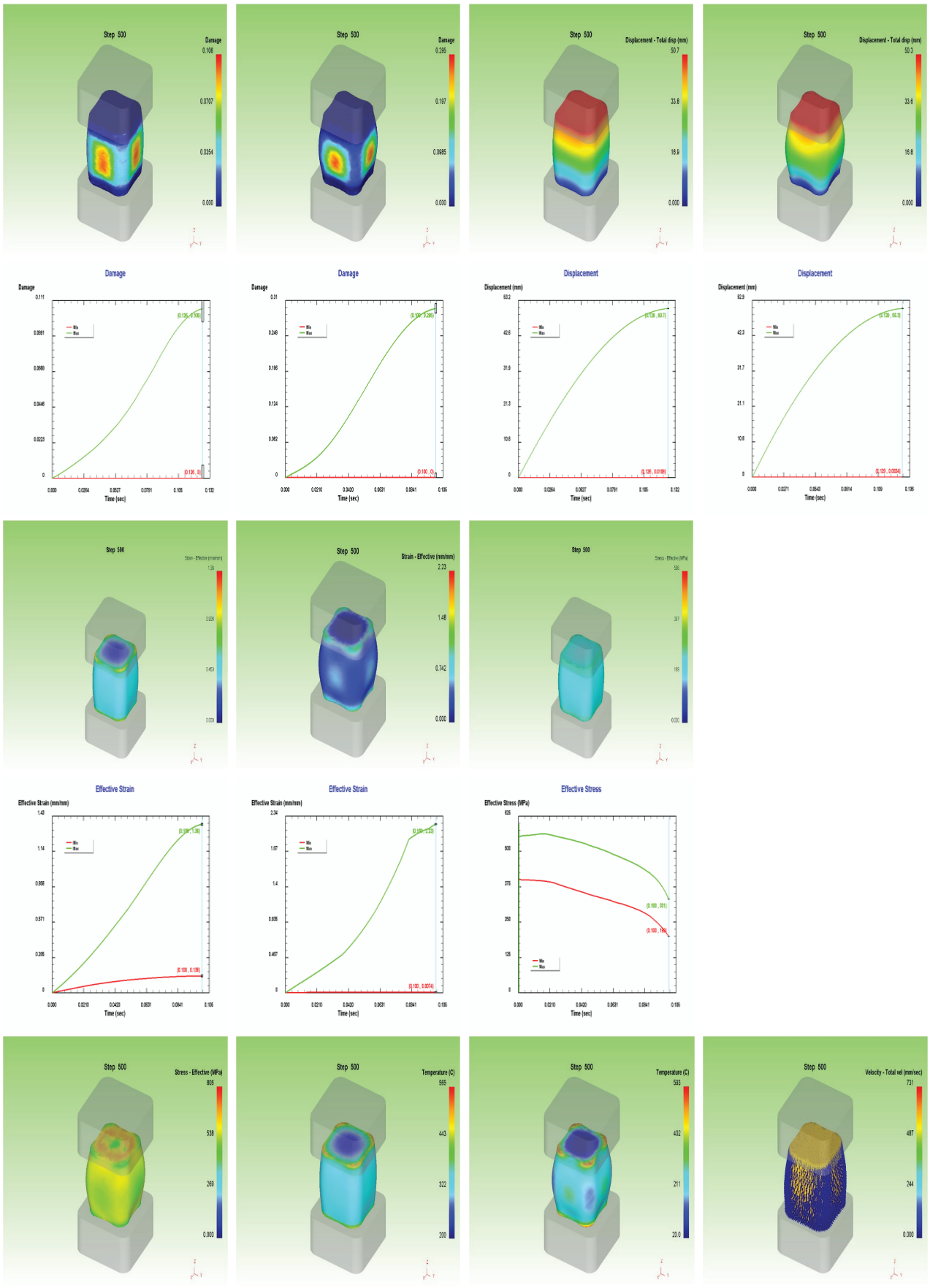
of 2.26-2.31 mm/mm and stress decreasing from 1410 MPa to 756 MPa with increasing temperature. Its Z-load also declined from 577 to 296 tons, although it remained significantly higher than that of Ti-6Al-6V-2Sn. The second stage employed a 1000-ton press under identical thermal conditions. Ti-6Al-6V-2Sn maintained low damage (0.108-0.114) and moderate strain, while effective stress decreased from 581 MPa to 331 MPa as temperature increased from 200 °C to 600 °C. Correspondingly, Z-load dropped from 300 to 148 tons, confirming enhanced plastic flow at elevated temperature. Ti-6Al-2Sn-4Zr-2Mo again showed higher damage (0.295-0.348), strain (2.23-2.27 mm/mm) and stress (1410-736 MPa), demonstrating its greater resistance to deformation and higher forming load requirements. Although effective stress decreased considerably with increasing temperature, the Ti-6Al-2Sn-4Zr-2Mo alloy consistently exhibited stress levels nearly twice those of Ti-6Al-6V-2Sn, confirming the superior strength of the Sn-Zr-Mo system. Its forging load decreased from 579 tons at 200 °C to 299 tons at 600 °C, yet remained substantially higher than that of the Al–V–Sn alloy under identical conditions. Material velocity increased with press load and temperature for both alloys, reaching approximately 46 mm/s for Ti-6Al-6V-2Sn and 47 mm/s for Ti-6Al-2Sn-4Zr-2Mo, indicating improved material flow during warm deformation. Under heavy-duty industrial conditions using a 2500-ton press, Ti-6Al-6V-2Sn maintained low damage (0.109-0.116) and stable strain (1.41-1.49 mm/mm), while its effective stress and Z-load decreased from 561 MPa and 286 tons to 346 MPa and 141 tons respectively. Conversely, Ti-6Al-2Sn-4Zr-2Mo showed higher damage (0.336-0.374) and a maximum Z-load of 701 tons at 600 °C due to strain hardening associated with large strain accumulation (~2.30 mm/mm).

Table III: Comprehensive results for Ti-6Al-6V-2Sn under varying force and temperature conditions.

Force (Ton)	Temperature (°C)	Damage	Total Displacement (mm)	Effective Strain (mm/mm)	Effective Stress (MPa)	Ultimate Temperature (°C)	Total Velocity (mm/sec)	Z Load (Tons)
700	200	0.106	50.7	1.36	568	517	38.1	290
	400	0.109	50.7	1.41	445	618	38	217
	600	0.116	50.6	1.49	347	729	37.8	144
1000	200	0.108	50.7	1.36	581	554	46.5	300
	400	0.11	50.7	1.4	445	636	46.4	224
	600	0.114	50.6	1.47	331	744	46.2	148
2500	200	0.109	50.7	1.41	561	551	36.5	286
	400	0.109	50.6	1.41	443	615	36.4	213
	600	0.116	50.6	1.49	346	726	36.3	141

Table IV: Comprehensive results for Ti-6Al-2Sn-4Zr-2Mo under varying force and temperature conditions.

Force (Ton)	Temperature **(°C)**	Damage	Total Displacement (mm)	Effective Strain (mm/mm)	Effective Stress (MPa)	Ultimate Temperature (°C)	Total Velocity (mm/sec)	Z Load (Tons)
700	200	0.351	50.3	2.26	1410	665	38.4	577
	400	0.331	50.4	2.31	1080	748	38.2	437
	600	0.298	50.4	2.27	756	830	37.9	296
1000	200	0.348	50.4	2.25	1410	676	46.9	579
	400	0.332	50.4	2.27	1070	760	46.9	400
	600	0.295	50.4	2.23	736	843	46.3	299
2500	200	0.353	50.3	2.29	1410	664	36.9	576
	400	0.336	50.3	2.25	1080	742	36.8	436
	600	0.374	50.3	2.3	1760	591	36.1	701


Step 500
Damage
Displacement - Total disp (mm)
Strain - Effective (mm/mm)
Stress - Effective (MPa)
Temperature (C)
Velocity - Total vel (mm/sec)
Damage
Displacement
Displacement (mm)
Effective Strain
Effective Strain (mm/mm)
Effective Stress
Effective Stress (MPa)
Time (sec)
Min
Max

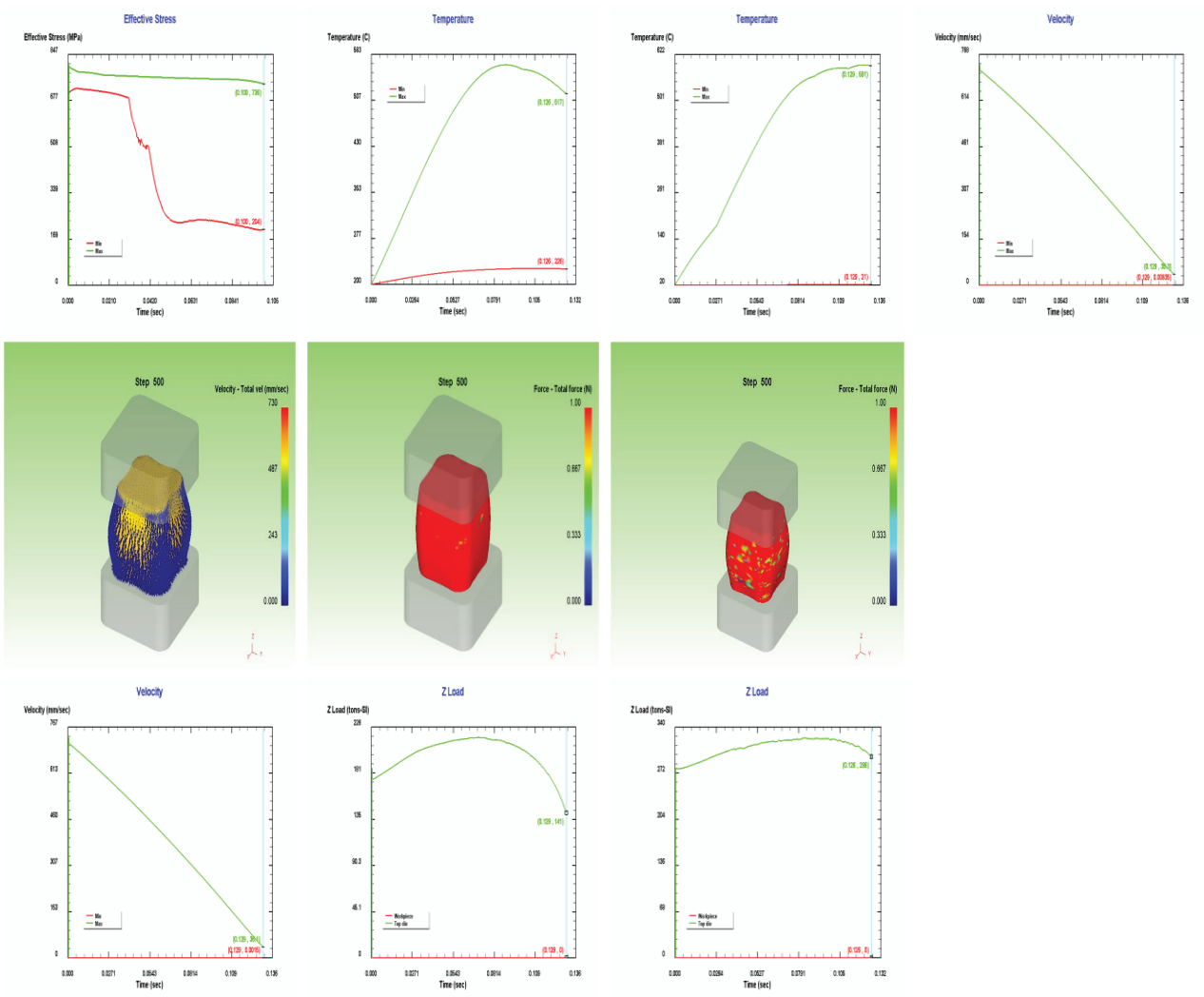


Fig. 3: Comparative thermo-mechanical distributions of Ti-6Al-6V-2Sn and Ti-6Al-2Sn-4Zr-2Mo under optimized warm-forming conditions, showing minimum damage, total displacement, effective strain, effective stress, ultimate temperature, total velocity and Z-load at 500 simulation steps and corresponding simulation times. Subfigures (a–b) represent damage, (c–d) displacement, (e–f) effective strain, (g–h) effective stress, (i–j) ultimate temperature, (k–l) total velocity and (m–n) Z-load distributions for both titanium alloys under different forming temperatures and press loads.

Fig. 3 presents a comprehensive comparison of the thermo-mechanical responses of Ti-6Al-6V-2Sn and Ti-6Al-2Sn-4Zr-2Mo under the investigated warm-forming conditions, highlighting the combined effects of billet temperature and alloy composition on deformation behavior. The numerical results demonstrate that increasing the billet temperature from 200 °C to 600 °C substantially reduces flow stress and forming load, with the Z-load decreasing by approximately 50% for Ti-6Al-6V-2Sn and 40-50% for Ti-6Al-2Sn-4Zr-2Mo. This trend is consistent with previously published experimental and finite-element investigations on titanium alloy warm forging, which reported progressive thermal softening, reduced forging force and improved material flow with increasing deformation temperature. Similarly, Ti-6Al-6V-2Sn exhibited excellent forgeability, characterized by very low damage (<0.12), moderate effective strain (~1.4 mm/mm), low effective stress (331 MPa), and a minimum Z-load of 141 tons, indicating stable plastic deformation and a low likelihood of defect initiation. In contrast, Ti-6Al-2Sn-4Zr-2Mo displayed higher damage (0.295-0.374), larger effective strain (~2.3 mm/mm) and significantly higher effective stress (736 MPa), reflecting its greater resistance to plastic flow due to solid-solution and precipitation strengthening. Despite exhibiting similar total displacement (~50 mm), the Sn-Zr-Mo alloy

showed more pronounced strain localization and required substantially higher forming loads. The simulations further revealed strong thermo-mechanical coupling, with ultimate billet temperatures increasing from 517-744 °C for Ti-6Al-6V-2Sn and 591-843 °C for Ti-6Al-2Sn-4Zr-2Mo because of adiabatic heating during deformation. Moreover, the effective stress curves exhibited a progressive decrease with simulation time, confirming thermal softening and dynamic recovery mechanisms reported in experimental warm-forging studies. Overall, the close agreement between the present numerical trends and published experimental observations supports the reliability of the DEFORM-3D simulations and demonstrates the superior warm-forging characteristics of Ti-6Al-6V-2Sn compared with Ti-6Al-2Sn-4Zr-2Mo.

4. CONCLUSIONS

This study presents a comprehensive comparative finite element investigation of the warm-forming behavior of two aerospace-grade titanium alloys, Ti-6Al-6V-2Sn and Ti-6Al-2Sn-4Zr-2Mo, using DEFORM-3D under different billet temperatures and press loads. Unlike previous studies that primarily focused on a single alloy or limited processing conditions, this work systematically established the relationships between thermo-mechanical parameters and key deformation characteristics, including damage, effective stress, strain, displacement, velocity, ultimate temperature and Z-load. The results demonstrated that Ti-6Al-6V-2Sn exhibited superior forgeability, achieving the lowest damage (0.106), minimum effective stress (331 MPa), and lowest Z-load (141 tons), indicating reduced forming resistance and improved process efficiency. In contrast, Ti-6Al-2Sn-4Zr-2Mo maintained higher strength but required greater forming loads because of its increased flow stress and strain localization. The comparative process-property analysis provides practical guidelines for selecting suitable warm-forming conditions, thereby improving energy efficiency, die life and component quality. These findings contribute valuable reference data for the numerical design and optimization of warm-forging operations for advanced titanium alloys. Future work will focus on experimental validation, constitutive model refinement, microstructural evolution and the integration of finite element simulation with advanced manufacturing technologies for high-performance titanium components.

REFERENCES

[1] E. Marin and A. Lanzutti, “Biomedical Applications of Titanium Alloys: A Comprehensive review,” Materials, vol. 17, no. 1, p. 114, Dec. 2023, doi: 10.3390/ma17010114.

[2] J. Yang, Y. Song, K. Dong, and E.-H. Han, “Research progress on the corrosion behavior of titanium alloys,” Corrosion Reviews, vol. 41, no. 1, pp. 5–20, Nov. 2022, doi: 10.1515/corrrev-2022-0031.

[3] J. O. Obiko, F. M. Mwema, and M. O. Bodunrin, “Validation and optimization of cutting parameters for Ti-6Al-4V turning operation using DEFORM 3D simulations and Taguchi method,” Manufacturing Review, vol. 8, p. 5, Jan. 2021, doi: 10.1051/mfreview/2021001.

[4] M. K. A. Raj et al., “Effect of titanium based alloys on Thermo-Mechanical Behavior in 3D Forging simulation,” Metals, vol. 12, no. 10, p. 1611, Sep. 2022, doi: 10.3390/met12101611.

[5] K. V. D. Rajesh and T. Buddi, “Finite element analysis of chromium and nickel alloyed steel billets forged under warm forming process using Deform-3D,” Advances in Materials and Processing Technologies, vol. 8, no. sup3, pp. 1386–1394, Jun. 2021, doi: 10.1080/2374068x.2021.1945269.

[6] W. Deng, Z. Wang, G. He, H. Zhang, M. Yu, and D. Jia, “Multi-objective optimisation of forging process parameters of Ti-6Al-4V alloy connecting rod based on orthogonal experiment,” Materials Today Communications, vol. 42, p. 111296, Dec. 2024, doi: 10.1016/j.mtcomm.2024.111296.

[7] Md. I. Equbal, A. Saood, and V. M. S. Hussain, “Forging Die Wear Optimization: A Combined Approach with Finite Element Analysis and Taguchi Methodology,” Applied Mechanics and Materials, vol. 922, pp. 89–96, Aug. 2024, doi: 10.4028/p-jpv8gf.

[8] H. Zhang, H. Tu, C. Yuan, Y. Li, X. Chen, and H. Wang, “Predicting forging defects using FEM: a brief review,” The International Journal of Advanced Manufacturing Technology, vol. 141, no. 3–4, pp. 1143–1157, Oct. 2025, doi: 10.1007/s00170-025-16697-z.

[9] Y.-Q. Wu and K.-K. Wang, “The ultra-high temperature forging process based on DEFORM-3D simulation,” International Journal on Interactive

Design and Manufacturing (IJIDeM), vol. 16, no. 1, pp. 99–108, Jan. 2022, doi: 10.1007/s12008-021-00811-y.

[10] M. Szala, G. Winiarski, T. Bulzak, and Ł. Wójcik, "Microstructure and Hardness of Cold Forged 42CrMo4 Steel Hollow Component with the Outer Flange," Advances in Science and Technology – Research Journal, vol. 16, no. 4, pp. 201–210, Sep. 2022, doi: 10.12913/22998624/152790.

[11] Z. Ozgeneci, O. Music, and C. Simsir, "Finite element analysis of damage in hot forging of bearing rings," The International Journal of Advanced Manufacturing Technology, vol. 137, no. 1–2, pp. 891–911, Feb. 2025, doi: 10.1007/s00170-025-15094-w.

[12] S. Lee, B. Kim, H.-J. Lee, and J. Yoon, "Warm forging of an aluminium alloy for the differential case in an automobile transmission," Proceedings of the Institution of Mechanical Engineers Part D Journal of Automobile Engineering, vol. 230, no. 8, pp. 1131–1139, Aug. 2015, doi: 10.1177/0954407015600900.

[13] M. M. F. N. Aghoun Khalid Shleej Zayed ,. Fatemeh, "Investigating of manufacturing of titanium hip prosthesis by cold forging process via FEM analysis," Journal of Modern Processes in Manufacturing and Production, Dec. 2024, doi: 10.71762/z6e6-aw80.

[14] X. Wang, P. Zhang, T. Zhang, and S. Ge, "Study on the Microstructural Evolution Mechanisms of TC4 Titanium Alloy during Hot Rolling Based on DEFORM-3D Simulation," Journal of Materials Engineering and Performance, vol. 34, no. 24, pp. 30097–30105, Jul. 2025, doi: 10.1007/s11665-025-11558-y.

[15] M. Bodunrin, J. Obiko, and D. Klenam, "On the Uniaxial Compression Testing of Metallic Alloys at High Strain Rates: An Assessment of DEFORM-3D Simulation," Applied Sciences, vol. 13, no. 4, p. 2686, Feb. 2023, doi: 10.3390/app13042686.

[16] N. Jantepa, N. Siripath, and S. Suranuntchai, "Predictive modeling and optimization of hot forging parameters for AISI 1045 ball joints using Taguchi methodology and finite element analysis," Metals, vol. 14, no. 10, p. 1198, Oct. 2024, doi: 10.3390/met14101198.

[17] P. Jedrasiak, H. Shercliff, S. Mishra, C. S. Daniel, and J. Q. Da Fonseca, "Finite element modeling of hot compression testing of titanium alloys," Journal of Materials Engineering and Performance, vol. 31, no. 9, pp. 7160–7175, Mar. 2022, doi: 10.1007/s11665-022-06750-3.

Impact of Magnetic Nanoparticle-based Priming on Potato Seed Germination in Bangladesh

Jakia Mustary Lina*, Shubro Biswas and Md. Mahmudur Rahman

Department of Electrical and Electronic Engineering, Dhaka University of Engineering & Technology, Gazipur, Bangladesh

ABSTRACT

Nanopriming, the pre-sowing treatment of seeds with engineered nanoparticles, has demonstrated promising superiority over conventional priming methods in enhancing germination, vigor, and stress resilience, with Fe_3O_4 magnetic nanoparticles (MNPs) emerging as particularly promising candidates owing to their remarkable advantages. Despite this potential, the effect of Fe_3O_4 MNPs on True Potato Seed (TPS) germination remains underexplored, even though poor TPS germination under conventional methods poses a direct threat to food security and farmer livelihoods in Bangladesh, where potato (*Solanum tuberosum L.*) is a strategically important crop. In this study, Fe_3O_4 MNPs were synthesized via chemical co-precipitation and characterized by X-ray Diffraction (XRD), Field Emission Scanning Electron Microscopy (FE-SEM), Energy Dispersive X-ray Spectroscopy (EDX), and Dynamic Light Scattering (DLS) with Zeta potential analysis to confirm phase purity, morphology, elemental composition, and colloidal stability. TPS of the Bari-1 variety were primed at 10, 40, and 70 mg/L for 8 h, and germination was monitored over 14 days under controlled laboratory conditions. Seeds treated at 40 mg/L achieved a peak germination rate of 85.15%, representing over 25% improvement compared to the hydroprimed control (64.99%), whereas the 70 mg/L treatment suppressed germination below control levels. These findings establish 40 mg/L as the optimal priming concentration and demonstrate the practical potential of Fe_3O_4 MNP nanopriming for enhancing TPS germination in Bangladesh.

Keywords: Nanopriming, Fe_3O_4 nanoparticles, True Potato Seeds (TPS), Seed germination, Sustainable agriculture, *Solanum tuberosum* L.

1. INTRODUCTION

Potato (Solanum tuberosum L.) ranks as the third most consumed crop globally, following rice and wheat. It constitutes a strategically important food source in Bangladesh. The nation stands among the world's leading potato producers, generating 9.87 million metric tons across 468.7 thousand hectares [1]. Seed germination represents the foundational stage of crop development. However, conventional priming methods, such as hydropriming and osmopriming, exhibit limited efficacy in improving germination performance. This limitation is particularly evident for inherently low-vigor seeds [2], [3]. These constraints have catalyzed a growing interest in advanced seed enhancement technologies. Consequently, nanotechnology has emerged as a promising frontier for achieving the rapid, vigorous, and uniform germination essential to modern agricultural productivity.

Seed nanopriming involves the pre-sowing treatment of seeds with engineered nanoparticles. It represents a scientifically credible and agriculturally practical advancement over conventional techniques. Nanoparticles possess exceptional physicochemical properties. These properties enable deeper tissue interaction and more intense metabolic activation than standard aqueous priming solutions can achieve [3], [5]. Furthermore, nanopriming offers practical scalability through ultralow dosage requirements. It also reduces ecological risks because residuals can be removed via simple aqueous rinsing [3], [5]. Nanoparticles enter seed tissues through direct diffusion, active transport, or transmembrane protein channels. This entry initiates physiological cascades that enhance water uptake, activate antioxidant mechanisms, and accelerate starch hydrolysis. These combined processes accelerate the generation of energy required for seedling growth [5], [6].

The controlled elevation of reactive oxygen species (ROS) serves as a critical molecular signal during germination. Nanoprimed seeds exhibit enhanced antioxidant enzyme activity that aligns with the established "oxidative window" concept. This alignment leads to higher germination rates and hastened seedling development [6], [8]. Beyond the immediate germination phase, nanopriming promotes uniform seedling establishment and improves tolerance to abiotic stresses.

*Corresponding author's email: jakiamustarylina@gmail.com

It also modulates hormonal balance to effectively reset the metabolic clock of the seed. This positions nanopriming as a transformative technology for agricultural systems where reliable crop establishment is a critical priority [3],[7]. A schematic illustration is presented in [Fig. 1] to visualize the expected germination outcomes as a function of priming treatment. This illustration was conceptualized based on findings reported in peer-reviewed literature. These studies collectively indicate that nanopriming enhances seed germination kinetics, accelerates metabolic activation, and promotes robust seedling establishment relative to conventional hydropriming [5], [8]. The upper pathway depicts the hydroprimed condition, which is characterized by delayed germination and limited root development. Conversely, the lower pathway represents the nanoprimed condition, which exhibits enhanced germination rates and more vigorous seedling morphology.The scientific investigation of nanopriming has yielded consistently encouraging results across diverse nanoparticle types and crop species. Metallic nanoparticles demonstrate clear advantages over conventional priming agents in enhancing germination performance and seedling vigor [3], [6]. Among these, silver and zinc oxide nanoparticles have been extensively studied. In fact, ZnO nanoparticles have become the most investigated priming agents globally across cereals and legumes [5]. In the Bangladeshi context, pioneering studies have established the efficacy of ZnO nanopriming for local vegetable crops, reporting germination improvements of up to 61.7% under optimized conditions [3].Recently, iron oxide magnetic nanoparticles (Fe_3O_4) have emerged as particularly promising agents. They offer unique magnetic properties, exceptional biocompatibility, and a superior capacity to regulate hormonal balance, antioxidant enzyme activity, and metabolic pathways [6], [8]. Studies on wheat, barley, and bean have demonstrated that

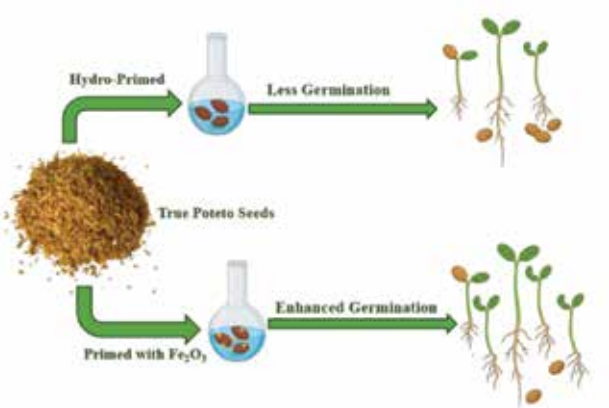


Fig.1: Experimental workflow comparing traditional hydropriming and Fe_3O_4 nanoparticle-mediated priming protocols for TPS.

Fe_3O_4 nanoparticles enhance germination rates, increase amino acid and soluble sugar content, and reduce solute leakage. They also improve stress defense mechanisms while maintaining seed viability. These effects compare favorably to other metallic nanoparticles [7], [8]. However, the nature of these physiological responses is highly concentration-dependent. Low doses typically promote growth, whereas high doses induce inhibition. This variability necessitates precise dosage optimization for each specific crop system [6].Despite the established promise of Fe_3O_4 magnetic nanoparticles in enhancing germination across various crops, their application to True Potato Seed (TPS) remains entirely unexplored. This gap in research is particularly consequential for Bangladesh, where potato production underpins national food security and rural livelihoods, yet conventional hydropriming offers only modest and inconsistent improvements in TPS germination performance.Research Significance and Novelty:This study addresses this fundamental deficiency by generating the first systematic experimental dataset on Fe_3O_4 magnetic nanoparticle priming of TPS. The research establishes precise, concentration-dependent response boundaries and identifies an evidence-based optimal dosage. By evaluating these nanomaterial interactions specifically within TPS for the first time, this work bridges a critical gap between advanced nanomaterial synthesis and practical agricultural applications. Ultimately, these insights advance both agricultural nanotechnology and sustainable crop establishment strategies for resource-constrained farming systems.

2. MATERIALS AND METHODS

2.1 Synthesis of Fe_3O_4 Magnetic Nanoparticles

2.1.1 Reagents and Materials

Magnetite nanoparticles were synthesized via a modified chemical co-precipitation method using analytical-grade reagents without further purification. Ferric chloride hexahydrate ($FeCl_3 \cdot 6H_2O$), ferrous sulfate heptahydrate ($FeSO_4 \cdot 7H_2O$), and ammonium hydroxide solution (NH_4OH, 25% w/v) were procured from Labtex Bangladesh. Deionized water (DI water, resistivity ≥ 18.2 MΩ·cm) and absolute ethanol (C_2H_5OH) served as solvents throughout the synthesis and washing steps. Photographic representation of the analytical-grade chemical precursors employed in the synthesis of Fe_3O_4 magnetic nanoparticles are shown in Fig. 2 (a)-(c).



(a) (b) (c)

Fig. 2: Photographic representation of the chemical precursors used in the co-precipitation synthesis of Fe_3O_4 magnetic nanoparticles (a) 25% ammonium hydroxide (NH4OH), (b) Ferric chloride hexahydrate (FeCl3·6H2O), (c) Ferrous sulfate heptahydrate (FeSO4·7H2O).

2.1.2 Synthesis Procedure

Magnetite (Fe_3O_4) nanoparticles were synthesized utilizing a modified chemical co-precipitation technique. A stoichiometric precursor solution was prepared by dissolving 6.1 g of ferric chloride hexahydrate ($FeCl_3.6H_2O$) and 4.2 g of ferrous sulfate heptahydrate ($FeSO_4 7H_2O$) in 100 mL of deionized water. This solution was heated to 90°C under continuous mechanical stirring. Upon reaching the target temperature, 10 mL of 25% ammonium hydroxide (NH_4OH) was rapidly introduced to the reaction vessel to induce precipitation.



(a) (b)

Fig. 3: Visual representation of the co-precipitation reaction (a) before and (b) after alkaline induction.

The mixture was maintained at 90∘C for 30 minutes to facilitate crystal growth and phase maturation. Following this duration, the suspension was allowed to cool to ambient temperature. The resulting black precipitate was isolated via vacuum filtration and washed repeatedly with deionized water to eliminate residual ionic impurities, yielding purified Fe3O4 nanostructures.



Fig. 4: Dried powder form of the synthesized Fe_3O_4 magnetic nanoparticles obtained after vacuum filtration and oven drying.

The nanoparticles were subsequently washed three times with deionized water and then dried in an oven for 72 hours. After complete drying, the nanoparticle powder was collected.

2.1.3 Seed Selection

True potato seeds (TPS) of Solanum tuberosum cultivar BARI-1 were obtained from the Tuber Crops Research Centre (TCRC), Gazipur, Bangladesh. Prior to use, seeds were visually inspected and only morphologically uniform, intact seeds were retained for the experiment. TPS was selected as the experimental material owing to its agronomic relevance as a cost-effective and disease-free propagation pathway for smallholder potato production in Bangladesh.



Fig. 5: True potato seeds (TPS) of *Solanum tuberosum L.* cultivar BARI-1 used as the experimental seed material.

2.2 Preparing of Priming Solution and Seed Priming

The synthesized MNPs, were utilized for seed priming at varying concentrations (10, 40 and 70 mg/L). Fresh priming solutions were prepared by dispersing the respective nanoparticles in deionized water using ultrasonic vibration (100 W, 40 kHz) for 30 minutes. Healthy, uniform-sized Solanum tuberosum (TPS) seeds were selected and thoroughly washed under running

tap water to ensure cleanliness. Prior to priming, seeds were surface-cleaned under running tap water and gently blotted dry with sterile tissue paper to remove surface moisture. Cleaned seeds were subsequently immersed in the respective MNP suspensions for 8 hours at room temperature. A hydroprimed control group, consisting of seeds soaked in deionized water under identical conditions, was included in all experimental runs. Following priming, seeds were removed from solution, blotted dry, and immediately transferred to germination assay conditions.

2.3 Germination Assay

Germination tests were carried out on primed and hydroprimed seeds in triplicate. Briefly, sterile filter paper (Whatman No. 1) was placed in sterile glass Petri dishes and moistened with 5 mL of deionized water. Thirty seeds were evenly placed in each dish, then covered with lids and sealed with Parafilm to prevent moisture loss. The dishes were incubated in the dark with a recorded mean temperature of 19.06°C and a relative humidity of 76.28%. Germination was evaluated by observing the appearance of the radicle, with observations recorded every 24 hours over a 14-day period. To maintain moisture, 5 mL of distilled water was added to each dish every other day.



Fig. 6: Germination of Fe_3O_4 MNP-primed and hydroprimed true potato seeds observed in sealed Petri dishes during the 14-day incubation period.

2.4 Physicochemical Characterization of Fe_3O_4 MNPs

The structural and physicochemical properties of the synthesized nanoparticles were assessed using a suite of complementary analytical techniques. Crystal phase identification and mean crystallite size estimation were performed by X-ray diffraction (XRD) using Cu Kα radiation (λ = 1.5406 Å), with the mean crystallite size calculated according to the Scherrer equation. Surface functional group analysis was carried out by Fourier-transform infrared spectroscopy (FTIR) over the range 400–4000 cm^{-1}. Particle morphology and size distribution were examined by field-emission scanning electron microscopy (FE-SEM) coupled with energy-dispersive X-ray spectroscopy (EDX) for elemental composition verification. Hydrodynamic diameter and colloidal stability of nanoparticle suspensions were determined by dynamic light scattering (DLS) and zeta potential measurements, respectively. All experiments were performed in triplicate, with data expressed as mean SEM and data visualization was performed using Origin 2021.

4. RESULTS AND DISCUSSION

4.1 Characterization of MNP

4.1.1 Crystalline Structures

The crystallographic structure, phase, and purity of the synthesized samples have been investigated using the XRD patterns. The crystalline nature of nanoparticles was confirmed by X-ray crystallography. The XRD pattern of the synthesized MNPs is shown in Fig. 8.

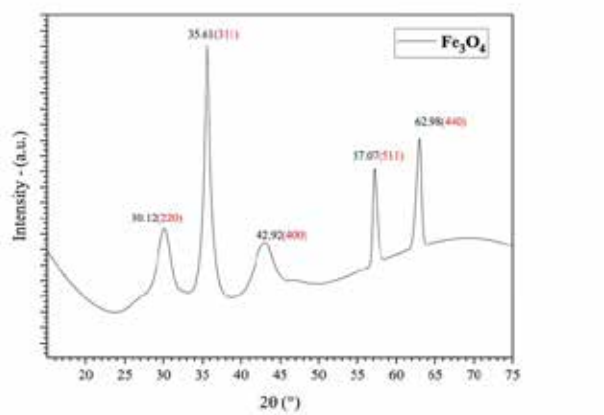


Fig. 7: X-ray diffraction pattern of the synthesized Fe_3O_4 magnetic nanoparticles confirming phase purity and cubic spinel crystal structure.

The diffracted intensities were recorded from 20 to 70 degrees. For the synthesized MNP, five strong Bragg reflections at 30.12, 35.62, 42.92, 57.07, and 62.98 degrees correspond to the planes of (220), (311), (400), (511), and (440), respectively, which can be indexed according to the facets of the face-centered cubic crystal structure of magnetite.[5],[10]. The average crystal size of the particles was calculated to be around 8.30nm using the Scherrer formula by averaging the full width at half maximum (FWHM) of the six aforementioned peaks, in accordance with established methodology [11].

4.1.2 Elemental Composition

The EDX spectroscopic analysis reveals a chemical profile characterized primarily by iron and oxygen, which serve as the fundamental constituents of the synthesized specimen. The spectrum identifies prominent peaks for Iron (Fe) and Oxygen (O) with mass concentrations of 59.81%

and 23.49%, respectively, while a minor carbon signal is observed, likely originating from the sample mounting media. The distribution of these elements, particularly the high atomic percentage of oxygen, strongly supports the successful formation of an iron oxide phase. The absence of extraneous signals suggests a high degree of elemental purity, indicating that the major detected components effectively define the chemical identity of the sample within the sensitivity limits of the measurement.

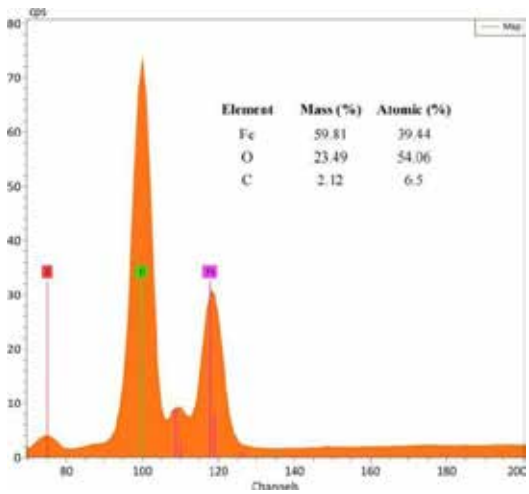


Fig. 8: Energy-dispersive X-ray spectrum and quantitative elemental composition of the synthesized Fe_3O_4 magnetic nanoparticles.

4.1.3 Particle Morphology and Size Distribution

The morphology and particle size distribution of the synthesized magnetic nanoparticles were evaluated by field emission scanning electron microscopy, as depicted in Fig. 9. The micrographs revealed a predominantly spherical morphology with a distribution comprising both smaller and larger particles. Quantitative analysis of 111 individual particles yielded a mean diameter of 10.38 ± 2.51 nm. Notable agglomeration was observed, with particles forming clusters incorporating both size fractions, a behavior characteristic of iron oxide nanoparticles at this scale.

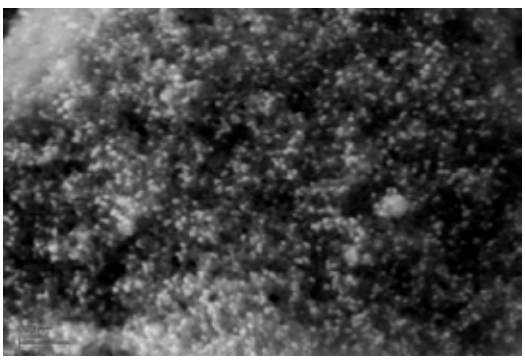


Fig. 9: Field-emission scanning electron microscopy micrograph of synthesized Fe_3O_4 magnetic nanoparticles.

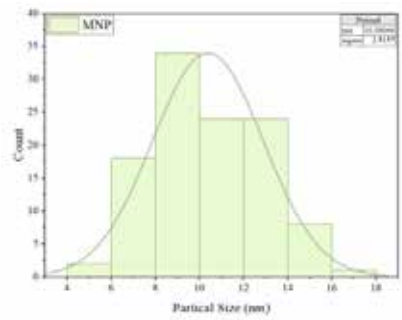


Fig. 10: FE-SEM micrograph and particle size distribution analysis of Fe_3O_4 magnetic nanoparticles.

The histogram reveals a right-skewed size distribution, with the predominant particle population concentrated in the 8–10 nm size range, consistent with the mean diameter of 10.38 ± 2.51 nm determined from image analysis. The normal distribution overlay confirms reasonable agreement with a Gaussian profile across the measured population, though a tail extending toward 16–18 nm reflects the presence of a minor fraction of larger particles, likely attributable to localized agglomeration during synthesis or drying. The relatively narrow distribution width corroborates the controlled nucleation conditions achieved under the co-precipitation protocol employed in this study.

4.1.4 Hydrodynamic Diameter and Colloidal Stability

The hydrodynamic size of the synthesized MNPs in aqueous solution was evaluated using dynamic light scattering (DLS), revealing a mean diameter of 259.1 ± 61.8 nm (Fig. 11). This hydrodynamic size is notably larger than the diameters typically observed via SEM or TEM, a discrepancy attributed to the solvation shell and surface stabilizers surrounding the particles in a liquid medium. [14],[9] The measured distribution reflects the effective size of the particles as they move through the solvent, providing a realistic representation of their behavior in a dispersed state.

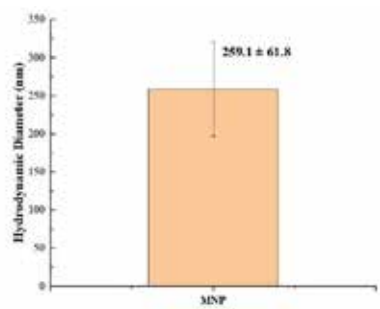


Fig. 11: Dynamic light scattering (DLS) analysis showing the hydrodynamic diameter distribution of Fe_3O_4 magnetic nanoparticles in aqueous suspension.

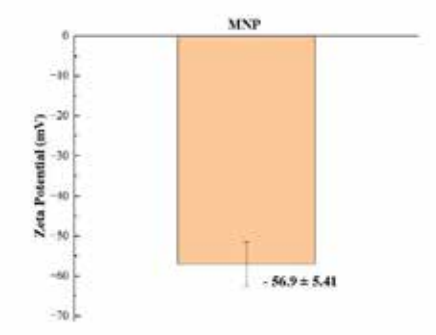


Fig.12: Zeta potential distribution of Fe_3O_4 magnetic nanoparticles in aqueous suspension.

The analysis reveals a zeta potential value of −56.9 ± 5.41 mV for the synthesized MNPs. Previous studies suggest that nanoparticles with high zeta potential values (with an absolute value greater than 30 mV) generally exhibit high colloidal stability [12],[13]. Accordingly, the observed negative zeta potential value for the MNPs indicates superior stability of these nanoparticles. This enhanced stability aligns with the expectation that particles with highly negative zeta potential values are less susceptible to aggregation due to stronger interparticle electrostatic repulsion.

4.2 Germination Response of TPS to Fe_3O_4-based Nanopriming

The germination performance of *Solanum tuberosum L.* cv. BARI-1 TPS subjected to Fe_3O_4 MNP nanopriming at 10, 40, and 70 mg L^{-1}, alongside the hydroprimed control, was monitored over a 14-day incubation period under controlled environmental conditions (mean temperature: 19.06 ± 0.5 °C; relative humidity: 76.28 ± 2.1%). All germination data represent the mean of three independent replicates, and the temporal germination profiles are presented in Fig. 13. To ensure statistical rigor, each concentration was evaluated in triplicate (3 sets), with all reported values representing the calculated mean of these replicates.The vertical lines on the bar chart represent the [Standard Deviation (SD)], visually mapping the variance within the replication sets. To mathematically validate the performance gaps, a Two-Way ANOVA (with Treatment Concentration and Time Interval as the main factors) has been conducted on the raw replication data-set.Standard compact letter displays (a, b, c) have been added above the bars in the updated figure to clearly illustrate which treatment groups are significantly different from the hydroprimed control and from each other at each time point. This standardized microclimate ensured that the observed variations in germination kinetics were primarily attributable to the MNP concentration gradients rather than external fluctuations.Temporal analysis of germination dynamics reveals a significant acceleration in metabolic transition for seeds treated with mid-range nanoparticle concentrations. By Day 10, the 40 mg/L MNP treatment emerged as the primary catalyst, yielding a germination rate of 73.10% a 12.5% improvement over the HydroPrimed control (64.99%). This initial momentum intensified by Day 12, where the 40 mg/L cohort achieved 79.25%, effectively widening the performance gap to 17% above the control. In contrast, the 70 mg/L concentration exhibited a definitive inhibitory threshold,

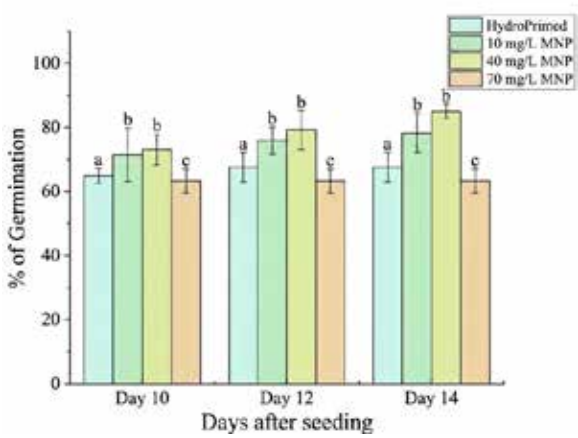


Fig. 13: Temporal germination rate (%) of Solanum tuberosum L. cv. BARI-1 true potato seeds primed with Fe_3O_4 magnetic nanoparticles at varying concentrations (10, 40, and 70 mg L^{-1}) and hydroprimed control over a 14-day observation period.

stagnating at 63.44% from Day 10 through the end of the observation period. By the Day 14 terminal assessment, the superiority of the 40 mg/L treatment was solidified, reaching a peak efficacy of 85.15% (a 25.7% increase over control), whereas the 70 mg/L treatment resulted in a 6.4% deficit relative to standard hydro-priming. The biphasic response observed here indicates that while low iron oxide nanopriming concentrations enhance seed coat porosity and imbibition, the 70 mg/L dosage triggers distinct phytotoxicity [16]. This high-dose inhibition stems from a combination of mechanical and physiological constraints: dense surface aggregation physically blocks aquaporin channels to restrict hydraulic conductivity, while excessive internal accumulation accelerates reactive oxygen species (ROS) production, causing severe membrane damage and lipid peroxidation [17]. Consequently, 70 mg/L represents a critical toxicological threshold where physical restriction and oxidative stress entirely override the developmental benefits of iron mobilization. These results suggest that

while optimized MNP concentrations significantly lower the energetic barriers to germination, supra-optimal dosing triggers physiological stagnation, underscoring the necessity of precision concentration for maximizing seed vigor.

5. CONCLUSION

This research identifies a nonlinear physiological response in True Potato Seed (TPS), pinpointing 40 mg/L of Fe_3O_4 magnetic nanoparticles as the optimal concentration for accelerating germination kinetics and lowering metabolic activation barriers. The subsequent stagnation observed at 70mg/L highlights a critical biostimulatory limit, beyond which nanotoxicity begins to impede physiological gains.

The significance of this study lies in its successful translation of agricultural nanotechnology from a theoretical laboratory concept to a scalable, eco-conscious cultivation strategy. By defining the precise therapeutic window for Fe_3O_4 nanoparticles in TPS, this work provides a reproducible framework to enhance crop vigor in vital agro-ecological zones like Bangladesh. Crucially, the next phase of this research will evaluate the performance of these MNP primed seeds under abiotic stress. This will determine whether the initial physiological boost discovered in this study successfully translates into sustained climate resilience against environmental volatilities.

6. ACKNOWLEDGEMENT

This research was financially supported by the University Teachers' Research Fund (Grant No. DUET-TRF/2025-2026/11) administered by Dhaka University of Engineering & Technology (DUET), Gazipur, and the authors gratefully acknowledge the Head of the Department of Electrical and Electronic Engineering, DUET. The authors extend sincere appreciation to the Semiconductor Technology Research Centre, University of Dhaka, and the Department of Electrical and Electronic Engineering, University of Dhaka, for generously facilitating access to material synthesis and characterization infrastructure. The authors acknowledge the Bangladesh University of Engineering and Technology (BUET) and the Bangladesh Atomic Energy Commission for providing access to advanced analytical facilities.

REFERENCES

[1] A. R. Sallam, A. A. Mahdi, and K. Y. Farroh, "Improving drought stress tolerance in potato (Solanum tuberosum L.) using magnetite and zinc oxide nanoparticles," Pakistan Journal of Biochemistry and Molecular Biology, vol. 23, no.37,2022,doi:https://doi.org/10.56557/PCBMB/2022/v23i37-387886.

[2] M. T. MacDonald and V. R. Mohan, "Chemical Seed Priming: Molecules and Mechanisms for Enhancing Plant Germination, Growth, and Stress Tolerance," Current Issues in Molecular Biology, vol. 47, no. 3, p. 177, Mar. 2025, doi: https://doi.org/10.3390/cimb47030177.

[3] S. H. Nile et al., "Nano-priming as emerging seed priming technology for sustainable agriculture—recent developments and future perspectives," Journal of Nanobiotechnology, vol. 20, no. 1, Jun. 2022, doi: https://doi.org/10.1186/s12951-022-01423-8.

[4] R. Javed, M. A. Ahmad, A. Gul, T. Ahsan, and M. Cheema, "Comparison of chemically and biologically synthesized nanoparticles for the production of secondary metabolites, and growth and development of plants," Comprehensive Analytical Chemistry, pp. 303–329, 2021, doi: https://doi.org/10.1016/bs.coac.2021.02.002.

[5] G. Vaidyanathan, S. Sendhilnathan, and R. Arulmurugan, "Structural and magnetic properties of $Co_{1-x}Zn_xFe_2O_4$ nanoparticles by coprecipitation method," Journal of Magnetism and Magnetic Materials, vol. 313, no. 2, pp. 293299,Jun.2007,doi:http://dx.doi.org/10.1016/j.jmmm.2007.01.010.

[6] K. Kornarzyński, A. Sujak, G. Czernel, and D. Wiącek, "Effect of Fe_3O_4 nanoparticles on germination of seeds and concentration of elements in Helianthus annuus L. under constant magnetic field," Scientific Reports, vol. 10, article no. 8068, 2020, doi: https://doi.org/10.1038/s41598-020-64849-w.

[7] N. Gupta, P. M. Singh, V. Sagar, A. Pandya, M. Chinnappa, R. Kumar, and A. Bahadur, "Seed priming with ZnO and Fe_3O_4 nanoparticles alleviate the lead toxicity in Basella alba L. through reduced lead uptake and regulation of ROS," Plants, vol. 11, no. 17, article 2227, 2022, doi: https://doi.org/10.3390/plants11172227.

[8] M. Smiri, "Environmental effect of magnetite nanoparticles (Fe_3O_4 NPs) on germination rate and seedling growth from bean," Polish Journal of Environmental Studies, vol. 33, no. 5, 2024, doi: https://doi.org/10.15244/pjoes/183080.

[9] S. Yeasmin, A. R. Dipto, A. B. Zakir, S. D. Shovan, M. A. H. Suvo, M. A. Bhuiyan, M. N. Amin, T. U. Rashid, S. Islam and A. Habib, Nanopriming and AI for Sustainable Agriculture: Boosting Seed Germination and Seedling Growth with Engineered Nanomaterials, and Smart Monitoring through Deep Learning, ACS Appl. Nano Mater., 2024, 7, 8703–8715.

[10] K. J. Esha et al., "Synthesis and Characterization of Polyethylenimine-Coated Magnetic Nanoparticles for DNA Binding toward Pollen-Directed Gene Delivery Applications," IEEE Transactions on NanoBioscience, pp. 1–1, 2026, doi: https://doi.org/10.1109/tnb.2026.3666861.

[11] M. Mascolo, Y. Pei, and T. Ring, "Room temperature co-precipitation synthesis of magnetite nanoparticles in a large ph window with different bases," Materials, vol. 6, no. 12, p. 5549–5567, Nov. 2013. [Online]. Available: http://dx.doi.org/10.3390/ma6125549.

[12] M. S. Mostafa, S. Yeasmin, M. M. H. Pranto, S. M. Reza, T. U. Rashid, H. Das, M. Rahman and A. Habib, Annealing-induced optimization of green-synthesized ZnO nanoparticles for improved nanopriming in sustainable agriculture, Nanoscale Adv., 2025, 7, 5589–5600.

[13] A. Brunelli, A. Foscari, G. Basei, G. Lusvardi, C. Bettiol, E. Semenzin, A. Marcomini and E. Badetti, Colloidal stability classi cation of TiO2 nanoparticles in arti cial and in natural waters by cluster analysis and a global stability index: In uence of standard and natural colloidal particles, Sci. Total Environ., 2022, 829, 154658.

[14] S. M. Savassa, N. M. Duran, E. S. Rodrigues, E. De Almeida, C. A. Van Gestel, T. F. Bompadre and H. W. P. de Carvalho, Effects of ZnO nanoparticles on Phaseolus vulgaris germination and seedling development determined by Xray spectroscopy, ACS Appl. Nano Mater., 2018, 1, 6414–6426.

[15] A. Konate, X. He, Z. Zhang, Y. Ma, P. Zhang, G. Alugongo and Y. Rui, Magnetic (Fe_3O_4) nanoparticles reduce heavy metals uptake and mitigate their toxicity in wheat seedling, Sustainability, 2017, 9, 790. https://doi.org/10.3390/su9050790

[16] M. Smiri, Environmental effect of magnetite nanoparticles (Fe_3O_4 NPs) on germination rate and seedling growth from bean, Pol. J. Environ. Stud., 2024, 33, 5284–5293. https://doi.org/10.15244/pjoes/183080.

Development of Rapid Feedback and Optimized Detection Algorithms to Enhance the Spatiotemporal Resolution of the ABEL Trap

Nahid Hasan, Rahul Islam, Md Asif Bin Sayed, Swopan Chandra Barman*, Sanjid-E-Elahi and Md. Mahmudur Rahman

Department of Electrical and Electronic Engineering, Dhaka University of Engineering & Technology, Gazipur, Bangladesh

ABSTRACT

This work presents a customized real-time particle tracking algorithm integrated with a Raspberry Pi-based feedback voltage controller to enhance the spatiotemporal resolution of the Anti-Brownian Electrokinetic (ABEL) trap. Unlike conventional ABEL trap implementations that rely on fluorescence modulation and specialized optical excitation geometries for particle localization, the proposed framework employs direct fluorescence imaging and real-time image processing to determine particle position, resulting in a simpler and more accessible feedback architecture. Using open-access video datasets for validation, our system achieved rapid feedback with a maximum latency of just 100 μs, more than 10 times faster than previous reports while maintaining voltage accuracy within 4% of the simulated values. This rapid feedback has the potential to offer more stable and longer nanoparticle confinement, making it highly suitable for delicate single-molecule studies. Our findings highlight how the simplified sensing architecture, precise voltage control, and optimized detection algorithms can substantially boost ABEL trap performance, paving the way for real-time tracking of faster and smaller biomolecules.

Keywords: optofluidic, ABEL trap, electrophoresis feedback single molecule trapping.

1. INTRODUCTION

Single-molecule techniques have revolutionized our understanding of dynamic processes by revealing a breadth of information, heterogeneities, and transient states that are inaccessible in typical bulk ensemble measurements [1]. Trapping individual molecules represents a foundational strategy in this regard that allows for precise control over the analytes of interest and prolonged observation timescales critical for quantitative analysis in a variety of disciplines, including biophysics, engineering, and molecular diagnostics. Optical trapping, pioneered by Arthur Ashkin in the 1970s, remains a method of choice for trapping and manipulation of single molecules [2]. Using photon momentum transfer, this approach non-invasively confines particles from micro to nanoscale, with the stability needed for a diverse range of applications, including force spectroscopy and live-cell biophysics [3], [4]. However, traditional optical traps often suffer from poor scalability for smaller particles and require high optical power, which can damage the particles and limit their effectiveness for nanoscale applications [5]. With recent advancements, miniaturized lab-on-chip technologies are becoming popular that enable integrated trapping platforms which offer enhanced functionality and flexibility by combining multiple techniques on a single platform [3], [4], [6]. Researchers have demonstrated various on-chip particle manipulation methods, such as optical tweezers [7], magnetic tweezers [3], [4], Photonic crystal fibers [5], [6], [8] and DNA curtains [9]), which provide precise control but are limited by issues like heat, low throughput, and specificity. Ring resonators [10], [11], Acoustic trapping [12] and dielectrophoretic methods [13] also face challenges related to integration and system complexity.

In recent years, the Anti-Brownian Electrokinetic (ABEL) trap has gained significant attention and positioned itself as a cutting-edge technique that enables precise single-molecule confinement by combining fluorescence-based tracking with electrokinetic feedback [14], [15]. Unlike optical tweezers that require intense illumination (often watt-level lasers) to generate sufficient gradient forces, the ABEL trap uses electrokinetic forces to counteract Brownian motion, requiring only microwatt-scale optical power for particle tracking [14], [15]. This dramatically reduces photodamage risks which is a critical advantage when studying delicate specimens like fluorescent proteins, live cells, or photosensitive nanomaterials. Since its first demonstration by Cohen

*Corresponding author's email: sbsm.swopan@gmail.com

and Moerner, the ABEL trap has enabled trapping of diverse biomolecules including viruses, DNA, and even small molecules (~1 kDa) in aqueous solution revealing its unique capability to confine nanoscale species that challenge conventional techniques. [3], [7]. While ABEL traps have demonstrated remarkable capabilities for single-molecule studies, their performance could be significantly enhanced by improving two critical factors. Firstly, improving particle tracking precision to precisely determine the particle position and track rapid Brownian motion, and secondly, faster voltage application to maintain stable trapping. These improvements are crucial because the effectiveness of an ABEL trap relies on rapid and accurate compensation of Brownian motion; any delay in particle localization or application of corrective voltages increases the likelihood of particle escape, thereby reducing trapping efficiency. Consequently, there is a need for feedback methodologies that not only minimize latency but also simplify the particle localization and control architecture while maintaining accurate real-time electrokinetic feedback. Such advancements would enable more stable confinement of delicate biological samples and expand the applicability of ABEL traps for investigating dynamic molecular processes that are currently challenging to study.

In this work, we present an improved ABEL trap methodology by integrating a custom Python-based particle tracking algorithm with a Raspberry Pi-based feedback voltage application. Building upon previous ABEL trap implementations, the proposed method employs direct fluorescence imaging and real-time image processing for particle localization instead of fluorescence modulation-based position estimation. This simplifies the sensing and feedback architecture while preserving the underlying electrokinetic trapping principle and enabling rapid real-time feedback. Our methodology was validated using published ABEL trap video datasets from Cohen and Moerner [16], Kuhn et al. [14], and Rahman et al. [17], demonstrating tracking precision and response times sufficient for stable nanoparticle confinement. . Following video frame extraction, our Python-based image processing algorithm performs real-time particle tracking to determine the particle position. Upon successful tracking of the particles, corresponding bidirectional feedback voltages are generated by the hardware which in theory should drag the particle to the desired trapping position with a stable 2D confinement, an approach following the electrokinetic feedback principle reported by Rahman et al. [17] .

2. METHODOLOGY

The ABEL trap is typically implemented by combining real-time optical detection with feedback control to counteract the Brownian motion of particles in solution, as illustrated in Fig. 1. A fluorescent molecule or nanoparticle is continuously imaged to determine its position, and a feedback system applies electrokinetic forces through microfluidic electrodes to push the particle back toward a defined trap center. This requires precise synchronization between optical measurements, position estimation, and voltage application. In the foundational work by Cohen and Moerner [16], the ABEL trap was realized using wide-field fluorescence microscopy coupled with real-time position estimation and electric field control executed on a custom-built software. Building on this concept, Kuhn et al. [14] developed a one-dimensional ABEL trap integrated onto a planar optofluidic chip that combined optical excitation, fluorescence detection, and electrokinetic feedback within a single microfabricated platform, as shown in Fig. 1(a). Their system employed solid-core waveguides embedded in the chip to deliver low-power laser excitation directly to the microfluidic channel, significantly reducing the optical power required for single-particle detection. Fluorescence emitted by the trapped particles was collected through the same chip-based architecture using a highly sensitive photodetector placed off-chip. Position estimation was based on the modulation of fluorescence intensity as the particle moved relative to the optical excitation pattern, which enabled real-time tracking.

Electrodes integrated along the microchannel applied feedback voltages to generate electroosmotic flow, effectively suppressing Brownian motion and keeping the particle confined near the trap center. This approach demonstrated the feasibility of miniaturized, power-efficient ABEL trapping, offering a scalable platform for portable single-particle analysis. Rahman et al. [17] further extended this concept by implementing two-dimensional electrokinetic feedback using intersecting optical waveguides, as illustrated in Fig. 1(b). Similar to Kuhn et al. [14], particle localization relied on fluorescence modulation, with the resulting position information used to generate feedback voltages that restored the particle to the trap center. The fully integrated optofluidic architecture provided a compact solution for single-particle trapping; however, the reported feedback latency remained on the order of a few milliseconds, limiting the trapping of smaller and faster-diffusing particles. Reducing this latency while simplifying the sensing and feedback architecture remains an important direction for improving ABEL trap performance.

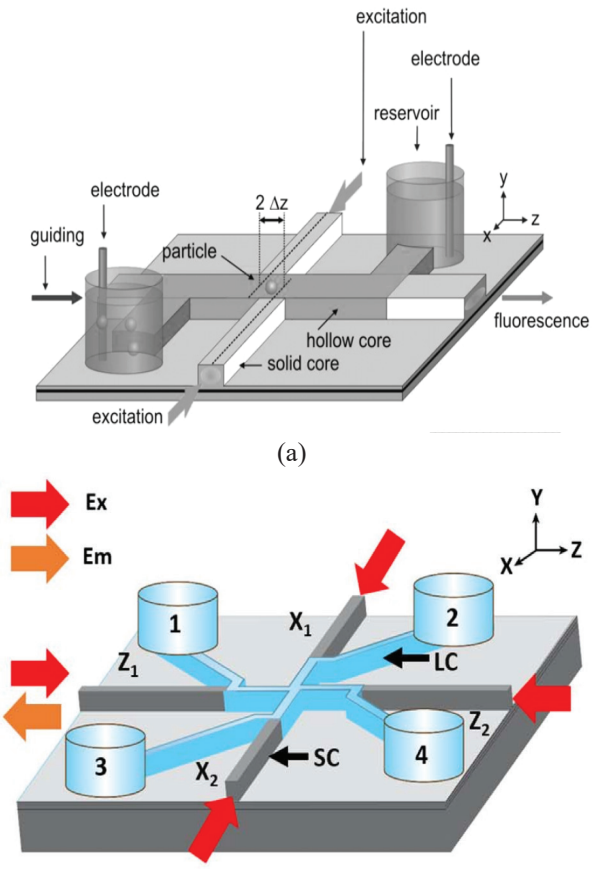


Fig. 1: Schematic representation of two ABEL traps designs: (a) simplified configuration introduced by Kuhn et al. [14] and (b) conventional configuration as presented by Rahman et al. [17].

Since rapid feedback is critical for efficient trapping particularly for smaller and more diffusive particles, it is essential to implement both fast voltage control and accurate particle tracking. To address this need, we have envisioned a methodology suitable for integration into typical on-chip systems, where fluorescent images of particles can be captured using a high-speed camera, such as a CCD (see Supplementary Section S1 for the proposed system architecture). Similar to conventional ABEL trap methods, our approach relies on image-based tracking coupled with a custom-developed algorithm to determine the particle's position in real time. Similar to Rahman et al. [17], our method assumes an anti-resonant reflecting optical waveguide (ARROW) platform featuring intersecting liquid-core waveguides, which facilitate analyte introduction through a standard glued reservoir. Unlike previous methods demonstrated by Kuhn et al. [14] and Rahman et al. [16], which rely on offset excitation waveguide geometries and periodic ON–OFF modulation of excitation beams, our technique does not require such configurations. This significantly simplifies the optical setup and removes the need for complex fluorescence-based modulation schemes. Furthermore, a straightforward top-down excitation with low optical power can also be used to excite fluorescence in labeled particles, enabling effective tracking through standard fluorescence imaging and appropriate filtering. As a result, the proposed method has the potential to offer a more accessible and adaptable platform for high-resolution ABEL trapping. Since our proposed method relies on fluorescence imaging of particles, an approach consistent with the techniques used in the previously mentioned studies, we validated our tracking algorithm using fluorescence videos published in those works. These videos, which capture the motion of fluorescently labeled particles, were processed through a custom-developed Python algorithm designed to accurately determine particle positions in each frame. The tracking data were then analyzed on a Raspberry Pi, which computed two-dimensional corrective voltages in real time. These voltages represent the electrokinetic feedback required to drive the particle toward the designated trap center, thereby demonstrating the viability of our approach for precise particle manipulation. The voltages can then be applied to the analyte via standard Ag–AgCl electrodes. The subsequent sections provide a comprehensive description of the system components, methodologies, and data collection procedures.

A real-time image processing algorithm was developed using Python to enable precise tracking, analysis of particle dynamics, and electric field-based manipulation for particle trapping. The fundamental concept underlying the algorithm is outlined in the flowchart depicted in Fig. 2.

The process begins with high-speed video frame acquisition of the trapping environment. Each captured frame transforms the Hue, Lightness, Saturation (HLS) color space, followed by thresholding operations for isolating the target particle. Following isolation, the algorithm detects the contour of the identified particle and computes the corresponding centroid. A positional error is then calculated by comparing the computed centroid with a predefined arbitrary target location. The system continuously iterates this process, acquiring new frames, updating the position, and applying corrections and thereby the particle is confined.

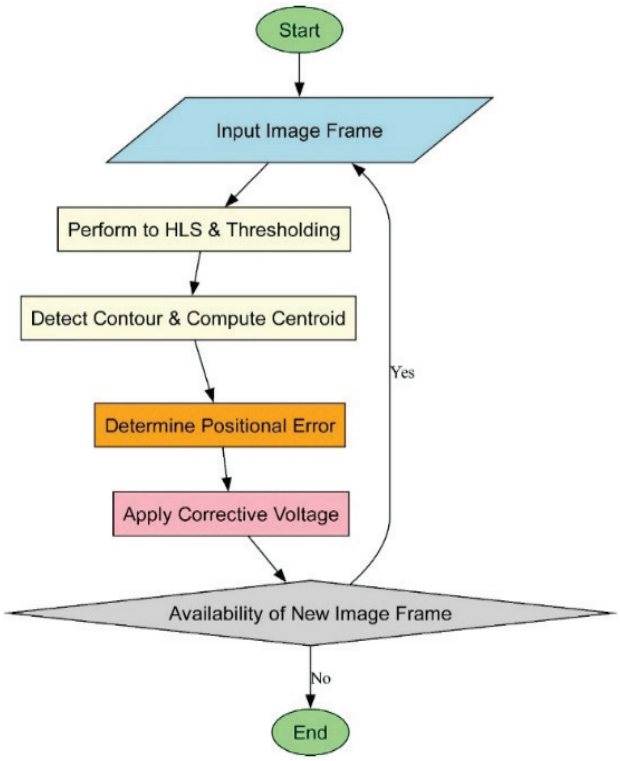


Fig. 2: Flowchart of the Real-Time ABEL Trap Biomolecule Tracking, Image Processing, and Voltage Adjustment Process

A predefined Region of Interest (ROI) is employed to localize the trapping region, thereby minimizing computational demand and enhancing algorithmic efficiency. Prior to system operation, the ROI is determined through an initial calibration stage to fully encompass the trapping region (see Supplementary Section S2 for further details).The ROI is mathematically represented as [18]:

$$ROI = \begin{cases} 1, \ if \ x_{lower} \le x \le x_{upper} \ and \ y_{lower} \le y \le y_{upper} \\ 0, \ otherwise \end{cases} \quad (1)$$

Where denote the predefined spatial boundaries that enclose the region under analysis.

Enhanced segmentation of the target particle against the background is achieved by converting each frame to the HSV (Hue, Saturation, Value) color space. This representation enables more distinct separation based on intensity and saturation gradients. The RGB-to-HSV conversion follows these expressions [19]:

Hue (H):

$$H = \begin{cases} 0° + 60° \times \dfrac{G - B}{max - min}, \ if \ max = R \\ 120° + 60° \times \dfrac{B - R}{max - min}, \ if \ max = G \\ 240° + 60° \times \dfrac{R - G}{max - min}, \ if \ max = B \end{cases} \quad (2)$$

Saturation (S):

$$S = \frac{\text{max-min}}{\text{max}} \quad (3)$$

Value (V)**:**

$$V = max \quad (4)$$

In these expressions, R, G, and B represent the red, green, and blue intensities, respectively, while H corresponds to hue in degrees, S denotes saturation, and V refers to the brightness component.

Using thresholding, a binary mask isolates particles with specific color profiles. The threshold values are selected during the initial calibration stage based on the fluorescence intensity and background characteristics of the acquired images to achieve reliable particle segmentation. Since these values depend on the imaging conditions, they are determined during the initial calibration stage prior to system operation (see Supplementary Section S2 for further details). The largest contour is then selected as the most probable particle candidate:

$$C = \arg\max\left(\text{Area}(C_i)\right), \qquad for\ Ci \quad \in S \quad (5)$$

Where, S represents the set of all detected contours, C is the contour with the largest area.

The centroid of the contour is computed to determine the precise location of the particle within the LC medium. The centroid coordinates (cX, cY) are calculated using the image moments:

$$cX = \frac{M_{10}}{M_{00}}, \quad cY = \frac{M_{01}}{M_{00}} \quad (6)$$

Where, are the spatial moments of the contour

The computed centroid coordinates, which are in pixel values due to video processing, are mapped to real-world values using a predefined scaling factor, allowing accurate positional tracking. The positional error is determined by calculating the difference between the detected particle position and a user-defined reference coordinate within the trapping region. The error is computed in terms of pixel distance from the trapping region coordinate:

$$E_x = X_{\text{ref}} - cX, \quad E_y = Y_{\text{ref}} - cY \quad (7)$$

Where, (X_{ref}, Y_{ref}) is the predefined target position for trapping.

A Raspberry Pi-based system performs real-time voltage control using the computed positional errors. Fig. 3(a) shows a sample video frame with a fluorescent biomolecule and the defined trapping point (x = 14.25 µm,

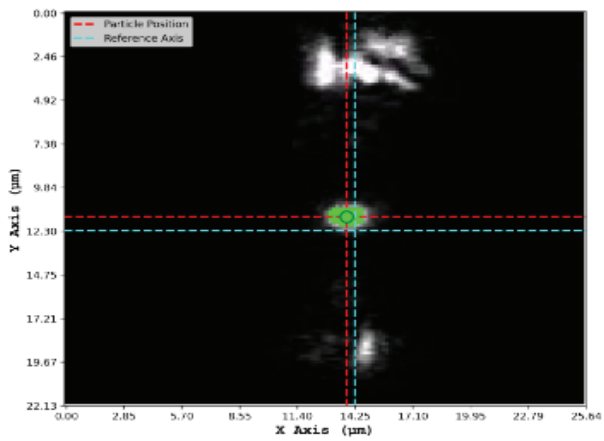
y = 12.30 µm). A maximum voltage of 3.3 V, of either polarity, is applied independently along the x- and y-axes. The voltages along these axes, denoted as Vx and Vy, are proportional to the positional error and are dynamically updated to steer the biomolecule toward the trapping point. This process is illustrated in Fig. 3(b).

Voltage adjustments follow:

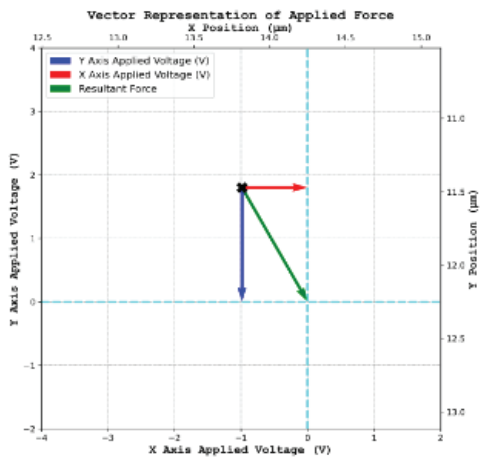
$$V_x = K_x \cdot E_x, \quad V_y = K_y \cdot E_y \tag{8}$$

Where, K_x and K_y are proportional gain constants selected during the initial calibration stage (see Supplementary Section S2 for further details).

The system continuously monitors subsequent frames, recalculating the positional error and adjusting the electric field until the particle reaches a static state.



(a)



(b)

Fig. 3: (a) Representative video frame extracted from Movie-3 in the supplementary material Khun et al.[14], illustrating the position of a fluorescent green biomolecule and the designated trapping point at (x = 14.25 µm, y = 12.30 µm). (b) Real-time voltage adjustment scheme for x and y-axis.

As shown in Fig. 4, the system utilizes a Raspberry Pi 5 receiving input image frames and two MCP4921 12-bit DACs, each paired with an amplifier for analog voltage output. The DACs, featuring a 4.5 µs settling time and 20 MHz SPI interface, convert digital control signals into analog voltages that are applied to the trapping electrodes. An oscilloscope is included in the setup for real-time monitoring of the output signals.

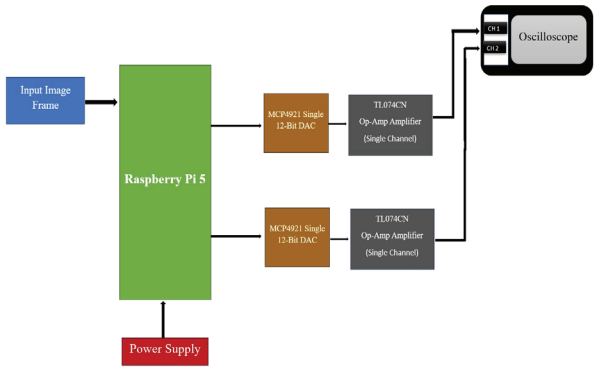


Fig. 4: A block diagram showing a Raspberry Pi 5-based system receiving input image frames and connected to two MCP4921 12-bit DACs and an oscilloscope for signal monitoring and analysis.

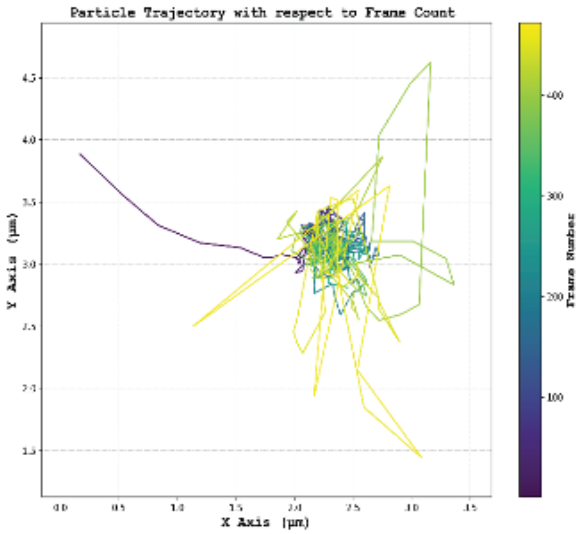
The trajectory of the trapped biomolecule is logged throughout the experiment. Both position data and voltage corrections are recorded and plotted to visualize movement patterns and the stabilization process. This real-time feedback system ensures accurate and dynamic trapping of particles within the ABEL trap, supported by high-speed imaging, efficient contour detection, and responsive field control.

3. RESULT AND DISCUSSION

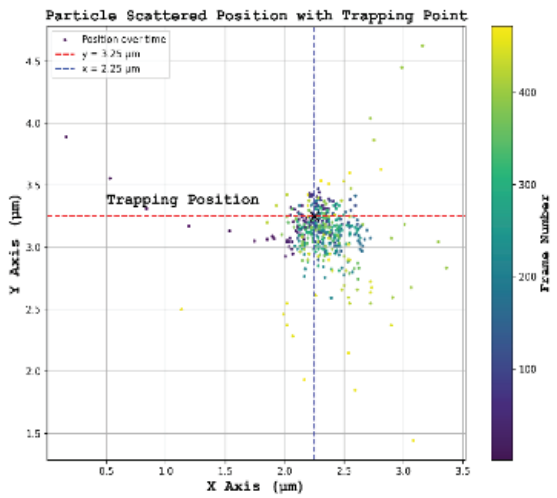
We validated the proposed image-processing-based ABEL trapping algorithm using publicly available videos from Cohen and Moerner [16] and Kuhn et al. [14], as outlined in the Methodology section, which simulate typical trapping conditions in ARROW optofluidic platforms.

In the first case, we utilized Movie-3 from the supplementary material of Cohen and Moerner [16], which demonstrates the tracking of individual large protein molecules such as B-phycoerythrin ~800 nm in diameter over 472 frames spanning 8 seconds. The trajectory in the x–y plane, as illustrated in Fig. 5(a), shows progressive localization toward a central region near (x = 2.25 µm, y = 3.25 µm), with a color gradient from purple to yellow indicating time progression across frames. A static

scatter plot shown in Fig. 5(b) further confirms stable confinement, with most positions constrained within approximately 0.3 µm of the target location.



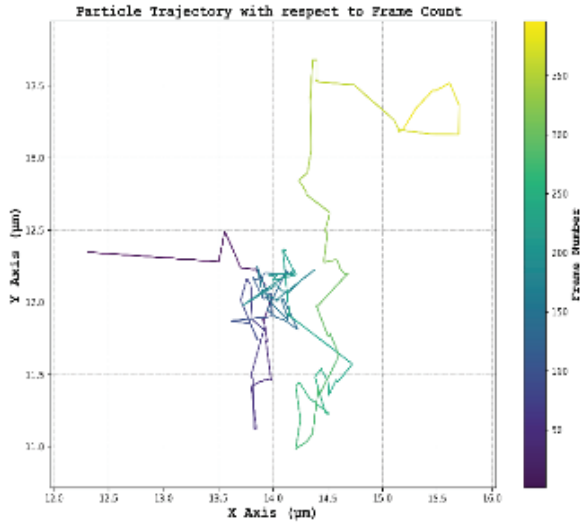
(a)



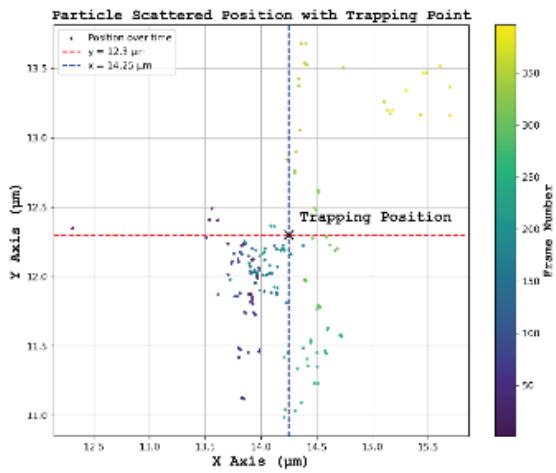
(b)

Fig. 5: Trajectory analysis of a large B-phycoerythrin protein molecule using the proposed image-processing algorithm. (a) Time-resolved trajectory extracted from the experimental video by Cohen and Moerner [16]. (b) Corresponding scatter plot showing spatial confinement near the trapping region.

Similarly, the trajectory extracted from Movie-3 in the supplementary material of Kuhn et al. [14] demonstrated consistent particle tracing within the designated trapping region. In this case, the trapped particle was a stained Escherichia coli (E. coli) bacterium. The trajectory, illustrated in Fig. 6(a) using a frame-color gradient, exhibits continuous tracking over 395 video frames. The x–y scatter plot shown in Fig. 6(b) confirms successful position detection near the trapping coordinate at (x = 14.25 µm, y = 12.30 µm). The particle remained confined within the ~2 µm excitation region throughout the duration of the sequence.



(a)



(b)

Fig. 6: Trajectory analysis of a stained E. coli bacterium using the proposed image-processing algorithm. (a) Time-resolved trajectory extracted from the experimental video by Kuhn et al. [14]. (b) Corresponding scatter plot showing spatial confinement near the trapping region.

Despite the variability in particle dynamics across the two video sources, the image-processing algorithm demonstrated robust and consistent real-time tracking performance. The algorithm achieved accurate frame-by-frame detection and localization of E. coli bacteria and B-phycoerythrin protein molecules throughout the recorded sequences, thereby validating the applicability and effectiveness of the proposed method across a broad range of biomolecular targets.

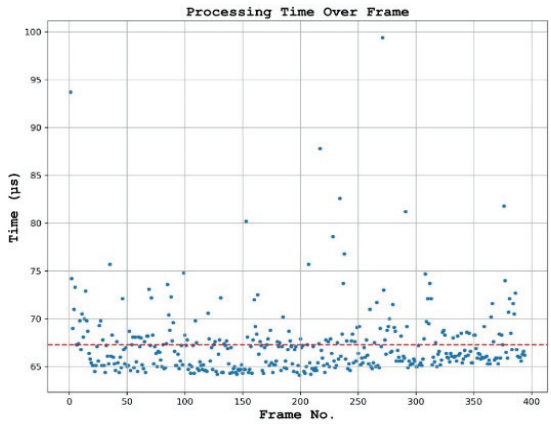
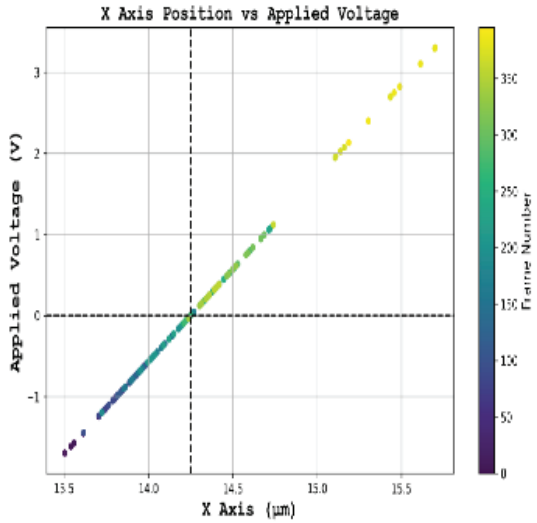
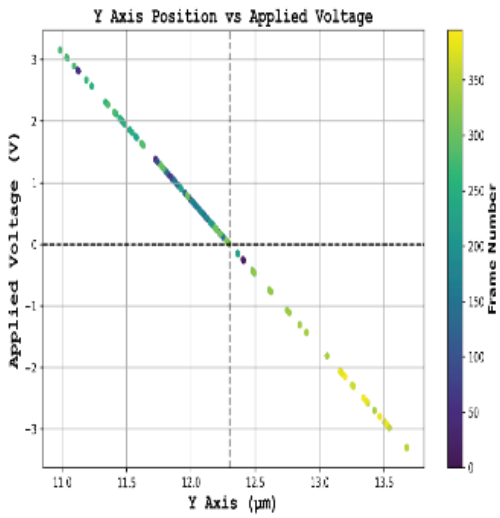


Fig. 7: Frame-by-frame processing time recorded by the image-processing algorithm for 395 video frames from Movie-3 of Kuhn et al. [16]. The latency was measured using internal timestamps, with the red dashed line representing the average duration per frame.

To assess the computational efficiency of our proposed image-processing-based ABEL trapping algorithm, we analyzed the algorithm-internal latency across 395 frames extracted from Movie-3 of the supplementary material in Kuhn et al. [16]. For each frame, the algorithm's processing duration was recorded in microseconds (µs), based on internal time-stamping mechanisms embedded within the codebase. As shown in Fig. 7, the algorithm exhibited highly consistent frame-wise processing latency. The average per-frame latency was approximately 67.5 µs, with a maximum of 100 µs. As shown in Fig. 7, the algorithm exhibited highly consistent frame-wise processing latency. The average per-frame latency was approximately 67.5 µs, with a maximum of 100 µs. Prior ABEL trap implementations reported closed-loop latencies limited by camera frame rate or fluorescence modulation cycle, approximately 3.4 ms for Cohen and Moerner [16] and 1–1.25 ms for Kuhn et al. [14] and Rahman et al. [17]. The sub-100 µs latency achieved by the proposed image-processing and feedback algorithm represents more than an order-of-magnitude reduction in processing latency compared with these reported implementations. However, since the present work was validated using published video datasets rather than a live ABEL trap, direct comparison with experimentally measured closed-loop trapping performance remains a subject of future work.However, it should be noted that the latency time is somewhat related to the size to the size of the ROI.



(a)



(b)

Fig. 8: Variation of the applied voltage on the two electrode axes for guiding the particle toward the trapping position. (a) Applied voltage along the x-axis electrodes. (b) Applied voltage along the y-axis electrodes.

We now present the analysis of electrokinetic feedback voltages generated by the image-based tracking system using the video dataset from Kuhn et al. [14] Fig. 8(a) shows the relationship between the particle position along the x-axis and the corresponding voltage applied to the Vx electrode. Likewise, Fig. 8(b) illustrates the particle position along the y-axis in relation to the applied Vy voltage. The control algorithm was conFig.d to maintain a target trapping point at 14.25 µm on the x-axis and 12.30 µm on the y-axis. As the particle moved away from these target coordinates, the Vx and Vy voltages were adjusted proportionally within a ±3.3 V range. These

voltage changes followed the direction of displacement, demonstrating the expected linear feedback behavior and confirming the system is capable of maintaining accurate positional control.

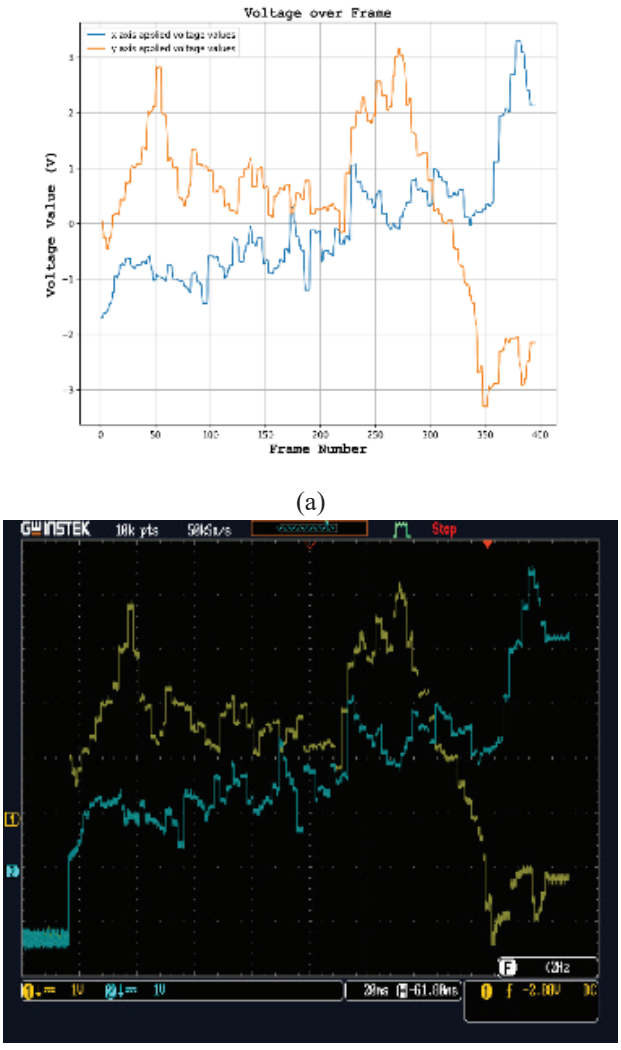


Fig. 9: Variation in the voltage waveform according to the position of particle in the recorded video by Kuhn et al. [14] (a) voltage output curves as a function of frames. (b) captured voltage waveform from the digital oscilloscope.

Furthermore, Fig. 9(a) presents the voltage output curves of Vx and Vy as a function of frame number. The yellow/orange trace corresponds to the Vy voltage, while the blue trace represents the Vx voltage. Over approximately 395 frames, both signals fluctuate within the range of –3.3 V to +3.3 V. Fig. 9(b) displays the voltage waveforms captured directly using a digital oscilloscope, representing the physically generated Vx and Vy signals. These waveforms closely align with the simulated voltage output curves, with the yellow/orange trace (Vy) exhibiting synchronized modulation bursts alongside the blue trace (Vx). Additionally, the oscilloscope data indicate that processing all 395 frames required approximately 162 ms. This demonstrates the system's efficiency in real-time feedback operations, as the video was processed at 2400 frames per second. However, performance may vary depending on the trapping zone or experimental setup.

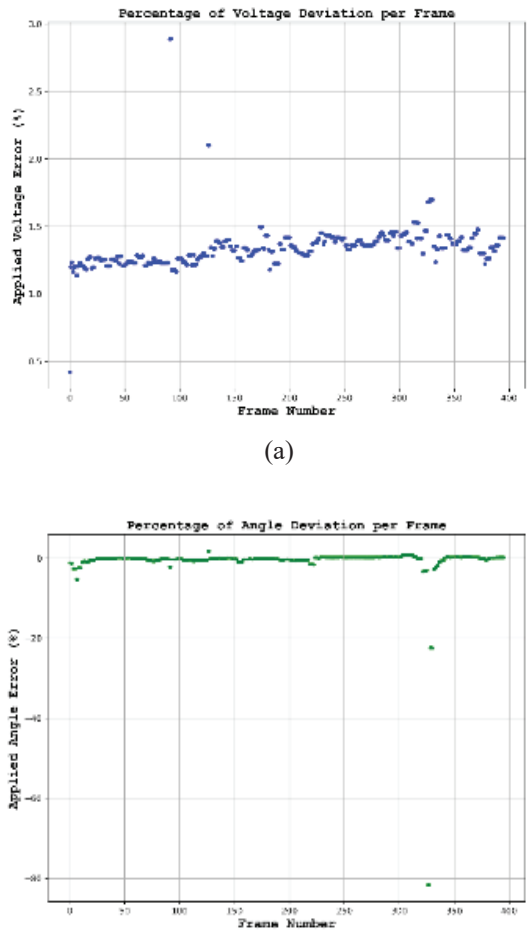


Fig. 10: Error analysis between physical setup data and simulation data: (a) resultant voltage error, (b) angle error.

Moreover, Fig. 10(a) presents the percentage error in the magnitude of the resultant voltage generated across 395 frames. The error remains within 1.5% for the majority of frames, with occasional spikes reaching up to 3%. Fig. 10(b) displays the angular error between the simulated and measured voltage vectors, where most values stay below 2%, indicating a strong agreement between the simulated outputs and the actual control signals. The occasional spikes in both magnitude and angular error occur primarily when the particle is located extremely

close to, or directly on, the reference trapping coordinate. In these instances, the required control voltages are in the low millivolt range. As a result, minor system noise may introduce relatively larger percentage deviations. However, these variations are not significant enough to disrupt the trapping performance, as the particle remains effectively within the desired region. These results confirm that the voltage control subsystem operates with high fidelity and robustness under real-time conditions.

4. CONCLUSION

In summary, we have developed an image-processing-based ABEL trapping system integrated with an efficient feedback voltage controller. The system combines real-time particle tracking with responsive electrokinetic feedback, enabling stable and consistent confinement of biomolecular targets. The proposed methodology was validated using publicly available video datasets, demonstrating effective performance across diverse particle types and trapping conditions. High agreement between simulated and measured control signals further confirms the accuracy of the system. Beyond reducing feedback latency, the proposed framework demonstrates that an image-processing-based feedback architecture can provide a practical and computationally efficient alternative for real-time ABEL trapping, offering a simpler implementation while maintaining accurate electrokinetic control. This work establishes a practical and adaptable framework for ABEL trapping, with strong potential for applications in single-molecule studies and real-time optofluidic manipulation.

ACKNOWLEDGEMENTS

NH (Nahid Hasan) and RI (Rahul Islam) contributed to the development of the algorithm and performed the data analysis. ABS (Md Asif Bin Sayed) was responsible for data collection and visualization. SE (Sanjid E Elahi) and MR (Mahmudur Rahman) developed the conceptual foundation of the article. SCB (Swopan Chandra Barman) contributed to the overall analysis and interpretation of the results. All authors have contributed to the writing, reviewing, and commenting on the article.

REFERENCES

[1] D. S. White, M. A. Smith, B. Chanda, and R. H. Goldsmith, "Strategies for Overcoming the Single-Molecule Concentration Barrier," *ACS Measurement Science Au*, vol. 3, no. 4, pp. 239–257, Aug. 2023, doi: 10.1021/acsmeasuresciau.3c00002.

[2] A. Ashkin, "History of Optical Trapping and Manipulation of Small-Neutral Particle, Atoms, and Molecules," *IEEE Journal of Selected Topics in Quantum Electronics*, vol. 6, no. 6, pp. 841–856, Dec. 2000, doi: 10.1109/2944.902132.

[3] D. Gao, W. Ding, M. Nieto-Vesperinas, *et al.*, "Optical manipulation from the microscale to the nanoscale: Fundamentals, advances and prospects," *Light: Science & Applications*, vol. 6, p. e17039, Jul. 2017, doi: 10.1038/lsa.2017.39.

[4] K. C. Neuman and A. Nagy, "Single-molecule force spectroscopy: optical tweezers, magnetic tweezers and atomic force microscopy," *Nature Methods*, vol. 5, no. 6, pp. 491–505, Jun. 2008, doi: 10.1038/nmeth.1218.

[5] F. Ye, R. P. Badman, J. T. Inman, M. Soltani, J. L. Killian, and M. D. Wang, "Biocompatible and High Stiffness Nanophotonic Trap Array for Precise and Versatile Manipulation," *Nano Letters*, vol. 16, no. 10, pp. 6661–6667, Oct. 2016, doi: 10.1021/acs.nanolett.6b03470.

[6] P. Jing, J. Wu, and L. Y. Lin, "Patterned Optical Trapping with Two-Dimensional Photonic Crystals," *ACS Photonics*, vol. 1, no. 5, pp. 398–402, May 2014, doi: 10.1021/ph500041m.

[7] K. C. Neuman and S. M. Block, "Optical trapping," *Review of Scientific Instruments*, vol. 75, no. 9, pp. 2787–2809, Sep. 2004, doi: 10.1063/1.1785844.

[8] D. Grass, J. Fesel, S. G. Hofer, N. Kiesel, and M. Aspelmeyer, "Optical trapping and control of nanoparticles inside evacuated hollow core photonic crystal fibers," *Applied Physics Letters*, vol. 108, no. 22, May 2016, doi: 10.1063/1.4953025.

[9] P. Rodríguez-Sevilla, L. Labrador-Páez, D. Jaque, and P. Haro-González, "Optical trapping for biosensing: Materials and applications," in *Optical Trapping and Optical Micromanipulation XIV*, F. J. G. de Abajo, Ed., vol. 10350, SPIE, 2017, pp. 69–75, doi: 10.1039/c7tb01921a.

[10] S. Lin, E. Schonbrun, and K. Crozier, "Optical manipulation with planar silicon microring resonators," *Nano Letters*, vol. 10, no. 7, pp. 2408–2411, Jul. 2010, doi: 10.1021/nl100501d.

[11] A. H. J. Yang and D. Erickson, "Optofluidic ring resonator switch for optical particle transport," *Lab on a Chip*, vol. 10, no. 6, pp. 769–774, 2010, doi: 10.1039/b920006a.

[12] A. Ashkin, J. M. Dziedzic, J. E. Bjorkholm, and S. Chu, "Observation of a single-beam gradient force optical trap for dielectric particles," *Optics Letters*, vol. 11, no. 5, pp. 288–290, May 1986, doi: 10.1364/ol.11.000288.

[13] R. S. Thomas, H. Morgan, and N. G. Green, "Negative DEP traps for single cell immobilisation," *Lab on a Chip*, vol. 9, no. 11, pp. 1534–1540, 2009, doi: 10.1039/b819267g.

[14] S. Kühn, B. S. Phillips, E. J. Lunt, A. R. Hawkins, and H. Schmidt, "Ultralow power trapping and fluorescence detection of single particles on an optofluidic chip," *Lab on a Chip*, vol. 10, no. 2, pp. 189–194, 2010, doi: 10.1039/b915750f.

[15] A. P. Fields and A. E. Cohen, "Electrokinetic trapping at the one nanometer limit," *Proceedings of the National Academy of Sciences*, vol. 108, no. 21, pp. E157–E164, May 2011, doi: 10.1073/pnas.1103554108.

[16] A. E. Cohen and W. E. Moerner, "Suppressing Brownian motion of individual biomolecules in solution," *Proceedings of the National Academy of Sciences*, vol. 103, no. 12, pp. 4362–4365, Mar. 2006, doi: 10.1073/pnas.0509976103.

[17] M. Rahman, M. A. Stott, Y. Li, A. R. Hawkins, and H. Schmidt, "Single-particle analysis with 2D electro-optical trapping on an integrated optofluidic device," *Optica*, vol. 5, no. 10, p. 1311, Oct. 2018, doi: 10.1364/optica.5.001311.

[18] D. Boateng, K. Chu, Z. J. Smith, J. Du, and Y. Dai, "Deep learning-based size prediction for optical trapped nanoparticles and extracellular vesicles from limited bandwidth camera detection," *Biomedical Optics Express*, vol. 15, no. 1, p. 1, Jan. 2024, doi: 10.1364/BOE.501430.

[19] H. Li, T. Yang, L. Li, S. Lv, and S. Li, "A Camouflaged Film Imitating the Chameleon Skin with Color-Changing Microfluidic Systems Based on the Color Information Identification of Background," *Journal of Bionic Engineering*, vol. 18, no. 5, pp. 1137–1146, Sep. 2021, doi: 10.1007/s42235-021-00091-y.

Evaluating the Feasibility of a Trumpet Interchange at Shibbari Intersection under Current and Future Traffic Growth: A Microsimulation Approach

Md. Jamil Mahmud Abdullah[1], Mahiman Zinnurain[1], Mohammad Kabir Hossain[1*], Noman Hasan Fahim[2], Md. Zakir Husen[1] and Jahid Hasan[1]

[1]Department of Civil Engineering, Dhaka University of Engineering & Technology, Gazipur, Bangladesh
[2]Graduate Research Assistant, Department of Civil and Environmental Engineering, Portland State University, USA

ABSTRACT

Traffic congestion at T-intersections in urban areas of developing countries is often intensified by non-lane based, heterogeneous traffic and the presence of dedicated Bus Rapid Transit (BRT) lanes. A trumpet interchange offers a potential solution by eliminating crossing conflicts and improving overall flow efficiency. However, such grade-separated interventions remain uncommon in Bangladesh. This study evaluates the feasibility of introducing a trumpet interchange at the Shibbari intersection, Gazipur, focusing on both current and future traffic conditions. Field data on roadway geometry, traffic volumes, and speeds were collected during peak hours over two weekdays and one weekend. A microscopic simulation model was developed in a micro simulation software to replicate existing conditions and evaluate two scenarios: (1) the current T-intersection (Base Case) and (2) the proposed trumpet interchange. Each scenario was analyzed under present traffic demand a 7% annual traffic growth projection representing future industrial expansion. Results indicate that the existing intersection operates acceptably under current demand but becomes highly congested under future conditions, with vehicle delays exceeding 1200 seconds, stop delays surpassing 1000 seconds, and queue delays reaching 182.9 seconds. In contrast, the trumpet interchange significantly improves performance by reducing conflict points and enhancing capacity. Under future conditions, queue delay at the Shimultoli approach decreases to 21.66 seconds, while Level of Service improves to A-C, although moderate congestion remains during peak periods. Overall operating speeds increase by approximately 23% compared to the base case. These results provide useful guidance for policymakers and urban planners when evaluating the implementation of trumpet interchanges in mixed-traffic environments.

Keywords: Trumpet interchange, BRT lane, micro simulation, traffic growth, intersection congestion.

1. INTRODUCTION

Rapid urbanization in developing countries such as Bangladesh has led to a sharp increase in travel demand, placing substantial strain on urban road networks [5]. As a result, traffic congestion has emerged as a critical issue in many rapidly expanding Bangladeshi cities. Intersections, which serve as the most sensitive components of a road network, frequently experience significant delays and operational inefficiencies, particularly under heterogeneous traffic conditions. Urban roadways in Bangladesh typically accommodate a diverse mix of vehicles including buses, trucks, private cars, auto-rickshaws, and non-motorized transport often operating without strict lane discipline [10]. This coexistence of fast- and slow-moving vehicles within the same space creates irregular traffic flow patterns, increasing the likelihood of disruptions and delays. The absence of effective lane management and enforcement further intensifies these issues, as vehicles with varying sizes and performance characteristics interact in an unstructured manner, leading to congestion and bottlenecks.

Within Gazipur, the Shibbari intersection stands out as one of the busiest and most congested junctions. Despite its strategic importance as a key access point to major industrial and residential zones, the intersection suffers from poor operational performance. These challenges underscore the urgent need for both policy-oriented and infrastructure-based interventions aimed at enhancing traffic efficiency and ensuring sustainable urban mobility. Compounding the problem is the limited infrastructure at the intersection, which is currently configured as an at-grade T-intersection. In this setup, all traffic movements occur on the same level, resulting in numerous conflict points as vehicles cross and turn across each other's paths.

*Corresponding author's email: hossain.kabir@duet.ac.bd

The absence of grade-separated facilities significantly restricts capacity and increases delays.

The situation is likely to become more complex with the planned introduction of dedicated Bus Rapid Transit (BRT) lanes through the intersection. Without proper grade separation, BRT operations would intersect with general traffic streams, potentially intensifying congestion and increasing the risk of gridlock. In this context, a modified trumpet interchange has been proposed as a potential solution. This type of grade-separated design is particularly suitable for T-intersections, as it diverts major turning movements onto ramps and elevated structures, thereby eliminating direct crossing conflicts. Implementing such a configuration at Shibbari could facilitate uninterrupted flow along primary corridors, including the BRT route, and substantially reduce delays. However, the adoption of grade-separated interchanges remains limited in Bangladesh's urban environment, raising concerns regarding feasibility, context-specific design adaptations, and cost-effectiveness. Nevertheless, the pressing need to minimize at-grade conflicts provides a strong justification for exploring such solutions.

In summary, the Shibbari intersection is affected by a combination of heterogeneous traffic composition, a high prevalence of slow-moving three-wheelers, and inadequate infrastructure. These factors collectively contribute to severe congestion and operational inefficiencies. Addressing these challenges requires an integrated approach that simultaneously manages traffic composition and enhances intersection design to achieve improved performance and sustainability.

2. LITERATURE REVIEW

Bangladesh's urban traffic operates under heterogeneous "mixed" conditions where diverse vehicle types from cars and buses to auto-rickshaws, cycle-rickshaws, and other non-motorized modes share the same road space without strict lane discipline. Drivers often ignore lane markings and traffic rules, weaving laterally through any available gaps to inch ahead at intersections [9]. Field studies in Dhaka show that average travel speeds drop to as low as 6.1 km/h during peak hours, significantly below global urban standards [16]. Combined with weak enforcement of traffic laws and frequent pedestrian interference (e.g., people crossing roads arbitrarily), this non-lane-based behavior creates numerous conflict points and chaotic maneuvers at both signalized and unsignalized intersections [13].

Consequently, intersections commonly suffer from long delays and frequent stops, along with inefficient use of space as vehicles jostle for position. The absence of proper channelization such as dedicated turning lanes or separate facilities for slower vehicles means that fast-moving and slow-moving traffic intermingle, reducing overall capacity and exacerbating congestion [17]. Similarly, research conducted in Gazipur demonstrates that intersections such as Chowrasta and Shibbari experience persistent gridlock due to heterogeneous vehicle composition. Surveys indicate that over 54% of commuters in Chowrasta lose 4–5 hours daily because of traffic blockages, where electric three-wheelers were identified as a key cause of delay [18]. Similarly, a study on Gazipur Chowrasta confirmed that congestion was chronic due to industrial land use and mixed traffic, with buses, trucks, cars, rickshaws, and easy bikes competing for limited road space [10].

Grade-separated interchanges are special types of road junctions where vehicles move on different levels using bridges or tunnels. This design removes at-grade conflicts and allows vehicles to move without stopping for crossing traffic, leading to continuous traffic flow [14]. Among various types, the trumpet interchange is commonly used where one major highway ends at another. It connects the two roads through a loop ramp that curves around like a trumpet shape [8]. These interchanges help reduce delays and improve safety by lowering the number of conflict points where vehicles would otherwise cross paths. For instance, studies show that building flyovers or interchanges significantly increases intersection capacity and enhances safety by separating traffic streams. A notable example is the 2-kilometer-long Baipail trumpet interchange in Dhaka, completed in 2024. This project was designed to ensure "seamless vehicular movement" at the Ashulia–Nabinagar junction and reduce traffic congestion [2]. Compared to regular at-grade intersections, trumpet and other grade-separated interchanges reduce the need for traffic signals and stops. This leads to fewer delays and higher traffic capacity [3]. Simulation-based studies also support these benefits. For example, research shows that adding a flyover or underpass can double capacity and shorten queue lengths dramatically [4]. In Dhaka, a grade-separated U-loop was found to reduce delays by over 90% compared to a signalized design [3]. As a result, cities like Dhaka have increasingly adopted such structures, including the Mohakhali flyover, to address ongoing traffic congestion [15]. In summary, grade-separated interchanges especially trumpet types are effective solutions for improving traffic flow, reducing delays, and enhancing road safety in both developed and developing urban areas.

3. METHODOLOGY

The research followed several structured steps. First, the research objective was defined, and the study area was selected. A literature review was then conducted to understand existing approaches and identify research gaps. Afterward, field data were collected, including traffic volume, road geometry, GPS-based speed data, and E3W occupancy. A questionnaire survey was also carried out to explore operational challenges and commuter needs. Next, a micro simulation model was developed and calibrated in PTV VISSIM to represent real traffic conditions. Several alternative scenarios were developed and systematically evaluated to assess their operational performance and identify the most effective solution for enhancing intersection efficiency.

3.1 Study Area: Shibbari Intersection Description

The study was carried out at the Shibbari Intersection in Gazipur City, Bangladesh. Gazipur is an industrial hub located north of Dhaka, hosting numerous factories,

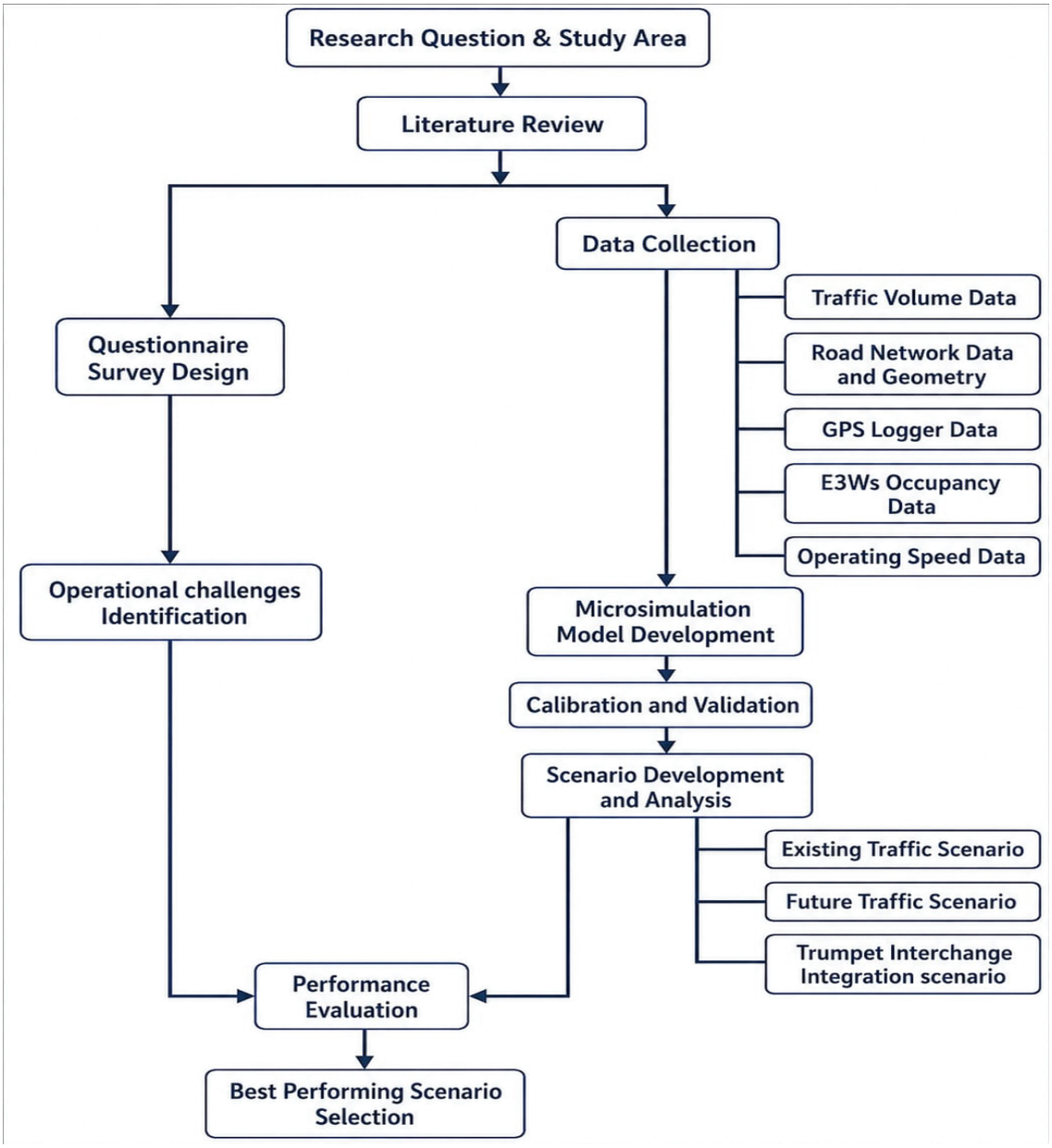


Fig. 1: Flow Chart of Methodology

offices (both government and private), and educational institutions. The Gazipur district spans approximately 23°53′–24°21′ N and 90°09′–92°39′ E, placing it near the center of Bangladesh [10]. Shibbari Intersection is about 37 km north of central Dhaka. This strategic urban location connects major highways and contributes to high traffic volumes, making it a relevant case for congestion analysis. The geographic location has been showed in the Fig. 2.

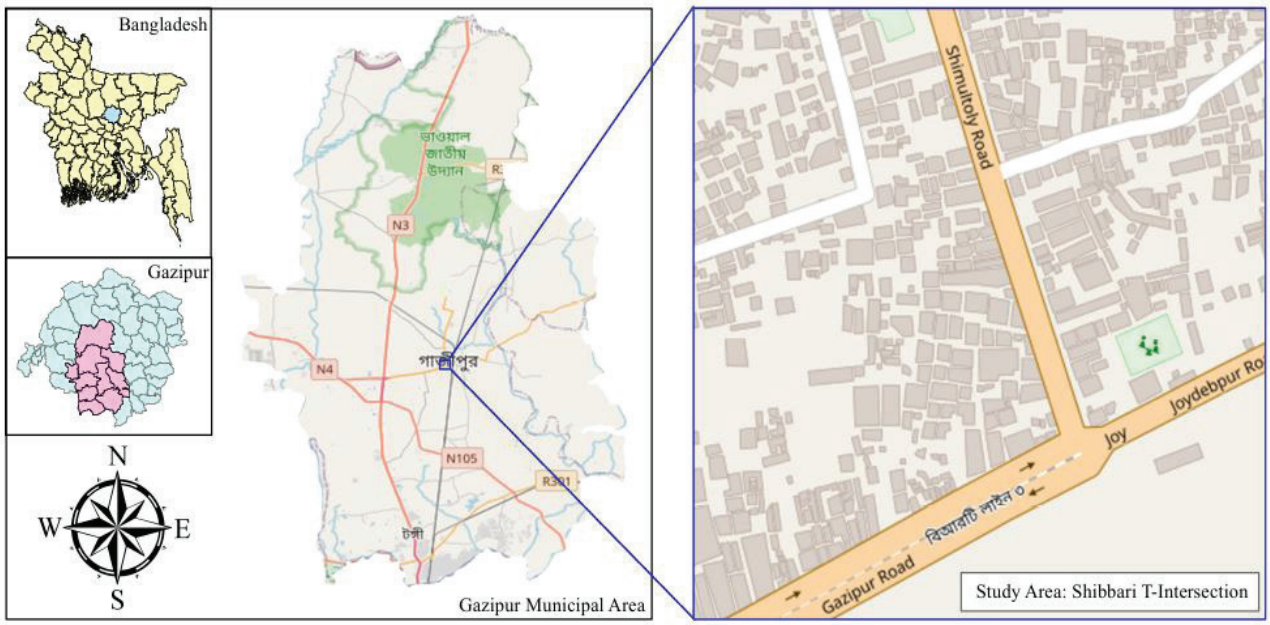


Fig. 2: Birds eye view of the study area: Shibbari Intersection

3.2 Data Collection

Data collection for this research was a challenging but essential task. It was carried out in two main phases. In the first phase, field data was collected from the study area (Shibbari intersection and nearby road links) to accurately build the road network model in PTV VISSIM. In the second phase, after calibration, simulation results were extracted to evaluate the effectiveness of different improvement strategies, especially grade-separated interchange solutions. Field data included traffic volume, vehicle composition, road geometry, E3W occupancy (6 persons, 4 persons and 2 persons capacity type vehicles), and travel speeds. Manual count was used to collect vehicle flow data during morning (8 am -10 am) and evening (4 pm – 6 pm) peak hours [10]. Additionally, GPS-based logger data was used to find desired speed distribution of several vehicles. Intersection layout and segment lengths were measured using basic instruments like measuring tapes. The calibration and validation were performed following the Florida Department of Transportation (FDOT) Handbook guidelines [20]. Table I summarizes the calibration results for Day 1, and Fig. 4 compares the simulated and observed traffic flows. All GEH values and link flow deviations were within the acceptable limits, confirming that the model accurately represents real-world traffic conditions and is suitable for further scenario analysis.

Table I: Sample Calibration Table for Day 01

Direction	Vehicle /Hr.	Vehicle /600 sec.	Simulation Vehicle /600 sec.	Difference (Veh/hr)	% Difference	GEH
From Shimultoli	684	114.0	113	6	0.88	0.0939
To Shimultoli	426	71.0	77	-36	-8.45	0.6975
From Railgate	980	163.3	160	20	2.04	0.2622
To Railgate	794	132.3	132	2	0.25	0.0290
From Chowrasta	1032	172.0	161	66	6.40	0.8525
To Chowrasta	1468	244.7	203	250	17.03	2.7850

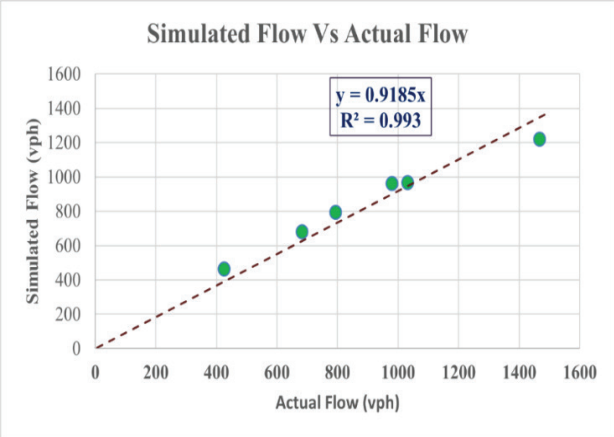


Fig. 3: Comparison between Simulated and Observed Traffic Flows

3.3 Future Traffic Scenario

The base condition scenario assumes that no improvements or geometric changes are made to the existing road network, even as traffic demand continues to grow in future years. According to the Roads and Highways Department (RHD) Pavement Design Guide (2005), the annual traffic growth rate for Regional Roads is 7% [19]. As the study corridor (R310: Joydebpur-Gazipur-Azmatpur-Itakhola Road) is an RHD Regional Road, a 7% annual traffic growth rate was adopted to forecast future traffic demand. Accordingly, projected traffic volumes for the years 2030, 2040, and 2050 were estimated using this growth rate. These projections were applied in the simulation to evaluate the likely increase in congestion and delay if the current infrastructure remains unchanged.

Table II: Traffic with E3Ws under 7% growth rate.

Direction	2025 (Base)	2030	2040	2050
From Shimultoli (veh/hr)	684	959	1,888	3,709
From Railgate (veh/hr)	980	1,375	2,704	5,320
From Chowrasta (veh/hr)	1032	1,448	2,849	5,603

Table II shows that traffic volumes are expected to increase sharply across all approaches under the do-nothing condition. The Chowrasta approach exhibits the highest projected flow, followed by Railgate and Shimultoli. By 2050, total traffic demand is predicted to rise by more than four times compared to the base year, indicating severe congestion if no mitigation measures are implemented.

3.4 Trumpet Interchange Integration Scenario

Here, a modified trumpet interchange is introduced at the intersection to allow uninterrupted vehicle movement through grade separation. The geometric design and lane assignments were prepared using reference studies such as Indian road congress (IRC) guidelines. The model was built in VISSIM and tested under current and future traffic. The VISSIM simulation was performed using a single simulation run with a fixed random seed of 42. The same random seed was used for all scenarios to ensure consistent and comparable simulation results. Table III briefly compares the IRC-recommended and provided geometric parameters of the proposed trumpet interchange. Most values meet or exceed the standards, confirming the design's suitability. Minor deviations, such as a slightly smaller direct-ramp radius, remain acceptable under site conditions, while overall dimensions ensure safe and efficient traffic operation [11, 12]

Table III: Recommended and Provided Geometric Design Parameters for Trumpet

Description	Recommended Measurement (IRC Guidelines)	Provided Measurement (Design Data)	Reference	Comment
Radius of Loop Ramp	Minimum 30 m	36.2 m	IRC:92-2017, Sec. 6.2.2, Table 6.1	Satisfies standard; adequate for design speed.
Radius of Semi-direct (Direct) Ramp	Minimum 60 m	56.8 m	IRC:92-2017, Sec. 6.2.2, Table 6.2	Slightly below recommended; still acceptable under constrained site conditions.

Description	Recommended Measurement (IRC Guidelines)	Provided Measurement (Design Data)	Reference	Comment
Width of Lane	3.5 m	3.5 m	IRC:86-2018, Sec. 5.4	Standard lane width considered in design.
Length of Curve / Ramp	15–50 m (for 20–80 km/h)	Loop = 170.5 m; Semi-Direct = 64.3 m	IRC:86-2018, Sec. 9.3, Table 9.2	Exceeds minimum requirement; ensures smoother turning movement.
Shoulder Width	Minimum 2 m	2 m	IRC:92-2017, Sec. 6.4	Fully satisfies standard.
Median Width	Minimum 1.2 m	1.2 m	IRC:92-2017, Sec. 6.4	Provided for safety separation between directions.
Approach Road Length	Minimum 90 m	130 m	IRC:92-2017, Sec. 6.5.2, Table 6.4	Adequate for approach alignment and sight distance.
Bridge Length	According to Roadway width	70 m	IRC:92-2017, Sec. 6.6.1	Suitable for grade separation and traffic volume.
Gradient	Maximum 6%	5 %	IRC:92-2017, Sec. 6.3	Within acceptable limit for ramp design.
Vertical Clearance	Minimum 5.5 m	6.5 m	IRC:92-2017, Sec. 6.6.2	Exceeds minimum requirement; ensures full clearance for heavy vehicles.

Fig. 4 shows the adopted geometric measurements of the modified trumpet.

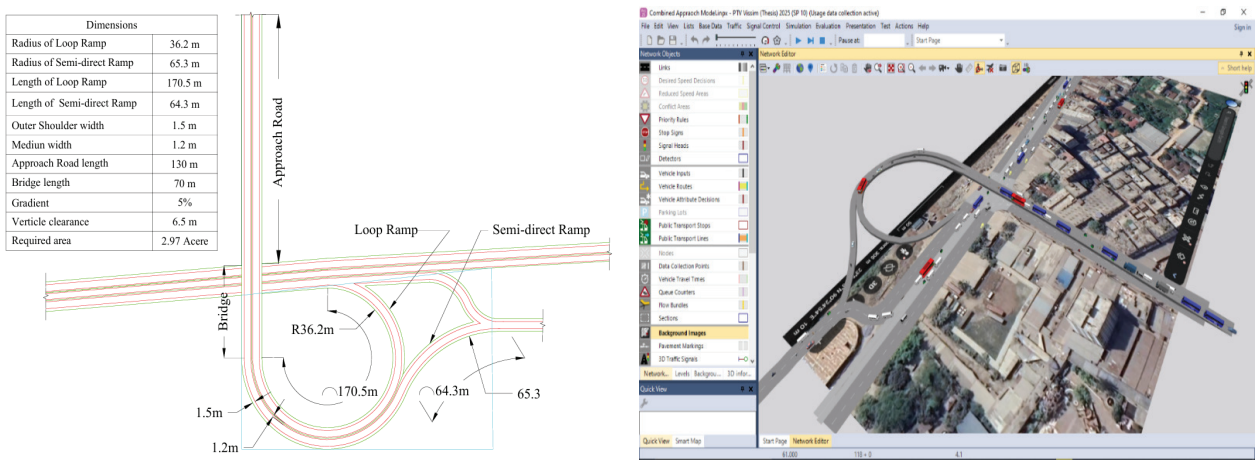


Fig. 4: Graphical representation of modified trumpet interchange

4. RESULTS AND DISCUSSION

4.1 Simulation Results for Existing Conditions

The simulation results for the existing traffic conditions, shown in Table IV, indicate that congestion at the Shibbari intersection increases notably with future traffic growth. Queue delays and occupancy rates rise sharply after 2030, especially on the Shimultoli and Railgate approaches, while both arithmetic and harmonic mean speeds gradually decrease. By 2050, severe congestion is evident, with delays exceeding 180 seconds and occupancy rates above 90 % on several approaches. These findings suggest that the existing intersection configuration will become highly inefficient under anticipated demand, emphasizing the need for geometric or operational enhancements.

Table IV: Simulation results for existing conditions.

Roadway	Year	Queue delay (all) sec	Speed avg. Arithmetic (all) km/h	Speed avg. Harmonic (all) km/h	Occupancy rate (all)
From Shimultoli	2025 (current)	4.22	14.10	10.79	47.31%
	2030	47.54	9.09	4.30	86.79%
	2040	110.35	8.63	5.27	91.77%
	2050	182.90	7.84	4.74	92.86%
To Shimultoli	2025 (current)	25.84	20.08	18.40	6.92%
	2030	37.00	19.33	17.91	9.15%
	2040	73.59	19.90	18.19	12.79%
	2050	80.66	18.48	17.54	21.54%
From Railgate	2025 (current)	0.31	17.23	15.80	17.82%
	2030	0.62	16.90	14.97	27.07%
	2040	10.53	13.49	10.00	74.64%
	2050	104.62	12.33	9.40	87.02%
To Railgate	2025 (current)	18.35	18.65	17.64	11.06%
	2030	23.17	17.77	16.85	14.52%
	2040	104.19	17.80	16.83	18.95%
	2050	56.23	16.84	16.09	36.39%
From Chowrasta	2025 (current)	0.19	17.11	16.22	15.74%
	2030	0.19	16.98	16.13	20.79%
	2040	50.28	14.42	9.33	83.50%
	2050	31.52	13.91	10.67	80.76%
To Chowrasta	2025 (current)	32.54	17.40	15.86	22.37%
	2030	52.46	17.66	16.24	26.22%
	2040	65.63	16.42	14.92	38.47%
	2050	114.60	16.04	14.61	45.15%

4.2 Simulation Results for Trumpet Interchange Scenario

The findings in Table V indicate that the trumpet interchange substantially enhances traffic performance compared to the existing scenario, especially up to 2030. Queue delays remain negligible in the early years, and average speeds stay relatively high across all approaches. However, as traffic demand grows beyond 2040, queue delays and occupancy rates begin to increase most noticeably on the Railgate and Chowrasta approaches though still at lower levels than in the base scenario. This indicates that the trumpet interchange effectively enhances network efficiency and delays severe congestion under future traffic growth.

Table V: Simulation results for Trumpet Interchange

Roadway	Year	Queue Delay (all) sec	Speed avg. Arithmetic (all) km/h	Speed avg. Harmonic (all) km/h	Occupancy rate (all)
From Shimultoli	2025 (current)	0.05	18.85	17.82	13.02%
	2030	0	18.16	17.17	17.44%
	2040	0.19	16.29	14.78	37.12%
	2050	21.66	11.51	7.29	84.43%
To Shimultoli	2025 (current)	0.49	19.14	18.02	6.44%
	2030	0.55	20.15	18.67	9.15%
	2040	3.14	18.28	16.89	18.06%
	2050	22.84	18.27	17.06	26.48%
From Railgate	2025 (current)	0.11	17.23	15.83	18.12%
	2030	0.35	17.08	15.74	25.58%
	2040	5.71	13.7	8.97	69.72%
	2050	113.37	13.75	10.24	82.09%
To Railgate	2025 (current)	0.68	19	17.88	12.46%
	2030	0.78	18.04	17.01	17.05%
	2040	5.58	17.34	16.52	30.87%
	2050	28.84	16.75	16.07	49.67%
From Chowrasta	2025 (current)	0.78	15.51	14.02	28.90%
	2030	0.45	14.87	13.64	36.39%
	2040	19.18	13.97	8.57	80.95%
	2050	42.44	12.44	8.63	86.54%
To Chowrasta	2025 (current)	15.73	18.31	17.01	20.61%
	2030	18.77	17.41	16.46	28.04%
	2040	51.97	16.62	15.8	44.02%
	2050	151.56	16.69	15.93	47.31%

4.3 Comparative Analysis of Scenarios

Fig. 5 indicates that vehicle delay increases progressively with time in all scenarios due to growing traffic demand. The base condition exhibits the highest rate of delay growth, rising sharply from approximately 120 seconds in 2025 to more than 1200 seconds by 2050, which reflects severe future congestion at the study intersection. In contrast, the trumpet interchange scenario substantially reduces vehicle delay throughout the analysis period. Although delay still increases gradually over time, the values remain considerably lower than those of the existing condition, indicating improved traffic operation and roadway efficiency.

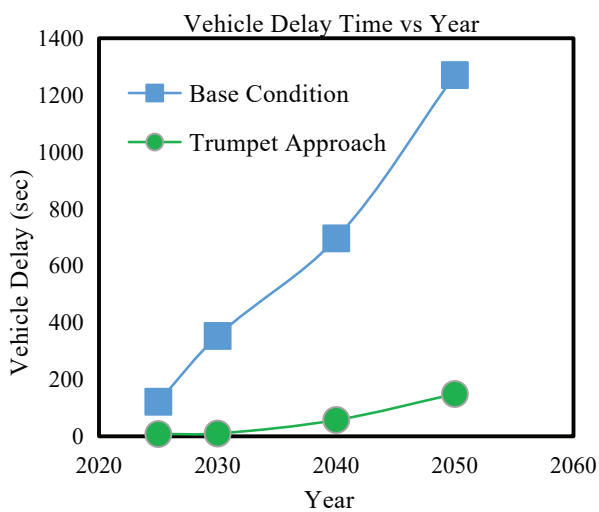


Fig. 5: Comparative analysis of scenarios with respect to vehicle delay

The trend in Fig. 6 Stop Delay Time vs Year shows a consistent increase in stop delay across all scenarios as traffic demand increases. The base condition experiences the highest and fastest growth, exceeding 1000 seconds by 2050, indicating worsening congestion and frequent stoppages. In contrast, the trumpet interchange scenario maintains significantly lower stop delay throughout the analysis period, demonstrating its effectiveness in improving traffic flow and reducing intersection congestion.

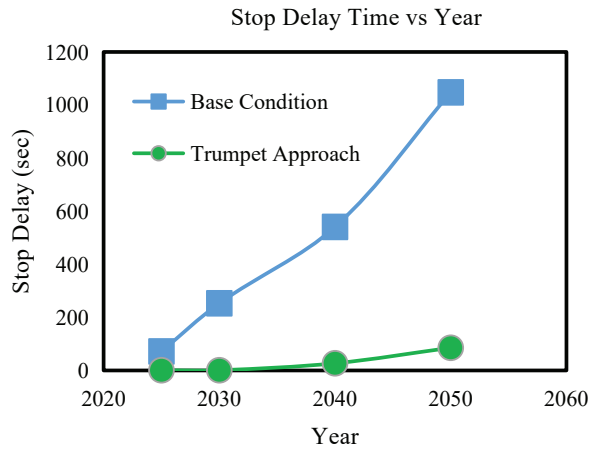


Fig. 6: Comparative analysis of scenarios with respect to stop delay

The Level of Service (LOS) distribution under the base condition shows a gradual decline over time. In 2025, most traffic movements operate at LOS A, reflecting smooth traffic flow. However, as traffic volume increases, the number of movements at LOS E and LOS F grows sharply, becoming dominant by 2050. This trend signifies that the existing intersection layout cannot handle future traffic demand efficiently and will experience severe congestion and unstable operations without substantial improvements. This condition is illustrated in Fig. 7.

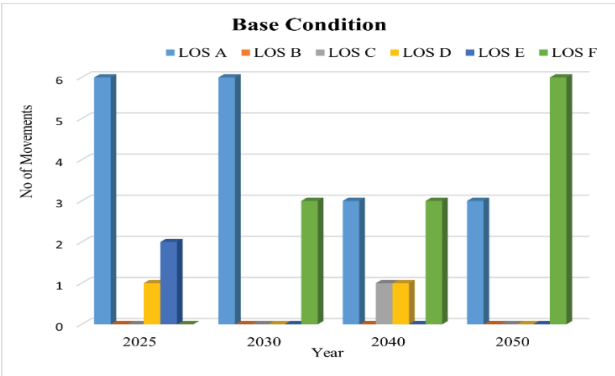


Fig. 7: Comparative analysis of scenarios with LOS under base condition

The Level of Service (LOS) results for the trumpet interchange scenario indicate a significant improvement in traffic performance compared to existing conditions. Up to 2030, all movements operate at LOS A, indicating free-flow conditions achieved through grade separation and reduced conflict points. Even by 2050, most movements still perform at LOS A-C, with only a few shifting to LOS E-F. This demonstrates that the trumpet interchange significantly enhances capacity, minimizes intersection delays, and sustains high operational efficiency over the forecast period. This condition is illustrated in Fig. 8.

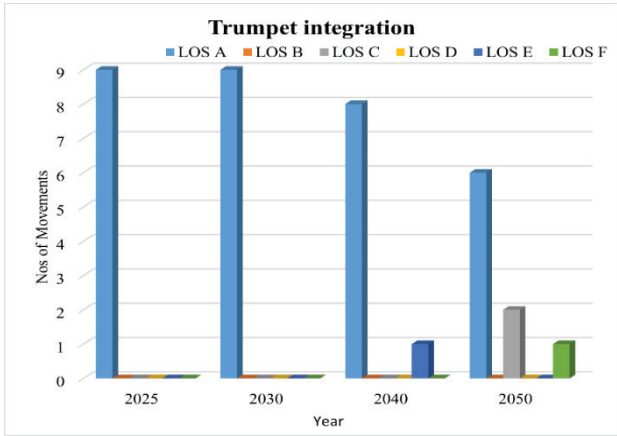


Fig. 8: Comparative analysis of scenarios with LOS under trumpet condition

The findings of this study are consistent with previous research on grade-separated intersections. Similar to earlier studies, the proposed trumpet interchange reduced traffic delays and improved traffic flow by eliminating at-grade conflict points [3], [4], [14], [15]. These findings also support the effectiveness of grade-separated facilities in heterogeneous traffic conditions commonly found in developing countries [9]. Compared with previous studies in Bangladesh [6], [17], this study further evaluates the long-term operational performance of a trumpet interchange under projected traffic growth and a dedicated BRT lane.

5. CONCLUSION

This study investigated traffic congestion at the Shibbari intersection in Gazipur and evaluated the effectiveness of a proposed trumpet interchange under existing and future traffic conditions. Simulation results for the existing condition indicate a substantial increase in delays as traffic grows. By 2050, vehicle delays exceeded 1200 seconds, stop delays surpassed 1000 seconds, and queue delays on the Shimultoli approach reached 182.9 seconds, with occupancy rates above 90.

The trumpet interchange scenario showed improved performance by eliminating traffic conflict points through grade separation. In 2050, Shimultoli's queue delay was 21.66 seconds, and average speeds remained around 11.5 km/h, though stop delays and occupancy rates still increased beyond 80%. LOS remained at A to C levels, but signs of congestion were still present.

Overall, the findings indicate that the trumpet interchange provides a more sustainable long-term solution for mitigating congestion at the Shibbari intersection under projected traffic growth conditions. The study highlights the potential applicability of grade-separated interchange facilities in mixed and heterogeneous traffic environments commonly observed in developing countries such as Bangladesh. This study assessed the feasibility of the proposed trumpet interchange only from a traffic operational perspective. Construction cost, land acquisition, right-of-way requirements, and BRT-related implementation feasibility were beyond the scope of this study and should be considered in future research.

REFERENCES

[1] M. F. M. Zisan, M. A. A. Mamun, M. A. A. Khan, and M. I. Bhuyia, "Traffic Growth Rate Estimation along the Dhaka-Chittagong Highway: A Longitudinal Analysis Using Demand Elasticity Method," in Proceedings of International Conference on Civil Engineering Research & Innovations (ICCEI 2025), Rajshahi, Bangladesh, pp. 1-6, Dec. 12-14, 2025.

[2] F. Ahmed, "Dhaka-Ashulia elevated expressway's plans modified, project costs to rise," The Business Standard, March 7, 2024. https:// www.tbsnews.net/bangladesh /transport/dhaka-ashulia-elevated-expressways-plans-modified-project-costs-rise-805154. Accessed: Oct. 29, 2025.

[3] S. Akter, "Rationale for signal free urban arterial operation with grade separated U-loops in Dhaka City," M.Sc. thesis, BUET, 2019.

[4] D. J. F. Belleza et al., "Simulation-based analysis of flyover and traffic light in Jose Abad Santos Avenue–Sta. Rita–Guagua road intersection using PTV VISSIM as a basis for traffic condition improvement," Int. J. Sci. Res. Eng. Dev., vol. 6, no. 3, pp. 978-993, 2023.

[5] R. Cervero and A. Golub, "Informal public transport: A global perspective," in H. T. Dimitriou and R. Gakenheimer (eds.), Urban Transport in the Developing World: A Handbook of Policy and Practice, Cheltenham: Edward Elgar, 2011, pp. 488-518.

[6] T. R. Chowdhury, "Investigation of road intersection operation using micro-simulation technique," M.S. thesis, BUET, 2019.

[7] Florida Department of Transportation (FDOT), "Traffic Analysis-Calibration and Validation Guidelines," 2024. [Online]. Available: https:// www.fdot.gov/. Accessed: Oct. 29, 2025.

[8] N. Gerges, "Types of interchanges and at-grade intersections (Issue 877)," Ministry of Transport, Cairo, 2010.

[9] M. Hadiuzzaman, M. Rahman, and M. A. Karim, "Saturation flow model at signalized intersection for non-lane-based traffic," Can. J. Transp., vol. 2, no. 1, pp. 77-90, 2008.

[10] M. K. Hossain, M. T. Ahmed, and M. R. Islam, "Vehicle characteristics and roadway level of service of industrial zone: A typical example of Gazipur Chowrasta intersection," DUET J., vol. 61, no. 2, 2019.

[11] Indian Roads Congress (IRC), Guidelines for the Design of Interchanges in Urban Areas (IRC:92-2017), New Delhi, India, 2017.

[12] Indian Roads Congress (IRC), Geometric Design Standards for Urban Roads and Streets (IRC: 86-2018), New Delhi, India, 2018.

[13] A.-A. Kafy et al., "Estimating traffic volume to identify the level of service in major intersections of Rajshahi, Bangladesh," Trends Civil Eng. & Architecture, vol. 2, no. 4, 2018.

[14] A. Maji, A. K. Maurya, S. Nama, and P. K. Sahu, "Performance-based intersection layout under a flyover for heterogeneous traffic," J. Modern Transp., vol. 23, no. 2, pp. 119-129, 2015.

[15] M. S. Mamun, S. Mohammad, M. A. Haque, and M. Y. A. Riyad, "Performance evaluation of Mohakhali flyover by using VISSIM simulation software," in Proc. 3rd Int. Conf. Advances in Civil

Engineering, pp. 21-23, Dec. 2016.

[16] M. S. Mashrur, "Modeling bus priority with intermittent bus lane for local traffic conditions," M.S. thesis, BUET, 2018.

[17] U. Saha, M. F. Islam, and M. N. Neema, "A microsimulation-based approach to investigate intersection performance: A case study on Bhulta intersection of Dhaka," in Proc. Int. Conf. Eng. Research and Practice (ICERP), 2019.

[18] M. S. Bin Siraj, M. Farjana, M. Billah, M. Hasan, and M. T. Azid, "Impact of traffic congestion in roundabout: A study on Gazipur Chowrasta," in Proc. Int. Conf. Planning, Architecture and Civil Engineering, Rajshahi, Bangladesh, pp. 306-311, Oct. 2023.

[19] Roads and Highways Department (RHD), Pavement Design Guide, Roads and Highways Department, Ministry of Communications, Government of the People's Republic of Bangladesh, Dhaka, Bangladesh, Apr. 2005.

[20] Florida Department of Transportation (FDOT), Traffic Analysis-Calibration and Validation Guidelines, Florida Department of Transportation, Tallahassee, FL, USA, 2024. Available: https://www.fdot.gov/. Accessed: Oct. 29, 2025.

Damage Assessment and Residual Capacity of Fire-Exposed RC Columns: A Multi-Parameter 3D FEA Study

Md. Sadman Sakib Khan[1], Md. Ashikuzzaman[2], Syed Samsudduha Bijoy[3*], Md. Shariar Hossain[4], Mahiman Zinnurain[3] and Shameem Ahmed[5]

[1]DC Office, Nilphamari, Bangladesh
[2]Bakhrabad Gas Distribution Company Limited, Dhaka, Bangladesh
[3] Department of Civil Engineering, Dhaka University of Engineering & Technology, Gazipur, Bangladesh
[4]Public Works Department, Dhaka Bangladesh
[5]Department of Civil Engineering, Bangladesh University of Engineering and Technology, Bangladesh

ABSTRACT

Fire is one of the most critical hazards to reinforced concrete (RC) structures, particularly threatening the load-carrying capacity of columns, the primary structural members. The primary objective of this study is to evaluate the residual axial load-carrying capacity and damage behaviour of RC columns under standard fire exposure by simultaneously investigating the combined effects of concrete cover thickness, fire exposure configuration, longitudinal reinforcement ratio, and fire duration. To achieve this objective, a three-dimensional nonlinear finite element model is developed using ABAQUS, incorporating the Concrete Damage Plasticity (CDP) constitutive model within a sequential thermal-mechanical analysis framework. Fire loading is applied according to the ISO 834 standard fire curve at 60, 120, and 180 minutes, representing short, moderate, and prolonged fire exposure conditions, respectively. The model is validated against the experimental data of Abdulraheem and Kadhum for concentrically loaded fire-exposed RC columns, achieving less than 5% error in peak load prediction and a maximum rebar-level temperature deviation of 8.3%, confirming model fidelity for parametric application. Results demonstrate that the 50 mm cover column maintains rebar temperatures approximately 120°C lower than those of the 37.5 mm cover column throughout all fire durations, while retaining 12% higher axial capacity at 180 minutes. Compression damage consistently concentrates in the inner core, while tension damage manifests at the outer surface; both modes are more severe at lower cover thickness. Four-sided fire exposure results in approximately 10% greater capacity loss than two-sided exposure at 180 minutes, confirming that the column enclosure provides quantifiable structural fire protection. A reinforcement ratio of 1.5% is identified as a practical fire-resilience threshold, beyond which additional reinforcement yields negligible capacity improvement. The validated parametric results provide a reliable computational basis for post-fire structural assessment of RC columns.

Keywords: Reinforced concrete column, Fire exposure, Finite element analysis, Concrete damage plasticity, Residual capacity

1. INTRODUCTION

Fire represents one of the most severe structural hazards to RC buildings, with RC columns being particularly critical because their failure under fire loading can trigger progressive collapse of the entire structure [1,2]. Exposure to elevated temperatures leads to simultaneous degradation of both concrete compressive strength and steel yield strength, significantly reducing the load-carrying capacity of columns [3,4].

Extensive numerical and experimental investigations have been conducted on the fire behavior of RC members. Early studies by [5] and [6] examined fire-exposed RC columns using simplified analytical models. [7] established fundamental principles of structural fire engineering design. The role of concrete cover in protecting steel reinforcement from heat penetration has been documented as a decisive factor [8]. More recently, [9] conducted a parametric ABAQUS-based study on residual compressive strength of RC columns,

*Corresponding author's email: samsudduhabijoy@gmail.com

[10] investigated post-fire behavior and repair of fire-damaged RC columns, [11] demonstrated the reliability of sequential thermal-mechanical FEA for fire-exposed RC members, and a recent review [12] confirmed that cover thickness and reinforcement ratio govern column fire resistance. Parametric studies of RC columns under Eurocode fire models have also been reported [13]. However, most existing studies address only one or two parameters at a time and typically assume uniform four-sided fire exposure. This condition does not represent corner or wall-adjacent columns in real buildings.

Despite these contributions, three notable gaps remain in the literature. First, most numerical studies on RC column fire resistance assume uniform four-sided fire exposure. This does not represent the realistic condition of corner or wall-adjacent columns that face fire from only two sides. Second, no previous study has simultaneously evaluated the combined effects of concrete cover thickness, fire exposure configuration, and longitudinal reinforcement ratio within a single validated three-dimensional CDP-based FEA framework for RC columns. Third, residual capacity values in the literature are rarely presented as normalized capacity ratios directly usable for post-fire structural assessment. The primary objective of this study is therefore to evaluate the residual axial load-carrying capacity and damage behavior of RC columns under ISO 834 standard fire exposure by simultaneously investigating concrete cover thickness (37.5 mm and 50 mm), fire exposure configuration (two-sided and four-sided), longitudinal reinforcement ratio (1%, 1.5%, and 2%), and fire duration (60, 120, and 180 minutes) within a single validated three-dimensional FEA framework incorporating the CDP model.

2. METHODOLOGY

A three-dimensional finite element model of an RC column was developed using ABAQUS to investigate the structural behavior under fire exposure. The numerical procedure was divided into model development, thermal analysis, validation, and parametric investigation stages.

The concrete component was modeled using the Concrete Damage Plasticity (CDP) constitutive model, which is widely used for nonlinear simulations of concrete cracking and crushing behavior. The CDP parameters were selected according to the procedure proposed by [7]. All material properties were defined as temperature-dependent functions. Thermal properties of concrete, including specific heat capacity and thermal conductivity as functions of temperature, were adopted from Eurocode 1 (EN 1991-1-2, 2002). The mechanical properties of concrete, compressive strength and modulus of elasticity as functions of temperature, and all thermal and mechanical properties of reinforcing steel were defined according to Eurocode 2 (EN 1992-1-2, 2004). Concrete density was taken as 2400 kg/m³ and steel density as 7850 kg/m³, both assumed constant with temperature. Reinforcing steel bars were embedded within the concrete body to represent composite action between concrete and steel.

Table I: Material Properties and Model Parameters

Parameter	Value	Reference
Column length	3048 mm	This study
Cross-section	508 mm × 508 mm	This study
Cross-section (reference)	254 mm × 254 mm	[7]
CDP dilation angle	30°	[7]
CDP eccentricity	0.1	Default (ABAQUS)
CDP viscosity	0.00025	[7]
Concrete tensile strength	10% of f_{ck}	[7]

The geometry of the reference column was defined with a square cross-section of 254 mm × 254 mm and a total height of 3048 mm. Appropriate material properties, section details, and reinforcement arrangements were assigned before meshing and analysis. The assembled model was discretized into finite elements suitable for coupled thermal and structural simulation. Table I: Material Properties and CDP Model Parameters Used in FEA.

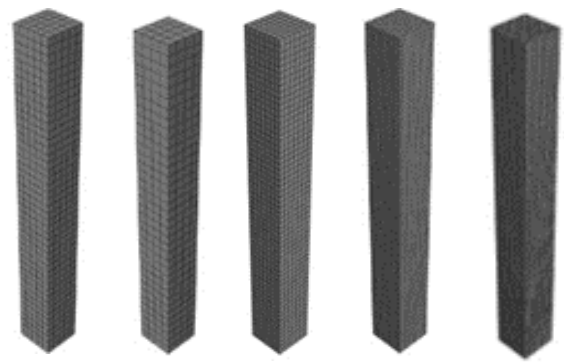


Fig. 1: Five mesh configurations (element sizes 25, 20, 15, 10, and 5 mm) evaluated in the mesh sensitivity study

The mesh convergence study showed that axial displacement varied by less than 1% between the 10 mm and 5 mm element sizes, confirming that the 10 mm mesh provides a mesh-independent solution. This mesh was therefore adopted for the validation model, while a 25 mm mesh was used for the parametric study columns to balance computational efficiency with accuracy. During the thermal analysis phase, the exposed surfaces of the column were subjected to elevated temperatures following the ISO 834 standard fire curve. Heat transfer was simulated by conduction within the solid body and convection-radiation at the exposed boundaries, with a convective heat transfer coefficient of 25 W/m²K on exposed surfaces and 9 W/m²K on unexposed surfaces. Emissivity values of 1.0 (fire) and 0.8 (concrete surface) were adopted per Eurocode 1. Fire exposure durations of 60, 120, and 180 minutes were applied.

After completion of the thermal step, the obtained temperature field was transferred to the structural analysis stage. Axial loading was then applied to determine the residual load-carrying capacity, deformation response, and damage pattern of the heated column. Compression damage, tensile cracking, and load–deflection behavior were extracted from the numerical results.

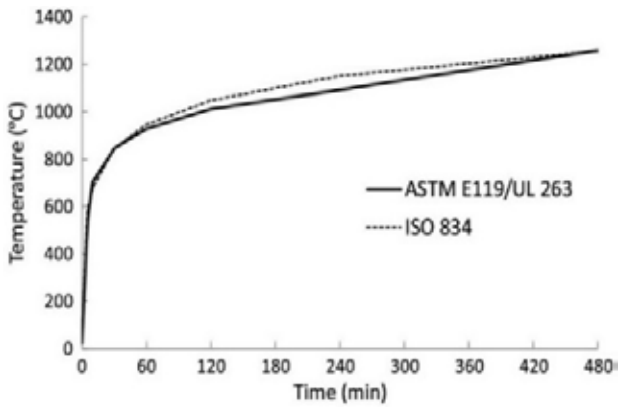


Fig. 2: ISO 834 and ASTM E119/UL 263 standard fire time-temperature curves, ISO 834 adopted in this study for all fire exposure simulations

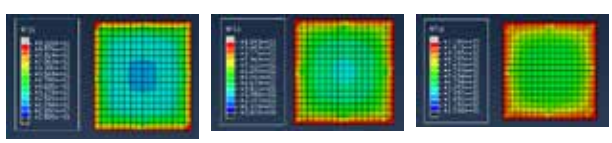
The developed model was validated against the experimental results reported by [1] for concentrically loaded fire-exposed reinforced concrete columns. The FEA-predicted peak axial load differed from the experimental value by less than 5%, and temperature predictions at the rebar level showed a maximum deviation of 8.3% relative to the published thermocouple readings. These quantitative metrics confirm that the developed model accurately represents the thermo-mechanical behavior of fire-exposed RC columns and is suitable for parametric application.

Following validation, a parametric study was conducted by systematically varying key design parameters of the reference column. The investigated parameters included cross-sectional size, reinforcement ratio, clear cover thickness, and fire exposure condition. Two-sided and four-sided fire exposures were considered to represent practical fire scenarios. It should be noted that concrete spalling was not explicitly modelled in this study. This simplification is conservative, as it assumes the concrete section remains intact throughout the fire duration. The effect of spalling on thermal penetration and structural capacity is acknowledged as a limitation and is recommended for inclusion in future extensions of this work.

3. RESULTS

3.1 Effect of Concrete Cover on Thermal and Structural Response

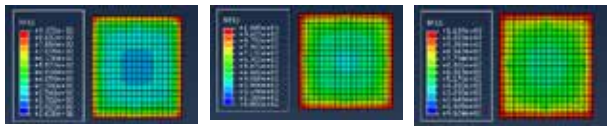
Figures 3 and 4 present the temperature distribution contours across the column cross-section at 60, 120, and 180 minutes for the 37.5 mm and 50 mm clear cover columns, respectively. In both cases, the outer surface of the column achieves the highest temperature immediately upon fire exposure. The heat progressively penetrates the cross-section as fire duration increases. The ABAQUS NT11 nodal temperature output shows a clearly progressive, non-uniform thermal gradient developing from the outer surface toward the inner core with increasing fire duration for both covers. For the 37.5 mm cover column, the temperature contours show a thermal front toward the rebar zone by 120 minutes, with the innermost concrete layer showing temperatures approximately 400°C at 180 minutes. In contrast, the 50 mm cover column demonstrates a measurably less thermal gradient across the cover layer, with the rebar zone temperature remaining below that of the 37.5 mm cover column. This visual comparison confirms that the additional 12.5 mm of concrete in the 50 mm cover column provides a meaningful supplementary thermal barrier.



a b c

Fig. 3: ABAQUS NT11 nodal temperature contours (°C) for 37.5 mm clear cover column under four-sided ISO 834 fire exposure at (a) 60 min, (b) 120 min, and (c) 180 min

Figure 5 quantifies this difference by plotting rebar temperature vs fire duration for both cover configurations. The rebar temperature in the 37.5 mm cover column rises from approximately 350°C at 60 minutes to nearly 780°C at 180 minutes, following a progressive non-linear growth trajectory



a b c

Fig. 4: ABAQUS NT11 nodal temperature contours (°C) for 50 mm clear cover column under four-sided ISO 834 fire exposure at (a) 60 min, (b) 120 min, and (c) 180 min.

Figure 5 shows rebar temperature for 37.5 mm and 50 mm cover. In the 50 mm cover column, rebar temperatures are approximately 120°C lower throughout the entire fire duration, reaching approximately 660°C at 180 minutes. This indicates that the 37.5 mm cover column enters the critical steel degradation regime earlier and sustains more severe strength loss over the same fire duration. Figure 6 presents the load-carrying capacity ratio (P/Po) for both cover columns at 60, 120, and 180 minutes. At 60 minutes, both columns retain comparable capacity, with the 37.5 mm and 50 mm cover columns achieving P/Po values of approximately 0.70 and 0.71, respectively. As fire duration increases, the capacity gap between the two cover configurations widens progressively. At 120 minutes, the 37.5 mm and 50 mm cover columns retain approximately 52% and 55%, respectively. At 180 minutes, the divergence is most pronounced. The 37.5 mm cover column capacity falls to approximately 41% while the 50 mm cover column retains approximately 46%, representing a P/Po advantage of 0.05 for the thicker cover, equivalent to approximately 12% higher retained capacity relative to the 37.5 mm cover column. This escalating benefit with fire duration confirms that concrete cover thickness becomes increasingly decisive as a structural fire protection parameter beyond 60 minutes of exposure.

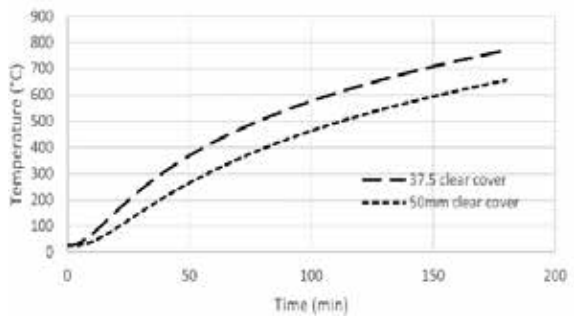


Fig. 5: Rebar temperature development vs fire duration for 37.5 mm and 50 mm clear cover columns

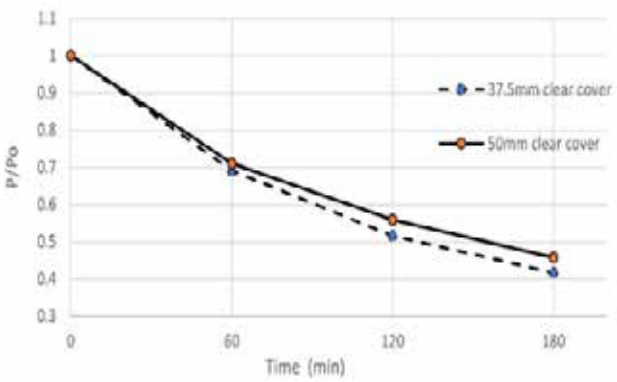


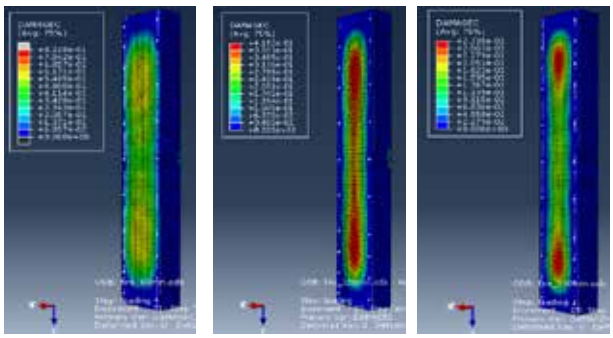
Fig. 6: Load-carrying capacity ratio (P/Po) vs fire duration for 37.5 mm and 50 mm clear cover columns

3.2 Compression and Tension Damage Patterns

DAMAGET and DAMAGEC contour values displayed in Figures 7 through 10 represent element-level output averaged at shared nodes following extrapolation from integration points, as performed by ABAQUS. Values marginally exceeding 1.0 in some contour plots result from this nodal averaging extrapolation procedure and do not indicate violation of the physical 0-to-1 bound of the scalar damage variable within the constitutive model. Figures 7 through 10 present the compression (DAMAGEC) and tension (DAMAGET) damage contours from the CDP model for both cover configurations at 60, 120, and 180 minutes of fire exposure.

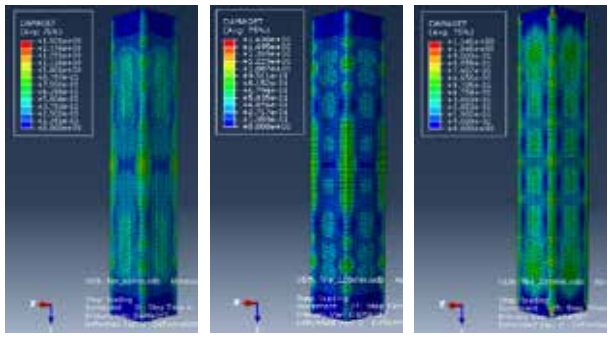
For the 37.5 mm clear cover column at 60, 120, and 180 minutes, compression damage consistently concentrates in Figure 7 within the inner core at mid-height, with maximum DAMAGEC indices of 0.8228, 0.4182, and 0.2735, respectively, for 3 different time durations. The damaged core zone expands progressively along the full column height, reflecting a redistribution of compressive stress across a wider volume. Tension damage in Figure 8 exhibits fundamentally different characteristics, manifesting exclusively at the outer surface of the column rather than the core. Maximum DAMAGET values of 1.5010, 1.6300, and 1.1410 for 3 different time durations confirm progressive surface cracking driven by thermal strain incompatibility between the hot exposed surface and the cooler interior.

For the 50 mm clear cover column, compression damage (Figure 9) follows the same inner core concentration pattern observed in Figure 7, with maximum DAMAGEC indices of 0.7459, 0.5236, and 0.2148 consistently lower than those for the 37.5 mm



a b c

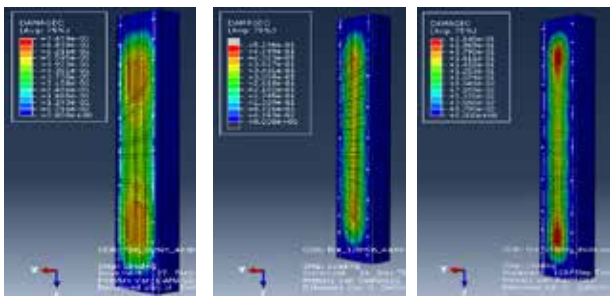
Fig. 7: ABAQUS DAMAGEC contours for 37.5 mm clear cover column under four-sided ISO 834 fire at (a) 60 min (max 0.8228), (b) 120 min (max 0.4182), and (c) 180 min (max 0.2735)



a b c

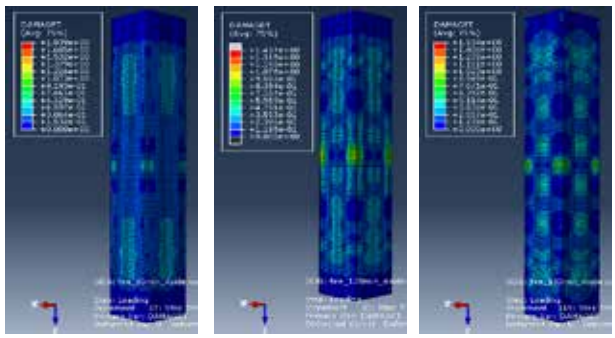
Fig. 8: ABAQUS DAMAGET contours for 37.5 mm clear cover column under four-sided ISO 834 fire at (a) 60 min (max 1.5010), (b) 120 min (max 1.6300), and (c) 180 min (max 1.1410

cover, directly reflecting the lower core temperatures and delayed thermal penetration afforded by the thicker cover. Similarly, tension damage in Figure 10 shows reduced severity, with maximum DAMAGET values of 1.8390, 1.4370, and 1.5340, rather than the continuous cracking pattern observed in Figure 8, indicating that the gentler thermal gradient across the 50 mm cover layer produces significantly lower surface cracking intensity across all fire durations.



a b c

Fig. 9: ABAQUS DAMAGEC contours for 50 mm clear cover column at (a) 60 min (max 0.7459), (b) 120 min (max 0.5236), and (c) 180 min (max 0.2148)

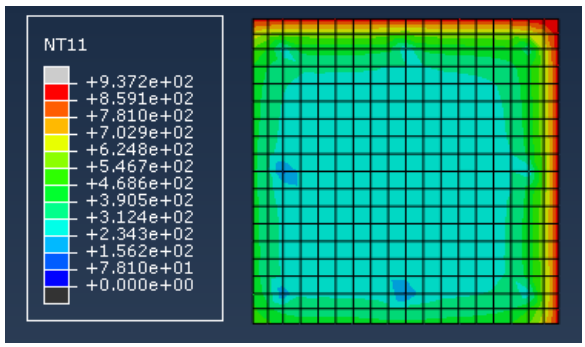


a b c

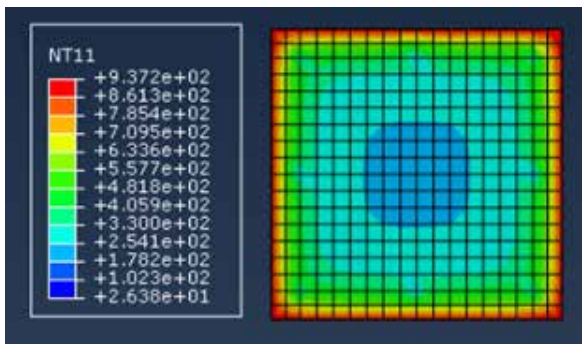
Fig. 10: ABAQUS DAMAGET contours for 50 mm clear cover column at (a) 60 min (max 1.8390), (b) 120 min (max 1.4370), and (c) 180 min (max 1.5340)

3.3 Effect of Fire Exposure Type Configuration

Figure 11 compares the cross-sectional temperature distribution under two-sided and four-sided fire exposure for the 50 mm clear cover column. Under two-sided exposure (Fig. 11a), the maximum surface temperature reaches 937°C at the two directly exposed faces, while the unexposed faces remain significantly cooler with 78°C



a



b

Fig. 11: ABAQUS NT11 cross-sectional temperature contours (°C) comparing (a) two adjacent side fire exposure and (b) four-sided fire exposure

temperatures. This strongly non-uniform thermal field results in differential rebar heating. Under four-sided

exposure (Fig. 11b), all faces simultaneously reach the maximum surface temperature of 937°C. The absence of any thermally protected rebar zone eliminates the compensating mechanism observed in the two-sided case.

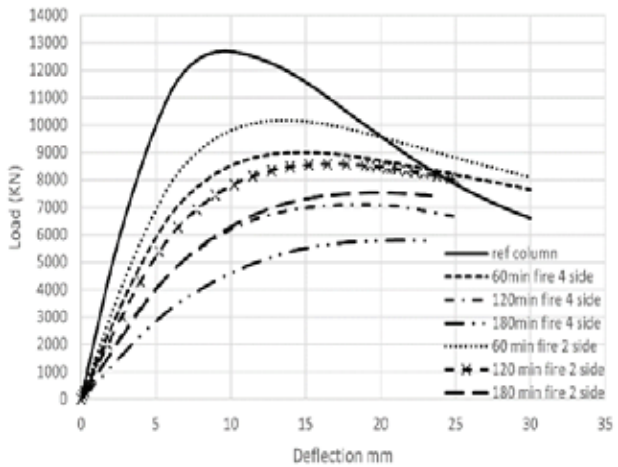


Fig. 12: Load vs deflection curves for 50 mm clear cover column under two-sided and four-sided ISO 834 fire exposure at 60, 120, and 180 minutes

Figure 12 quantifies the structural consequence of this thermal difference through load-deflection curves for both exposure configurations at 60, 120, and 180 minutes. The reference column (50 mm cover column) achieves a peak load of approximately 12,800 kN. Under two-sided exposure, peak loads of approximately 10,800 kN, 9,400 kN, and 7,800 kN are recorded at 60, 120, and 180 minutes, respectively. These represent capacity retentions of approximately 84%, 73%, and 61%, respectively. Under four-sided exposure, the corresponding peak loads of approximately 10,200 kN, 8,200 kN, and 6,500 kN yield capacity retentions of approximately 80%, 64%, and 51% at 180 minutes.

The four-sided exposure column, therefore, loses approximately 10% more capacity than the two-sided exposure column. The post-peak descent is also notably steeper for four-sided exposure at longer durations, indicating more brittle post-fire failure behavior as a consequence of uniform reinforcement degradation across the entire section.

3.4 Effect of Reinforcement Ratio

Three reinforcement ratios were investigated using a 508 mm × 508 mm (20”×20”) column cross-section of 3048 mm height. Table II describes the three configurations as C21, C22, and C23, all sharing identical geometry and fire exposure conditions to isolate the effect of steel content on post-fire structural performance.

Table II: Different Reinforcement Ratios

Identification	Size	Reinforcement Ratio	Rebars
C21	20″×20″	2%	8 - #9
C22	20″×20″	1.5%	8 - #8
C23	20″×20″	1%	8 - #7

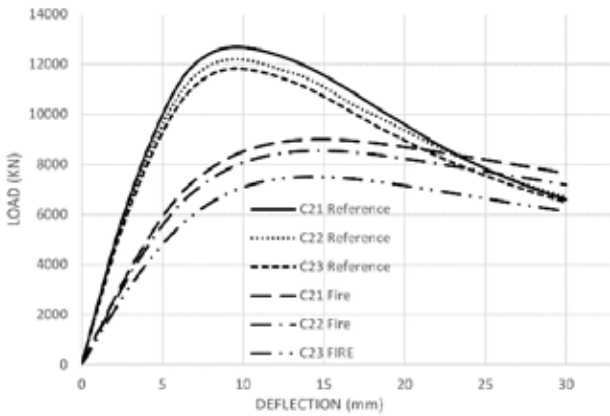


Fig. 13: Load vs deflection curves for columns C21 (2%), C22 (1.5%), and C23 (1%) under ambient reference and post-fire loading conditions

Figure 13 presents the load-deflection response for all three columns under both reference and post-fire loading conditions. Under ambient conditions, reference peak loads of approximately 12,700 kN, 12,200 kN, and 11,600 kN are recorded for C21, C22, and C23, respectively. After fire exposure, all three columns exhibit substantial capacity reduction, with post-fire peak loads of approximately 8,900 kN, 7,600 kN, and 6,500 kN for C21, C22, and C23, respectively. The post-peak descent becomes progressively steeper with decreasing reinforcement ratio, indicating more brittle post-fire failure behavior in columns.

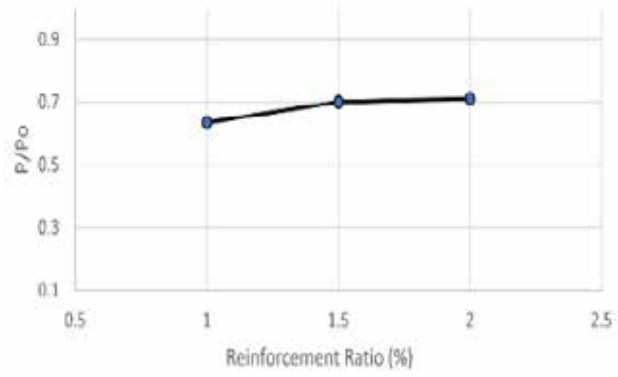


Fig. 14: Capacity Ratio for different reinforcement ratios

4. CONCLUSION

This study presented a validated three-dimensional sequential thermo-mechanical FEA model developed in ABAQUS incorporating the Concrete Damage Plasticity (CDP) model to investigate the thermal response, damage behavior, and residual axial capacity of RC columns under ISO 834 standard fire exposure. The following conclusions are drawn:

1. The validated FEA model accurately predicted both temperature distribution and load-deflection response, with less than 5% error in peak load and a maximum rebar-level temperature deviation of 8.3% compared to experimental data [1], confirming its reliability for parametric application.
2. Column residual capacity degrades progressively with fire duration, with the rate of degradation accelerating significantly beyond 60 minutes of fire exposure.
3. The 50 mm cover column maintains rebar temperatures approximately 120°C lower than the 37.5 mm cover column, resulting in a P/Po advantage growing from 0.01 at 60 minutes to 0.05 at 180 minutes, equivalent to approximately 12% higher retained capacity.
4. Four-sided fire exposure causes approximately 10% greater capacity loss than two-sided exposure at 180 minutes, confirming that wall enclosure of columns provides quantifiable structural fire protection.
5. Compression damage concentrates in the inner core while tension damage manifests at the outer surface; both modes are more severe at lower cover thickness and longer fire duration.
6. A reinforcement ratio of 1.5% is identified as a practical fire-resilience threshold, beyond which additional reinforcement yields negligible capacity improvement.

Future work should incorporate concrete spalling, the post-fire cooling phase, and eccentric loading of the model.

ACKNOWLEDGEMENT

The authors express their gratitude to Almighty Allah for the completion of this work. We extend our sincere appreciation to the Department of Civil Engineering at Bangladesh University of Engineering and Technology (BUET).

REFERENCES

[1] M. S. Abdulraheem and M. M. Kadhum, "Experimental and numerical study on post-fire behaviour of concentrically loaded reinforced reactive powder concrete columns," *Construction and Building Materials*, vol. 168, pp. 877–892, 2018, doi: 10.1016/j.conbuildmat.2018.02.123.

[2] C. Bailey, "Holistic behaviour of concrete buildings in fire," *Structures and Buildings*, vol. 152, no. 3, pp. 199–212, 2002, doi: 10.1680/stbu.152.3.199.38988.

[3] A. F. Bingöl and R. Gül, "Residual bond strength between steel bars and concrete after elevated temperatures," *Fire Safety Journal*, vol. 44, no. 6, pp. 854–859, 2009, doi: 10.1016/j.firesaf.2009.04.001.

[4] A. H. Buchanan and A. K. Abu, *Structural Design for Fire Safety*, 2nd ed. 2016, pp. 1–415, doi: 10.1002/9781118700402.

[5] N. M. Fawzi, M. S. Essa, and M. M. Kadhum, "Behaviour of fire exposed reinforced concrete columns," *Journal of Engineering*, vol. 17, no. 3, pp. 412–429, 2011, doi: 10.31026/j.eng.2011.03.05.

[6] I. A. Fletcher, S. Welch, J. L. Torero, R. O. Carvel, and A. Usmani, "Behaviour of concrete structures in fire," *Thermal Science*, vol. 11, no. 2, pp. 37–52, 2007, doi: 10.2298/TSCI0702037F.

[7] M. Hafezolghorani, F. Hejazi, R. Vaghei, M. S. B. Jaafar, and K. Karimzade, "Simplified damage plasticity model for concrete," *Structural Engineering International*, vol. 27, no. 1, pp. 68–78, 2017, doi: 10.2749/101686616X1081.

[8] G. A. Khoury, "Effect of fire on concrete and concrete structures," *Progress in Structural Engineering and Materials*, vol. 2, no. 4, pp. 429–447, 2000, doi: 10.1002/pse.51.

[9] B. Ellingwood and T. D. Lin, "Flexure and shear behavior of concrete beams during fires," Journal of Structural Engineering, vol. 117, no. 2, pp. 440–458, Feb. 1991.

[10] S. Mirzabagheri and O. Salem, "Parametric study on the residual compressive strength of RC columns subjected to different standard fire durations and load ratios," *Journal of Structural Fire Engineering*, vol. 14, no. 3, pp. 344–364, 2023, doi: 10.1108/JSFE-04-2022-0017.

[11] A. R. Belakhdar, M. S. Dimia, M. Baghdadi, M. Bouderradji, S. Gherabli, and N. Alaoui, "Post-fire behavior and repair of fire-damaged RC columns us-

ing composite jackets," *Annales de Chimie - Science des Matériaux*, vol. 47, no. 4, pp. 247–257, 2023, doi: 10.18280/acsm.470407.

[12] A. Suhaimi, I. S. Ibrahim, and M. A. Ab Kadir, "The effects of pre-loading on structural behavior of reinforced concrete beams under fire condition: A review," *Journal of Structural Fire Engineering*, 2024, doi: 10.1108/JSFE-11-2023-0041.

[13] C. Liu, X. Wu, and J. Du, "Fire resistance of steel-reinforced concrete columns: A review of ordinary concrete to ultra-high performance concrete," *Buildings*, vol. 16, no. 1, Art. no. 24, 2025, doi: 10.3390/buildings16010024.

[14] M. Baghdadi, M. S. Dimia, and D. Baghdadi, "A parametric study of fire-damaged reinforced concrete columns under lateral loads," *Engineering, Technology & Applied Science Research*, vol. 12, no. 5, pp. 9113–9119, 2022, doi: 10.48084/etasr.5172.

GIS-Based Spatial Analysis and Identification of Road Traffic Accident Hotspots: A Case Study of the Dhaka-Mymensingh Highway (N3), Gazipur, Bangladesh

Md Ibrahim Khalil*, Pias pal, Shariful Islam, Mahiman Zinnurain, Mohammad Kabir Hossain and Hriday Chandra Bhoumik

Department of Civil Engineering, Dhaka University of Engineering & Technology, Gazipur, Bangladesh

ABSTRACT

Road traffic accidents are a major public safety concern in Bangladesh, especially along national highways carrying heavy and mixed traffic. The Tongi-Mawna segment of the Dhaka-Mymensingh Highway is one of the most critical corridors in Gazipur, where frequent crashes cause serious human and economic losses. However, limited studies have examined this corridor using recent police-based data with integrated temporal and GIS-based spatial analysis. This study aims to identify and analyze accident-prone locations along the Tongi-Mawna road using geospatial and statistical techniques. Accident records from 2021 to 2025 were collected from nearby police stations. Temporal trend analysis was carried out using Microsoft Excel, while Severity Index (SI), Kernel Density Estimation (KDE), and Getis-Ord Gi* hotspot analysis were applied in ArcGIS to assess accident severity, spatial concentration, and clustering patterns. A total of 304 accidents were recorded during the study period, affecting 335 individuals, including 227 fatalities, 80 serious injuries, and 28 minor injuries. The results show that accident occurrence increased in recent years, with 2025 recording the highest number of crashes. Trucks were the most involved vehicle type, while buses and three-wheelers also showed notable involvement. Male victims accounted for the highest proportion across fatal and injury categories. The SI analysis identified 12 black spots out of 31 accident-prone locations, while KDE and hotspot analyses revealed major accident concentrations in the southern, central, and northern sections of the corridor. The findings indicate that accidents along the Tongi-Mawna road are spatially concentrated and severe in nature. These findings provide valuable information for prioritizing road safety interventions, supporting transportation planning, and implementing targeted measures to reduce crash frequency and severity along the Tongi-Mawna corridor.

Keywords: GIS Analysis, Accident Hotspots, Severity Index, Kernel Density Estimation, Getis-Ord Gi*

1. INTRODUCTION

Road traffic accidents (RTAs) are a major global public health concern, causing significant loss of life and economic burden worldwide. According to the World Health Organization, approximately 1.3 million people die annually due to road traffic accidents, making it one of the leading causes of death globally [1]. The impact is particularly severe in low and middle-income countries, where rapid motorization is not adequately supported by road infrastructure and safety measures [2]. In the Asian region, road traffic accidents remain a critical challenge due to high population density, rapid urbanization, and heterogeneous traffic conditions. Studies have indicated that accident occurrences in Asia are significantly influenced by unsafe driving behavior, poor roadway design, and weak enforcement of traffic regulations [3]. The increasing demand for transportation and industrial development has further intensified accident risks across major highway corridors in this region. In Bangladesh, the situation is more alarming due to mixed traffic flow, lack of traffic discipline, and insufficient road safety management. National highways, especially those passing through industrial zones, are highly vulnerable to accident occurrence [4]. Research has shown that factors such as overspeeding, improper overtaking, roadside activities, and inadequate pedestrian facilities play a significant role in accident causation [5].

Previous studies have demonstrated that road traffic accidents are not randomly distributed but tend to cluster in specific locations due to roadway geometry, traffic composition, and human behavior [6]. To address this issue, Geographic Information System (GIS) has been widely adopted as an effective tool for analyzing accident data, as it enables the integration of spatial and

*Corresponding author's email: mdibrahimkhalil808@gmail.com

non-spatial information and facilitates visualization of accident patterns [7]. GIS-based techniques support the identification of accident-prone locations and provide a strong basis for traffic safety planning and decision-making. Several spatial analysis methods have been applied in accident studies to identify hotspots and analyze accident distribution. Kernel Density Estimation (KDE) is commonly used to generate density surfaces and identify areas with high accident concentration [8]. Similarly, hotspot analysis using the Getis-Ord Gi* statistic has been widely applied to detect statistically significant clusters of accident occurrences [9]. Studies such as Afolayan et al. [7] and Khatun et al. [5] demonstrated the effectiveness of GIS-based hotspot identification in detecting high-risk locations and supporting safety improvement measures. Furthermore, severity-based approaches, such as the Severity Index (SI), have been used to rank accident-prone locations based on fatalities and injuries [5]. In addition to spatial analysis, temporal analysis plays an important role in understanding accident trends over time. Statistical tools such as Microsoft Excel have been widely used to analyze yearly variations in accident frequency, severity, and vehicle involvement [8]. Such trend analysis helps in identifying increasing or decreasing patterns of accidents and provides valuable insights into the effectiveness of safety interventions.

Despite the application of these advanced techniques in different regions, limited studies have focused on the Tongi-Mawna segment of the Dhaka-Mymensingh Highway using recent accident data along with combined spatial and temporal analysis. Considering the strategic importance of this highway and its exposure to high traffic demand, a comprehensive analysis integrating both GIS-based spatial methods and statistical trend analysis is essential. Therefore, the objective of this study is to analyze the spatial distribution, temporal trends, and severity of road traffic accidents along the Tongi-Mawna segment using GIS and statistical techniques. The study integrates Kernel Density Estimation, hotspot analysis, and Severity Index methods along with trend analysis to identify high-risk locations and provide insights to support effective road safety planning and improvement measures.

2. METHODOLOGY

2.1 Study Route

The Tongi-Mawna segment of the Dhaka–Mymensingh Highway (N3), shown in Figure 1, is located in Gazipur district under the Dhaka division of Bangladesh. This highway connects Tongi with Mawna and serves as a major transportation corridor linking Dhaka with the northern

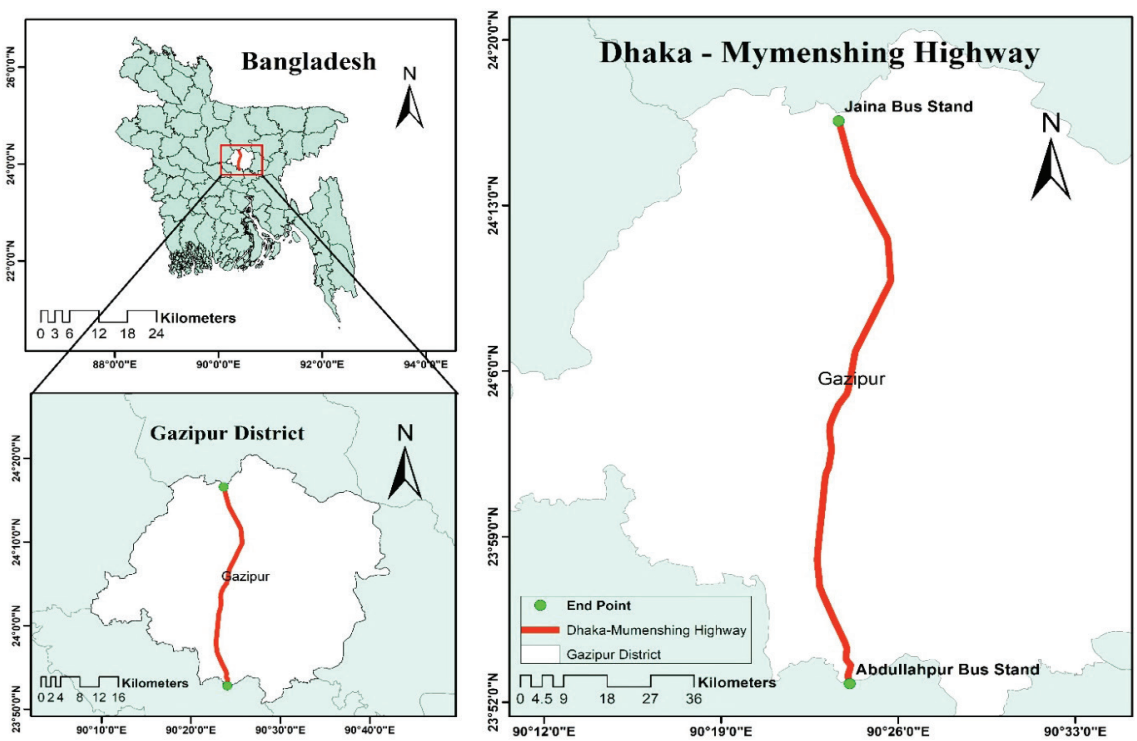


Fig. 1: Study area of the Tongi-Mawna segment of Dhaka-Mymensingh Highway (N3), Gazipur, Bangladesh.

regions of the country. The study route lies approximately between latitudes 23°52′N and 24°13′N and longitudes 90°19′E and 90°26′E, covering a length of about 40 km. The corridor is a multi-lane bituminous road that carries high traffic volume due to surrounding industrial zones, commercial activities, and regional connectivity.

2.2 Data Collection and Analysis

Accident data were collected from local police stations and highway police records for the Tongi-Mawna segment of the Dhaka-Mymensingh Highway (N3) covering the period from 2021 to 2025. A total of 304 accidents were analyzed, including 227 fatal, 80 serious injury, and 28 minor injury cases. The dataset contains information on vehicle type, number of deaths, injury severity, date and time of the collision, and crash location (latitude and longitude).

Accident locations were georeferenced using Google Earth Pro and imported into ArcGIS 10.8 for spatial analysis. Temporal trend analysis was performed using Excel, while spatial analysis was conducted in GIS to identify accident distribution patterns. Kernel Density Estimation (KDE) and hotspot analysis (Getis-Ord Gi*) were applied to identify high-risk zones, and the Severity Index (SI) method was used to assess accident severity.

2.2.1 Severity Index (SI)

The Severity Index (SI) was used to evaluate the severity of road traffic accidents and to identify accident-prone locations. Since accident frequency alone may not adequately represent the actual impact of crashes, weighted indices are commonly applied to provide a more reliable assessment [10]. In this method, different weights are assigned to accident outcomes based on their level of severity. A weighting scheme of 5, 3, and 1 was used for fatal, serious injury, and minor injury cases, respectively, as widely adopted in previous studies [11]. The Severity Index is calculated as:

$$SI = 5D + 3S + L$$

where D represents the number of fatalities, S denotes serious injuries, and L indicates minor injuries. Based on previous studies and the observed distribution of SI values, locations with SI values greater than 40 were considered as accident black spots [11].

2.2.2 Kernel Density Estimation (KDE)

Kernel Density Estimation (KDE) was applied to analyze the spatial distribution of road traffic accidents and to identify areas with high accident concentration. KDE is a non-parametric method that converts discrete accident point data into a continuous density surface, allowing visualization of accident intensity across the study area [8]. The density at a given location is estimated using the following equation:

$$f(x,y) = \frac{1}{nh^2}\sum_{i=0}^{n} k\left(\frac{d_i}{h}\right)$$

where $f(x,y)$ represents the estimated density at location (x,y), n is the total number of observations, h is the bandwidth, d_i denotes the location of each accident point, and K is the kernel function [8]. In this study, a bandwidth of 4000 m and a cell size of 100 m were used to generate the density surface. Higher density values indicate greater accident concentration and represent potential high-risk zones.

2.2.3 Hotspot Analysis (Getis-Ord Gi*)

Hotspot analysis was conducted to determine the spatial clustering of road traffic accidents within the study area. This method identifies statistically significant clusters of high and low accident values using the Getis-Ord Gi* statistic [9]. The Gi* statistic evaluates the relationship between a location and its neighboring features to determine whether the observed clustering is statistically significant. High positive values indicate hotspots, while negative values indicate cold spots. Values close to zero represent random distribution patterns. The Getis-Ord Gi* statistic is expressed as:

$$G_i^* \frac{\sum_{j=1}^{n} w_{i,j}x_j - \bar{x}\sum_{j=1}^{n} w_{i,j}}{S\sqrt{\frac{[\sum_{j=1}^{n} w_{i,j}^2 - (\sum_{j=1}^{n} w_{i,j})^2]}{n-1}}}$$

where x_j is the attribute value at location j, $w_{i,j}$ is the spatial weight between locations i and j, n is the total number of features, $\bar{x}$ is the mean, and S is the standard deviation.

3. RESULTS AND DISCUSSION

3.1 Accident Trend Analysis

The analysis of accident data along the Tongi-Mawna road from 2021 to 2025 provides important insights into the temporal variation and severity distribution of road traffic accidents. Fig. 2 presents the yearly distribution of fatal, serious injury, and minor injury cases, while Fig. 3 illustrates the overall proportion of accident severity within the study corridor. During the study period, a total of 304 accidents were recorded, including 227

fatalities, 80 serious injuries, and 28 minor injuries. The results indicate that fatal accidents constitute a dominant proportion of total accident cases, reflecting the high severity of road traffic incidents along this route.

As shown in Fig. 2, the highest number of accidents was observed in 2025, whereas the lowest occurred in 2022. A noticeable increasing trend in accident frequency is observed from 2022 onwards, accompanied by a significant rise in both fatal and serious injury cases.

Fig. 3 further reveals that fatal accidents account for 68%, followed by serious injuries (24%) and minor injuries (8%). This distribution clearly indicates that a large proportion of accidents results in severe outcomes.

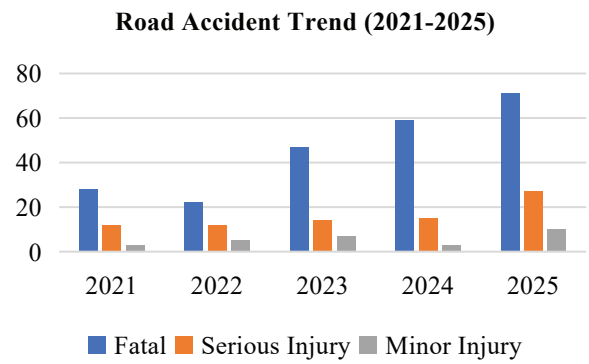


Fig. 2: Year-wise accident distribution (2021-2025)

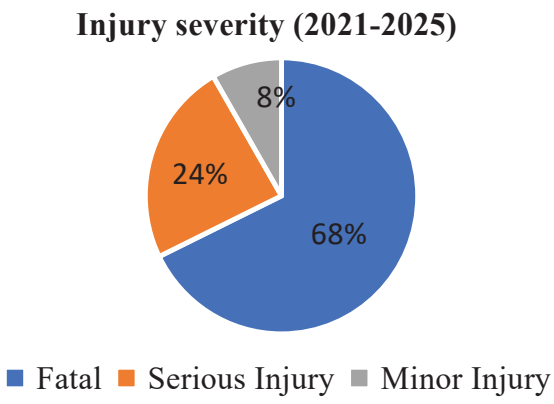


Fig. 3: Accident severity distribution (%)

3.1.1 Vehicle Involvement in Road Traffic Crashes

The involvement of different vehicle types in road traffic crashes (RTCs) was analyzed to identify the major contributors to accident occurrence along the Tongi-Mawna road. Table I presents the distribution of accidents by vehicle category. The results indicate that trucks account for the highest proportion of accidents (46.3%). Among other vehicle types, buses (20.9%) and three-wheelers (17.9%) also show significant involvement in accident occurrence. In contrast, other vehicle categories such as cars (5.0%), motorcycles (5.0%), CNG (2.5%), and private cars (1.0%) contribute comparatively lower proportions.

The high involvement of heavy vehicles, particularly trucks and buses, suggests their significant role in accident occurrence, which may be associated with traffic volume, speed variation, and mixed traffic conditions along the study corridor.

Table I: Distribution of accidents by vehicle type.

Category	Vehicular types	%
Vehicle factors	Truck	46.3
	Bus	20.9
	Three-wheeler	17.9
	Car	5.0
	Motorcycle	5.0
	CNG	2.5
	Private Car	1.0

3.1.2 Severity and Consequences of Road Traffic Crashes

The severity of road traffic crashes was analyzed based on fatal, serious injury, and minor injury categories, along with gender-wise distribution. Table II presents the classification of accident victims during the study period. Fatal cases dominated across all years, with male victims accounting for the highest proportion. For example, in 2025, male fatalities reached 55.7%, compared to 13.6% for females. A similar pattern was observed for serious injuries, with males consistently representing a larger share than females. Although minor injury cases were comparatively fewer, male victims remained predominant throughout the study period, indicating their higher exposure to road traffic risks.

3.2 Accident black spots identification analysis

3.2.1 Accident severity

Based on the calculated severity index (SI) values, accident-prone locations were identified and ranked accordingly. Table III presents the ranking of locations along the Tongi-Mawna road. Out of a total of 31 accident-prone locations, 12 locations were identified as black spots. Among these, Master Bari, Tongi College Gate, and Mowna Chowrasta were identified as the most critical locations due to their higher accident severity. The other

black spots include Jaina Bazar, Hotapara, Borobari Bazar, Bagher Bazar, M.C. Bazar, Wapder Mor, Rangila Bazar, Rajendropur Chowrasta, and Board Bazar. In contrast, the remaining locations exhibit comparatively lower severity and are not classified as black spots. Overall, the results indicate that certain sections of the corridor experience a higher concentration of severe accidents and therefore require priority in road safety improvements.

Table II: Distribution of accident victims by severity and gender (2021-2025).

Year	Category	Variable	n	%
2021	Death	Female	6	14.3
		Male	21	50.0
	Serious injury	Female	2	4.8
		Male	10	23.8
	Minor injury	Male	3	7.1
2022	Death	Female	5	15.2
		Male	14	42.4
	Serious injury	Female	3	9.1
		Male	7	21.2
	Minor injury	Male	4	12.1
2023	Death	Female	17	25.8
		Male	28	42.4
	Serious injury	Female	3	4.5
		Male	11	16.7
	Minor injury	Female	2	3.0
		Male	5	7.6
2024	Death	Female	14	20.9
		Male	38	56.7
	Serious injury	Male	12	17.9
	Minor injury	Female	1	1.5
		Male	2	3.0
2025	Death	Female	12	13.6
		Male	49	55.7
	Serious injury	Female	8	9.1
		Male	15	17.0
	Minor injury	Female	4	4.5

3.2.2 Kernel Density Analysis

Fig. 4 shows the spatial distribution of road traffic accidents along the Tongi-Mawna corridor. High accident density is observed in the southern section, particularly around Tongi College Gate, Gazipura, and Borobari. Another concentration of accidents is found in the central section near Mowna Chowrasta, Rangila Bazar, and M.C. Bazar. In contrast, the northern and intermediate sections exhibit relatively lower accident density.

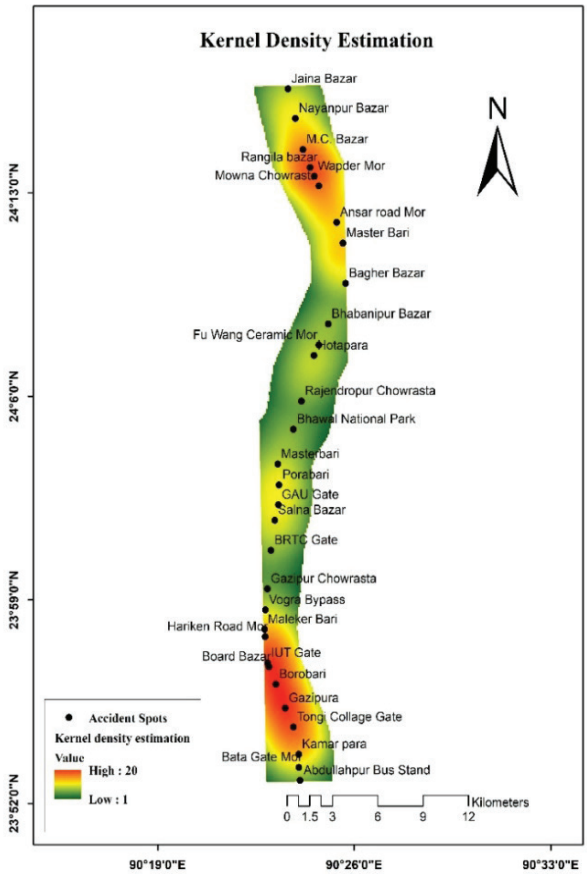


Fig. 4: Kernel density map of road traffic accidents.

3.2.3 Accident Hotspot Analysis Fig. 5 represents the spatial clustering of accident-prone locations along the Tongi-Mawna corridor, while Table IV presents the statistically significant hotspot locations with their corresponding confidence levels. The results indicate that major hotspot clusters are concentrated in the central and northern sections of the corridor. The most significant hotspot locations include Mowna Chowrasta, Master Bari, Bagher Bazar, Ansar Road Mor, Rangila Bazar, Wapder Mor, and M.C. Bazar, which exhibit high accident concentration with strong confidence levels. Additionally, Jaina Bazar and Navanpur Bazar are also identified as hotspot areas in the northern section, while Tongi College Gate and Gazipura represent notable hotspots in the southern part of the corridor. In contrast, several locations such as Masterbari, Porabari, Salna Bazar, and BRTC Gate are identified as cold spots, indicating comparatively lower accident concentration. Some intermediate locations show moderate or insignificant clustering.

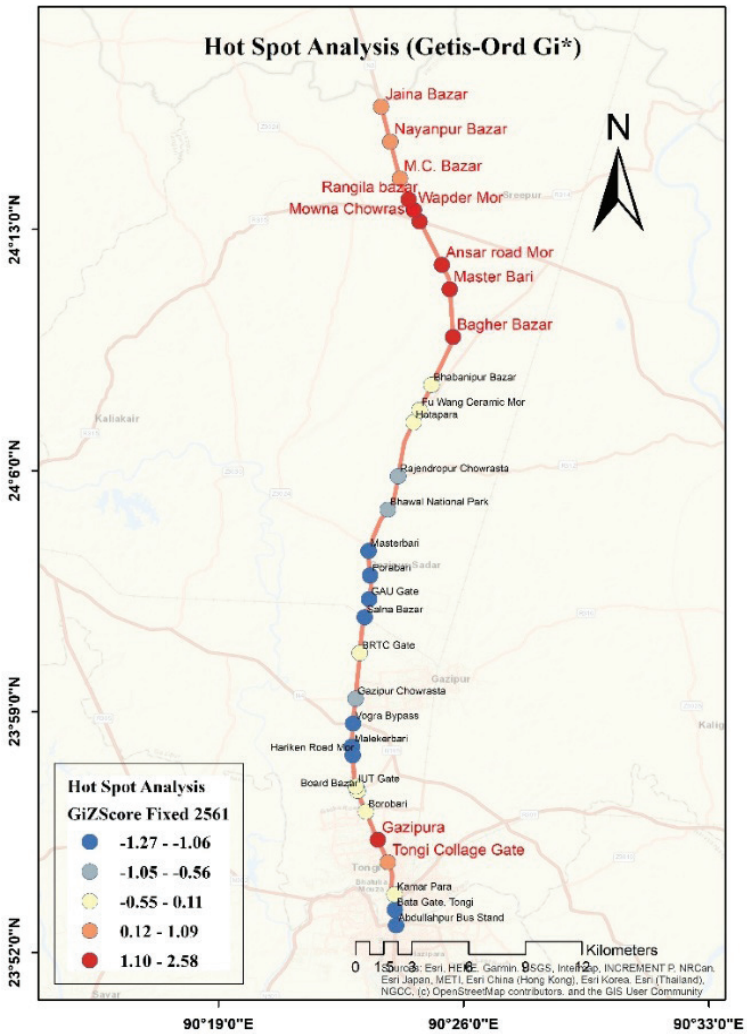


Fig. 5: Hotspot analysis map (Getis-Ord Gi*).

Table III: Ranking of accident-prone locations based on severity index

Serial no.	Black Spots	Latitude	Longitude	SI Value	Ranking
1	Master Bari	24.18776211	90.42667181	88	1st
2	Tongi Collage Gate	23.91029655	90.39726615	75	2nd
3	Mowna Chowrasta	24.22058696	90.41238251	68	3rd
4	Jaina Bazar	24.27618117	90.39407239	61	4th
5	Hotapara	24.12329333	90.40944852	57	5th
6	Borobari Bazar	23.93485769	90.38683245	55	6th
7	Bagher Bazar	24.16469792	90.42825994	53	7th
8	M.C. Bazar	24.24142719	90.40296643	45	8th
9	Wapder More	24.22611919	90.40965315	44	9th
10	Rangila Bazar	24.2311956	90.40715139	42	10th
11	Rajendropur Chowrasta	24.09723283	90.40209846	42	11th
12	Board Bazar	23.94486925	90.38279666	40	12th

Table IV: Statistically Significant Hotspot Locations and Confidence Levels

Serial no.	Name	latitude	longitude	No. of Accident	Confidence Level
1	Jaina Bazar	24.27618117	90.39407239	15	95
2	Nayanpur Bazar	24.25924386	90.39843356	6	95
3	M.C. Bazar	24.24142719	90.40296643	11	95
4	Rangila Bazar	24.2311956	90.40715139	10	99
5	Wapder Mor	24.22611919	90.40965315	10	99
6	Mowna Chowrasta	24.22058696	90.41238251	16	99
7	Ansar Road More	24.19959633	90.42295326	5	99
8	Master Bari	24.18776211	90.42667181	20	99
9	Bagher Bazar	24.16469792	90.42825994	13	99
10	Gazipura	23.92117358	90.39245258	7	99
11	Tongi Collage Gate	23.91029655	90.39726615	18	95

4. CONCLUSION

This study investigated the spatial and temporal characteristics of road traffic accidents along the Tongi-Mawna segment of the Dhaka-Mymensingh Highway using GIS-based techniques and statistical analysis. The findings reveal that road traffic accidents remain a serious safety concern along this corridor, with 304 recorded accidents during the study period, including a notably high proportion of fatal cases. The temporal analysis further indicates an increasing trend in accident occurrence in recent years, with 2025 recording the highest number of accidents. The results also show that heavy vehicles, particularly trucks and buses, are major contributors to accident occurrence along the study route. In addition, the severity analysis demonstrates that male victims account for the highest proportion across fatal and injury categories, reflecting their greater exposure to traffic risk. The severity index analysis identified 12 black spots out of 31 accident-prone locations, indicating that several sections of the corridor experience a higher concentration of severe crashes. The spatial analyses provide further support for these findings. Kernel density analysis highlights pronounced accident concentration in specific sections of the corridor, while hotspot analysis identifies statistically significant clusters of accident-prone locations. Taken together, these results confirm that road traffic accidents along the Tongi-Mawna corridor are spatially concentrated rather than randomly distributed.

Overall, the combined application of GIS-based spatial analysis and statistical methods proved effective in identifying accident-prone locations and understanding accident patterns along the Tongi-Mawna corridor. The findings provide useful information for planners, engineers, and traffic authorities to support targeted road safety planning and accident risk reduction.

REFERENCES

[1] World Health Organization, “Global Status Report on Road Safety,” 2015.

[2] D. Mohan, G. Tiwari, M. Khayesi, and F. M. Nafukho, “Road traffic injury prevention training manual,” 2006.

[3] Asian Development Bank, “Road Safety in Asia Report.”

[4] M. M. Hoque, “The Road to Road Safety: Issues and Initiatives in Bangladesh,” *Regional Health Forum*, vol. 8, no. 1, pp. 39–51, 2004.

[5] M. S. Khatun, M. A. Hossain, M. A. Kabir, and M. A. Rahman, “Identification and analysis of accident black spots using Geographic Information System (GIS): A study on Kushtia-Jhenaidah national highway (N704), Bangladesh,” Heliyon, vol. 10, no. 3, Feb. 2024, doi: 10.1016/j.heliyon.2024.e25952.

[6] S. Erdogan, I. Yilmaz, T. Baybura, and M. Gullu, “Geographical information systems aided traffic accident analysis system case study: city of Afyonkarahisar,” Accid. Anal. Prev., vol. 40, no. 1, pp. 174–181, Jan. 2008, doi: 10.1016/j.aap.2007.05.004.

[7] A. Afolayan, S. M. Easa, O. S. Abiola, F. M. Alayaki, and O. Folorunso, “GIS-Based Spatial Analysis of Accident Hotspots: A Nigerian Case

Study," Infrastructures (Basel)., vol. 7, no. 8, Aug. 2022, doi: 10.3390/infrastructures7080103.

[8] Z. Xie and J. Yan, "Kernel density estimation of traffic accidents in a network space," Accid. Anal. Prev., vol. 40, pp. 396–406, 2008.

[9] A. Getis and J. K. Ord, "The Analysis of Spatial Association by Use of Distance Statistics," Geogr. Anal., vol. 24, no. 3, pp. 189–206, 1992, doi: 10.1111/j.1538-4632.1992.tb00261.x.

[10] G. W. T. B. and K. V. K. Geurts, "Identification and ranking of black spots: Sensitivity analysis," Transp. Res. Rec., vol. 1897, pp. 34–42, 2004.

[11] K. G. Le, P. Liu, and L. T. Lin, "Determining the road traffic accident hotspots using GIS-based temporal-spatial statistical analytic techniques in Hanoi, Vietnam," Geo-Spatial Information Science, vol. 23, no. 2, pp. 153–164, Apr. 2020, doi: 10.1080/10095020.2019.1683437.

Assessment of Land Use and Land Cover (LULC) Changes along the MRT-6 Corridor in Dhaka Using Multi-Temporal Satellite Data

Pias Pal*, Md. Ibrahim Khalil, Swe Kya Waiy Marma, Mahiman Zinnurain, M. Afzal Hossain and Md. Sabbir Hosen

Department of Civil Engineering, Dhaka University of Engineering & Technology, Gazipur, Bangladesh

ABSTRACT

The development of metro rail infrastructure plays a significant role in shaping urban land use and accelerating urban growth in rapidly developing cities. This study analyzes the spatio-temporal changes in land use and land cover (LULC) within the MRT-6 station buffer zones in Dhaka, Bangladesh, in the period between 2021 and 2025. Satellite-based GIS and remote sensing techniques were used to classify LULC into four major categories: built-up area, vegetation, open land, and water bodies. Multiple MRT-6 stations were analyzed to gain an insight into patterns of urban transformation. These findings demonstrate that built-up areas in most station buffer zones increase significantly in the period between 2023 and 2025, following the introduction of the metro. Concurrently, vegetation, open land, and water bodies have been diminishing gradually, demonstrating the conversion of land by the growing infrastructure and business activities. Notably, Kazipara recorded the highest built-up area in 2021 at 1.79 km², increasing further to 1.85 km² by 2025, while Uttara South recorded the lowest built-up coverage in both years, starting at just 0.19 km² in 2021 and 0.47 km² in 2025, reflecting urban growth along the corridor. The results indicate that the availability of metro promotes residential and commercial development, increases land value, and accelerates urban expansion. Altogether, MRT-6 has led to the tremendous urban change in its route. Although the metro system provides a way of sustainable transportation and reduces traffic congestion, it also causes environmental pressure due to the decrease in the natural land cover. The study highlights the importance of integrating transportation planning with land use management to help in balancing and sustainable development of urban centers in Dhaka.

Keywords: Land Use Land Cover (LULC), Dhaka Metro Rail, Geographic Information System, Transit Oriented Development.

1. INTRODUCTION

Urbanization in developing countries has been increasing rapidly, with the number of people living in urban areas expected to rise from about 2.0 billion in 2000 to nearly 5.5 billion by 2050 [1]. This rapid population growth puts significant pressure on land resources and often leads to environmental problems, inefficient transportation systems, and unplanned urban expansion [2]. With the growth of the population, cities are growing at a rate that is outpacing the population growth of the country, which is a sign of poor land development. Despite the necessity of sustainable development, rapid urban development poses significant challenges that should be properly planned and addressed to achieve balanced urban development [2], [3]. Rapid urbanization in megacities poses significant challenges, especially in the transport systems and sustainable planning of land use [4], [5]. Urbanization and human activities brought about changes in land use and land cover (LULC) that greatly influence climate, biodiversity, and environmental quality [6]. Simultaneously, the increasing number of vehicles contributes to traffic congestion, air pollution, and ineffective land use patterns, generating severe environmental and social issues [7]. Thus, the need to come up with efficient and sustainable transportation systems has become critical in enhancing the living conditions and economic performance of urban life [8]. Dhaka Mass Transit Company Limited (DMTCL) is a key player in changing urban transportation in Dhaka under the MRT Line-6 project [9]. Launched as part of the Strategic Transport Plan (STP) and running since 2022, MRT-6 already serves a route of around 20.1 km with 16 stations between Uttara and Motijheel [10], [11]. It aims to reduce severe traffic congestion and provide a fast, reliable, and environmentally friendly public transport system to the increasing population [12]. MRT-6 is a component of a multi-phase metro network that enhances urban mobility and connectivity and meets the growing transportation demands as a result of the rapid

*Corresponding author's email: piaspal102@gmail.com

urbanization [13]. Under the system, it is anticipated that land use patterns and urban development will be affected greatly along the corridor [14]. It is vital to analyze the relationship between the transport systems and patterns of land use because integrated planning is required to achieve sustainable urban development [15]. Efficient public transportation systems like MRT-6 can reduce emissions, minimize congestion, and support economic growth by improving accessibility. In addition, MRT-6 facilitates sustainable mobility through a decrease in the use of personal vehicles, which is significant in terms of climate change and resource limitations. Nevertheless, the intensive urbanization process still exerts pressure on the natural resources and ecological balance in Dhaka [16]. Although this has happened, the effects of MRT-6 on land use patterns and environmental dynamics have not been adequately investigated. This paper examines the construction and operation stages of MRT-6 and its influence on surrounding areas. In particular, it looks at the spatio-temporal changes in LULC within 0-800 m buffer zones along the MRT-6 corridor in the years 2021, 2023, and 2025. The study aims to assess how MRT-6 influences urban growth and land use transformation and to support sustainable urban planning and policy-making in rapidly growing megacities like Dhaka.

Understanding the spatial extent of urban transformation around metro corridors is increasingly important for evidence-based planning. By comparing pre-operation, initial operation, and post-operation phases, this study provides a more granular perspective on how metro accessibility drives localized land use shifts. The outcomes are expected to contribute valuable empirical evidence for transport and urban planners, helping guide future infrastructure decisions and land use policies.

2. LITERATURE REVIEW

The role of urban transit systems has been growing in significance as it has increased the level of accessibility and made urban living a better experience. Land use and transportation planning have become a common practice in controlling uncontrolled urban sprawl that has been brought about by overreliance on personal vehicles [18]. This combined method is believed to be an efficient way of reducing adverse environmental and social impacts and encouraging sustainable city growth [19]. Transit-oriented development (TOD) can be viewed as an important factor in enhancing the economic development of metropolitan regions and their livability. TOD was introduced by Peter Calthorpe in the late 1980s and focuses on high-density, mixed-use development around transit stations, and facilitates access to workplaces and services via walking and cycling. Though there were not many considerations on accessibility in early TOD models, this has been enhanced over the years [20]. The growth of the metro rail has also helped in making urban areas more alive and economically active, as land values grow with the growth of urban areas, and commercial activities are more likely to occur around transit corridors [21].

In the context of Dhaka, Metro rail systems like MRT-6 have greatly enhanced accessibility and urban mobility. But environmental and social issues can be generated through such a large-scale infrastructure development. It has been found that this type of project can cause habitat destruction, deforestation, soil erosion, and urban heat island (UHI) effects, which harm the ecological balance. Furthermore, the activities of metro construction can lead to the enhancement of metal pollution, which can be a threat to human health [22]. Another significant issue is the uneven development, where the regions nearer to the metro stations are likely to have a better economic growth than those that are farther away, thus creating spatial inequalities. Moreover, the increased accessibility and lowered traveling expenses could stimulate development in the regions that were less reachable in the past, which could lead to urban sprawl and demographic shifts.

Despite these challenges, metro lines like MRT-6 have a significant impact on the growth and socio-economic development of the city in terms of connectivity and supporting growth based on TOD. The high population densities and mixed-use development promoted by the compact city concept are facilitated by efficient public transportation systems that promote the concept of compact cities in controlling urban sprawl. Additionally, MRT-6 increases the comfort of passengers and promotes the connection to other means of transport, which is a part of a multimodal urban transport system. Therefore, sustainable urban development will need improved integration of transport and land-use planning, infrastructure optimization, and encouragement of sustainable mobility options to maximize the benefits of MRT-6 in Dhaka [17]. No prior study has examined station-level LULC changes within buffer zones along the MRT-6 corridor.

3. METHODOLOGY

3.1 Study Area

The study area is MRT Line-6 within Dhaka, which is among the busiest and fastest-growing megacities. MRT-6 was the first metro railway to be opened in Bangladesh,

aimed at alleviating traffic congestion and enhancing urban mobility. It is a path that links Uttara North and Motijheel and has a distance of 20.1 km, which passes through 16 stations at strategic areas in the city [9], [10]. These are the Uttara North, Uttara Center, Uttara South, Pallabi, Mirpur-11, Mirpur-10, Kazipara, Shewrapara, Agargaon, Bijoy Sarani, Farmgate, Karwan Bazar, Shahbagh, Dhaka University, Secretariat, and Motijheel. It started serving partially (between Uttara North and Agargaon) in December 2022 and was expanded fully to serve Motijheel in 2023 [9]. This phased development significantly improved accessibility and connectivity, making the corridor suitable for analyzing urban transformation. Fig. 1 explains that an 800 m buffer was applied around each of the stations in order to investigate the immediate impact. This distance is an average walking distance in a transit-oriented development study [11]. The change in LULC is determined in the years 2021, 2023, and 2025 to study the trend of growth of the urban areas as a result of the metro.

3.2 Materials

Sentinel-2 satellite images from 2021, 2023, and 2025 were used to examine land use and land cover changes along the MRT-6 corridor in Dhaka. The images have a spatial resolution of 10 m, which made them suitable for identifying the main land-cover features of the study area. Before classification, the images were aligned through image-to-image registration to maintain spatial consistency. Radiometric and geometric corrections were also carried out to reduce atmospheric and sensor-related errors. All images were projected using the WGS 84 datum and UTM Zone 46N so that changes between the selected years could be compared accurately. Finally, the study area was classified into four main categories: built-up area, vegetation, open land, and water bodies, based on their spectral characteristics.

3.3 Methods

Buffer zone analysis was applied to assess the impact of MRT-6 on urban growth and land cover change. A 0-800 m buffer was established at all the stations to examine the immediate effect of the metro infrastructure. Multi-temporal satellite data were analyzed using GIS tools, including geo-referencing and subsetting. The supervised classification method, Maximum Likelihood Classification (MLC), was used to classify the images into four LULC types: built-up area, vegetation, open land, and water bodies. Buffer zones were superimposed on 2021, 2023, and 2025 LULC maps to evaluate the changes over the years. Classification accuracy was assessed using reference samples to evaluate the reliability of the classified LULC maps.

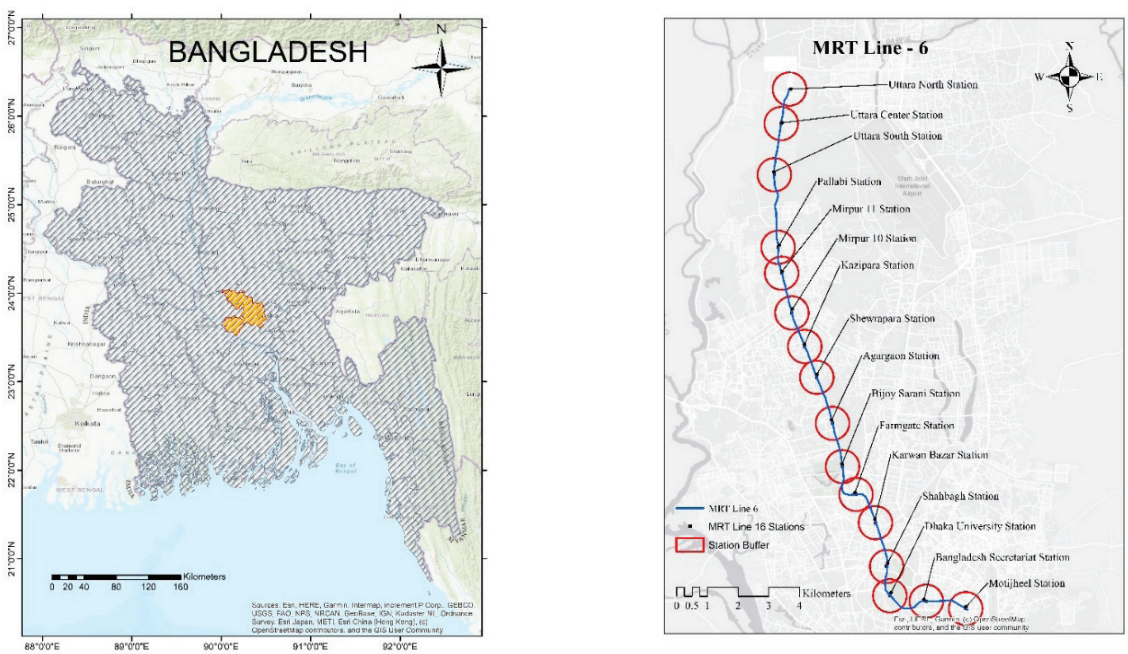


Fig. 1: Study Area (MRT LINE-6)

4. RESULT AND DISCUSSION

4.1 Temporal Changes in LULC along MRT-6 Corridor

Table 1 presents the land use and land cover conditions within the 0-800 m buffer zones of the MRT-6 stations for 2021, 2023, and 2025. The results show an overall increase in built-up land, together with a gradual decline in vegetation, open land, and water bodies. Considering the summed values of all station buffers, built-up land increased from 16.65 km² in 2021 to 19.73 km² in 2025, representing an increase of 3.07 km² or 18.46%. During the same period, vegetation decreased from 8.21 km² to 6.61 km², showing a decline of 19.53%. Open land fell from 5.21 km² to 4.27 km², while water bodies decreased from 2.17 km² to 1.61 km². These changes represent reductions of 17.95% and 25.91%, respectively. The results suggest that much of the new built-up development occurred through the gradual conversion of vegetation and open land.At the same time, vegetation has been decreasing gradually in most of the stations, implying that the growing development force is converting the green areas into urban land use. This fall is further visible in the central stations, where the population density, land demand, and development of infrastructure are a bit more noticeable. In addition, a reduction in open land is also present in several stations. This means that previously unused land, unoccupied land, or land that was put to ineffective use is now being converted to residential premises, commercial areas, and facilities that support the infrastructure. The reduction in water bodies in some of the areas is minimal, and compared to other categories of land use, the reduction is not much. This means that urbanization is majorly happening through vegetation and open land conversion, and water bodies are comparatively less affected. They are, however, relatively stressed due to human activities in the environment. Minor intrusion at the edges of the water can also be observed in some of the stations, which can be regarded as environmental issues of long-term concern if this trend continues.

Overall, the table indicates that there is a progressive shift in the natural and semi-natural land covers to the built-up land covers within the period 2021 to 2025. The other interesting observation is that an expansion in the built-up areas is more pronounced after 2023, which corresponds to the operational phase of MRT-6-Kazipara, which had the highest built-up area of 1.79 km² in 2021, further increased to 1.85 km² by 2025, while Uttara South remained the least urbanized, rising modestly from 0.19 km² to 0.47 km². This means that enhanced access and connectivity have played a key role in development activities in and around the stations. In general, the observed changes reveal that there exists a close and direct correlation between the development of the metro and the transformation of land use.

4.2 Spatial and Graphical Representation of LULC Changes

Fig. 2 illustrates the percentage variation of different land use and land cover (LULC) classes over the study period. The results clearly indicate a consistent increase in built-up areas, accompanied by a progressive decline in vegetation cover, open land, and water bodies. This pattern confirms that urban expansion within the study area is predominantly occurring through the conversion of natural and semi-natural land covers. The GIS-based LULC maps for 2021, 2023, and 2025 (Fig. 3) further offer a clear spatial interpretation of these temporal changes. The maps demonstrate a continuous and spatially concentrated expansion of built-up areas along the MRT-6 corridor. This expansion is particularly prominent in and around centrally located stations, where enhanced accessibility and higher economic attractiveness have contributed to intensified land development.

A more detailed observation is evident at Uttara North station (Fig 4), where comparative analysis of LULC maps reveals a pronounced transformation over time. Built-up land has expanded substantially, while vegetation and open land have experienced notable reductions. This indicates that even peripheral urban zones are undergoing accelerated land use transformation, primarily driven by improved metro connectivity and associated urban development pressures.

4.3 Impact of MRT-6 on Urban Development

The findings of this study have clearly indicated that MRT-6 has had an enormous impact on urban development along its route. Increased access and speed in connectivity have stimulated residential and commercial activity, which has resulted in observable changes in land use within the buffer zones throughout the study period. Much of the developed growth has occurred through the transformation of vegetation and undeveloped land. This implies that the transport infrastructure contributes significantly to the development of the patterns of urban growth. It is more significant in central stations like Farmgate, Karwan Bazar, and Motijheel, where the intensity of development is high due to more economic activity and a higher land value. In contrast, peripheral stations show relatively slower but steady transformation.

Environmentally, MRT-6 has both positive and negative impacts. On the one hand, it will contribute to the sustainable transportation process and help to reduce the problem of road traffic congestion. However, it may also cause the urban heat island effect, loss of biodiversity, and an ecological imbalance unless well managed. Generally, the results indicate the significance of land use and transport planning that is integrated. Strategies such as Transit-Oriented Development (TOD) play a vital role in balancing urban development and environmental preservation. The accuracy assessment showed that the overall classification accuracy ranged from 80% to 90%, indicating acceptable reliability of the classified LULC maps.

Table 1: LULC distribution within MRT-6 station buffer zones (2021, 2023, and 2025)

Station	2021				2023				2025			
	Water body (Sq.km)	Vegetation (Sq.km)	Buildup (Sq.km)	Open land (Sq.km)	Water body (Sq.km)	Vegetation (Sq.km)	Buildup (Sq.km)	Open land (Sq.km)	Water body (Sq.km)	Vegetation (Sq.km)	Buildup (Sq.km)	Open land (Sq.km)
Uttara North	0.2114	0.5592	0.4747	0.765	0.1958	0.5466	0.5713	0.6989	0.1529	0.394	0.8685	0.5949
Uttara Centre	0.2201	0.4389	0.3563	1.003	0.2074	0.4171	0.4213	0.97	0.1868	0.4054	0.4794	0.9392
Uttara South	0.6867	0.4565	0.1944	0.6829	0.6539	0.3911	0.2982	0.6704	0.5588	0.3143	0.4679	0.6695
Pallabi	0.129	0.3216	1.3247	0.2421	0.0907	0.3	1.3809	0.2312	0.0591	0.2915	1.4745	0.1862
Mirpur-11	0.0257	0.256	1.653	0.0879	0.0258	0.2163	1.6914	0.079	0.0108	0.1417	1.814	0.0443
Mirpur-10	0.0379	0.2647	1.5982	0.1095	0.0289	0.2461	1.6416	0.0962	0.0277	0.2399	1.6549	0.0948
Kazipara	0.03	0.1185	1.7876	0.0779	0.0195	0.1065	1.8308	0.0504	0.0136	0.096	1.8529	0.0477
Shewrapara	0.2603	0.3325	1.201	0.2166	0.2274	0.3171	1.263	0.2113	0.117	0.143	1.5793	0.1711
Agargaon	0.0911	0.7433	0.6176	0.584	0.0848	0.6944	0.6799	0.5733	0.0833	0.6722	0.7512	0.517
Bijoy Sarani	0.1106	0.8261	0.6224	0.452	0.10951	0.7749	0.6817	0.4414	0.1073	0.7193	0.7626	0.4219
Farmgate	0.035	0.4058	1.3549	0.2134	0.0338	0.3898	1.4439	0.1513	0.0315	0.3581	1.4827	0.1398
Karwan Bazar	0.0932	0.2388	1.6038	0.0845	0.0702	0.2221	1.6986	0.0316	0.0975	0.2104	1.6937	0.0187
Shabbag	0.0707	0.947	0.8424	0.1508	0.062	0.8351	1.0268	0.0887	0.0543	0.8151	1.0611	0.08304
DU	0.0492	1.2044	0.4674	0.2897	0.0488	0.9985	0.7235	0.2414	0.0405	1.0004	0.7792	0.1916
Bangladesh Secretariat	0.0535	0.6239	1.2064	0.1267	0.0276	0.5251	1.3916	0.066	0.0115	0.4948	1.3798	0.1244
Motijheel	0.07	0.4749	1.3467	0.1193	0.068	0.3317	1.5758	0.0477	0.0585	0.3123	1.6235	0.0266

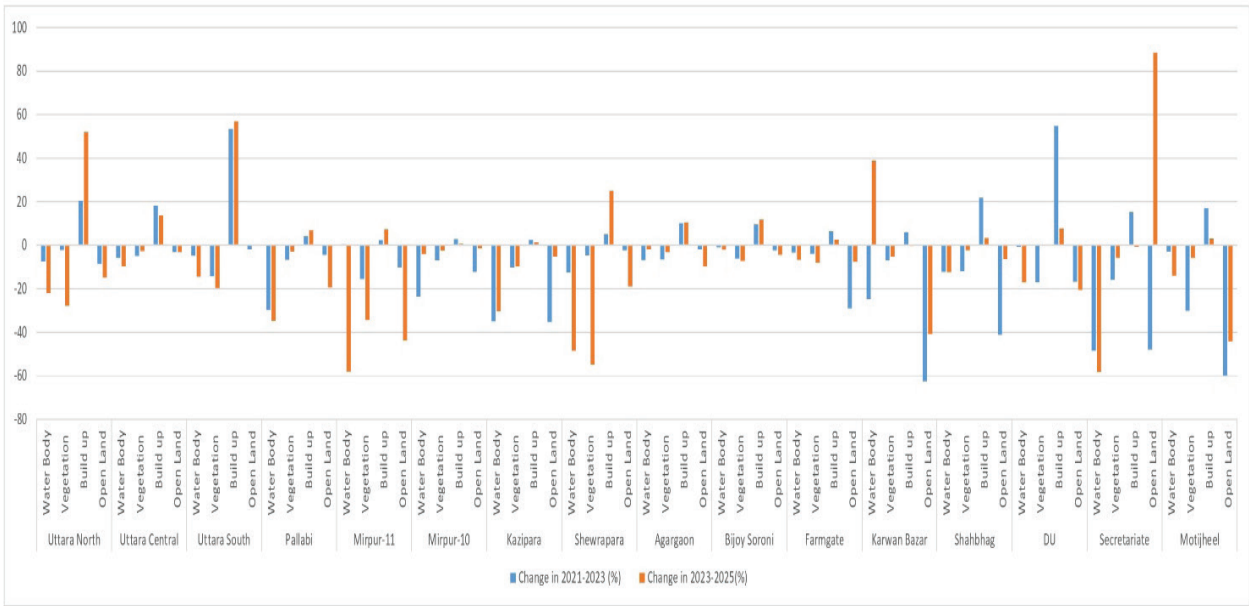


Fig. 2: Percentage (%) change in LULC along MRT-6

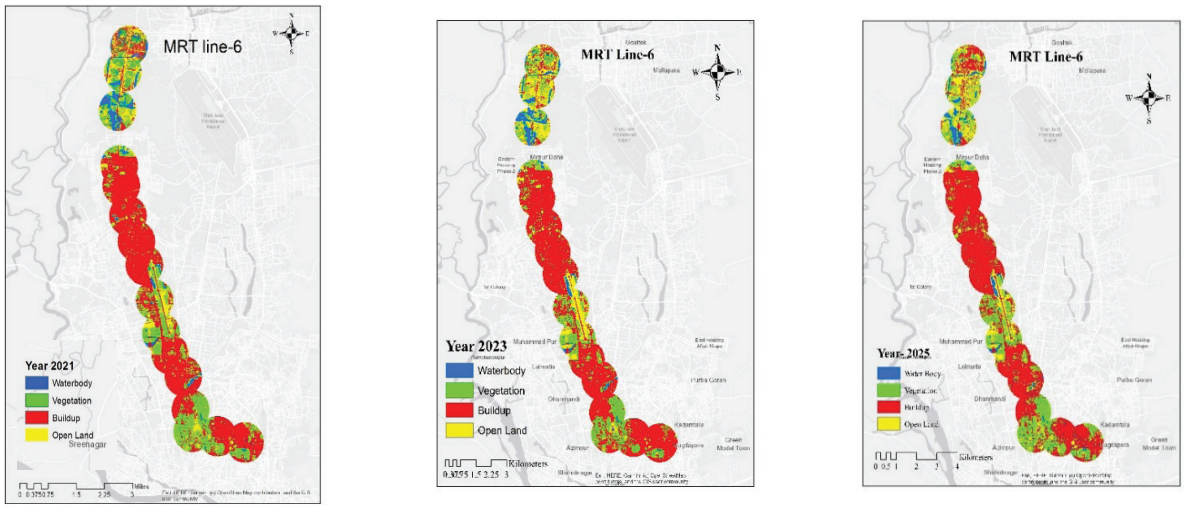


Fig. 3: Spatio-temporal LULC change along MRT-6

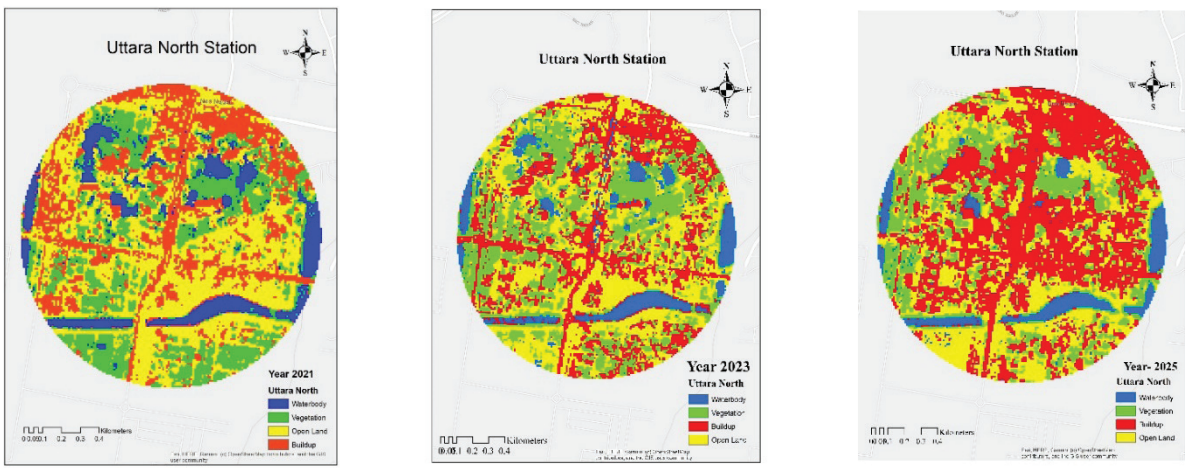


Fig. 4: LULC map of Uttara North Metro station

5. CONCLUSION

This study investigated how land use and land cover changed around the MRT-6 stations in Dhaka between 2021 and 2025. The findings reveal a noticeable shift toward urban development along the corridor. The total built-up area increased from 16.65 km² in 2021 to 19.73 km² in 2025, showing an overall growth of 18.46%. At the same time, vegetation, open land, and water bodies declined by 19.53%, 17.95%, and 25.91%, respectively. The changes were more visible around stations such as Uttara North, Shewrapara, Dhaka University, Motijheel, and Uttara South.

The results suggest that improved accessibility provided by MRT-6 may have encouraged residential, commercial, and infrastructure development near the stations. However, these changes cannot be linked only to the metro rail, as population growth, rising land values, existing urban expansion, and planning decisions may also have played important roles.

This study has some limitations, including the use of only three observation years, 10 m resolution satellite images, overlapping station buffers, and the lack of a control area. Future studies should include longer time-series data, higher-resolution imagery, different buffer

distances, and socioeconomic information. Proper land-use zoning, protection of green spaces and water bodies, and planned transit-oriented development are therefore necessary to achieve balanced and environmentally sustainable growth along the MRT-6 corridor.

REFERENCES

[1] I. Haddad, "A new tropism of the urban fabric in the face of risk and uncertainty in the developing countries," *European Modern Studies Journal*, vol. 8, no. 1, pp. 106-118, 2024. doi: 10.59573/emsj.8(1).2024.11.

[2] X. Liu *et al.*, "High-spatiotemporal-resolution mapping of global urban change from 1985 to 2015," *Nature Sustainability*, vol. 3, no. 7, pp. 564-570, 2020. doi: 10.1038/s41893-020-0521-x.

[3] A. Sharma, B. Nikam, and D. S. Bagri, "Urbanization trends and challenges: A case study in the Asan watershed of Uttarakhand on urban growth patterns and sustainable land use planning," 2023. doi: 10.21203/rs. 3. rs-3660810/v1.

[4] World Bank, *Enhancing Urban Resilience in Greater Dhaka*, Washington, DC, USA, 2015.

[5] Asian Development Bank (ADB), *Dhaka Urban Transport Project*, Manila, Philippines, 2020.

[6] P. K. Yadav *et al.*, "Ecosystem health assessment of East Kolkata Wetlands, India: Implications for environmental sustainability," *Journal of Environmental Management*, vol. 366, p. 121809, 2024. doi: 10.1016/j.jenvman.2024.121809.

[7] H. Al-Mousawi, V. L. Leong, and H. Al-Jameel, "The influence of ring roads on traffic characteristics in urban cities," *BIO Web of Conferences*, vol. 97, p. 00067, 2024. doi: 10.1051/bioconf/20249700067.

[8] A. A. Umoh *et al.*, "Incorporating energy efficiency in urban planning: A review of policies and best practices," *Engineering Science & Technology Journal*, vol. 5, no. 1, pp. 83-98, 2024. doi: 10.51594/estj.v5i1.729.

[9] Dhaka Mass Transit Company Limited (DMTCL), *About DMTCL*, Dhaka, Bangladesh, 2023.

[10] Dhaka Mass Transit Company Limited (DMTCL), *MRT Line-6 Project Overview*, Dhaka, Bangladesh, 2023.

[11] Japan International Cooperation Agency (JICA), *Preparatory Survey on Dhaka Mass Rapid Transit Development Project*, Tokyo, Japan, 2016.

[12] Asian Development Bank (ADB), *Bangladesh: Dhaka Mass Rapid Transit Development Project (Line-6)*, Manila, Philippines, 2021.

[13] Government of Bangladesh, *Revised Strategic Transport Plan (RSTP) for Dhaka*, Dhaka, Bangladesh.

[14] World Bank, *Towards Great Dhaka: A New Urban Development Paradigm Eastward*, Washington, DC, USA, 2015.

[15] A. Roukouni *et al.*, "Land use around metro stations," *International Journal of Civil and Environmental Engineering*, vol. 6, no. 5, pp. 289-293, 2012.

[16] M. S. Joy *et al.*, "Urban green park suitability analysis," *Urbanization and Sustainability Society*, 2024.

[17] M. Panwar *et al.*, "Environmental co-benefits of transport system," *Alexandria Engineering Journal*, vol. 57, no. 4, pp. 2649-2658, 2018.

[18] H. Suzuki, R. Cervero, and K. Iuchi, *Transforming Cities with Transit*. Washington, DC: World Bank Publications, 2013.

[19] A. A. S. Hameed, "Urban and regional planning strategies to achieve sustainable urban development," *International Journal of Advanced Science Research and Engineering*, vol. 7, no. 3, pp. 22-27, 2021. doi: 10.31695/ijasre.2021.33980.

[20] K. V. Vessali, "Land use impacts of rapid transit: A review of the empirical literature," *Berkeley Planning Journal*, 2012. doi: 10.5070/bp311113054.

[21] K. R. Zamir *et al.*, "Effects of transit-oriented development on trip generation," *Transportation Research Record*, vol. 2413, no. 1, pp. 45-53, 2014. doi: 10.3141/2413-05.

[22] D. Lin *et al.*, "Metro systems: construction, operation and impacts," *Tunnelling and Underground Space Technology*, vol. 143, p. 105373, 2024. doi: 10.1016/j.tust.2023.105373.

Multi-Objective Optimization of Window-to-Wall Ratio for Thermal and Visual Comfort: The Impact of Vertical Spatial Positioning in Hot-Humid Climates

Maria Jebin, Shunila Binte Ahsan* and Md. Galib Nur Anan

Department of Architecture, Dhaka University of Engineering & Technology, Gazipur, Bangladesh

ABSTRACT

In university dormitories, residents occupy identical rooms for extended hours with little control over their environment. The problem arises when identical rooms on different floors behave differently. Solar exposure, wind access, and proximity to the roof all shift with height, meaning a window configuration suited to one floor may underperform on another. This study takes that variation seriously. The case study is a five-storey dormitory in Gazipur, Bangladesh. Corner rooms were selected from each floor as they share the same geometry and orientation. Window to Wall Ratio (WWR) was treated as the primary design variable, tested between 10% and 100%. Parametric models were built in Rhinoceros 3D and Grasshopper, daylight and thermal simulations were run using Climate Studio and Energy Plus, and multi-objective optimization was carried out through the Octopus plugin. The objectives were to maximize Spatial Daylight Autonomy (sDA), Mean Illuminance, and Percentage of Comfort and minimize Percentage of Discomfort. sDA stayed below 10% on all floors, and mean illuminance ranged from just 98 to 127 lux for base case. Adaptive discomfort was high too, affecting 57.98% to 59.83% of occupied hours. After optimization, the Pareto-balanced solutions raised sDA to 83.33–100% and mean illuminance to 569.17–744.21 lux, while cutting adaptive discomfort down to 25.25–27.54%. The optimal WWR shifted by floor: 70% for the ground floor, 60% for the first floor, and 65% for the second through fourth floors. These results show that a single WWR cannot deliver the best daylight–thermal balance across every floor. Floor-specific WWR configurations are therefore necessary for naturally ventilated dormitories in hot-humid climates.

Keywords: Window-to-wall ratio, multi-objective optimization, thermal comfort, spatial daylight autonomy, hot-humid climate, naturally ventilated dormitory.

1. INTRODUCTION

Windows are one of the typical building elements, yet decisions about their size and placement can determine whether a room feels habitable or insufferable. In hot-humid climates like Bangladesh, where solar radiation is intense, ambient humidity is persistently high, and mechanical cooling remains inaccessible to much of the population, window size and placement becomes a matter of great concern. In university dormitories especially, where occupants spend hours studying, sleeping, and resting in identical rooms they cannot modify, the indoor thermal environment is a topic directly associated with learning.

Studies state that adaptive thermal comfort is a concept where occupants tend to feel more comfortable with a wider range of indoor conditions, linked to outdoor climate conditions and their own ability to adapt. It suggests that window-to-wall ratio is not merely a geometric design variable but a key determinant of adaptive thermal comfort, because it shapes ventilation potential, solar exposure, and occupants' ability to regulate indoor conditions through behavior and opening control [1]. A larger window admits more daylight, supporting variable daylight quality and reducing dependence on artificial lighting. But at the same time, windows increase solar heat gain, pushing indoor temperatures toward discomfort. On the contrary, a smaller window limits overheating but may leave a room dim and poorly cross-ventilated. Neither extreme serve occupants well, which is why identifying the appropriate WWR for a given climate and building type matters. Work across hot and dry climates has placed optimal WWR values roughly between 20% and 50%, varying by facade orientation [2]. In tropical residential buildings, shape, orientation, and glazing ratio together determine indoor thermal conditions in ways that no single factor can address in isolation [3]. Controlling these parameters has been shown to cut annual cooling loads and lighting

*Corresponding author's email: shunila.ahsan@duet.ac.bd

energy demand substantially, with associated reductions in CO_2 emissions [4]. Daylighting and thermal comfort do not optimize in the same direction, and this is what makes window design genuinely difficult. More glass means better daylight autonomy but also higher heat gain and potential glare, a conflict noted repeatedly in the literature [5], [6]. Single-objective approaches cannot resolve this; they simply shift the problem elsewhere. Multi-objective optimization, particularly using genetic algorithms, is better suited to the task. Rather than converging on one solution, genetic algorithms generate a Pareto front- a set of designs where no metric can be improved without degrading another, allowing designers to make informed trade-off decisions based on actual building conditions [7], [8]. Studies applying such frameworks to buildings in hot humid climate have demonstrated simultaneous gains in energy efficiency, daylight quality, and thermal comfort [9], [10]. The BNBC (2020) provides prescriptive glazing selection criteria, SHGC and SC; based on Window-to-Wall Ratio (WWR) alone, without accounting for floor-level variation, orientation, or the specific demands of naturally ventilated typologies [11].

Naturally ventilated dormitories in South Asia, however, appear rarely in this body of work. This study attempts to fill that gap. A five-storey university dormitory in Gazipur, Bangladesh, forms the case study, with five identical corner rooms in each floor was selected to isolate the effect of vertical positioning on performance. Using Rhinoceros 3D and Grasshopper for parametric modelling, EnergyPlus with a Dhaka weather file for thermal simulation, and the Octopus plugin for multi-objective optimization, the study tests WWR values between 10% and 100%. Metrics that frame the assessment are Spatial Daylight Autonomy (sDA), Annual Sunlight Exposure (ASE), Mean Illuminance, Adaptive Comfort Hour Percentage and Adaptive Discomfort Hour Percentage. The result is a set of floor-specific configurations that reflect the genuine thermal and daylight conditions of each level, offering a grounded, evidence-based reference point for dormitory window design in Bangladesh's climate.

2. METHODOLOGY

A parametric approach is adopted in this study to optimize window design with particular emphasis on daylight and thermal performance. A representative university dormitory building in Gazipur served as the basis for investigation, from which corner rooms across five floors were selected for detailed parametric analysis. The Window-to-Wall Ratio is used as the primary design variable. Building geometry was modelled using Rhinoceros 3D along with Grasshopper, and optimization was carried out through the Octopus plugin operating within the Grasshopper environment.

The study is organized into three main parts: (1) development of the base case models, (2) performance evaluation of the base case rooms, and (3) parametric optimization to identify potential design solutions for the studied rooms.

2.1 Daylight Metric

Spatial Daylight Autonomy (sDA) and Annual Sunlight Exposure (ASE), proposed by the Illuminating Engineering Society of North America [12], are widely used dynamic metrics that describe daylight quality in architectural spaces more effectively than point-based evaluations [13]. sDA measures the percentage of floor area achieving a minimum illuminance of 300 lux for 50% of occupied hours annually, with thresholds of 40%, 55%, and 75% earning one, two, and three LEED credits respectively. ASE is a codified LEED v4.1 metric representing conditions of potential visual discomfort from excessive direct sunlight. The IES recommends that no more than 10% of the floor area receive 1000 lux for 250 or more occupied hours per year to qualify for LEED recognition [12, 14]. Along with sDA and ASE, mean illuminance was used to provide an additional quantitative description of daylight distribution within the room and to support the comparison of base and optimized cases. Mean illuminance, expressed in lux, is commonly used as the average illuminance over a defined plane or area and serves as a supplementary indicator of overall light availability in daylighting studies [15].

2.2 Thermal Performance Metric

As the dormitory rooms in this study are naturally ventilated, the Adaptive Thermal Comfort Model was used. Occupants in naturally ventilated buildings tend to accept a wider range of indoor temperatures. This depends on outdoor conditions and how much air movement is available. ASHRAE 55 and EN 16798 both define comfort bands using the running mean outdoor temperature [16]. Hours are then classified as comfortable or uncomfortable based on how far indoor conditions fall from these bands. Based on this, two metrics were used: Percentage of Comfort Hours and Percentage of Discomfort Hours. These capture how much of the occupied time falls within, or outside, the adaptive comfort zone. Dormitory rooms are occupied for long stretches of the day, and thermal comfort has a direct bearing on occupant wellbeing.

For this reason, these metrics were considered more suitable than static comfort indices for this study. They also allow the effect of different WWR configurations to be compared directly, since WWR influences solar heat gain and, in turn, indoor air temperatures relative to the outdoor benchmark.

2.3 Case Study Description

A five-storied residential dormitory building located in Gazipur, Bangladesh was selected as the case study (Fig. 1). The building follows a repetitive floor plan in which individual rooms share identical design characteristics, including orientation, window configuration, and spatial layout, but differ in their positional context within the building (Fig. 2). This quality made the building particularly well suited for isolating the effect of vertical positioning on indoor thermal conditions, separate from any variation in room geometry or envelope design. Five rooms were selected from the same vertical stack, each situated on a different floor from ground to fifth level (Fig. 3). Table I describes the major parameters of the studied rooms.

Table I: Parameters of the case studies

Parameters	Case 1 (101)	Case 2 (201)	Case 3 (301)	Case 4 (401)	Case 5 (501)
Room Dim.	4.1m x 3.6m				
Window Orientation	North				
Window Size	1.27m X 1.29m				
Sill Level	0.91 m				
Lintel Level	2.20 m				
Window Type	Sliding glass window with 50% operable area				
Wall	150mm brick plaster wall, off-white color				
Ceiling	Concrete slab, white color				
Floor	Mosaic floor, beige color				



(a) (b)

Fig. 1: (a) Exterior view of the case building; (b) Interior view of the corner room

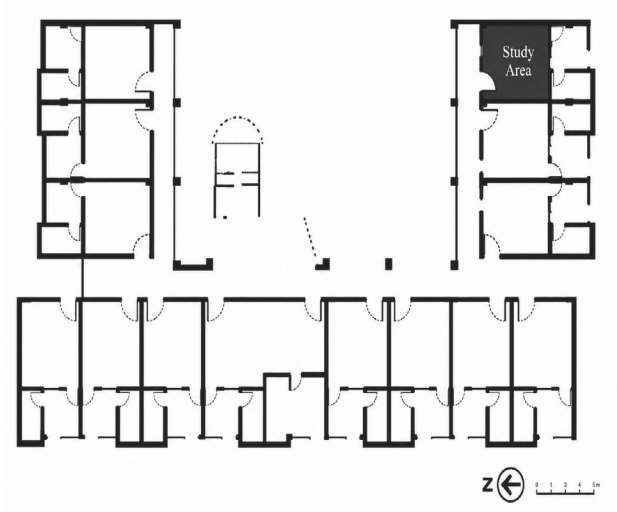


Fig. 2: Floor plan of the case building.

The selected rooms were a corner unit because corner rooms have greater exposure to the outdoor environment than internal rooms. The north–south orientation of opening was chosen to reflect a typical dormitory condition allowing natural airflow, while also keeping the room geometry consistent for comparison across floors. Since boundary conditions remain consistent across these rooms in plan, observed differences in lighting and thermal performance can reasonably be attributed to factors that vary with floor level, primarily solar exposure, wind availability, and proximity to the roof, all of which influence indoor temperatures in meaningfully different ways within the Bangladeshi climatic context.

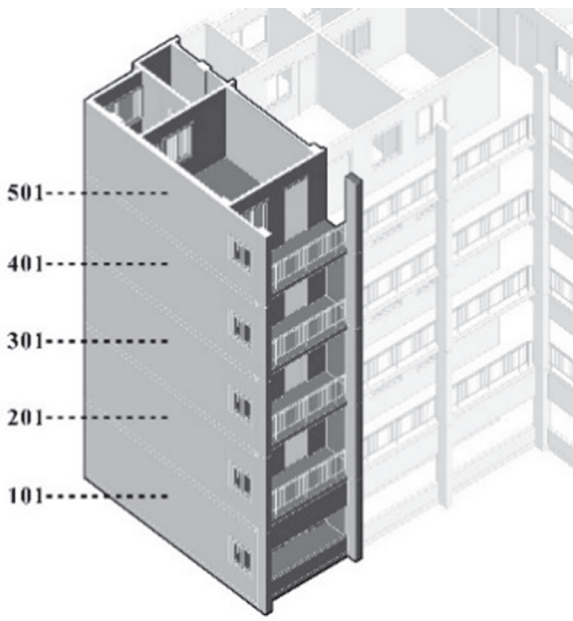


Fig. 3: 3D model of the case building.

2.4 Base Case Model

Simulation models were built based on the actual building design and documented material properties. Rhinoceros 3D with the Grasshopper plugin was used to model building surfaces and assign EnergyPlus material properties to envelope components. The Dhaka .epw climate file provided the weather dataset. Full-year daylight and thermal simulation was conducted with sDA, ASE, Mean Illuminance, and Percentage of Comfort and Discomfort Hours as the primary output. Occupancy density was set at 0.16 persons per square meter. Natural ventilation operated between indoor temperatures of 22°C and 28°C and outdoor temperatures of 17°C and 28°C, following EN 15251 thresholds.

2.5 Optimization Approach for Building Performance

Building performance optimization has become a standard part of architectural practice for addressing complex design challenges [17]. The process identifies maximum or minimum values of a function by manipulating variables within defined constraints [18]. Performance-based optimization typically combines parametric design, building simulation, and Genetic Algorithms [19]. A parametric design systematically varies parameters across a defined range to explore multiple solutions, supporting informed decision-making by identifying designs that meet predefined criteria [20]. The optimization framework consists of two components: design variables, defining geometric or physical characteristics, and objective functions, representing performance indicators assessed through simulation [21]

2.6 Multi-Objective Optimization

This step aims to optimize the WWR to simultaneously improve visual comfort by maximizing sDA, Mean Illuminance, Percentage of Comfort Hours and minimizing Percentage of Discomfort Hours. Since these objectives can conflict with one another in practice, the optimization produces a range of trade-off solutions rather than a single answer, from which appropriate design decisions can be drawn.

2.7 Optimization Parameters

Windows significantly influence a building's thermal performance due to their higher heat transfer coefficients compared to opaque envelope components. Window U-values are typically five times greater than those of walls or doors, accounting for 20% to 40% of building energy loss. Poor window design leads to thermal discomfort and increased energy consumption. While prior studies have explored optimal WWR for various climates, they often prioritize energy efficiency over thermal comfort. WWR ranging from 10% to 100% was used as the primary design parameter to evaluate its impact on visual and thermal environment.

2.8 Optimization Process

Multi-objective optimization was performed using the Octopus plugin within Grasshopper. Octopus uses an evolutionary algorithm that encodes design variables, in this study WWR, as genome within a population of candidate solutions. Each generation is evaluated against the fitness objectives, and through selection, crossover, and mutation, successive generations progressively move toward better-performing solutions across all criteria simultaneously. Figure 4 shows the script developed to run the optimization for each floor. The fitness objectives were defined as maximizing sDA, Mean Illuminance, Percentage of Comfort Hours and minimizing Percentage of Discomfort Hours.

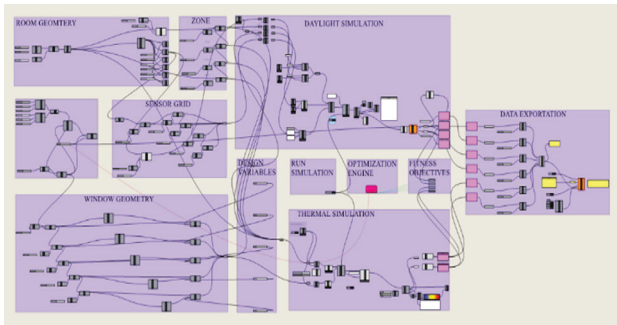


Fig. 4: Grasshopper script for optimization

The algorithm was configured with a population size of 50 and a maximum of 5 generations. the study used only one design genome, WWR, within a fixed range of 10–100%, so the search space was relatively small. A population size of 50 and 5 generations generated 250 candidate solutions per floor. This was used as a manageable Pareto-based design exploration rather than a claim of complete global convergence. The design variable and fitness objectives used for the optimization are shown in Fig. 5.

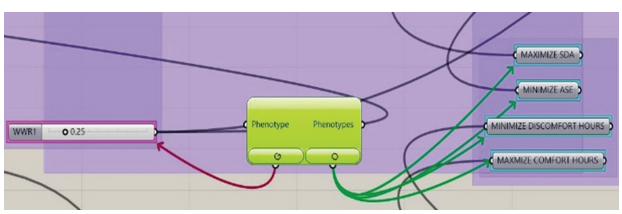


Fig. 5: Octopus genomes and fitness objectives

3. RESULTS AND DISCUSSION

The results were evaluated floor by floor to examine whether the same WWR can provide similar daylight and thermal performance across the vertical stack of the dormitory. Since the selected rooms have the same geometry, orientation, and spatial configuration, the variation in performance can mainly be attributed to differences in vertical position, including floor height, solar exposure, and thermal response. This directly supports the main objective of the study: to test whether WWR should be uniform across all floors or adjusted according to floor level.

3.1 Base Case Performance

Before optimization, the building's baseline performance was assessed for all five floors using daylight and adaptive thermal comfort indicators. Daylight levels were poor: sDA ranged from 4.76% to 9.52% and average illuminance was only 98 to 127 lux. ASE was 0% on every floor, indicating that direct sunlight was minimal, primarily because the existing windows allowed very little daylight into the spaces.

Adaptive comfort results were also unsatisfactory, with comfort scores between 40.17% and 42.02% and adaptive discomfort at 57.98% to 59.83%. Although the upper floors fared a little better, more than half of occupied hours still fell outside the adaptive comfort band.

Table II: Base case performance across each floor

Floor	sDA (%)	ASE (%)	Mean illuminance (lux)	Adaptive comfort (%)	Adaptive discomfort (%)
Ground floor	7.14	0	102	40.17	59.83
1st floor	4.76	0	98	41.11	58.89
2nd floor	9.52	0	102	41.48	58.52
3rd floor	9.52	0	123	41.78	58.22
4th floor	7.14	0	127	42.02	57.98

Overall, the base case provided inadequate daylight and offered poor thermal performance. This justified optimizing the window-to-wall ratio to increase daylight availability and reduce adaptive discomfort across the floors.

3.2 Best Daylight Performance Solutions

The first stage of the results analysis identified the best daylight solution for each floor. The goal was to find the smallest window-to-wall ratio (WWR) that produced 100% sDA while also keeping mean illuminance at a strong level. Larger WWRs, such as 100%, did increase mean illuminance but are not ideal design recommendations because too much glazing can worsen thermal comfort. For that reason, the preferred daylight solution was the minimum WWR that achieved full daylight autonomy, not the largest possible glazing area. Since ASE remained 0% for all tested WWR configurations across all floors, it showed no performance variation and was therefore excluded from the final optimization analysis.

Table III: Best daylight performance solutions for all floors

Floor	WWR (%)	sDA (%)	Mean Illuminance (lux)	Adaptive comfort (%)	Adaptive discomfort (%)
Ground floor	65	100	680.39	71.42	28.58
1st floor	71	100	715.13	70.09	29.91
2nd floor	70	100	733.98	72.78	27.22
3rd floor	68	100	717.00	74.08	25.92
4th floor	66	100	693.89	74.70	22.46

All The results indicate that every floor can achieve full sDA, but each floor requires a different window-to-wall ratio (WWR) to do so. The necessary WWRs span from 65% to 71%, showing that daylight performance changes with floor level. Level 1 reaches 100% sDA at a WWR of 65%, whereas Level 2 needs 71%. Levels 3, 4, and 5 hit full sDA at 70%, 68%, and 66% WWR respectively.

This spread is important because it shows that a single WWR cannot be relied to deliver the same daylight outcome throughout the building. Even when room types are identical and stacked vertically, the minimum WWR needed for full daylight autonomy shifts depending on the floor. Looking at the cases that maximize daylight, Level 3 recorded the highest average illuminance, 733.98 lux at a 70% WWR. Level 1 reached full sDA with the smallest required WWR, 65%, and had an average illuminance of 680.39 lux. From a daylight-only perspective, the ideal WWR therefore lies roughly between 65% and 71%, varying by floor height.

The comfort analysis reveals that the brightest daylight solutions aren't always the most comfortable thermally. For example, even though Level 2 achieves 100% sDA at 71% WWR, its adaptive discomfort remains relatively high at 29.91%. This highlights the trade-off between maximizing daylight and keeping thermal conditions acceptable.

3.3 Best Thermal Performance Solutions

The second phase identified the optimal thermal strategy for each floor using the ASHRAE 55 adaptive comfort model. Strategies were selected to maximize occupants' adaptive comfort and to minimize adaptive discomfort percentage. Because the dormitory relies on natural ventilation, the adaptive approach is more appropriate than a fixed PMV/PPD metric; occupants in naturally ventilated settings generally accept a wider comfort range influenced by outdoor conditions and airflow.

Table IV: Best thermal performance solutions for all floors

Floor	WWR (%)	sDA (%)	Mean illuminance (lux)	Adaptive comfort (%)	Adaptive discomfort (%)
Ground floor	70	100	744.21	73.03	26.97
1st floor	60	83.3	569.17	72.46	27.54
2nd floor	65	97.6	659.57	73.57	26.43
3rd floor	65	97.6	668.18	74.17	25.83
4th floor	65	97.6	679.43	74.75	25.25

The best thermal solutions fall mostly within a WWR range of 60% to 70%. Level 1 achieved its top thermal result at 70% WWR, registering 73.03% adaptive comfort and 26.97% adaptive discomfort. Level 2 reached its best thermal performance at a lower WWR of 60%, with adaptive comfort at 72.46%. Levels 3, 4, and 5 each showed their strongest thermal outcomes at 65% WWR.

This pattern shows that thermal behavior varies by floor: a WWR that works well on one level may not be ideal on another. At 65% WWR, Level 5 recorded the highest adaptive comfort, 74.75%, and the lowest adaptive discomfort, 25.25%. Level 4 was close behind at the same WWR, with 74.17% adaptive comfort. By contrast, Level 2's reduced WWR of 60% lowered discomfort but weakened daylight performance, producing only 83.3% sDA.

Taken together, the results imply that increasing WWR improves thermal performance only up to a limit. More glazing does not consistently lower discomfort and can raise heat gain. The best thermal results therefore occur within a controlled WWR band of roughly 60% to 70%, not at the maximum WWR values.

3.4 Pareto-Optimal Balanced Solutions

The final stage found Pareto-optimal balanced solutions by evaluating the four main objectives together: Maximizing sDA, Maximizing mean illuminance, maximizing adaptive comfort hour percentage and minimizing adaptive discomfort hour percentage

These objectives pull in different directions. Raising the WWR tends to improve daylight metrics and average illuminance, but it can also increase solar heat gain and reduce thermal comfort. Therefore, the best answer is not simply the largest WWR or the highest daylight reading. The Pareto-optimal solutions instead represent the best compromise between daylight performance and adaptive thermal comfort for each floor.

Table V: Pareto-optimal balanced solutions for all floors

Floor	WWR (%)	sDA (%)	Mean illuminance (lux)	Adaptive comfort (%)	Adaptive discomfort (%)
Ground floor	70	100	744.21	73.03	26.97
1st floor	60	83.33	569.17	72.46	27.54
2nd floor	65	97.62	659.57	73.57	26.43
3rd floor	65	97.62	668.18	74.17	25.83
4th floor	65	97.62	679.43	74.75	26.97

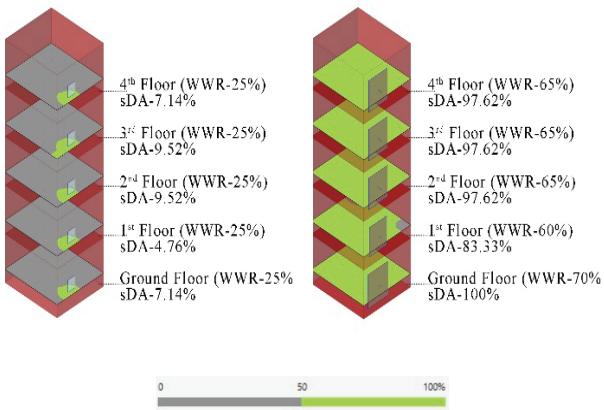
The Pareto analysis makes clear that a single WWR across all floors is not appropriate. The best WWRs lie between 60% and 70%, and they change with floor height. Level 1 needed 70% WWR to reach the best combined daylight and thermal result. Level 2 performed best at 60% WWR. Levels 3, 4, and 5 each found their optimum at 65% WWR.

This pattern backs the study's main point: daylight and thermal responses change with vertical position, even when room geometry and WWR are unchanged. For example, 65% WWR gives a balanced outcome on Levels 3–5, but Level 1 does better at 70% and Level 2 at 60%. Put differently, floor height alters daylight access, solar exposure, and thermal behavior, so the ideal WWR shifts by level. Level 5 at 65% WWR provides the best overall thermal balance: adaptive comfort 74.75%, adaptive discomfort 25.25%, and sDA 97.62%. Level 4 at 65% WWR is also strong, with 97.62% sDA, mean illuminance 668.18 lux, and 74.17% adaptive comfort. Level 3 shows a similar balanced result at 65% WWR. These outcomes indicate 65% WWR is a reliable choice for the upper floors, while the lower floors need different WWR settings.

Overall, the analysis recommends varying WWR by floor rather than using a single value across the whole façade. A floor-by-floor WWR approach lets the design respond to each level's specific daylight and thermal conditions.

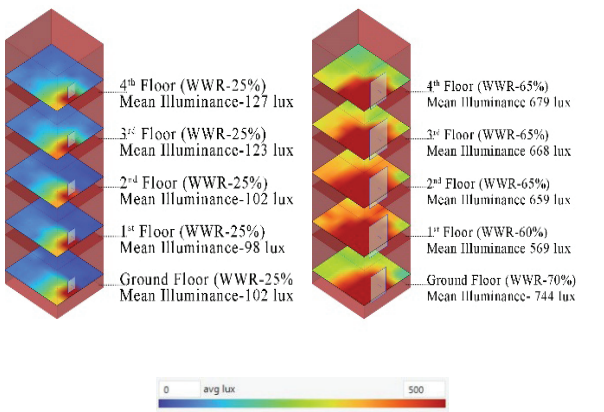
3.5 Comparison of Base Case and Optimal Case

After optimization, daylight performance improved markedly on every floor. sDA rose from 4.76–9.52% in the base case to between 83.33% and 100% in the optimized scenarios, and mean illuminance increased from 98–127 lux to 569.17–744.21 lux. Thermal comfort also got better. Comfort hours climbed from 40.17–42.02% up to 72.46–74.75%, while discomfort hours fell from 57.98–59.83% down to 25.25–27.54%. Figure 6-8 shows the comparison of the daylight and thermal performance of the base case and optimal test case.



(a) (b)

Fig. 6: (a) Base case sDA; (b) Test case sDA



(a) (b)

Fig. 7: (a) Base case Mean Illuminance; (b) Test case Mean Illuminance

Overall, the comparison demonstrates that optimizing WWR for each floor significantly enhances both daylighting and adaptive thermal comfort, showing that a single, uniform WWR is not appropriate across all floors.

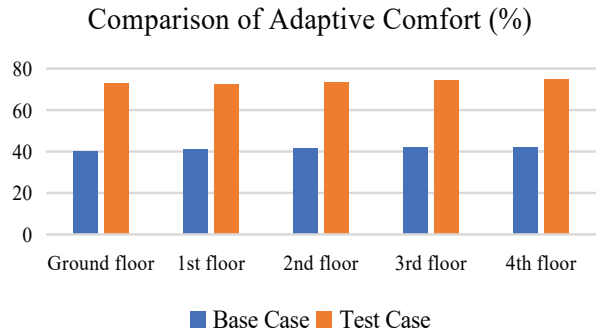


Fig. 8: Comparison of Adaptive Comfort Percentage between Base Case and Test Case

4. CONCLUSION

This research investigated whether a single, uniform window-to-wall ratio (WWR) can satisfactorily provide both daylight and thermal comfort for rooms on different floors of a naturally ventilated dormitory in a hot-humid climate. The study found that it cannot. Even though the selected rooms shared the same geometry, orientation, and layout, their daylighting and thermal outcomes differed with floor level, showing that vertical position matters when optimizing WWR.

The base case left every level underlit and thermally uncomfortable: sDA stayed under 10 percent, mean illuminance never exceeded 127 lux, and occupants spent more than half of their hours outside the adaptive comfort band. Once WWR was tuned for each floor, sDA climbed to between 83 and 100 percent, illuminance rose into the 569–744 lux range, and comfort hours nearly doubled to 72–75 percent, with discomfort cut to roughly a quarter of occupied time.

The improvement did not come from one universal setting, The ground floor needed a 70 percent WWR to balance daylight and heat gain, the first floor settled at 60 percent, and floors two through four converged on 65 percent. Although all of the rooms were built with the same template, the vertical position of the rooms in the building mattered in practice.

These findings push gently against how the BNBC (2020) currently treats windows: Solar Heat Gain Coefficient (SHGC) and Shading Coefficient (SC) limits are tied to WWR, but not to floor level. Our results indicate that incorporating floor-specific SHGC/SC limits, rather than applying a uniform requirement, could improve thermal performance and occupant comfort in naturally ventilated dormitories under this climate.

It needs to be added that, the five floors if Gazipur do not speak for every climate, orientation, or dormitory typology, and everything reported here comes from simulation rather than measurements inside occupied rooms. WWR was also the only variable in play; shading devices, glazing specification, infiltration, and how occupants actually operate their windows were all held constant. Future research should include field validation and examine a broader range of facade parameters and building typologies.

ACKNOWLEDGEMENT

This work was supported by "Teachers' Research Fund" of DUET, Gazipur. The authors would like to thank all the committee members of "CASR, DUET" for selecting this research to support. Special thanks go to Head, Department of Electrical and Electronic Engineering and Director, Research and Extension for their continuous support during the research.

REFERENCES

[1] H. Ben, S. Walker, and P. Desnerck, "The impact of adaptive thermal comfort on energy savings in office buildings under various insulation levels," in Proc. ACEEE Summer Study on Energy Efficiency in Buildings, 2024.

[2] M. Alwetaishi, "Investigation into energy performance of a school building in a hot climate: Optimum of window-to-wall ratio," Indoor Built Environ., vol. 29, no. 1, pp. 24–39, 2019, doi: 10.1177/1420326X19842313.

[3] D. Kurniawan et al., "Effect of building shape, orientation, window to wall ratios and zones on energy efficiency and thermal comfort of naturally ventilated houses in tropical climate," Apr. 2026.

[4] K. G. Al-Anzi and M. S. Krarti, "Impact of window parameters on the building envelope on the thermal comfort, energy consumption and cost and environment," Energy Build., vol. 108, pp. 307–316, 2015, doi: 10.1016/j.enbuild.2015.09.024.

[5] Y. Yang, J. Yin, J. Cai, X. Wang, and J. Zeng, "Study on the influence of window size on the thermal comfort of traditional one-seal dwellings (Yikeyin) in Kunming under natural wind," Buildings, vol. 15, no. 15, Art. no. 2714, 2025, doi: 10.3390/buildings15152714.

[6] N. M. Al-Tamimi, S. F. Syed Fadzil, and W. M. Wan Harun, "The effects of orientation, ventilation, and varied WWR on the thermal performance of residential rooms in the tropics," J. Sustain. Dev., vol. 4, no. 2, pp. 142–149, Apr. 2011, doi: 10.5539/jsd.v4n2p142.

[7] G. Chiesa, A. Acquaviva, M. Grosso, L. Bottaccioli, M. Floridia, E. Pristeri, and E. Sanna, "Parametric optimization of window-to-wall ratio for passive buildings adopting a scripting methodology to dynamic-energy simulation," Sustainability, vol. 11, no. 11, Art. no. 3078, Jun. 2019, doi: 10.3390/su11113078.

[8] A. N. Nair et al., "Multi-objective building retrofit optimisation: Balancing energy efficiency and comfort using XGBoost, SHAP, and MOBO," in Proc. 19th IBPSA Conf., Brisbane, Australia, Aug. 2025, doi: 10.26868/25222708.2025.1345.

[9] T. Xia, A. S. Ali, and N. Mahyuddin, "Multi-objective optimization of window design for energy and thermal comfort in school buildings: A sustainable approach for hot-humid climates," Sustainability, vol. 17, no. 19, pp. 1–34, Sep. 2025.

[10] Z. Wu, Y. Xu, and Z. Wang, "Multi-objective optimization of energy, view, daylight and thermal comfort for building's fenestration and shading system in hot-humid climates," PLoS ONE, vol. 20, no. 6, p. e0325290, Jun. 2025, doi: 10.1371/journal.pone.0325290.

[11] Housing and Building Research Institute (HBRI), Bangladesh National Building Code (BNBC) 2020, Dhaka, Bangladesh: Ministry of Housing and Public Works, Government of the People's Republic of Bangladesh, 2021

[12] Illuminating Engineering Society of North America (IESNA), *IES LM-83-12: Approved Method: IES Spatial Daylight Autonomy (sDA) and Annual Sunlight Exposure (ASE)*, New York: IESNA, 2012.

[13] Y. Liu, J. Wang, and H. Li, "Climate-based daylight modelling for spatial daylight autonomy assessment in building design," *Building and Environment*, vol. 228, pp. 109-124, 2023

[14] P. Pilechiha, M. Mahdavinejad, F. Pour Rahimian, P. Carnemolla, and S. Seyedzadeh, "Multi-objective optimisation framework for designing office windows: quality of view, daylight and energy efficiency," *Applied Energy*, vol. 261, pp. 114-356, 2020.

[15] ISO/CIE, ISO/CIE 10916:2024 Daylight in Buildings. Geneva, Switzerland: International Organization for Standardization, 2024.

[16] CEN, EN 16798-1:2019 Energy Performance of Buildings — Part 1: Indoor Environmental Input Parameters for Design and Assessment of Energy Performance of Buildings Addressing Indoor Air Quality, Thermal Environment, Lighting and Acoustics. Brussels, Belgium: European Committee for Standardization, 2019.

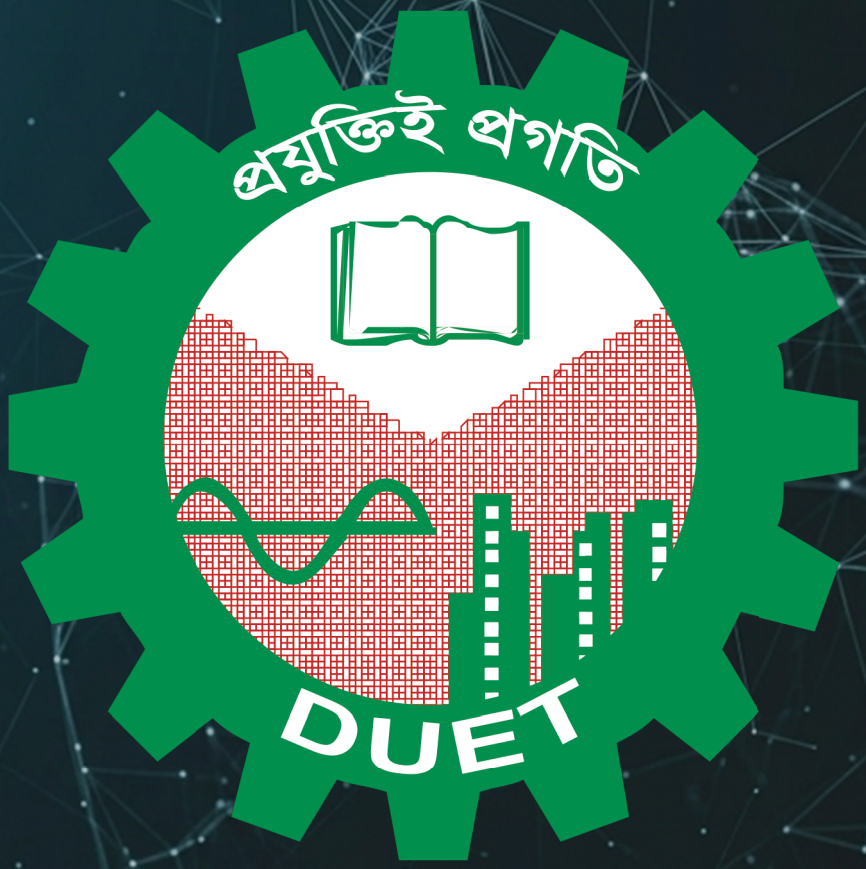
[17] V. Machairas, A. Tsangrassoulis, and K. Axarli, "Algorithms for optimization of building design: A review," *Renewable and Sustainable Energy Reviews*, vol. 31, pp. 101-112, 2014.

[18] K. Negendahl, "Building performance simulation in the early design stage: An introduction to integrated dynamic models," *Automation in Construction*, vol. 54, pp. 39-53, 2015.

[19] R. Evins, "A review of computational optimisation methods applied to sustainable building design," *Renewable and Sustainable Energy Reviews*, vol. 22, pp. 230-245, 2013.

[20] M. Qingsong and H. Fukuda, "Parametric design and performance optimization of building facades," *Frontiers of Architectural Research*, vol. 9, no. 1, pp. 1-18, 2020.

[21] X. Shi, Z. Tian, W. Chen, B. Si, and X. Jin, "A review on building energy efficient design optimization from the perspective of architects," *Renewable and Sustainable Energy Reviews*, vol. 65, pp. 872-884, 2017.



Web: jesa.duetbd.org